UNIVERSITY OF SOUTHAMPTON
Faculty of Engineering and Physical Sciences
Aerodynamics and Flight Mechanics

Dispersion of Small Inertial Particles in Characteristic Atmospheric Boundary Layer Flows

by Thorsten Wittemeier

Supervisor: Prof. John Shrimpton
Co-supervisor: Dr. Zheng-Tong Xie

Thesis for the degree of Doctor of Philosophy

October 18, 2021

UNIVERSITY OF SOUTHAMPTON

ABSTRACT

FACULTY OF ENGINEERING AND PHYSICAL SCIENCES
AERODYNAMICS AND FLIGHT MECHANICS

Dispersion of Small Inertial Particles in Characteristic Atmospheric Boundary Layer Flows

by Thorsten Wittemeier

The aim of this work is to improve the accuracy of atmospheric dispersion modelling for small inertial particles. Using data available in the literature it could be shown that small particles in the order of $1\,\mu m$ are expected to exhibit dispersion behaviour similar to a gas, whereas particles of diameters $\sim 10\,\mu m$ are expected to be dominated by inertia in windy situations and dominated by gravity during calm weather. Direct numerical simulations of particles in homogeneous isotropic turbulence confirm this observation. Estimates of the near-wall behaviour of atmospheric aerosols suggest that both at the ground and at building walls particle clustering can be expected to be a relevant process that potentially has a strong influence on the results in urban dispersion modelling.

A universal scaling relation for the concentration-based D measure for particle clustering in homogeneous isotropic turbulence has been established, which suggests that simulations at moderately high Reynolds numbers can be sufficient to understand the small-scale behaviour of particles. This needs to be confirmed for more complex flows.

In order to obtain realistic simulation results, real validation data is needed. So far it has been considered difficult to use anything other than wind-tunnel data for the validation of time-resolved atmospheric dispersion simulations. A new method that is robust enough to evaluate noisy time series has been developed in this work. One of its distinguishing features is the fact that it gives stronger weight to good-quality releases than to bad-quality (i.e. low dosage) releases. These filtering properties allow for the evaluation of field data without the need to introduce empirical thresholds. Therefore the method is objective and reliable in situations where established methods have not been successful.

The DNS code PANDORA 2.0 has been extended to allow for any form of homogeneous turbulence that can be described by a deformation tensor for the mean flow. First tests of shear flow simulations show typical characteristics of homogeneous shear flows in terms of shear stresses, turbulent kinetic energy and the development of elongated structures. However, further verification and validation is needed.

Acknowledgements

I would like to use the opportunity to thank my supervisor, Prof. John Shrimpton, and my co-supervisor, Dr. Zheng-Tong Xie, as well as our industrial partners from the Defence Science Technology Laboratory (DSTL), Tim Foat, Dr. Steven Herring and Dr. Simon Parker, for their support. Each and every one of these people have provided very constructive and helpful feedback and have helped me to understand the topic of my PhD project from a broad variety of different viewpoints.

This research is funded by the Defence Science Technology Laboratory (DSTL) and by EPSRC under Centre for Doctoral Training grant EP/L015382/1. Additional computing resources were provided by the EPSRC under the standard research grant EP/L000261/1 (UK Turbulence Consortium) as well as within the EPSRC-funded project e639 'Dispersion of Small Heavy Particles in Linear Shear Turbulence'. I acknowledge the use of the IRIDIS High Performance Computing Facility, and associated support services at the University of Southampton, as well as the ARCHER UK National Supercomputing Service (http://www.archer.ac.uk) in the completion of this work.

Contents

Nomenclature

Latin

$\hat{p}$	Wavespace pressure
$\hat{\mathbf{c}}$	Nonlinear term
$\hat{\mathbf{u}}$	Wavespace velocity
$\langle S_{ij} \rangle$	Mean rate of strain
$\langle u \rangle$	Mean velocity
C_ϵ	Dissipation constant (Kolmogorov)
D	D measure
$D(t)$	Turbulent diffusivity
d_p or d	Particle diameter
g	Gravity acceleration
$g(r)$	Radial distribution function
k	Wavenumber
L	Integral length scale
m_f	Fluid mass displaced by a particle
m_p	Particle mass
N_p	Number of particles
P	Total number of particle pairs in the domain
P_r	Number of particle pairs at distance $r \pm \Delta r/2$
q	Turbulent kinetic energy
R_{ij}	Two-point correlation

S Shear rate

S_{ij} Rate of strain

s_{ij} Fluctuating rate of strain

T_E Eddy turnover time

u Velocity

u' Velocity fluctuation

u_* or u_τ Friction velocity

u_f Fluid velocity

u_p Particle velocity

V Volume of the domain

v_g Settling velocity

$\mathbf{k}$ Wave vector

Greek

δ_ν Viscous length scale

ϵ Dissipation rate

η Kolmogorov length scale

κ von Karman constant

λ Mean particle density

λ Taylor microscale

μ Dynamic viscosity

ν Kinematic viscosity

Φ_m Mass loading (of the dispersed phase)

ϕ_m Dimensionless wind shear

Φ_v Volume fraction (of the dispersed phase)

ρ_f Fluid density

ρ_p Particle density

σ Standard deviation of a measured particle distribution

$\sigma_{Poisson}$ Standard deviation of a Poisson distribution

τ_η Kolmogorov time scale

τ_ν Viscous time scale

τ_f Characteristic fluid time scale

τ_p Particle relaxation time

τ_w Wall shear stress

u_η Kolmogorov velocity

Symbols

ΔV_r Volume of a spherical shell of thickness Δr at centre distance r

Operators

$\Delta = \nabla^2$ Laplace operator

$\hat{}$ Fourier transform

$\langle\rangle$ Mean

$\nabla\cdot$ Divergence operator

∇ Gradient operator

$'$ Fluctuation

Subscripts

f Fluid

p Particle

Abbreviations

PM_{10} Size fraction of atmospheric particles collected by a sampler with a collection efficiency of 50 % at the upper cutpoint of $d_p = 10\,\mu m \pm 0.5\,\mu m$

DNS Direct Numerical Simulation

LES Large-eddy simulation

RANS Reynolds-averaged Navier Stokes

Non-dimensional numbers

Fr_η Kolmogorov scale Froude number

Re Reynolds number

Re_τ	Friction Reynolds number
Re_λ	Taylor-scale Reynolds number
S^*	Non-dimensional shear rate
Sc_p	Particle Schmidt number
St	Stokes number
St_η	Kolmogorov-scale Stokes number
St_τ	Friction Stokes number
v_g^*	Non-dimensional settling velocity

List of Figures

List of Tables

Research Thesis: Declaration of Authorship

Print name: Thorsten Wittemeier

Title of thesis: Dispersion of Small Inertial Particles in Characteristic Atmospheric Boundary Layer Flows

I declare that this thesis and the work presented in it are my own and has been generated by me as the result of my own original research.

I confirm that:

1. This work was done wholly or mainly while in candidature for a research degree at this University;

2. Where any part of this thesis has previously been submitted for a degree or any other qualification at this University or any other institution, this has been clearly stated;

3. Where I have consulted the published work of others, this is always clearly attributed;

4. Where I have quoted from the work of others, the source is always given. With the exception of such quotations, this thesis is entirely my own work;

5. I have acknowledged all main sources of help;

6. Where the thesis is based on work done by myself jointly with others, I have made clear exactly what was done by others and what I have contributed myself;

7. Parts of this work have been published as:

Wittemeier, T., & Shrimpton, J. S. (2018). Explanation of differences in experimental and computational results for the preferential concentration of inertial particles. Computers & Fluids, 173, 37-41.

Wittemeier, T., Foat, T. G., Herring, S., Shrimpton, J. S., & Xie, Z. T. (2019). A new method for the evaluation of puff dispersion field experiments for the validation of time-resolved dispersion simulations. Atmospheric Environment, 210, 171-176.

Signature:

Date:

Chapter 1

Introduction

Whereas atmospheric aerosols exist at sizes from less than $1\,\mu m$ to various hundreds of micrometres, it is the respirable fraction that is of utmost importance in the context of hazards [52].

Comparatively few studies are dedicated to the dispersion of fine particles in the atmospheric boundary layer [15] and quantitative measurement data on their dispersion characteristic is scarce [53]. While there exist methods that specifically address certain aspects of particle dispersion [16, 26, 90, 45], often it is simply approximated as a gas [53]. However, the few available data on simultaneous particle and gas dispersion show that their behaviour is decidedly different [18, 31]. The approximation as a gas is more likely to be true in a rural environment and usually does not work very well in urban environments [53].

Large-eddy simulations applied to the atmospheric boundary layer can typically be resolved at length scales in the order of metres [12, 23]. On the other hand, small heavy particles exhibit a very distinguished behaviour at the smallest turbulent scales [83, 106] that in the atmospheric boundary layer are typically on the order of $\sim 1\,mm$ [111].

The goal of this work is to improve the accuracy of atmospheric dispersion modelling for small heavy particles, which, as the above considerations show, is a non-trivial task. There should be a clear outcome in the form of a suitable subgrid-scale model that can be used in large-eddy simulations.

As will be seen in the following chapter, both the fluid subgrid-scale and the small-scale behaviour of particles pose considerable difficulties in this context. Two standard approaches for improving and validating subgrid-scale models, the a priori and a posteriori analysis, will be presented. Whereas the goal of the latter is to compare LES results to validation data (either from DNS or experiments), the former provides direct insight into the physics of a model by comparing filtered and exact velocities (and any results based on them) directly within a direct numerical simulation.

This thesis starts with the modest task of identifying the expected characteristic behaviour of typical small heavy particles in the atmospheric boundary layer and getting an idea of their relevance. Particle characteristics and typical atmospheric turbulent conditions are gathered from the available literature and direct numerical simulations of homogeneous isotropic turbulence with small heavy particles are presented

In **chapter 2** an introduction to turbulent flows and the dispersion of small heavy particles in turbulent flows is given, followed by an overview of particles in the atmospheric boundary layer. Based on typical particle and atmospheric characteristics, estimates of the relevant Stokes and Froude numbers are given.The chapter finishes with an overview of numerical methods with a focus on the pseudospectral simulation of turbulent flows and the simulation of particles in turbulent flows.

A new method for the evaluation of field experiments is presented in **chapter 3**. It is shown how reliable validation quantities at the shortest measurable time scales can be obtained from tracer gas releases in the atmospheric boundary layer. This method will be applied to existing experimental data during the course of the PhD.

Chapter 4 contains the results of direct numerical simulations of particles in homogeneous isotropic turbulence and gives a first idea about the behaviour of typical atmospheric aerosols.

In order to progress from isotropic simulations to more complex flows, in particular homogeneous shear flows, a new improved version of the pseudospectral direct numerical simulation code PANDORA was developed. **Chapter 5** introduces the modified code. The improved version PANDORA 2.0 is described and the development of additional code for homogeneous turbulence using the Rogallo transform is presented. Furthermore extensive validation simulations and grid convergence studies are presented.

While the simulations in chapter 5 demonstrate the usefulness of the homogeneous shear flow code at low Reynolds numbers, in **chapter 6** high-Reynolds number simulations of homogeneous shear flows are presented and results compared to measured fluid statistics. The dispersion of passive and inertial particles at these higher Reynolds numbers is investigated.

The main focus of **chapter 7** is the usefulness of rapid distortion theory for the development of particle subgrid models for atmospheric large-eddy simulations. Inviscid and viscous rapid distortion theory approximations are compared to results from direct numerical simulations.

Finally in **chapter 8** the results are discussed and suggestions for future work based on these results are given.

Chapter 2

Background

This chapter gives an introduction to turbulent flows and the dispersion of small inertial particles in turbulent flows, followed by an overview of particles in the atmospheric boundary layer. The chapter finishes with an overview of numerical methods with a focus on the pseudospectral simulation of turbulent flows and the simulation of particles in turbulent flows.

In order to understand the turbulent dispersion of heavy particles in the atmospheric boundary layer, it is necessary to have an understanding of turbulent flows as well as the movement of particles in these flows. Therefore this chapter starts with an overview of the characteristics of turbulent flows, followed by an introduction to the dispersion of small inertial particles in turbulent flows and a summary of some of the most important results in the context of the project.

In the section about dispersion of small inertial particles in the atmospheric boundary layer, the current understanding of the atmospheric surface layer is summed up, followed by a summary of typical characteristics of common atmospheric aerosols. Finally a short overview of the state of the art in atmospheric dispersion modelling for small inertial particles will be given.

The rest of this chapter focuses on numerical methods for the simulation of turbulent flows, with an emphasis on pseudospectral methods, and the simulation of particles.

2.1 Turbulent flows

2.1.1 Properties of turbulent flows

The overwhelming majority of flows in nature, in particular the motion of air in the earth's boundary layer, is turbulent by nature [119]. Turbulent flows are three-dimensional

and are dominated by rotational motions, which play a crucial role in the transfer of energy from larger to smaller scales of motion [74]. Another important characteristic of turbulent flows is their randomness [119]. An event is random if it is neither certain nor impossible, but there is a probability that it may occur [93]. Due to its randomness statistical approaches are the preferred method of describing turbulence [119].

The behaviour of a flow can be characterised through a *Reynolds number Re* that relates its characteristic length scale L_{char}, its characteristic velocity scale U_{char} and the kinematic viscosity ν of the fluid [74]:

$$Re = \frac{L_{char} U_{char}}{\nu} \tag{2.1}$$

Geometrically similar flows are expected to behave similarly if their Reynolds number is the same [93].

A velocity field is *statistically stationary* if its moments are invariant under a shift in time, *statistically homogeneous* if its moments are invariant under a shift in space, and *statistically isotropic* if its moments are invariant under a rotation or reflection of the coordinate system [93].

If a velocity field is statistically stationary, it can be decomposed into a mean and a fluctuating part, the Reynolds decomposition [119]:

$$u_i = \langle u_i \rangle + u_i' \tag{2.2}$$

The mean $\langle\rangle$ can be understood as either the average of all possible values, weighted by the probability density function [93], or the time average [119]:

$$\langle u_i \rangle = \lim_{T \to \infty} \frac{1}{T} \int_{t_0}^{t_0+T} u_i \, \mathrm{d}t \tag{2.3}$$

The change in velocity at a fixed point in space can be described by the substantial derivative in conservative form [93]:

$$\frac{\mathrm{D}u_j}{\mathrm{D}t} = \frac{\partial u_j}{\partial t} + \frac{\partial}{\partial x_i} \left(u_i u_j \right). \tag{2.4}$$

It can be shown that the mean change in velocity is [93]:

$$\left\langle \frac{\mathrm{D}u_j}{\mathrm{D}t} \right\rangle = \frac{\partial \langle u_j \rangle}{\partial t} + \langle u_i \rangle \frac{\partial \langle u_j \rangle}{\partial x_i} + \frac{\partial}{\partial x_i} \left\langle u_i' u_j' \right\rangle. \tag{2.5}$$

The products $\left\langle u_i' u_j' \right\rangle$ of the velocity fluctuations form the *Reynolds stress tensor*, where the diagonal components ($i = j$) are the *normal stresses* and the off-diagonal components are the *shear stresses* [119]. The *turbulent kinetic energy* q is defined as half the trace of the Reynolds stress tensor [93]:

$$q = \left\langle \frac{u_i' u_i'}{2} \right\rangle . \tag{2.6}$$

The *rate of strain* S_{ij} of a flow is described by [93]

$$S_{ij} = \frac{1}{2} \left(\frac{\partial u_i}{\partial x_j} + \frac{\partial u_j}{\partial x_i} \right) \tag{2.7}$$

Using the Reynolds decomposition, the rate of strain can be decomposed into a mean rate of strain $\langle S_{ij} \rangle$ and a fluctuating rate of strain s_{ij} [93]:

$$\langle S_{ij} \rangle = \frac{1}{2} \left(\frac{\partial \langle u_i \rangle}{\partial x_j} + \frac{\partial \langle u_j \rangle}{\partial x_i} \right) \tag{2.8}$$

$$s_{ij} = S_{ij} - \langle S_{ij} \rangle = \frac{1}{2} \left(\frac{\partial u_i'}{\partial x_j} + \frac{\partial u_j'}{\partial x_i} \right) \tag{2.9}$$

In a steady homogenous pure shear flow with constant mean strain rate, the following relation between the mean strain rate and the fluctuating strain rate can be derived [119]:

$$- \left\langle u_i' u_j' \right\rangle \langle S_{ij} \rangle = 2\nu \langle s_{ij} s_{ij} \rangle . \tag{2.10}$$

The left-hand side term is the *turbulent production* P [119]:

$$P = - \left\langle u_i' u_j' \right\rangle \langle S_{ij} \rangle \tag{2.11}$$

and the right-hand side term is the *viscous dissipation* ϵ [119]:

$$\epsilon = 2\nu \langle s_{ij} s_{ij} \rangle \tag{2.12}$$

2.1.2 Homogeneous isotropic turbulence (HIT)

When a turbulent flow has no mean velocity gradient, it will decay, because it has no source of energy [119]. In order to maintain homogeneous isotropic turbulence in

simulations, a variety of forcing schemes have been devised to compensate the energy loss (for example [89] [35]). In wind tunnel experiments, homogeneous isotropic turbulence is approximated by observing the decaying turbulence downstream of a grid [51]. Hwang and Eaton [57] used jet actuators to produce near-isotropic turbulence without a mean flow inside a turbulence chamber.

Homogeneous isotropic turbulence is of enormous importance, because most of turbulence theory is based on it [93]. It has been intensively studied in fundamental turbulence research [123], but also in the context of the behaviour of inertial particles in turbulent flows [83].

Turbulent flows can be characterised by the *two-point correlation* R_{ij} between the velocity $u_j(\mathbf{x})$ at a point $\mathbf{x}$ and the velocity $u_i(\mathbf{x}+\mathbf{r})$ at distance $\mathbf{r}$ from this point [93]:

$$R_{ij}(\mathbf{r},t) = \langle u_i(\mathbf{x}+\mathbf{r})u_j(\mathbf{x})\rangle \,. \tag{2.13}$$

In homogeneous turbulence, by definition R_{ij} is independent of the location $\mathbf{x}$.

In homogeneous isotropic turbulence R_{ij} can be expressed in terms of a longitudinal scalar function $f(r)$ and a transverse scalar function $g(r)$ [93]. The (longitudinal) *integral length scale* L is defined as the integral of $f(r)$ over r [93]. The *eddy turnover time* T_E, the time scale characterising the energy-containing eddies, can be expressed using the turbulent intensity u' and the integral length scale L as [35]

$$T_E = \frac{L}{u'} \tag{2.14}$$

The *Taylor microscale* λ is defined through the second derivative of $f(r)$ [93]:

$$\lambda = \left[-\frac{1}{2}\frac{\partial^2 f(r)}{\partial r^2}_{r=0}\right]^{-1/2} . \tag{2.15}$$

Using the turbulent intensity u' and the Taylor microscale λ as the characteristic velocity and length scales, a Taylor-scale Reynolds number Re_λ is defined as [93]:

$$Re_\lambda = \frac{u'\lambda}{\nu} \tag{2.16}$$

One of the fundamental statements of the famous theory proposed by Kolmogorov in 1941 [69] is that the energy spectrum of isotropic turbulence is fully determined by the kinematic viscosity ν and the dissipation rate ϵ [74]. Energy is transferred from large eddies to smaller eddies and then transformed into heat by viscous energy dissipation

[119]. The length scale below which viscosity becomes dominant, the *Kolmogorov length scale*, is defined as [74]

$$\eta = \left(\frac{\nu^3}{\epsilon}\right)^{1/4}. \tag{2.17}$$

Analogously a *Kolmogorov time scale* τ_η and a *Kolmogorov velocity* u_η can be defined as [93]

$$\tau_\eta = \left(\frac{\nu}{\epsilon}\right)^{1/2}. \tag{2.18}$$

and

$$u_\eta = (\nu\epsilon)^{1/4}. \tag{2.19}$$

A *Kolmogorov acceleration* can be defined as [59]

$$\left(\frac{\epsilon^3}{\nu}\right)^{1/4}. \tag{2.20}$$

In the centre of the energy spectrum of isotropic turbulence there is an *inertial range* in which the turbulent kinetic energy decays with $k^{-5/3}$ where k is the wavenumber.

Based on the assumption of local isotropy, it is expected that the dissipation rate is related to turbulent kinetic energy and the integral length scale through a universal constant C_ϵ [123]:

$$\epsilon = C_\epsilon \frac{u'^3}{L} \tag{2.21}$$

This also leads to the following relation between the ratio of integral and Taylor length scales and the Taylor-scale Reynolds number [123]:

$$\frac{L}{\lambda} \sim C_\epsilon Re_\lambda \tag{2.22}$$

Whereas for statistically stationary isotropic turbulence many workers, both through grid turbulence and numerical simulations, have found indications that C_ϵ is indeed constant [123], this seems not to be the case locally [22]. Furthermore it has been observed

that the instantaneous dissipation rate lags behind turbulent kinetic energy in a quasi-periodic oscillation [48].

2.1.3 Homogeneous shear flows

Homogeneous turbulent shear flows (HTSF) are often studied as the next step in complexity from isotropic turbulence [19]. Whereas they can be easily implemented in numerical simulations (e.g. [101], [19]), they can only be approximated in experiments in near-homogeneous *uniformly sheared flow (USF)* [121].

In simulations of homogeneous shear flows, Ahmed and Elghobashi [2] identified coherent structures, in particular spanwise vortex layers that are stretched and inclined towards the streamwise direction. Vanderwel and Tavoularis [121] observed in uniformly sheared flow in a water tunnel that shear was concentrated in large vortices with high shear rates that were separated by regions of near uniform velocity.

A homogeneous shear flow with a uniform mean shear rate S

$$S = \frac{\mathrm{d}\langle u \rangle}{\mathrm{d}y} \tag{2.23}$$

is characterised by its Taylor Reynolds number Re_λ and its non-dimensional shear rate S^* [112]:

$$S^* = \frac{Sq^2}{\epsilon}. \tag{2.24}$$

S^* measures the shear strength relative to the turbulence time scale [61].

2.1.4 Wall-bounded flows

At a solid wall the shear stress is entirely viscous, since the velocity at the wall disappears, and the wall shear stress is given by [93]:

$$\tau_w = \rho\nu \left(\frac{\mathrm{d}\langle u \rangle}{\mathrm{d}y} \right)_{y=0} \tag{2.25}$$

where y is the height. Based on the wall shear stress and the fluid density and viscosity, the relevant velocity scales and length scales can then be defined as [93]

$$u_* = \sqrt{\frac{\tau_w}{\rho}} \tag{2.26}$$

and

$$\delta_\nu = \nu\sqrt{\frac{\rho}{\tau_w}} = \frac{\nu}{u_*}, \tag{2.27}$$

where u_* is called *friction velocity* and δ_ν is called *viscous length scale.*

A *viscous time scale* can be defined as [106]

$$\tau_\nu = \frac{\nu}{u_*^2}. \tag{2.28}$$

A *friction Reynolds number* based on the friction velocity and a relevant length δ, in the case of a channel flow half the height of the channel, δ, is given by [93]

$$Re_\tau = \frac{u_*\delta}{\delta_\nu}. \tag{2.29}$$

Several characteristic (quasi-)coherent structures can be observed in boundary layers, of which *ejections* of low-speed fluid away from the wall and *sweeps* of high-speed fluid towards the wall are of particular importance [93].

Hunt and Morrison [56] found based on rapid distortion theory and experimental data that at lower Reynolds numbers ($Re_\tau < 10^4$ based on the boundary layer thickness), boundary layers are dominated by ejection events, whereas for $Re_\tau > 10^4$, as can be found in the atmospheric boundary layer, sweep events are expected to be more common. In contact with the wall, the downward moving structures develop inner boundary layers whilst the vertical velocity is forced to zero by blocking through the wall [55].

2.2 Dispersion of small inertial particles in turbulent flows

2.2.1 Movement of a single spherical particle in a fluid

If a particle is smaller than the smallest fluid scale, it can be considered a point particle [71]. The force on a point particle moving in a fluid can be described as [34]

$$
\begin{aligned}
m_p \frac{\mathrm{d}u_{p,i}}{\mathrm{d}t} \qquad & \text{(particle acceleration)} \\
= m_p \frac{1}{\tau_p}(u_{f,i} - u_{p,i}) \qquad & \text{(drag)} \\
+ m_f \frac{\mathrm{D}u_{f,i}}{\mathrm{D}t} \qquad & \text{(pressure gradient and viscous stresses)} \\
+ \frac{1}{2} m_f \left(\frac{\mathrm{D}u_{f,i}}{\mathrm{D}t} - \frac{\mathrm{d}u_{p,i}}{\mathrm{d}t_p} \right) \qquad & \text{(added mass)} \\
+ 6 d_p^2 (\pi \rho_f \mu)^{\frac{1}{2}} \int_{t_{p0}}^{t_p} \frac{\mathrm{d}/\mathrm{d}\tau (u_i - v_i)}{(t_p - \tau)^{\frac{1}{2}}} \mathrm{d}\tau \qquad & \text{(memory force)} \\
+ (m_p - m_f) g_i \qquad & \text{(buoyancy or gravity)}
\end{aligned}
\tag{2.30}
$$

where

- m_p: particle mass
- m_f: fluid mass displaced by the particle
- $u_{p,i}$: particle velocity in direction i
- $u_{f,i}$: fluid velocity in direction i at the position $x_{p,i}(t)$ of the particle
- μ: dynamic viscosity of the fluid
- ρ_f: fluid density

The particle relaxation time τ_p can be expressed as

$$
\tau_p = \frac{1}{18} \frac{\rho_p}{\rho_f} \frac{d_p^2}{\nu}, \tag{2.31}
$$

where ρ_p is the particle density, d_p the particle diameter and ν the kinematic viscosity of the fluid [76]. It can be understood as the time it takes for a particle to adapt to the instantaneous flow [71].

The drag and gravity forces are often the most relevant terms [34]. Whereas the memory term can be very significant for light particles, it is usually negligible for heavy particles ($\rho_p/\rho_f \gg 1$) [27]. Elgobashi and Truesdell analysed the magnitude of all forces in direct numerical simulations of turbulent flows at moderate Reynolds numbers and found that the presure and added-mass terms were always between one and three orders of magnitude smaller than the memory term [34].

2.2.2 Particles in turbulent flows

Multiphase flows in which the interface between the phases is not of importance and in which a dispersed phase, such as liquid or solid particles, is transported by a (often turbulent) carrier flow are known as dispersed multiphase flows [7]. The *volume fraction* Φ_v is the fractional volume occupied by the dispersed phase and the *mass loading* Φ_m is the ratio between the mass of the dispersed phase and the mass of the carrier phase [7]. If $\Phi_v < 10^{-5}$ or $\Phi_m < 10^{-2}$, the fluid flow is not affected by the dispersed phase [83]. Such a flow regime is called *one-way coupled* [7].

The behaviour of inertial particles in turbulent flows can be characterised by the *Stokes number*, defined as the ratio of the particle relaxation time τ_p and a representative time scale of the flow τ_f [40]:

$$St = \frac{\tau_p}{\tau_f} \tag{2.32}$$

In turbulent flows, often the Kolmogorov time scale τ_η is chosen as the representative fluid time scale, thus defining the *Kolmogorov-scale Stokes number* [83]:

$$St_\eta = \frac{\tau_p}{\tau_\eta} \tag{2.33}$$

One of the most important characteristics of turbulent motion is its ability to transport and mix matter, momentum or energy, which is often described as *turbulent diffusion* in analogy to molecular diffusion [119]. The transport of a fluid point or a particle can be described in terms of the mean square displacement $\langle x^2 \rangle$ by the turbulent diffusivity $D(t)$ [2]

$$D(t) = \frac{1}{2}\frac{d}{dt}\left\langle x^2(t)\right\rangle . \tag{2.34}$$

To compare the dispersion of particles to that of fluid points, a *turbulent Schmidt number* Sc_p can be defined as the ratio of the fluid point diffusivity D_f and the particle diffusivity D_p [34]:

$$Sc_p = \frac{D_f}{D_p}. \tag{2.35}$$

2.2.3 Preferential concentration of particles

In turbulent carrier flows, particles that are denser than the fluid tend to form clusters and depleted regions, a phenomenon commonly known as *preferential concentration* [83].

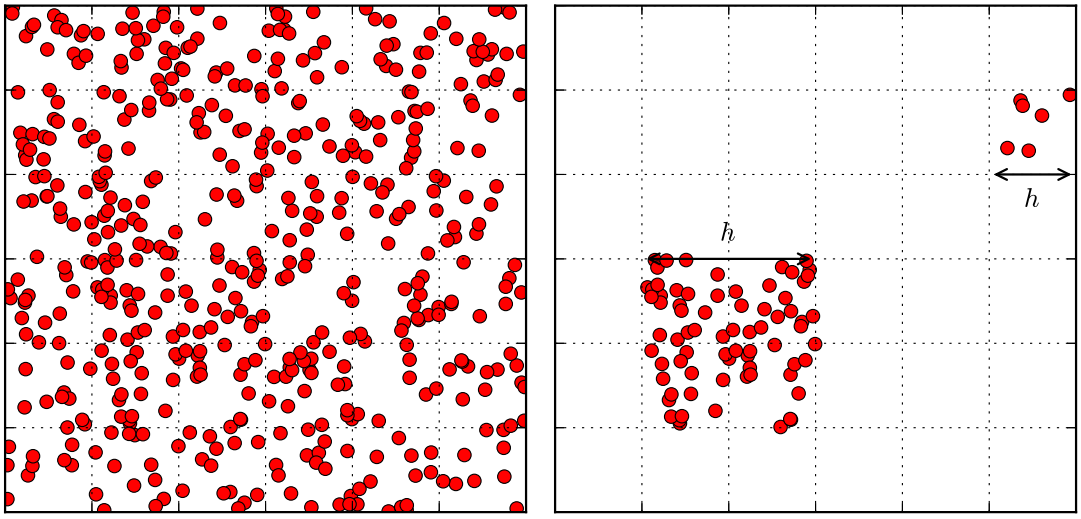

FIGURE 2.1: Illustration of binning of particles for determining the D measure.

To quantify preferential concentration, Fessler et al. [40] compared the standard deviation σ of a measured particle distribution to the standard deviation $\sigma_{Poisson}$ of a randomly positioned set of particles by defining the D measure:

$$D = \frac{\sigma - \sigma_{Poisson}}{\lambda} \tag{2.36}$$

where λ is the mean particle number per box. The mean particle number λ is determined by counting the particles in bins of a given size and depends on the chosen size [105], as illustrated in figure 2.1. From the definition it can be seen that $D = 0$ when the particle distribution is a Poisson distribution and $D < 0$ for a uniform particle distribution [40].

Aliseda et al. [3] found a maximum of D at bin sizes corresponding to $10\,\eta$ and concluded that $10\,\eta$ is a typical average cluster size. Wood et al. [132] observed a peak corresponding to Kolmogorov lengths between 8 and 20 and observed that the peak is at larger sizes for higher Stokes numbers.

Monchaux et al. [82] used Voronoi diagrams to quantify clustering. A Voronoi cell is the ensemble of points that are closer to a particle than to any other particle and its volume is therefore the inverse of local concentration [83]. As opposed to D, Voronoi diagrams do not require choosing a bin-size [82]. For a Poisson distribution, the standard deviation for a Voronoi cell can be determined analytically, which allows for a quantification of particle clustering [83].

Sundaram et al. [115] introduced the radial distribution function $g(r)$, which represents the number of particle pairs at a given separation compared to a uniform particle distribution [68]. It can be determined by counting all particles at a distance $r \pm \Delta r/2$ around each particle [67], or in other words by counting all particles in a spherical shell around

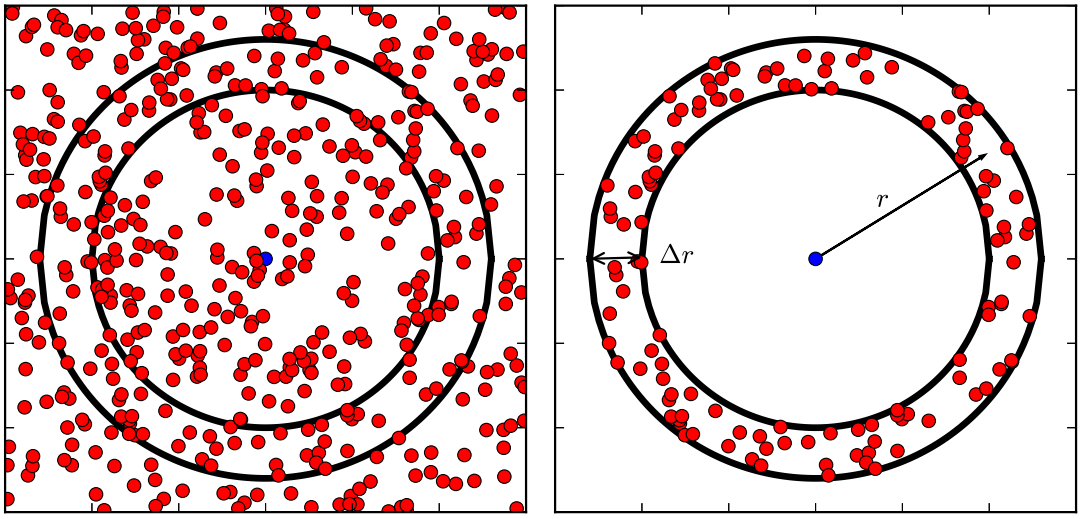

FIGURE 2.2: Annular shell around a particle for determining the radial distribution function (simplified two-dimensional illustration).

each particle [132], as shown in figure 2.2. The number of particle pairs in the volume of the spherical shell is then compared to the number of particles in the volume of the entire domain as follows, defining the radial distribution function $g(r)$ [67]:

$$g(r) = \frac{P_r/\Delta V_r}{P/V}, \tag{2.37}$$

where

P_r:	number of particle pairs at distance $r \pm \Delta r/2$
P:	total number of particle pairs in the domain
ΔV_r:	volume of a spherical shell of thickness Δr at centre distance r
V:	volume of the domain

For a given total number of particles N_p the total number of particle pairs in the domain is [98]

$$P = \frac{N_p(N_p - 1)}{2}. \tag{2.38}$$

Clustering of particles has been found over a wide range of Stokes numbers from $St_\eta = 0.05$ [58] up to several hundred [83]. In the centre plane of a channel flow, Fessler et al. [40] measured the strongest preferential concentration at $St_\eta \approx 1$. Wood et al. measured the preferential concentration of particles in a turbulence chamber with near-isotropic turbulence characteristics and observed the strongest clustering at Stokes numbers between $St_\eta \approx 0.57$ and $St_\eta \approx 1.33$. A maximum at $St_\eta \approx 1$ was found by several other workers using measurements and direct numerical simulations (e.g. [3],

[58]) and there is broad consensus that the strongest clustering occurs at St_η around unity [7].

In a recent wind-tunnel experiment at Re_λ between 230 and 400, Obligado et al. found peak preferential concentration at $St_\eta \approx 4$ [87], though they recognised that the effects of Stokes numbers, Reynolds numbers and volume fraction could not be easily separated due to the limited number of experiments. Sumbekova et al. performed wind-tunnel experiments over a wide range of Stokes numbers (between $St_\eta = 0.1$ and $St_\eta = 5$) and Reynolds numbers (between $Re_\lambda = 170$ and $Re_\lambda = 450$) [114]. They found no significant Stokes number dependence, but a strong dependence on both the Reynolds number Re_λ and the volume fraction Φ_v.

Collins and Keswani [28] studied the clustering of particles using direct numerical simulations of homogeneous isotropic turbulence at Re_λ between ~ 65 and ~ 150. They found that the radial distribution function $g(r)$ seems to reach a plateau at high Reynolds numbers. The results of recent simulations by Ireland et al. [58] at Re_λ up to ~ 600 appear to confirm this observation. The author of this report is not aware of results for higher Reynolds numbers.

Whereas the radial distribution function seems to become independent of the Reynolds number at sufficiently high Reynolds numbers, quantities based on particle concentration seem to exhibit a more complex behaviour. D has been observed to decrease with increasing Reynolds number [105]. Using Voronoi diagrams (and hence evaluating local particle concentrations), Obligado et al. found preferential concentration to increase up to $Re_\lambda = 300$ and then go down again [87]. However it was not possible to distinguish between Reynolds number and Stokes number effects in their experiments. Sumbekova et al. [114] performed a broader set of experiments and, using Voronoi diagrams, concluded that the preferential concentration of particles increases with the Reynolds number, whereas according to their results there is no Stokes number dependence.

In an experimental study based on Voronoi analysis, Monchaux et al. [82] found a non-linear dependence of the particle concentration inside clusters on the global particle loading (which in an experiment is usually equivalent to the volume fraction Φ_v [83]). Sumbekova et al. [114] observed a nonlinear increase of local particle concentrations inside clusters with the volume fraction in experiments at Reynolds numbers up to $Re_\lambda = 450$.

2.2.4 Gravity effects on particles in turbulent flows

The *settling velocity* v_g of a particle in a quiescent fluid is given by [52]

$$v_g = g\tau_p \tag{2.39}$$

where g is the gravitational acceleration. To characterise the settling of particles in a turbulent flow, a non-dimensional settling velocity can be defined as [67]

$$v_g^* = \frac{v_g}{u'} \tag{2.40}$$

where u' is the turbulence intensity.

A Froude number, defined as the ratio of turbulent acceleration and gravity acceleration, has been used in previous publications about the clustering of heavy particles [13, 59] to measure the effects of gravity independently of the particle relaxation time and hence independently of the Stokes number. Using the Kolmogorov acceleration, this can be expressed as [13]

$$Fr_\eta = \frac{\epsilon^{3/4}}{g\nu^{1/4}}. \tag{2.41}$$

Wang and Maxey [125] found that the settling velocity of particles in a turbulent flow is increased compared to the terminal velocity in a quiescent fluid. In numerical simulations at Reynolds numbers up to $Re_\lambda \approx 600$, Ireland et al. [59] found that for low Stokes numbers $St_\eta \leq 0.1$ the settling velocity is independent of the Reynolds number, whereas for higher Stokes numbers there is a Reynolds-number dependence. They also found that preferential concentration of particles is reduced at small and intermediate Stokes numbers and enhanced at higher Stokes numbers.

Aliseda et al [3] found that the increase in settling velocity depends on the global particle loading and that there is a quasi-linear relation between the local concentration and the settling velocity.

Elgobashi and Truesdell [34] investigated the effect of gravity on particle dispersion and found that lateral diffusivities are reduced by gravity, i.e. the turbulent Schmidt numbers are > 1.

2.2.5 Particles in shear flows

In direct numerical simulations of particles in homogeneous shear flow, Ahmed and Elghobashi [2] found that turbulent transport of particles in streamwise direction is significantly larger than in the lateral directions. They attributed this anisotropy to the interaction with spanwise vortex layers.

Nicolai et al. [85] released glass spheres with Stokes numbers $St = 0.3$ and $Re_\lambda = 540$ in a homogeneous shear flow in a water channel and observed preferential concentration. Furthermore they found that the anisotropy of the velocity fluctuations induces a preferential orientation of the particle clusters.

Vanderwel and Tavoularis [122] investigated the role of coherent structures in a uniformly sheared turbulent flow generated in a water tunnel. The dye used in the experiment was found to be preferentially accumulated far away from vortices and less likely to appear in close proximity to vortices. Hairpin vortices were found to be responsible for large scalar flux events. The scalar flux vector had a preferential inclination with respect to the streamwise direction. They found that dye that was injected to the vortex core stayed in the core, whereas dye injected outside the core was pushed outside the vortex or wrapped around it.

2.2.6 Particles in wall-bounded flows

Near a solid wall, particle motion is significantly influenced by coherent wall structures, which leads to the formation of particle streaks near the wall [65]. Vinkovic et al. [124] showed that in their direct numerical simulations of a channel flow the upward movement of particles coincided with ejection events. They observed preferential concentration of particles in regions of sweeps and ejections.

In experiments in an open channel flow, Niño and Garcia [86] observed that the deposition of particles to the wall were rarely associated with sweep events, but could rather be attributed to slow sedimentation to the wall. However, in an analysis of direct numerical simulations and large-eddy simulations of channel flows, Soldati and Marchioli [107] showed that the downward movement of lighter particles ($St \approx 0.1$) coincided strongly with sweeps.

A *friction Stokes number* St_τ that characterises the near-wall behaviour of particles can be established based on the viscous time scale τ_ν [76]:

$$St_\tau = \frac{\tau_p}{\tau_\nu} \tag{2.42}$$

Height [m]	Inertial Range Power Law
10	$k^{-1.4}$
1.01	$k^{-1.05}$
0.115	$k^{-0.83}$

TABLE 2.1: Power laws from atmospheric turbulence measurements at the Silsoe Research Institute [99]

2.3 Dispersion of small inertial particles in the atmospheric boundary layer

2.3.1 Structure of the atmospheric boundary layer

While the troposphere extends on average up to 11 kilometres from the ground, only the lowest part of the troposphere, the atmospheric boundary layer, exhibits some influence of the Earth's surface [111]. Its depth can vary from 30 metres in stable conditions to more than 3 kilometres in convective conditions [54]. Traditionally it is subdivided into a **surface layer** of about 100 metres, characterised by approximately constant shearing stress [116], and the layer above the surface layer up to about 1000 metres, the Ekman layer, in which there exists a balance between the Coriolis force, the pressure gradient force, and the viscous stress [54]. Above the Ekman layer, in the **free atmosphere**, surface friction may be neglected [116].

Turbulence is assumed to approach isotropy above the surface layer, but is strongly anisotropic closer to the ground [116]. In recent years, a further subdivision of the surface layer into an **eddy surface layer (ESL)** in the lowest ~ 10 metres and a **shear surface layer (SSL)** above the ESL has been proposed. Whereas the main process in the SSL is shear production of turbulence, the ESL is dominated by the interaction of turbulent structures with the wall [32].

Atmospheric turbulence measurements at the Silsoe Research Institute show that near the ground the decay of turbulent energy with wavenumber k does not follow a $k^{-5/3}$ [99]. The measured power laws, summarised in table 2.1, show that the high-wavenumber (i.e. small-scale) becomes more dominant with decreasing height.

2.3.2 Typical conditions in the atmospheric boundary layer

In the atmospheric boundary layer little change of air density and viscosity can be expected. Some typical values [111] are summarised in table 2.2 [111].

To get a quantitative idea about turbulence in the atmospheric boundary layer, some measurements in a low-level nocturnal jet [43] and during a frontal passage [92] have

Density	ρ_f	1.225	kg/m^3
Viscosity	ν	$1.461 \cdot 10^{-5}$	m^2/s

TABLE 2.2: Typical values of air density and viscosity in the atmosphere [111].

Source	$U[m/s]$	$\sigma_u(m/s)$	$\sigma_v(m/s)$	$\sigma_w(m/s)$	$\epsilon[m^2/s^3]$	$\eta[mm]$	Re_λ
Frehlich et al. [43]		0.14			$3.44 \cdot 10^{-4}$	1.77	1078
Piper et al. [92]	3.2	0.55	0.36	0.27	0.027	0.61	2000
Piper et al. [92]	6.3	1.33	0.98	0.54	0.105	0.42	5000
Piper et al. [92]	10.8	2.36	1.52	0.90	0.760	0.27	8000

TABLE 2.3: Some turbulent properties taken from measurements in the atmospheric boundary layer in a low-level nocturnal jet [43] and during a frontal passage [92].

been summarised in table 2.3. Reynolds numbers over a broad range from $Re_\lambda \approx 1000$ to $Re_\lambda \approx 8000$ can be found, and the Kolmogorov length varies from $\eta = 0.27$ to $\eta = 1.77$. The lowest values of the Kolmogorov length should be considered estimates rather than exact measurements due to instrumental limitations [92]. Although the dissipation rates summarised here range from $\epsilon \approx 10^{-4}$ to $\epsilon \approx 1$, lower values of $\epsilon \approx 10^{-6}$ can befound with a diurnal variation between the lowest dissipation rates at night time and the highest values at day time [111].

Some values for friction velocities in the atmosphere can be found in measurements during a frontal passage [92], covering a range between $u_* = 0.15\,m/s$ and $u_* = 0.85\,m/s$, and measurements in a developing stable boundary layer [24] with values between $u_* = 0.06\,m/s$ and $u_* = 0.31\,m/s$.

It is useful to define a dimensionless dissipation [133]

$$\frac{\kappa z \epsilon}{u_*^3}. \tag{2.43}$$

Under the assumption of horizontal homogeneity a dimensionless wind shear ϕ_m can be defined as [111]

$$\phi_m = \frac{\kappa z}{u_*} \frac{\partial \langle u \rangle}{\partial z}. \tag{2.44}$$

Using the above approximation of ϕ_m, some atmospheric shear rates can be estimated from [92]. The resulting dimensionless shear rates S^* are between 8.6 and 14, as summarised in table 2.4.

$u[m/s]$	$u_*[m/s]$	z/L	ϕ_m	$S[s^{-1}]$	$q^2/\epsilon[s]$	S^*
3.2	0.2	0.475	3.23	0.51	18.7	9.6
6.3	0.5	0.030	1.14	0.49	28.8	14.0
10.8	0.8	0.014	1.06	0.75	11.4	8.6

TABLE 2.4: Friction velocities u_* and shear rates during a frontal passage (based on data from [92])

Material	Density $[g/cm^3]$
Wood (dry)	0.4 - 1.0
Fly ash	0.7 - 2.6
Oils	0.88 - 0.94
Water	1.00
Granite	2.4 - 2.7
Iron	7.0 - 7.9
Lead	11.3
Mercury	13.6

TABLE 2.5: Densities of some common aerosol materials [52].

2.3.3 Properties of atmospheric aerosols

In order to estimate Stokes numbers of particles relevant for atmospheric dispersion, information about typical densities and sizes are needed.

The densities of some common aerosol materials [52] are summarised in table 2.5. The values range from $0.4\,g/cm^3$ to $13.6\,g/cm^3$.

Typical atmospheric particle diameters cover a broad range of sizes from less than $1\,\mu m$ to various hundreds of micrometres. In the context of hazards, the concept of respirable dust is commonly used. The aspiration efficiency, defined as the fraction of particles originally in a volume of air that enter the nose or mouth, ranges from about 70 to 100 % for particle diameters as large as $30\,\mu m$ [52].

However, only a small percentage of particles $> 15\,\mu m$ penetrate the trachea, limiting the direct health effects of these particle sizes to the upper respiratory tract. Particles smaller than about $2.5\,\mu m$ are of particular importance, since they are more likely to reach the gas-exchange region of the respiratory tract than larger particles [81].

Based on health considerations, PM_{10} has been defined as the size fraction of atmospheric particles collected by a sampler with a collection efficiency of 50 % at the upper cutpoint of $d_p = 10\,\mu m \pm 0.5\,\mu m$ [127].

2.3.4 Dispersion of particles

Compared to the dispersion of gases, far less studies have been published about the dispersion of particulate matter in the atmosphere [15]. In particular, there are only

very few field measurements that provide data for the simultaneous dispersion of gases and particles [53]. A comparison of available studies seems to suggest that in an open environment, the dispersion of particles is fairly similar to that of gases, whereas in urban areas particles exhibit a significantly different behaviour than gases. [53]

Blocken et al. [15] performed RANS simulations in which they treated particles as a gas. Bouvet et al. [16] used a modified Langevin equation that takes the particle settling velocity into account to simulate the small-scale behaviour of particles in a RANS simulation. They validated their simulations of glass bead deposition near a fence against field measurements and reached an agreement within about 30 %. Chamecki et al. [26] simulated the dispersion of pollen using large-eddy simulations in combination with an Eulerian advection-diffusion equation. They paremetrised the ground deposition through the lower boundary condition. Fuka and Brechler [45] carried out large-eddy simulations of radioactive particulate matter by solving an Eulerian equation for a passive scalar with additional gravitational settling and dry deposition. They found the results for surface contamination to be extremely sensitive to the particle size distribution, which lead to a large uncertainty.

Given the typical domain size of large-eddy simulations in the atmospheric boundary layer, a coarse resolution compared to typical particle sizes can be expected. In an intercomparison of large-eddy simulations [12] for a domain size of $400\,m \times 400\,m \times 400\,m$, grid resolutions between $1\,m$ and $12.5\,m$ were used. In simulations representing an urban street system, Castro et al. [23] used grid resolutions of 1/16 of the obstacle height.

2.4 Estimate of particle characteristics in the atmospheric boundary layer

Based on the turbulence characteristics of the atmosphere described in 2.3.2 and the properties of typical atmospheric aerosols described in 2.3.3, the behaviour of particles in the atmospheric boundary layer can be understood in terms of characteristic Stokes and Froude numbers. The following estimates are based on particle density of $1\,g/cm^3$, particle diameters between $1\,\mu m$ and $10\,\mu m$, dissipation rates between $10^{-6}\,m^2/s^3$ and $1\,m^2/s^3$ and friction velocities between $10^{-2}\,m/s$ and $1\,m/s$.

2.4.1 Particles far away from surfaces

In a first step it is assumed that the particles are far away from the ground or other solid surfaces like buildings. Assuming local isotropy, the small-scale particle behaviour can then be characterised by Kolmogorov-scale Stokes and Froude numbers.

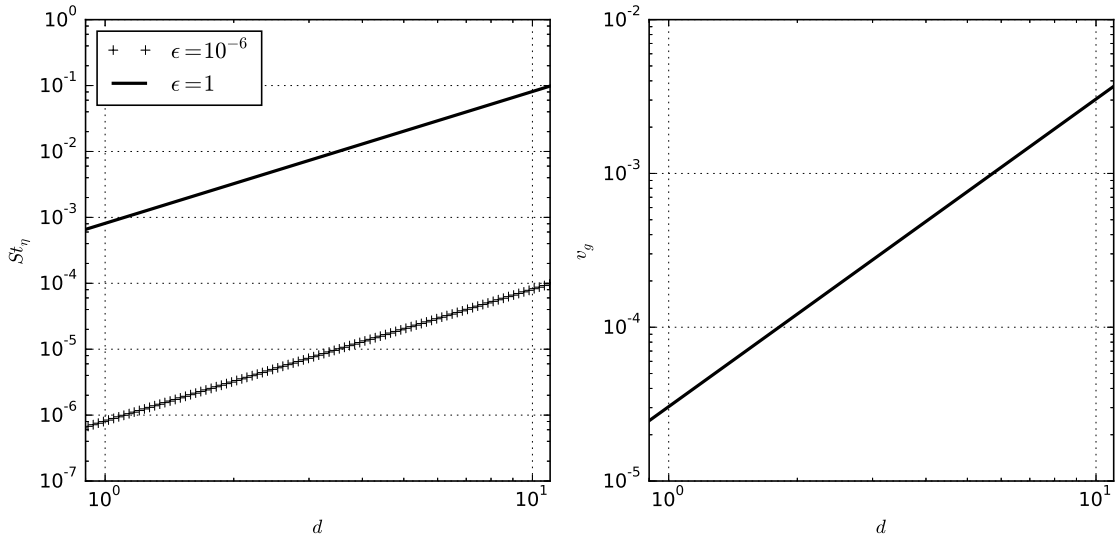

FIGURE 2.3: Particle characteristics as a function of diameter (in μm). Left: Kolmogorov scale Stokes number St_η. Right: settling velocity v_g (in m/s).

All estimates have been made by a simple application of the definition of St_η (2.34) and Fr_η (2.41).

The left-hand side of figure 2.3 shows the Kolmogorov-scale Stokes numbers St_η for particle diameters between $1\,\mu m$ and $10\,\mu m$ at two dissipation rates. $\epsilon = 10^{-6}\,m^2/s^3$ corresponds to very calm weather that is most likely to occur at night, whereas $\epsilon = 1\,m^2/s^3$ corresponds to very windy, turbulent situations. For the lower dissipation rate, Stokes numbers range from about 10^{-6} and 10^{-4}. Inertia effects can be considered to be negligible under these conditions. For the higher dissipation rate the Stokes numbers lie in a range between 10^{-3} and 10^{-1}. Whereas for the smallest particles no significant inertia effects can be expected, for particles $> 5\,\mu m$ the inertia effects become more relevant. Based on the results from the literature described in 2.2.2, clustering can be expected at the largest particle sizes and dissipation rates.

The influence of the dissipation rate is shown in more detail on the left-hand side of figure 2.4 for particle diameters $1\,\mu m$ and $10\,\mu m$. Comparing to typical weather conditions associated with the dissipation rates (see 2.3.2), these results indicate that inertia effects are limited to the windiest situations.

Gravity has only a small effect on the particles considered here, as demonstrated by the settling velocitiesas a function of particle diameter shown on the right-hand side of figure 2.3. For the smallest particles, the settling velocities are in the order of tens of $\mu m/s$, whereas for the larger particles settling velocities up to a few mm/s can be expected. To understand the influence of gravity under different atmospheric conditions, Froude numbers have been estimated for a range of atmospheric dissipation rates as shown on the right-hand side of figure 2.4. The Froude numbers range from less than 10^{-4} at

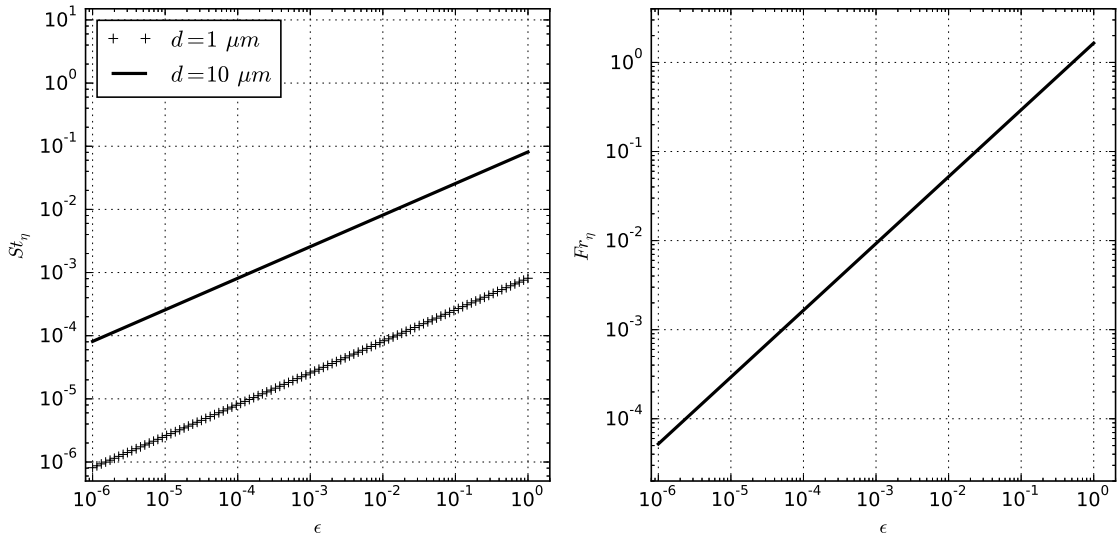

FIGURE 2.4: Characteristics of $10\,\mu m$ and $1\,\mu m$ particles as a function of atmospheric dissipation rates (in m^2/s^3. Left: Stokes number St_η. Right: Kolmogorov scale Froude number Fr_η.

$\epsilon = 10^{-6}\,m^2/s^3$ to about 2 at $\epsilon = 1\,m^2/s^3$. This gives and indication that gravity plays a bigger role in calm situations.

To sum up the above results, the smallest particle sizes considered are expected to show little difference in their dispersion behaviour compared to gases, whereas larger particles are expected to show some inertia effects in windy situations and some gravity effects in calm situations. Both inertia and gravity effects can be expected to be comparatively small. A quantitative estimate of their relevance based on numerical simulations will be given in A.

2.4.2 Particles near walls

The behaviour of particles close to the wall can be characterised by the friction Stokes number St_τ as described in 2.2.6. Friction Stokes numbers for particle diameters $1\,\mu m$ and $10\,\mu m$ have been estimated using a range of friction velocities from $10^{-2}\,m/s$ (calm) to $1\,m/s$ (windy). As in the previous section, all estimates have been made by simple application of the definition.

As can be seen from the left-hand side of figure 2.5, friction Stokes numbers between around 10^{-5} and around 10^{-1} are expected for the smaller particles, whereas for the larger particles the friction Stokes numbers cover a range from 10^{-3} to around 20. Therefore inertial effects near the wall can be expected at high friction velocities for the small particles and under almost all except the calmest situations for the larger particles. The viscous length scales, shown on the right-hand side of the figure are in the order of millimetres for the lowest friction velocities and in the order of tens of micrometres for

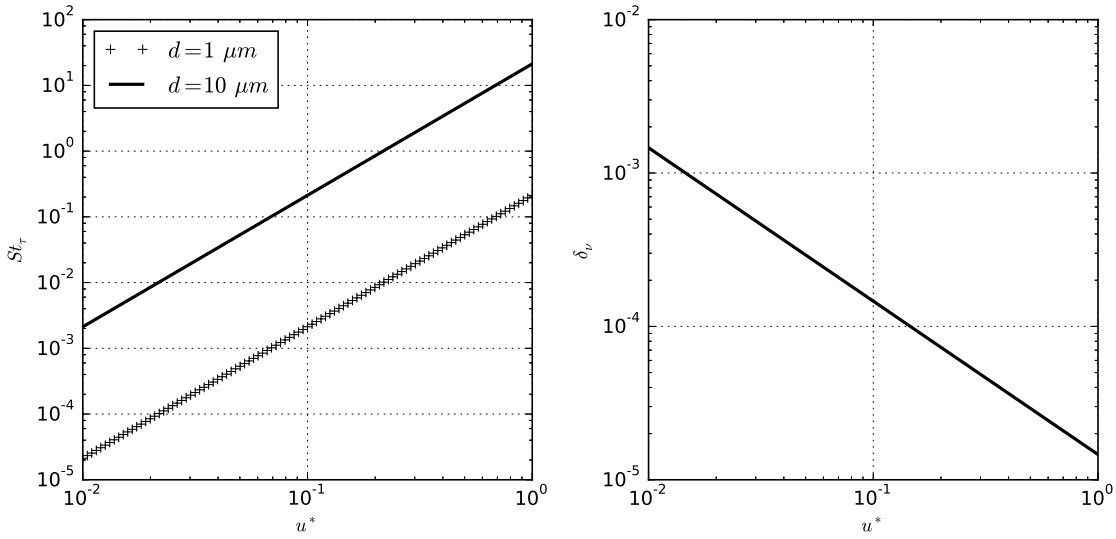

FIGURE 2.5: Estimate of near-wall properties as a function of friction velocity (in m/s). Left: friction Stokes number St_τ. Right: viscous length scale δ_ν.

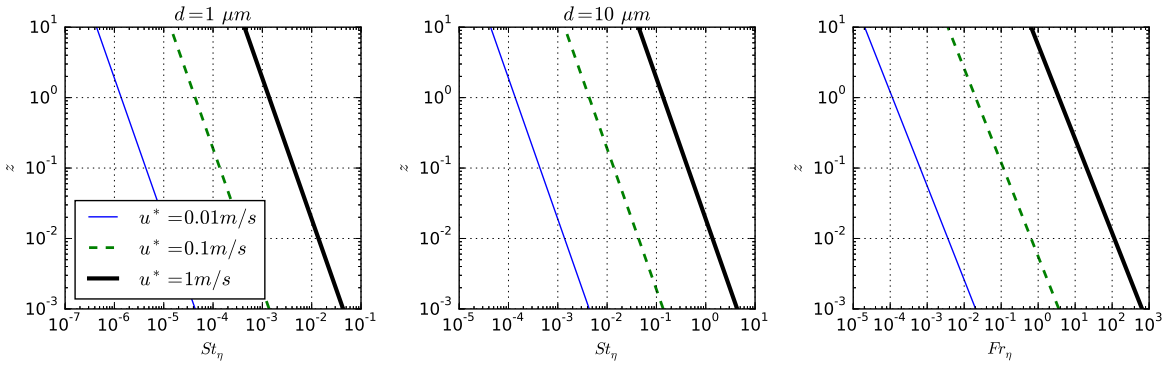

FIGURE 2.6: Profiles of local Kolmogorov scale Stokes numbers St_η for $1\,\mu m$ particles (left) and $10\,\mu m$ particles (centre) and of local Kolmogorov scale Froude numbers Fr_η (right). All heights z in m.

the highest friction velocities. This would indicate that the relevant regions are very close to the ground compared to typical atmospheric length scales.

To get a better understanding of the particle behaviour with height, local dissipation rates are estimated from the idealised relation [133]

$$\frac{\kappa z \epsilon}{u_*^3} = 1 \tag{2.45}$$

where z is the height, $\kappa = 0.35$ is the value of the von Karman constant as suggested by the authors of [133] and the effect of atmospheric stability is neglected. The dissipation rates can then be used to estimate Kolmogorov-scale Stokes and Froude numbers between $1\,mm$ and $10\,m$ height.

The local St_η profiles for $1\,\mu m$ particles (left-hand side) and $10\,\mu m$ particles (centre) are shown in figure 2.6 for three different friction velocities, $10^{-2}\,m/s$, $10^{-1}\,m/s$ and $1\,m/s$. For the small particles at low and moderate friction velocities the Stokes numbers are no higher than 10^{-3}, indicating little inertia effects at these heights. At $u_* = 1\,m/s$ the Stokes numbers between around $1\,mm$ and around $1\,cm$ are between 10^{-2} and 10^{-1}, indicating potential weak inertia effects.

For the larger particle size, St_η of 10^{-2} and higher can be found at $u_* = 10^{-1}\,m/s$ in the lowest $10\,cm$ and at $u_* = 1\,m/s$ over the whole profile. This would indicate that under these very turbulent conditions particle clustering could be expected, in particular at heights of about $1\,cm$, where $St_\eta \approx 1$.

An estimate of the relevance of gravity is given by the local Froude numbers Fr_η shown on the right-hand side of figure 2.6. For the highest friction velocities, Froude numbers are in the order of 1 at $10\,m$ height and 10^3 at $1\,mm$ height, pointing at very little gravity influences. On the other hand, for $u_* = 10^{-2}\,m/s$ the Froude numbers lie between 10^{-5} at $10\,m$ height and 10^{-2} at $1\,mm$ height. Therefore gravity can be expected to be more relevant under these atmospheric conditions. The Froude numbers span various decades over the profile, which would suggest that particles are lesss likely to go beyond a certain height, but exhibit more gas-like dispersion behaviour closer to the ground.

2.4.3 Particles in a fictive emission source

To get an idea of the particle characteristics in an emission source, dissipation rates from pipe flow mearuements have been used to estimate Kolmogorov-scale Stokes and Froude numbers. Bailey et al. [6] measured local dissipation scales in the ONR Superpipe [135], which has a diameter of $129\,mm$. In the centre of the pipe dissipation rates between $0.07\,m^2/s^3$ and $1.31\,m^2/s^3$ were measured at Re_λ between 76 and 135, whereas at $y/R = 0.1$, i.e. about $6.5\,mm$ above the pipe surface, dissipation rates between $2.4\,m^2/s^3$ and $14\,m^2/s^3$ were measured at Re_λ between 155 and 214. The complete data are summarised in table 2.6 for the measurements at the centre and in table 2.7 for the measurements at $y/R = 0.1$.

From the measurement data it can be seen that, even at high mean velocities, all dissipation rates closer to the surface are significantly higher than those measured at the centre of the pipe.

Based on these data, Stokes numbers have been estimated for particle diameters of $1\,\mu m$ and $10\,\mu m$ (left-hand side of figure 2.7). Similar to the results under atmospheric conditions, the Stokes numbers for $1\,\mu m$ particles are small, between $2 \cdot 10^{-4}$ and $3 \cdot 10^{-3}$. For $10\,\mu m$ particles the estimated Stokes numbers lie between 10^{-2} and 10^{-1} at the centre of the pipe and between 0.1 and 0.3 at $y/R = 0.1$. Therefore inertia effects are expected

Mean velocity $[m/s]$	Re_λ	ϵ $[m^2/s^3]$
3.3	76	0.07
3.9	87	0.13
4.9	92	0.21
6.0	106	0.39
7.2	116	0.62
8.3	124	0.90
9.5	135	1.31

TABLE 2.6: Mean velocities, Taylor scale Reynolds numbers and dissipation rates measured at the centre of a pipe [6]

Mean velocity $[m/s]$	Re_λ	ϵ $[m^2/s^3]$
3.4	155	2.4
5.1	185	6.8
6.7	214	14

TABLE 2.7: Mean velocities, Taylor scale Reynolds numbers and dissipation rates measured in a pipe at $y/R = 0.1$ [6]

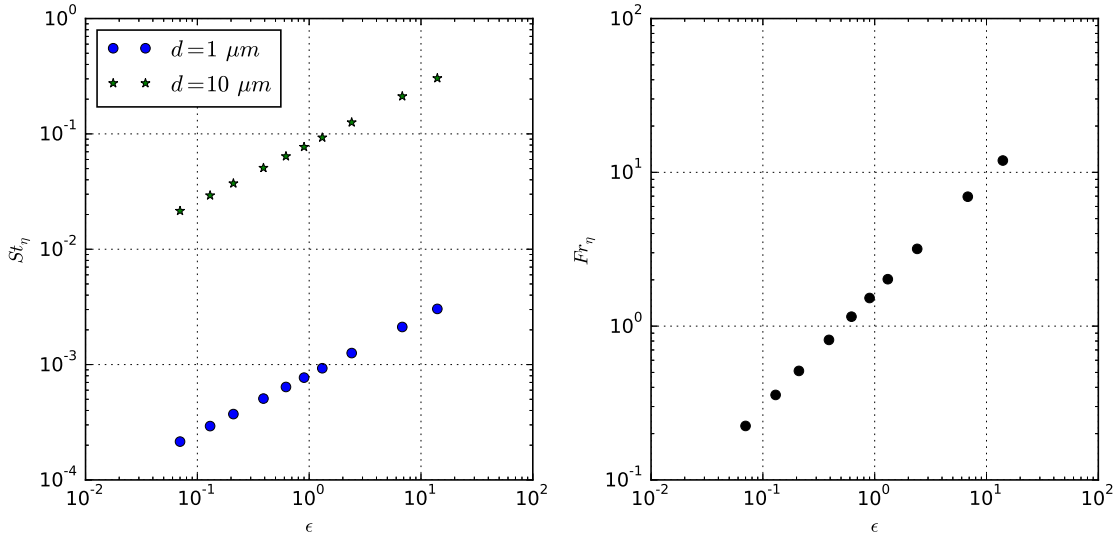

FIGURE 2.7: Estimate of particle characteristics for $1\,\mu m$ and $10\,\mu m$ particles as a function of dissipation rates (in m^2/s^3) in a pipe flow. Left: Kolmogorov scale Stokes numbers St_η. Right: Kolmogorov scale Froude numbers Fr_η. The three highest dissipation rates correspond to points at $0.1R$ (i.e. close to the wall), the others to the centre of the pipe.

to be insignificant for the smallest particles considered, but are expected to lead to significant clustering for the larger particles.

The Froude numbers, shown on the right-hand side of figure 2.7, span two decades between about 10^{-1} and 10^{1}. These Froude numbers are comparatively high and suggest that gravity effects are not relevant, which is consistent with the results obtained under atmospheric conditions.

2.4.4 Summary

An estimate of atmospheric aerosol properties has shown that small particles with diameters in the order of $1\,\mu m$ can be expected to show almost gas-like dispersion behaviour, whereas larger particles of approximately $d_p > 5\,\mu m$ are increasingly influenced by inertia and gravity effects. Inertia effects including clustering can be expected in windy situations, whereas in calm situations gravity can become relevant. The Kolmogorov-scale Stokes numbers St_η can be expected to be in the order of 10^{-6} to 10^{-4} for $1\,\mu m$ particles and in the order of 10^{-3} to 10^{-1} for $10\,\mu m$ particles. This suggests that out of the approaches discussed in chapter 2, the dusty-gas approach is sufficient for the smaller particles, whereas for the larger particles the equilibrium method seems to provide an appropriate level of description.

For larger particles a strong clustering behaviour near walls (in practical terms the ground as well as building walls) can be expected, which means that correct near-wall concentrations are of significance for the dispersion modelling of fine particulate matter. This near-wall behaviour can be expected to be extremely weather-dependent, which poses an additional challenge. The friction Stokes numbers, which are relevant for the near-wall behaviour, suggest that for large particles with diameters in the order of $10\,\mu m$ and for friction velocities $u_* > 0.1 m/s$ Eulerian methods will be increasingly inaccurate with friction Stokes numbers in the order of $St_\tau \approx 1$ to $St_\tau \approx 1$.

2.5 Numerical simulation of turbulent flows

An incompressible fluid flow can be fully described by a momentum conservation equation, the Navier-Stokes equation, and a mass conservation equation, the continuity equation [39]. Several approaches that differ in their completeness and level of description, accuracy and computational cost have been developed for the numerical solution of these equations [93].

The simplest approach from a conceptual point of view as well as the most accurate approach is the full resolution of all scales of motion, the *Direct Numerical Simulation*

(DNS) [39]. However, its computational cost is extremely high and increases rapidly with the Reynolds number [93].

By using the Reynolds decomposition (equation 2.2) to only resolve the mean flow, the computational cost can be drastically reduced, an approach known as *Reynolds-Averaged Navier Stokes* (RANS) [39]. A variety of methods for modelling the unresolved, turbulent, motions, which are usually only sufficiently accurate for specific application areas, have been devised [93]. Due to the non-linear nature of the Navier-Stokes equation, turbulence models should be considered engineering approximations and not scientific laws [39].

In *Large-eddy Simulations* (LES) only the largest turbulent structures, containing at least 80 % of the turbulent kinetic energy, are resolved [93]. The separation between resolved and unresolved scales is achieved by a filtering operation that is described in more detail in section 2.6.2. The filtered Navier-Stokes equation is not closed and the subgrid Reynolds stresses need to be modelled [79]. One way of modelling the subgrid Reynolds stresses is to relate them to the resolved strain rate, which is the underlying principle of the most widely used subgrid model, the *Smagorinsky model* [39].

Whereas in the original Smagorinsky model the subgrid stresses are related to the resolved strain by a constant with a fixed value [93], Germano [46] developped a subgrid model in which this constant is dynamically determined based on the assumption of similarity between different scales of motion. Pope [94] showed that not the assumption of scale similarity, but choosing a constant that is independent of the grid resolution is the reason why this dynamic model gives good results.

Another approach to modelling the subgrid-scale motions, the *deconvolution method*, is to estimate them from an inverted filter operation [39]. The deconvolution method belongs to a family of *structural methods* whose goal is to obtain an estimate of the unfiltered velocities, the most accurate as well as most computationally expensive of these being the explicit evaluation on an auxiliary grid [103].

The validity of a subgrid-scale model needs to be tested by comparison to experimental or DNS data, which is known as *a posteriori* test [79]. Another type of test that is commonly performed is the *a priori* validation, in which the filtered velocity is directly obtained from the DNS results [103]. Whereas a priori tests provide more insight into the physics of a given subgrid model, the validity of a subgrid model can only be ascertained a posteriori [79]. Typically subgrid models yield better results for homogeneous turbulence than in more complex flows [103].

2.6 Spectral and pseudospectral simulation of turbulent flows

2.6.1 Pseudospectral formulation of the Navier-Stokes equation

The incompressible Navier-Stokes and continuity equations for homogeneous flows with periodic boundary conditions [21] can be expressed in physical space by:

$$\frac{\partial \mathbf{u}}{\partial t} + \mathbf{u} \cdot \nabla \mathbf{u} = -\nabla p + \nu \Delta \mathbf{u} \tag{2.46}$$

$$\nabla \cdot \mathbf{u} = 0 \tag{2.47}$$

with the boundary and initial conditions

- $u_i(x) = u_i(x) + 2\pi$
- $\mathbf{u} = \mathbf{u}_0$ at $t = 0$

Using the Fourier series for $\mathbf{u}$ and p

$$\mathbf{u}(\mathbf{x}, t) = \sum_{\mathbf{k}} \hat{\mathbf{u}}_{\mathbf{k}}(t) e^{i\mathbf{k}\cdot\mathbf{x}} \tag{2.48}$$

and

$$p(\mathbf{x}, t) = \sum_{\mathbf{k}} \hat{p}_{\mathbf{k}}(t) e^{i\mathbf{k}\cdot\mathbf{x}}, \tag{2.49}$$

the Fourier space equivalents of equations 2.46 and 2.47 are

$$\left(\frac{d}{dt} + \nu|\mathbf{k}|^2\right) \hat{\mathbf{u}}_{\mathbf{k}} = -i\mathbf{k}\hat{p}_{\mathbf{k}} + \hat{\mathbf{c}}_{\mathbf{k}} \tag{2.50}$$

$$i\mathbf{k} \cdot \hat{\mathbf{u}}_{\mathbf{k}} = 0 \tag{2.51}$$

with the nonlinear term

$$\hat{\mathbf{c}}_{\mathbf{k}} = -\left(\widehat{\mathbf{u} \cdot \nabla \mathbf{u}}\right)_{\mathbf{k}} \tag{2.52}$$

Solving the nonlinear term in Fourier space requires solving convolution sums

$$\sum_{\mathbf{k}=\mathbf{p}+\mathbf{q}} u_\beta(\mathbf{p}) u_\gamma(\mathbf{q}), \tag{2.53}$$

which brings about a computational cost of order $(N^3)^2$. Patterson and Orszag suggested transforming u_β and u_γ into real space, computing the real space product, and transforming back into Fourier space. The cost is thus reduced to order $3N^3 \log_2 N^3$ operations [91].

2.6.2 Filtering and large-eddy simulation

A scale separation can be achieved by applying a high-pass filter in real space or a low-pass filter in Fourier space [103]. In real-space the filtering operation can be expressed by the convolution of a function $f(\mathbf{x})$ with a filter function $G(\mathbf{x})$ [73]:

$$\bar{f}(\mathbf{x}) = \int G(\mathbf{x} - \mathbf{x}') f(\mathbf{x}') d\mathbf{x}' \tag{2.54}$$

If the function $f(\mathbf{x})$ has a Fourier transform

$$\hat{f}(\mathbf{k}) = \mathcal{F}\left\{f(\mathbf{x})\right\}, \tag{2.55}$$

the Fourier equivalant of the filtered function $\bar{f}(\mathbf{x})$ is

$$\hat{\bar{f}}(\mathbf{k}) = \mathcal{F}\left\{\bar{f}(\mathbf{x})\right\} = \hat{G}(\mathbf{k}) \hat{f}(\mathbf{k}), \tag{2.56}$$

where

$$\hat{G}(\mathbf{k}) = \int_{-\infty}^{\infty} G(\mathbf{x}') e^{-i\mathbf{k}\mathbf{x}'} d\mathbf{x}' = 2\pi \mathcal{F}\left\{G(\mathbf{x}')\right\} \tag{2.57}$$

is the transfer function, i.e. the Fourier space equivalent of the filter function $G(\mathbf{x})$ [93].

If a filter fulfils the conditions

1. Conservation of constants: $\bar{a} = a$
2. Linearity: $\overline{\phi + \psi} = \bar{\phi} + \bar{\psi}$ (this is automatically satisfied by the convolution)
3. Commutation with derivation:

$$\overline{\frac{\partial \phi}{\partial s}} = \frac{\partial \bar{\phi}}{\partial s}, s = \mathbf{x}, t, \tag{2.58}$$

the filtered Navier-Stokes equation in Fourier Space can be obtained by multiplication with the transfer function [103].

By applying a transfer function $\hat{G}(\mathbf{k})$ to equation 2.50, the filtered Navier-Stokes equation reads

$$\left(\frac{d}{dt} + \nu|\mathbf{k}|^2\right) \hat{G}\hat{\mathbf{u}}_\mathbf{k} = -i\mathbf{k}\hat{G}\hat{p}_\mathbf{k} + \hat{G}\hat{\mathbf{c}}_\mathbf{k} \tag{2.59}$$

Note that the non-linear term $\hat{\mathbf{c}}_\mathbf{k}$ contains the unfiltered velocities.

2.6.3 Gibbs oscillations

A specific problem of spectral methods is the *Gibbs phenomenon* [112]. Truncated Fourier series cannot resolve the entire high-wavenumber part of the spectrum associated with discontinuities in real space, like square waves, which causes numerical artefacts [21]. A way of addressing these issues is to apply specific spectral filters that attenuate the higher wavenumbers [21]. Advanced methods try to detect discontinuities, but this comes at the price of a high computational cost [112].

2.7 Simulation of particles in turbulent flows

The most detailed method for simulating the movement of particles in a turbulent flow is fully-resolved DNS, i.e. the exact computation of the fluid flow around the particle [71]. This method is prohibitively expensive for the number of particles typically required [7] and the necessity of a sufficiently resolved grid for the fluid flow means that it is only practicable for particles $\gg \eta$ [71].

Other simulation methods can be categorised as Lagrangian point-particle methods, in which the trajectory of particles is computed in a Lagrangian sense, and Eulerian methods, in which particle concentration and velocity fields are computed [71]. All of these methods are based on the approximation of the particles as point particles, either explicitly in Lagrangian point-particle methods, or implicitly through the assumptions used for deriving the Eulerian equations [7].

2.7.1 Eulerian methods

The motion of particles can be solved in an Eulerian sense by treating the carrier phase and the disperse phase as separate, but interpenetrating fluids [7]. For tiny particles a dusty gas method can be used, in which the particles are simply moved with local fluid velocity [38]. An intermediate method is the equilibrium Eulerian approach in which the particle velocity is expressed as an expansion in fluid velocity [7]. The underlying assumption is that particle velocities are in an equilibrium state in which the particle velocity is uniquely determined by the surrounding fluid field [38].

Expanding the particle velocity in the fluid velocity yields [7]

$$\vec{v} = \vec{u} + \vec{w} - St(1 - \frac{3}{(2(\rho_p/\rho_f) + 1)})\frac{D\vec{u}}{Dt} + \vec{w} \cdot \nabla\vec{u} \tag{2.60}$$

where

- $\vec{u}$: fluid velocity normalised by the Kolmogorov velocity
- $\vec{v}$: particle velocity normalised by the Kolmogorov velocity
- $\vec{w}$: settling velocity normalised by the Kolmogorov velocity

The method has successfully been used to simulate particles and in isotropic turbulence [95] and channel flows [38]. In both cases the best results were obtained when the relevant Stokes number was $St < 1$. Preferential concentration was reproduced in both applications.

All Eulerian methods are based on the assumption that particle concentrations and velocities can be represented by a unique field [7]. They cannot be applied if the particle inertia is so high that the particle velocities cannot be represented by a unique field or if the particle number concentration is so low that it cannot be described as a continuum [38].

In poly-disperse systems, the particle concentration and velocity fields usually need to be computed separately for each particle size [38]. However, in Eulerian methods based on probability density functions, polydispersity can be handled by including particle size as a phase space variable [38].

2.7.2 Lagrangian point-particle method

In Lagrangian point-particle methods the trajectory of a particle is computed [7]. The equation of motion described in 2.2.1 is typically used, often reducing it to the most relevant terms [33]. As opposed to Eulerian methods, they can easily handle polydisperse particle distributions and their applicability is not limited by particle inertia [7]. They can also be used for low number concentrations, where the continuum assumption is not

valid [38]. Whilst Lagrangian methods can be used for particles of any Stokes number, Eulerian methods are typically preferable for small Stokes number particles due to their lower computational cost [7]. Lagrangian point-particle methods can represent particles of different velocities in the same control volume, which is usually not possible in an Eulerian method [7].

Since the position of a particle on a Lagrangian trajectory generally does not coincide with the Eulerian fluid mesh, an interpolation of the fluid velocity at the particle position is necessary [8].

Assuming periodic boundary conditions, by far the most accurate interpolation is the direct summation of spectral coefficients over all wavenumbers, which is exact [8]. However this method is prohibitively expensive and therefore rarely ever applied [60].

Van Hinsberg et al. compared several interpolation methods using a theoretical evaluation of the error as well as a validation using direct numerical simulations of homogeneous isotropic turbulence. Of the interpolation schemes they examined, linear interpolation showed the largest error, whereas a B-Spline interpolation was the most exact. The error from the Hermite interpolation was only slightly bigger than that from the B-Spline interpolation. However the Hermite interpolation comes at a significant computational expense. Lagrange interpolation showed an error about one order of magnitude bigger compared to B-Spline and Hermite interpolation, but various orders smaller than linear interpolation. An analysis of the acceleration spectrum of an inertial particle showed that all interpolation schemes introduced high-frequency oscillations. This is even the case for a spectral interpolation, which is due to the discretisation error rather than the interpolation itself [120].

Ireland et al. found that a B-Spline interpolation scheme provides the best trade-off between accuracy and computational effort for direct numerical simulations of homogeneous isotropic turbulence [60].

2.7.3 Specific considerations regarding particles in large-eddy simulations

In large-eddy simulations, **filtered velocities** are predicted, whereas the non-linear term containing the unfiltered velocities is modelled. However, when introducing inertial particles into the simulation, the unfiltered velocities are needed in the equation of motion of the particles. The forces that depend on the unfiltered velocity are the drag, history, pressure gradient and added-mass forces. [71]. Another error source, especially on coarse grids, is the **interpolation** of the fluid velocity seen by the particle. The inaccuracies due to the filtered velocity and the interpolation accumulate over the Lagrangian particle trajectory and lead to an incorrect prediction of the particle path [75].

In cases where the particle relaxation time is large compared to the turbulent fluctuation time scale, the error introduced by using the filtered velocity is small. If this condition is not met, some kind of closure is needed [71]. The closure methods that are commonly applied can be categorised as **stochastic methods**, which are based on stochastic modelling of the high wavenumbers, and **structural methods**, which are based on reconstructing the unfiltered velocities [75].

Evidence from filtered DNS

Armenio et al. performed direct numerical simulations of $St = 1$ particles in a channel flow and compared selected particle statistics (one-particle dispersion, one-particle autocorrelation, Lagrangian integral time scale, turbulent diffusivity and two-particles rms dispersion) to those obtained from filtered DNS as well as separate large-eddy simulations. They found differences in the results between DNS and filtered DNS only when a significant fraction of the turbulent kinetic energy was removed from the velocity field. Whereas LES with a Smagorinsky model introduced errors, the results of LES with a dynamic eddy-viscosity model were mainly affected by the filtering itself [4].

Fede and Simonin carried out direct numerical simulations of homogeneous isotropic turbulence and computed the one-way coupled movement of inertial particles in the flow field as well as the filtered flow field. The DNS was carried out at a resolution of about $\kappa_{max}\eta = 2$. A sharp spectral filter was applied with various cutoff wavenumbers corresponding to a resolution between $\kappa_{max}\eta \approx 0.25 \ldots 0.9$. They found the particle dispersion and kinetic energy to be dominated by the energy-containing turbulent eddies, with a small dependence on the filtering. Preferential concentration was found to be dependent on a subgrid Stokes number, defined as the ratio of the particle response time and the subgrid integral time scale. It was not modified by the filtering for large subgrid Stokes numbers ($St > 5$), whereas for small subgrid Stokes numbers ($St < 0.5$) preferential concentration was shown to be induced by subgrid eddies. In the intermediate range they found that the subgrid turbulence acted as a stochastic force, whereas the particles interacted with the energy-containing eddies [36].

Ray and Collins conducted a similar study at higher Reynolds numbers and obtained similar results. They found that the radial distribution function decreases with filtering for small Stokes numbers and increases with filtering for large Stokes numbers. Their results showed that even with strong filtering some preferential concentration can be observed. Filtering had the effect of shifting the maximum RDF towards higher Stokes numbers [96].

Stochastic methods

In stochastic models, some kind of diffusion equation is typically used [75]. While some of them are based on a generalised Langevin model for the fluid velocity seen by the particle, others apply a transport equation for the subgrid-scale kinetic energy [71].

Structural methods

The idea of the approximate deconvolution method is to reconstruct the filtered data from a series expansion of the inverse filter. The estimate of the unfiltered data is then used to compute the nonlinear terms in the filtered Navier-Stokes equations. All operators can be computed either in real or spectral space. The method can be applied to any filter with a positive transfer function [110].

Kuerten compared direct numerical simulations and large-eddy simulations of particle-laden channel flows at several Reynolds and Stokes numbers. With a filtered fluid velocity from the LES, the particle fluctuations were also reduced, leading to an inaccurate prediction of particle behaviour. The results from the LES were improved using the approximate deconvolution method that predicts the fluid velocity statistics better [70].

In *kinematic simulations* it is attempted to model the subgrid-scale velocity field in terms of randomly assigned Fourier modes that follow a prescribed energy spectrum [75]. Ray and Collins [97] successfully modelled preferential conctration of $St_\eta \geq 2$ particles in homogeneous isotropic turbulence. However, their model did not predict clustering at lower Stokes numbers.

Comparison of different methods

In a recent review of dispersed flow modelling approaches for LES, Marchioli came to the conclusion that 'no universal model (perhaps not even a good-enough model) is yet available '[75].

Jin and He investigated the effect of subgrid-scale motions on the dispersion of heavy particles in large-eddy simulations. They found that a model based on stochastic differential equations showed better results than the approximate deconvolution method for Stokes numbers < 2 [62].

Cernick et. al compared results from approximate deconvolution methods and stochastic methods and confirmed that the stochastic models perform better at small Stokes numbers. However, they are not able of predicting preferential concentration. The approximate deconvolution method improves results, but is only capable of recovering part

of the subgrid-scale turbulent kinetic energy. It showed improvement of preferential concentration predictions for all Stokes numbers, but was not able to match the DNS results [25].

2.8 Summary

In this chapter it was seen that small-scale turbulence in the atmospheric surface layer is dominated by shear production of turbulence and, close to surfaces, by (blocking) interactions with the surfaces. With increasing height the surface interactions as well as the wind shear become less relevant. Therefore it seems appropriate to use simplified physical models for understanding the small-scale dispersion of small inertial particles in the atmosphere.

A literature review of particles in turbulent flows showed that various aspects of the small-scale dispersion of particles are present in the simplest turbulent flow, homogeneous isotropic turbulence. Very efficient numerical methods are available for simulating this type of flow and therefore a first understanding will be gained using this approach. Particle simulations in homogeneous shear flow allow for taking into account an additional characteristic, the interaction with coherent structures. The final building block, the interaction with walls, can be taken into account in another simple flow, the channel flow. Both experiments and simulations in this type of flow show that close to the walls the flow timescales become so small that the relevant Stokes numbers increase, leading to very different particle behaviour near the wall.

The entire literature on particles in turbulent flows is limited to comparatively low Reynolds numbers, which are significantly lower than characteristic atmospheric Reynolds number. It is therefore crucial to fully understand the Reynolds number dependence of particle dependence in each of the relevant flow regimes.

It has been seen that in atmospheric dispersion modelling the best-resolved large-eddy simulations are still far coarser than the relevant particle scales. On the other hand, a literature review on large-eddy simulations of particles has shown that subgrid models that give a good approximation of particle behaviour are only available for very large particles. A priori and a posteriori analysis of LES subgrid models are standardised methods that can be applied to this problem. Whereas in a priori analysis the filtered velocity field is compared to the exact DNS velocity field within the direct numerical simulation itself, in an a posteriori analysis the results of LES are compared to the results of DNS. The first method is useful to gain more physical insight, the second method is necessary to provide a clear validation of a given model.

It will be seen in chapter 2.4 that the typical Stokes numbers of atmospheric aerosols allow for a computationally efficient approach for the simulation of particle dispersion,

the equilibrium Euler method. This method is only valid for small Stokes numbers, since it is based on the assumption that the particles rapidly return to an equilibrium with the fluid velocity.

Chapter 3

A new method for the validation of time-resolved dispersion simulations based on field experiments

Parts of this chapter have been published under the title 'Technical Note: A new method for the evaluation of puff dispersion field experiments for the validation of time-resolved dispersion simulations' [129].

The use of field measurement data for the validation of time-resolved dispersion modelling, such as LES models, with a low enough uncertainty to allow for a meaningful comparison has so far been considered to be difficult, if not impossible, to achieve [50]. Due to this difficulty, validation data for LES simulations are almost exclusively based on wind tunnel experiments, typically consisting of either concentration or dosage based quantities [14]. In this chapter a radically different approach is proposed. The aim is to provide an evaluation of field measurements with the required accuracy to develop a suitable LES subgrid model.

3.1 Introduction

Almost a century ago, Richardson [100] described concentration distributions in puffs using a one-dimensional distance-neighbour function along the spatial direction x

$$q(\Delta x, t) = \frac{\int_{-\infty}^{\infty} c(x,t)c(x+\Delta x,t)dx}{\int_{-\infty}^{\infty} c(x,t)dx^2} \tag{3.1}$$

where $c(x,t)$ is the concentration at point x and time t and $c(x+\Delta x,t)$ is the concentration at a distance Δx. Both from theoretical [11] and experimental [113] results it

is known that its shape can be approximated by a normal distribution. Batchelor [11] emphasises its importance for describing the way in which turbulence modifies the shape of particle clouds.

Whereas the original distance-neighbour function [100] and its three-dimensional extension [11] are based on integration in space (which is equivalent to a Lagrangian description), we choose integration over time in order to be able to evaluate measurements from a limited number of in-situ detectors with a high temporal resolution such as the ultraviolet ion collector described by Griffiths et al. [49].

It will be shown that a generalised form of the distance-neighbour function is a powerful and robust tool for characterising the behaviour of puff releases in the atmospheric boundary layer at the resolution limit of available detectors (e.g. 0.02 s in the case of ultraviolet ion collectors [49]). Several validation quantities with a clearly defined uncertainty can be derived using this method. The author believes that using this method it will be possible to derive high-quality datasets from measurements, suitable for validation of time-resolved dispersion modelling, in particular large-eddy simulation. Large-eddy simulations of atmospheric dispersion have been performed with spatial resolutions of about $1\,m$ [12, 23], and it can be expected that with increasing computer power finer resolutions will be used in the future. Assuming typical wind speeds of $> 1\,\mathrm{m/s}$ at ground level, meaningful validation quantities needed for validating LES models at time scales well below one second are needed. Furthermore there are several highly relevant applications like the dispersion of toxic gases, combustible materials or malodours [64] where instantaneous concentrations are far more important than temporal averages.

3.2 Methods

It is assumed that the concentration time series $c(\mathbf{x}, t)$ are measured by a set of detectors at fixed positions $\mathbf{x}$ in space and define the generalised distance-neighbour functions $q_t(\mathbf{x}, \Delta t)$, $q_{\mathbf{x}}(\mathbf{x}, \Delta\mathbf{x})$ and $q_{\mathbf{x},t}(\mathbf{x}, \Delta\mathbf{x}, \Delta t)$ as follows (note the underlying assumption that the signal contains at least some noise such that the denominator is never zero).

$$q_t(\mathbf{x}, \Delta t) = \frac{\int_{-\infty}^{\infty} c(\mathbf{x}, t)c(\mathbf{x}, t + \Delta t)dt}{\int_{-\infty}^{\infty} c^2(\mathbf{x}, t)dt} \tag{3.2}$$

$$q_{\mathbf{x}}(\mathbf{x}, \Delta\mathbf{x}) = \frac{\int_{-\infty}^{\infty} c(\mathbf{x}, t)c(\mathbf{x} + \Delta\mathbf{x}, t)dt}{\sqrt{\int_{-\infty}^{\infty} c^2(\mathbf{x}, t)dt}\sqrt{\int_{-\infty}^{\infty} c^2(\mathbf{x} + \Delta\mathbf{x}, t)dt}} \tag{3.3}$$

$$q_{\mathbf{x},t}(\mathbf{x}, \Delta\mathbf{x}, \Delta t) = \frac{\int_{-\infty}^{\infty} c(\mathbf{x}, t)c(\mathbf{x} + \Delta\mathbf{x}, t + \Delta t)dt}{\sqrt{\int_{-\infty}^{\infty} c^2(\mathbf{x}, t)dt}\sqrt{\int_{-\infty}^{\infty} c^2(\mathbf{x} + \Delta\mathbf{x}, t)dt}} \tag{3.4}$$

The mathematical structure of the distance-neighbour functions $q_t(\mathbf{x}, \Delta t)$, $q_{\mathbf{x}}(\mathbf{x}, \Delta \mathbf{x})$) and $q_{\mathbf{x},t}(\mathbf{x}, \Delta \mathbf{x}, \Delta t)$ corresponds to that of the auto-correlation, space correlation and cross correlation functions respectively, which are commonly used in turbulence analysis (see e.g. [29, 42, 47, 20, 5]).

As Fisher and Davies [42] point out, both the auto-correlation and space correlation are special cases of the cross correlation, where the auto-correlation is the cross correlation for zero distance in space and the space correlation is the cross correlation for zero distance in time. The same is true for $q_t(\mathbf{x}, \Delta t)$ and $q_{\mathbf{x}}(\mathbf{x}, \Delta \mathbf{x})$, which are special cases of $q_{\mathbf{x},t}(\mathbf{x}, \Delta \mathbf{x}, \Delta t)$.

In contrast to the original definition given by Richardson [100], the distance-neighbour functions given here describe puffs in an Eulerian sense, i.e. in a fixed frame defined by an array of detectors. They are also normalised using $\int_{-\infty}^{\infty} c^2(\mathbf{x}, t)dt$ measured at a given position $\mathbf{x}$, similar to the normalisation of correlation coefficients as used in turbulence statistics. Therefore by definition

$$q_t(\mathbf{x}, \Delta t = 0) = q_{\mathbf{x}}(\mathbf{x}, \Delta \mathbf{x} = 0) = q_{\mathbf{x},t}(\mathbf{x}, \Delta \mathbf{x} = 0, \Delta t = 0) = 1 \tag{3.5}$$

The first of the distance-neighbour functions, $q_t(\mathbf{x}, \Delta t)$, characterises the temporal behaviour of concentrations measured at position $\mathbf{x}$. Under the assumption that the concentration signal is clearly distinguished from the background concentration, it can be expected that in a time series of identical puff releases the shape of $q_t(\mathbf{x}, \Delta t)$ will be determined by the puff duration and the turbulence it experiences.

Similarly, the streamwise and spanwise puff size can be characterised using $q_{\mathbf{x}}(\mathbf{x}, \Delta \mathbf{x})$. However, the turbulent structures cannot be easily deduced for these functions.

Finally, the third distance-neighbour function, $q_{\mathbf{x},t}(\mathbf{x}, \Delta x, \Delta t)$, can be used to derive the convection velocity of puffs through a detector array. For a signal measured at two different positions $\mathbf{x}$ and $\mathbf{x} + \Delta \mathbf{x}$ in space, a time difference Δt can be found at which $q_{\mathbf{x},t}(\mathbf{x}, \Delta \mathbf{x}, \Delta t)$ is maximal. From the time difference Δt and distance $\Delta \mathbf{x}$ in space the convection velocity can then be obtained. This method is formally similar to one of several methods for determining the convection velocity of turbulent structures (denoted U_{c_1} in [47]). Cross correlations have been widely used for determining the convection velocity (see e.g. [47, 20]). However, the convection velocity of turbulent eddies obtained by different methods gives different results [47], and for non-frozen turbulence it is known that in particular the method described above (i.e. finding a time interval with maximum correlation for a fixed distance in space) gives a convection velocity that is different from the mean velocity of the flow [42]. For a puff signal travelling through a detector array, however, it can be expected that the finite dimensions of the puff are dominating over the turbulent structures and hence the convection velocity of the puff deduced by this method will correspond well to the mean wind speed.

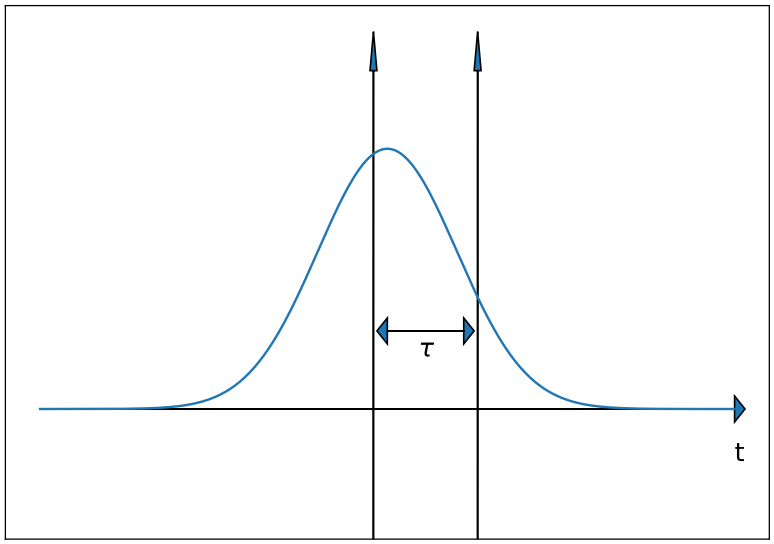

FIGURE 3.1: One-dimensional Gaussian puff over time t. The signal at t and $t+\tau$ can be compared using the generalised distance-neighbour functions.

From the convection velocity and the puff duration the puff size in the streamwise direction can be obtained. If there are several detectors in the streamwise direction, the puff size can also be obtained directly from $q_{\mathbf{x}}(\mathbf{x}, \Delta\mathbf{x})$, and hence an error estimate from comparing these independent results is possible.

3.3 Theory

3.3.1 Some analytic solutions for Gaussian puff signals

In this section the mathematical properties of the distance-neighbour functions defined in the previous section are investigated and it is shown how they can be applied to idealised puffs. All the analytical results in this section are based on applying the computer algebra system SymPy [80].

1-D

We start by investigating a normal distribution along the time axis t observed at two times separated by the time interval τ (see figure 3.1 for an illustration).

Integrating the product of the normal distribution observed at t and $t+\tau$ over time

$$\begin{aligned}&\int_{-\infty}^{\infty} \exp\left(-\frac{t^2}{2\sigma_t^2}\right) \exp\left(-\frac{(t+\tau)^2}{2\sigma_t^2}\right) dt \\ &= \sigma_t\sqrt{\pi}\exp\left(-\frac{\tau^2}{4\sigma_t^2}\right) = \sigma_t\sqrt{\pi}\exp\left(-\frac{\tau^2}{2\left(\sqrt{2}\sigma_t\right)^2}\right)\end{aligned} \tag{3.6}$$

yields another normal distribution with a standard deviation scaled by $\sqrt{2}$.

This result can give an estimate of $q_t(\mathbf{x}, \Delta t)$ (equation 3.2) and agrees with the theoretical [11] and experimental [113] findings that the distance-neighbour function as defined by Richardson [100] has a Gaussian shape. However, we have assumed a one-dimensional puff that does not change over time. This assumption is only likely to be true for small time differences τ. For a real puff a change in measured puff duration can be expected due to change in shape (through turbulent diffusion) and due to horizontal and vertical movements, which mean that a different part of the puff is observed.

Defining the puff arrival and leaving times as the times where the concentration reaches 5 % of the peak concentration, the puff duration of a Gaussian signal can be obtained by solving

$$\exp\left(-\frac{t^2}{2\sigma_t^2}\right) = 0.05 \tag{3.7}$$

for the time t. Using the scaling relation obtained from equation 3.6 we find that the puff duration T is given by

$$T = 2\sqrt{2}\sigma_{q_t}\sqrt{\log(\frac{1}{0.05})} \tag{3.8}$$

where $\sigma_{q_t} = \sqrt{2}\sigma_t$ is the standard deviation of $q_t(\mathbf{x}, \Delta t)$.

Analogously we obtain the puff size in streamwise direction as

$$X = 2\sqrt{2}\sigma_{q_x}\sqrt{\log(\frac{1}{0.05})} \tag{3.9}$$

where $\sigma_{q_x} = \sqrt{2}\sigma_x$ is the standard deviation of $q_{\mathbf{x}}(\mathbf{x}, \Delta\mathbf{x} = (\Delta x, 0, 0))$.

Under the assumption that the size of the puff (and hence the puff duration) changes along the way and describing the puff durations at time t_1 and time t_2 by standard deviations σ_1 and σ_2, we obtain

$$\begin{aligned}\int_{-\infty}^{\infty} \exp\left(-\frac{t^2}{2\sigma_1^2}\right) \exp\left(-\frac{(t+\tau)^2}{2\sigma_2^2}\right) dt \\ = \frac{\sqrt{2\pi}\sigma_1\sigma_2}{\sqrt{\sigma_1^2+\sigma_2^2}} \exp\left(-\frac{\tau^2}{2(\sigma_1^2+\sigma_2^2)}\right)\end{aligned} \tag{3.10}$$

which is another normal distribution with a standard deviation depending on the puff durations at both times.

Equation 3.10 can not only be interpreted as an estimate of the behaviour of $q_t(\mathbf{x}, \Delta t)$ (equation 3.2), but also as a description of $q_{\mathbf{x},t}(\mathbf{x}, \Delta\mathbf{x}, \Delta t)$ (equation 3.4), the cross correlation between two different detectors. As described above, the time difference τ can be used together with the distance between two detectors to derive the convection velocity of the puff.

In practice $q_{\mathbf{x},t}(\mathbf{x}, \Delta\mathbf{x}, \Delta t)$ will be evaluated for an entire time series of various puff releases made under atmospheric conditions that are affected by variations in wind speed. We can estimate how this modifies the result of equation 3.10 by introducing a random error τ' in τ and introducing a normal distribution for τ' with the standard deviation σ_τ. The latter normal distribution is a probability density function of the error τ'.

$$\begin{aligned}\int_{-\infty}^{\infty}\int_{-\infty}^{\infty} \exp\left(-\frac{\tau'^2}{2\sigma_\tau^2}\right) \exp\left(-\frac{t^2}{2\sigma_1^2}\right) \exp\left(-\frac{(t+\tau+\tau')^2}{2\sigma_2^2}\right) dt d\tau' \\ = \frac{2\sqrt{\pi}\sigma_\tau\sigma_1\sigma_2}{\sqrt{\sigma_1^2+\sigma_2^2+\sigma_\tau^2}} \exp\left(-\frac{\tau^2}{2(\sigma_1^2+\sigma_2^2+\sigma_\tau^2)}\right)\end{aligned} \tag{3.11}$$

The resulting normal distribution is wider than the one obtained from equation 3.10. Assuming that the two detectors are sufficiently far apart that the change in puff duration between one detector and the next is much greater than the change while the puff is detected by one of the detectors, reasonable estimates of the standard deviations σ_1 and σ_2 at the positions of two detectors 1 and 2 can be obtained from $q_t(\mathbf{x}, \Delta t)$. Knowing σ_1 and σ_2 we can then quantify the fluctuation σ_τ of the convection velocity by solving

$$\frac{1}{2\sigma^2} = \frac{1}{\sigma_1^2+\sigma_2^2+\sigma_\tau^2} \tag{3.12}$$

for σ_τ, where σ is the observed standard deviation of $q_{\mathbf{x},t}(\mathbf{x}, \Delta\mathbf{x}, \Delta t)$. The fluctuation σ_τ is then given by

$$\sigma_\tau = \sqrt{2\sigma^2 - \sigma_1^2 - \sigma_2^2} \tag{3.13}$$

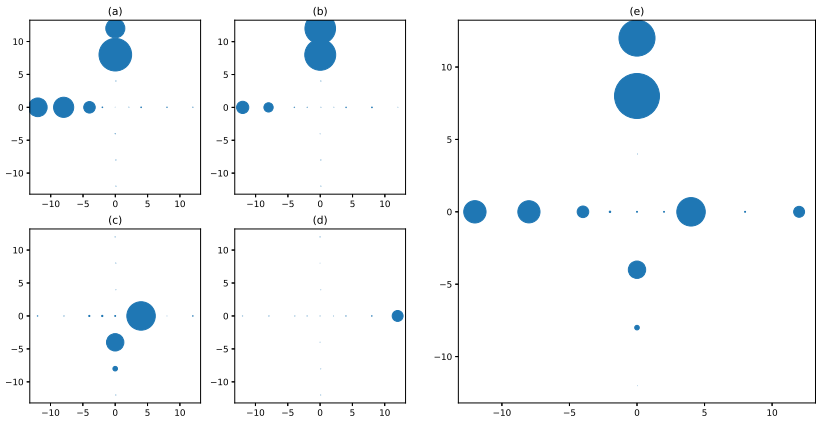

FIGURE 3.2: (a) to (d) Dosages measured in a detector array for a series of four puff releases and (e) total dosage for all four puffs. Marker sizes are proportional to the dosage. The position of each marker corresponds to the detector position in the horizontal plane (in metres).

2-D

So far the focus has been on puff durations and streamwise puff size. Generally we are interested in evaluating a longer time series, in particular a series of many puff releases. As shown in figure 3.2, a single puff is typically only detected in parts of a detector array, whereas the dosage measured over a longer time series results is distributed over a larger extent of the detector array.

Figure 3.3 illustrates the underlying process. The wind direction is fluctuating and therefore puffs travel in slightly different directions. On a spanwise axis y this can be described as a difference μ from the origin. In the following we will assume that the probability distribution of μ is, again, a normal distribution.

Integrating over the fluctuation μ and the streamwise direction x we obtain

$$\begin{aligned} &\int_{-\infty}^{\infty}\int_{-\infty}^{\infty} \exp\left(-\frac{\mu^2}{2\sigma_\mu^2}\right)\exp\left(-\frac{x^2}{2\sigma_x^2}-\frac{(y-\mu)^2}{2\sigma_y^2}\right)\cdot \\ &\exp\left(-\frac{\mu^2}{2\sigma_\mu^2}\right)\exp\left(-\frac{x^2}{2\sigma_x^2}-\frac{(y+a-\mu)^2}{2\sigma_y^2}\right)\,d\mu\,dx \qquad (3.14) \\ =\ &\frac{\sigma_x\sigma_y\sigma_\mu\sqrt{\sigma_y^2+\sigma_\mu^2}\pi}{\left(\sigma_y^2+\sigma_\mu^2\right)}\exp\left(-\frac{2\sigma_y^2+\sigma_\mu^2}{4\sigma_y^2\left(\sigma_y^2+\sigma_\mu^2\right)}a^2-\frac{1}{\sigma_y^2+\sigma_\mu^2}ay-\frac{1}{\sigma_y^2+\sigma_\mu^2}y^2\right) \end{aligned}$$

This is again a normal distribution that has its centre at the position of the detector on the spanwise axis for which it is evaluated. The standard deviation of this normal

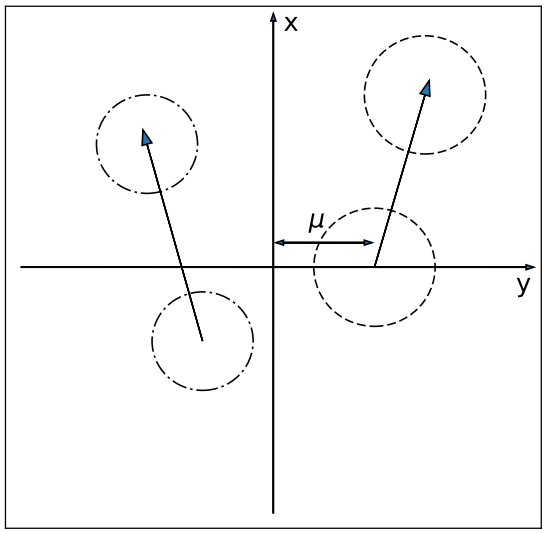

FIGURE 3.3: Illustration of puffs travelling in streamwise direction x. Fluctuations in the wind direction can be seen as distance μ from the centre in spanwise direction y.

distribution depends on both the spanwise puff size σ_y and the fluctuation σ_μ. In order to obtain either of σ_y or σ_μ we therefore need another, independent, equation.

Describing the dosage of a single puff by a normal distribution and using the same probability density function for μ we find that

$$\begin{aligned}\int_{-\infty}^{\infty} \exp\left(-\frac{\mu^2}{2\sigma_\mu^2}\right) \exp\left(-\frac{(y-\mu)^2}{2\sigma_y^2}\right) d\mu \\ = \frac{\sqrt{2\pi}\sigma_y\sigma_\mu}{\sqrt{\sigma_y^2+\sigma_\mu^2}} \exp\left(-\frac{a^2}{2(\sigma_y^2+\sigma_\mu^2)}\right)\end{aligned} \tag{3.15}$$

Then we find the following system of equations

$$\frac{1}{2\sigma_{corr}^2} = \frac{2\sigma_y^2+\sigma_\mu^2}{4\sigma_y^2\left(\sigma_y^2+\sigma_\mu^2\right)} \tag{3.16}$$

from $q_{\mathbf{x}}(\mathbf{x}, \Delta\mathbf{x})$ with a measured standard distribution σ_{corr} and

$$\sigma_y = \sqrt{\frac{1}{2}\left(\sigma_{corr}^2 + \sqrt{\sigma_\mu^4+\sigma^4} - \sigma_\mu^2\right)} \tag{3.17}$$

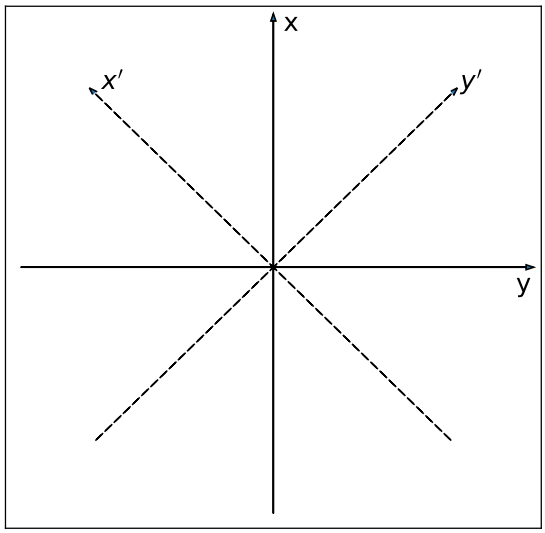

FIGURE 3.4: Illustration of the rotated coordinate system used in several measurements. Puffs move in streamwise direction x, whereas the detectors are positioned on a detector array at an angle of 45 ° on the axes x' and y'.

$$\frac{1}{2\sigma_{dos}^2} = \frac{1}{2\left(\sigma_y^2 + \sigma_\mu^2\right)} \tag{3.18}$$

from the dosage with a measured standard distribution σ_{dos}. Solving this system for σ_μ and σ_y we find

$$\sigma_\mu = \sqrt{2}\sigma_{dos}\sqrt{\frac{\sigma_{dos}^2 - \sigma_{corr}^2}{2\sigma_{dos}^2 - \sigma_{corr}^2}} \tag{3.19}$$

$$\sigma_y = \sigma_{corr}\sigma_{dos}\sqrt{\frac{1}{2\sigma_{dos}^2 - \sigma_{corr}^2}} \tag{3.20}$$

Rotated system

So far we assumed that detectors are arranged along either the streamwise or spanwise directions. We now investigate a rotated system as illustrated in figure 3.4. The puffs move along the streamwise direction x, with the fluctuation in wind speed being present in spanwise direction y. The detectors are arranged on axes x' and y'.

Transforming into the $x' - y'$ system results in

$$\begin{aligned} &\exp\left(-\frac{\mu^2}{2\sigma_\mu^2}\right)\exp\left(-\frac{(y-\mu)^2}{2\sigma_y^2}-\frac{x^2}{2\sigma_x^2}\right) \\ =\exp\left(-\frac{\mu^2}{2\sigma_\mu^2}\right)&\exp\left(-\frac{\left(\sqrt{2}y'-\sqrt{2}x'+2\mu\right)^2}{8\sigma_y^2}-\frac{(y'+x')^2}{4\sigma_x^2}\right) \end{aligned} \tag{3.21}$$

As on the x' axis $y'=0$, this simplifies to:

$$\exp\left(-\frac{\mu^2}{2\sigma_\mu^2}\right)\exp\left(-\frac{\left(\sqrt{2}x'+2\mu\right)^2}{8\sigma_x^2}-\frac{x'^2}{4\sigma_y^2}\right) \tag{3.22}$$

Equivalently we obtain for the y'

$$\exp\left(-\frac{\mu^2}{2\sigma_\mu^2}\right)\exp\left(-\frac{\left(\sqrt{2}y'-2\mu\right)^2}{8\sigma_x^2}-\frac{y'^2}{4\sigma_y^2}\right) \tag{3.23}$$

We see that the puffs observed on both axes are symmetrical and can thus reduce our investigation to one axis. Integrating over μ yields

$$
\begin{aligned}
&\int_{-\infty}^{\infty} \exp\left(-\frac{\mu^2}{2\sigma_\mu^2}\right) \exp\left(-\frac{\left(\sqrt{2}x' - \sqrt{2}y' + 2\mu\right)^2}{8\sigma_x^2} - \frac{\left(x'+y'\right)^2}{4\sigma_y^2}\right) \cdot \\
&\exp\left(-\frac{\mu^2}{2\sigma_\mu^2}\right) \exp\left(-\frac{\left(\sqrt{2}\left(x'+a\right) - \sqrt{2}y' + 2\mu\right)^2}{8\sigma_x^2} - \frac{\left(\left(x'+a\right)+y'\right)^2}{4\sigma_y^2}\right) d\mu \\
&= \int_{-\infty}^{\infty} \exp\left(-\frac{\mu^2}{2\sigma_\mu^2}\right) \exp\left(-\frac{\left(y-\mu\right)^2}{2\sigma_y^2} - \frac{x^2}{2\sigma_x^2}\right) \cdot \\
&\exp\left(-\frac{\mu^2}{2\sigma_\mu^2}\right) \exp\left(-\frac{\left(\sqrt{2}y + a - \sqrt{2}\mu\right)^2}{4\sigma_y^2} - \frac{\left(\sqrt{2}x^2 + a\right)}{4\sigma_x^2}\right) d\mu \\
&= \frac{\sqrt{2}\sqrt{\frac{\sigma_\mu^2\sigma_y^2}{2}\left(\sigma_\mu^2+\sigma_y^2\right)}}{\sigma_\mu^2+\sigma_y^2} \exp\Bigg(\\
&-\frac{2\sigma_\mu^2\sigma_y^2 + \sigma_\mu^2\sigma_x^2 + 2\sigma_y^4 + 2\sigma_y^2\sigma_x^2}{8\sigma_y^2\sigma_x^2\left(\sigma_\mu^2+\sigma_y^2\right)}a^2 - \frac{\sqrt{2}}{2\sigma_\mu^2+2\sigma_y^2}ay - \\
&\frac{\sqrt{2}}{2\sigma_x^2}ax - \frac{1}{\sigma_\mu^2+\sigma_y^2}y^2 - \frac{1}{\sigma_x^2}x^2\Bigg) \\
&= \frac{\sqrt{2}\sqrt{\frac{\sigma_\mu^2\sigma_y^2}{2}\left(\sigma_\mu^2+\sigma_y^2\right)}}{\sigma_\mu^2+\sigma_y^2} \exp\Bigg(\\
&-\frac{2\sigma_\mu^2\sigma_y^2 + \sigma_\mu^2\sigma_x^2 + 2\sigma_y^4 + 2\sigma_y^2\sigma_x^2}{8\sigma_y^2\sigma_x^2\left(\sigma_\mu^2+\sigma_y^2\right)}a^2 - \frac{1}{2\sigma_\mu^2+2\sigma_y^2}a\left(x'-y'\right) - \\
&\frac{1}{2\sigma_x^2}a\left(x'+y'\right) - \frac{1}{2\left(\sigma_\mu^2+\sigma_y^2\right)}\left(x'-y'\right)^2 - \frac{1}{\sigma_x^2}\left(x'+y'\right)^2\Bigg)
\end{aligned}
\tag{3.24}
$$

Again we find a normal distribution that has its centre at the position of the detector being looked at. The standard distribution depends on the three variables σ_x, σ_y and σ_μ. We cannot just integrate over x, because the axis is partially oriented in streamwise direction. However, we can find the travel speed of puffs through the array as described above and therefore we have an independent means of obtaining σ_x.

In analogy to the detectors on the spanwise axis, we again evaluate the dosage and find

$$
\begin{aligned}
&\int_{-\infty}^{\infty} \exp\left(-\frac{\mu^2}{2\sigma_\mu^2}\right) \exp\left(-\frac{\left(\sqrt{2}y' - \sqrt{2}x' + 2\mu\right)^2}{8\sigma_y^2} - \frac{\left(y'+x'\right)^2}{4\sigma_x^2}\right) d\mu \\
&= \frac{\sqrt{2\pi}\sigma_y\sigma_\mu}{\sqrt{\sigma_y^2+\sigma_\mu^2}} \exp\left(-\frac{\sigma_y^2+\sigma_\mu^2+\sigma_x^2}{4\sigma_x^2(\sigma_y^2+\sigma_\mu^2)}x'^2 - \frac{\sigma_y^2+\sigma_\mu^2+\sigma_x^2}{4\sigma_x^2(\sigma_y^2+\sigma_\mu^2)}y'^2 - \frac{\sigma_y^2+\sigma_\mu^2-\sigma_x^2}{2\sigma_x^2(\sigma_y^2+\sigma_\mu^2)}x'y'\right)
\end{aligned}
\tag{3.25}
$$

Solving the system

$$\frac{1}{2\sigma_{corr}^2} = \frac{\sigma_\mu^2\sigma_x^2 + 2\sigma_\mu^2\sigma_y^2 + 2\sigma_x^2\sigma_y^2 + \sigma_y^4}{8\sigma_x^2\sigma_y^2\left(\sigma_\mu^2 + \sigma_y^2\right)} \tag{3.26}$$

and

$$\frac{1}{2\sigma_{dos}^2} = \frac{\sigma_y^2 + \sigma_\mu^2 + \sigma_x^2}{4\sigma_x^2(\sigma_y^2 + \sigma_\mu^2)} \tag{3.27}$$

we then obtain

$$\sigma_\mu = \frac{\sigma_x}{\sigma_{corr}\sqrt{2\left(2\sigma_x^2 - \sigma_{dos}^2\right)}}\Bigg(-2\sigma_x^2\sigma_{corr}^2 + 4\sigma_x^2\sigma_{dos}^2 + \sigma_{corr}^2\sigma_{dos}^2 + \sqrt{4\sigma_x^4\sigma_{corr}^4 - 16\sigma_x^4\sigma_{corr}^2\sigma_{dos}^2 + 16\sigma_x^4\sigma_{dos}^4 + 12\sigma_x^2\sigma_{corr}^4\sigma_{dos}^2 - 8\sigma_x^2\sigma_{corr}^2\sigma_{dos}^4 - 3\sigma_{corr}^4\sigma_{dos}^4}\Bigg)^{1/2} \tag{3.28}$$

$$\sigma_y = \frac{\sigma_x}{\sigma_{corr}\sqrt{2\left(2\sigma_x^2 - \sigma_{dos}^2\right)}}\Bigg(2\sigma_x^2\sigma_{corr}^2 - 4\sigma_x^2\sigma_{dos}^2 + \sigma_{corr}^2\sigma_{dos}^2 + \sqrt{4\sigma_x^4\sigma_{corr}^4 - 16\sigma_x^4\sigma_{corr}^2\sigma_{dos}^2 + 16\sigma_x^4\sigma_{dos}^4 + 12\sigma_x^2\sigma_{corr}^4\sigma_{dos}^2 - 8\sigma_x^2\sigma_{corr}^2\sigma_{dos}^4 - 3\sigma_{corr}^4\sigma_{dos}^4}\Bigg)^{1/2} \tag{3.29}$$

$$\sigma = 2\sigma_x\sigma_y\sqrt{\frac{\sigma_\mu^2 + \sigma_y^2}{\sigma_\mu^2\sigma_x^2 + 2\sigma_\mu^2\sigma_y^2 + 2\sigma_x^2\sigma_y^2 + \sigma_y^4}} \tag{3.30}$$

$$\sigma_y = \sqrt{\frac{\sigma_\mu^2\sigma^2 - 2\sigma_\mu^2\sigma_x^2 + \sigma^2\sigma_x^2 \pm \sqrt{\sigma_\mu^4\sigma^4 - 4\sigma_\mu^4\sigma^2\sigma_x^2 + 4\sigma_\mu^4\sigma_x^4 + \sigma_\mu^2\sigma^4\sigma_x^2 + \sigma^4\sigma_x^4}}{4\sigma_x^2 - \sigma^2}} \tag{3.31}$$

3.3.2 Application to some measured puff signals

Up to this point, the method developed has relied on the assumption of idealised Gaussian puffs. Rather than providing rigorous proof of the validity of this assumption, which we consider very difficult to achieve, we will now demonstrate the behaviour of q_t when applied to puff measurements selected from field experiments. The concentration signals shown in the upper row of figure 3.5 were measured simultaneously at four different locations during a puff dispersion field experiment in a desert location in Nevada [63]. Details of the experiment are not relevant at this point. The upper row of figure 3.5

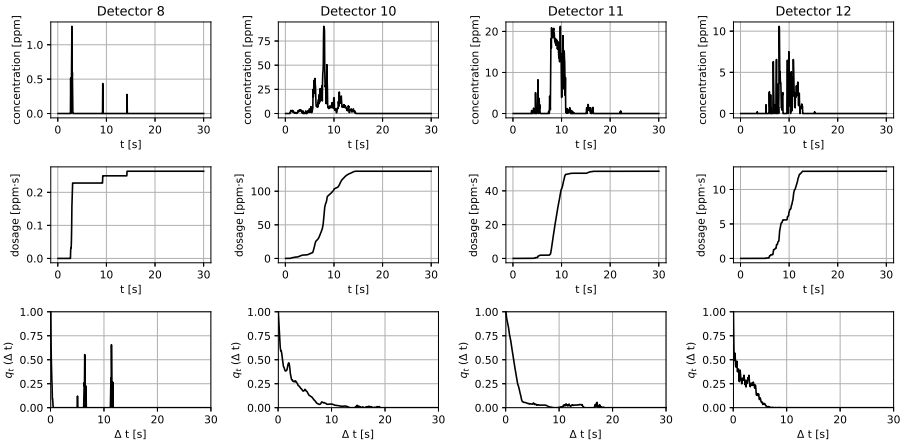

FIGURE 3.5: Upper row: concentration measurements at four different detectors during a puff release experiment in a desert location in Nevada [63]; middle row: cumulative dosages corresponding to the concentrations in the first row; bottom row: $q_t(\Delta t)$ corresponding to the concentrations in the first row.

shows the measured concentrations, the middle row shows the cumulative dosage over time, and the bottom row shows the distance function $q_t(\Delta t)$.

Both the orders of magnitude of the concentration and the structure of the signals show very different characteristics at the different detectors. The concentration measured at detector 8, shown on the upper left of figure 3.5, contains three spikes at a low concentration value. Given that the total dosage measured at this detector is two or even three orders of magnitudes smaller than at the other detectors, it could be assumed that this is merely noise. However, the cumulative dosage over time shows a staircase shape that is caused by the fact that there are several spikes. Applying a definition of the arrival time and leaving time as 5 % and 95 % of the dosage respectively would result in unrealistically long puff durations. While this could be mitigated by applying a threshold, it is not evident what threshold would be appropriate. The generalised distance function $q_t(\Delta t)$ is continuous for the shortest time scales and rapidly decays to zero, with the correlation between the spikes resulting in peaks at larger time scales. Defining the puff duration as the time Δt at which $q_t(\Delta t)$ has decayed to $q_t(\Delta t) = 0.05$ leads to a result of the order of less than half a second, which we consider an appropriate description in this case.

At detectors 10, 11 and 12 significantly higher dosages were measured, and the concentration over time, although not Gaussian, is consistent with what one might expect from a puff travelling through a full-scale detector array. For these the total dosage is confined to a single time interval, as opposed to multiple spikes at detector 8. We therefore have reason to believe that the definition of arrival and leaving times will result in realistic estimates of the puff duration for these detectors.

We will compare the resulting puff durations in more detail later.

Whereas the time in which $q_t(\Delta t)$ decays to zero is in a similar order of magnitude for detectors 10, 11 and 12, its shape at smaller time scales is very different for the different detectors, and certainly doesn't show the characteristics of a Gaussian signal (although detector 11 might come close). Therefore we need to investigate if this has an influence on the puff duration derived from $q_t(\Delta t)$.

To test our previous assumption that the puffs are Gaussian, we now create synthetic signals with similar characteristics compared to those of the measured signals in terms of duration and dosage. Applying our criterion $q_t(\Delta t) = 0.05$ for the puff duration and the previous finding (equation 3.6) that the standard deviation of a Gaussian function and the corresponding $q_t(\Delta t)$ are related by the factor $\sqrt{2}$, we can define an artificial Gaussian signal such that the puff duration based on $q_t(\Delta t)$ is identical to that of the corresponding measured signal. We further define the dosage of the artificial signal to be identical to that of the measured one. The position in time of the artificial signal can be arbitrarily chosen. However, for ease of visual comparison we use a Gaussian fit based on least squares (which does **not** provide the correct standard deviation and dosage) to find a realistic estimate of the peak time.

The result is shown in figure 3.6. For ease of comparison the measured concentrations and their corresponding dosages and $q_t(\Delta t)$ are also shown (in light grey). By definition $q_t(\Delta t)$ for the measured and Gaussian signals overlap at $q_t(\Delta t) = 0.05$ and also the total dosages are identical. We can also see that the start and end times of the artificial signal correspond fairly well with those of the measured signal in the case of detectors 10 and 12, whereas for detector 8 the first spike is approximated. In the case of detector 11 the boundaries of the Gaussian signal correspond approximately to those of the most dominant peak.

A much stronger similarity can be found when comparing the dosage over time. In the case of detectors 10, 11 and 12 there is very little difference between the artificial and measured dosage curves. For detector 8 the dosage curves correspond over the time interval corresponding to the first spike, but the staircase shape due to the two further spikes is not reproduced by the synthetic signal.

We now compare the resulting puff durations quantitatively, as shown in table 3.1. The dosages given in the table as well as the puff durations based on $q_t(\Delta t)$ are by definition identical for the measured signal and the corresponding Gaussian signal.

For detector 8 there is a strong disagreement between the puff durations of the measured signal based on dosage and $q_t(\Delta t)$, which could be expected based on the above discussion. For the other detectors, the puff durations based on the two methods are not identical, but of similar orders. The dosage-based duration of the artificial Gaussian signal is in fairly good agreement with the puff durations of the measured signal based on $q_t(\Delta t)$. They also agree well with the dosage-based puff durations of the measured signal for detectors 10, 11 and 12.

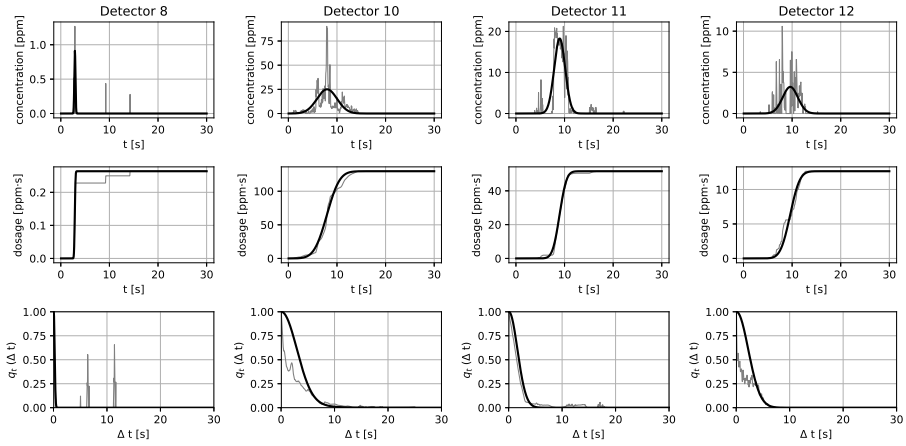

FIGURE 3.6: Approximation of the quantities in figure 3.5 by synthetic Gaussian puffs. The original signal is shown in light grey for comparison.

Detector	Dosage [ppm s]	Duration [s] (q_t)	Duration [s] (dosage) Measured Signal	Duration [s] (dosage) Gaussian Signal
8	0.26	0.40	11.60	0.40
10	129.77	7.15	7.60	6.80
11	51.61	3.90	3.00	3.70
12	12.65	5.40	5.35	5.15

TABLE 3.1: Comparison of dosages and of puff durations based on dosages and based on q_t for the results shown in figures 3.5 and 3.6.

The above examples demonstrate that the proposed method leads to reasonable results for a large-scale description of puffs. However the method goes beyond producing similar results to established methods in a different way. Referring back to figures 3.5 and 3.6, we now discuss the short time-scale information contained in $q_t(\Delta t)$. The concentration time series measured at detector 10 has two significant peaks at about 7 seconds and a second at about 9 seconds. We can find these peaks represented by a peak in $q_t(\Delta t)$ at $\Delta t \approx 2\,\mathrm{s}$. From visual inspection it could be argued that the concentration signal measured at detector 12 is noisier than that at detector 10, which in turn is still noisier than the signal at detector 11. We find this reflected in $q_t(\Delta t)$. For the signal at detector 12, which visibly contains a significant amount of noise at short time-scales, $q_t(\Delta t)$ drops sharply until $\Delta t \approx 0.15\,\mathrm{s}$ and then falls at a smaller rate. The last part of the curve is almost identical with that of the artificial Gaussian signal (see figure 3.6). Looking at $q_t(\Delta t)$ for detector 11, we see that it does not go down to zero in a continuous curve, but changes its characteristics at $\Delta t \approx 3\,\mathrm{s}$, whereafter it falls at a much lower rate. This reflects the characteristic of the concentration signal with three different peaks, one of them significantly stronger than the others.

3.4 Results

3.4.1 Application to wind-tunnel data

To compare puff durations obtained from our method to those obtained from a dosage-based approach, we selected data from a set of puff releases made in a wind tunnel from the CEDVAL-LES database [1, 10, 41]. All the puff releases in this dataset are provided with a quality flag which allows the user to distinguish between high-quality releases above a certain dosage threshold, and low-quality ones that fall below. We selected a dataset containing 35 high-quality releases and 140 low-quality ones, because the low number of high-quality releases is similar to what could be expected from typical field measurement data.

We computed the puff duration based on the dosage and based on the distance-neighbour function q_t to compare the performance of these methods. In order to estimate the accuracy that could be achieved for a given number of experiments, we selected 100 random ensembles of various sizes from 1 up to the total number of available experiments in each case. This was done separately for the high-quality and low-quality releases and for the entire set.

The puff duration was obtained from the dosage by computing the difference between leaving time, defined as the time at which 95 % of the dosage has arrived, and arrival time, defined as the time at which 5 % of the dosage has arrived. For each ensemble the average was computed. The average puff duration from q_t on the other hand was directly computed from a time series formed by connecting all the randomly selected samples of each ensemble.

Figure 3.7 shows a scatter plot for the puff duration computed using both methods from the complete set of high and low-quality releases. The left-hand part of the figure shows the puff duration for all ensembles based on the dosage, the right-hand part shows the same based on q_t. It can be seen that with increasing ensemble size the dosage-based and the q_t-based series converge to significantly different values for the duration. When comparing an ensemble size of 1, i.e. randomly selected single releases, it becomes obvious that the dosage-based approach leads to puff durations over the whole range from 0 to roughly the duration of each experiment itself, whereas q_t is biased towards small durations. The difference is likely to be found in the lowest and therefore noisiest signals, as discussed in the previous section (see figure 3.5, in particular detector 8). Whereas the dosage, when used without any further processing, sums up random noise, q_t finds only short correlation times for these low signals. For larger ensembles, the arithmetic mean of durations from the dosage-based approach results in an overestimated value of the average puff duration, since the erroneous values from the low-signal releases are not discarded. q_t on the other hand computes a weighted average with a preference for

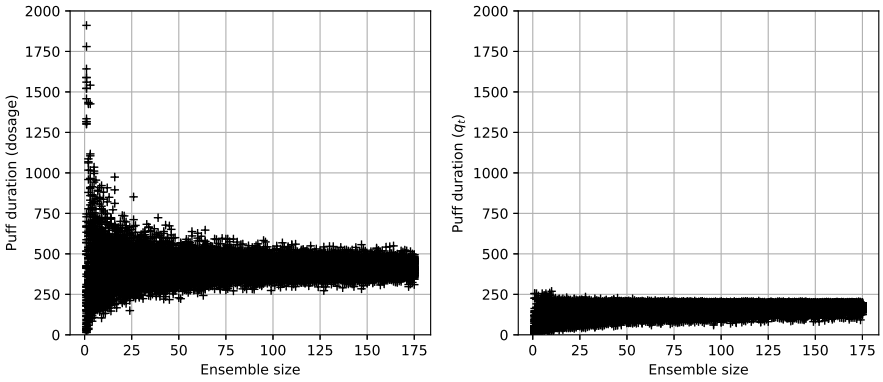

FIGURE 3.7: Scatter plot of the puff duration based on dosage (left) and q_t (right) for random combinations of puff releases (taken from a series of measurements at one detector as provided in [1]) with ensemble sizes up to the total number of releases. All releases are included. The results have been computed for 100 different ensembles for each ensemble size.

stronger signals (as can be seen from the definition), which explains why with increasing ensemble size there are less ensembles with an underestimated average duration.

Section 3 showed that puff durations based on the two methods differ significantly for noisy signals with low dosages, but not for stronger signals (see table 3.1). This can indeed be found when selecting only high-quality releases from this dataset. This is illustrated in figure 3.8, which shows the average puff duration over all 100 ensembles as a function of the ensemble size. The left-hand side of figure 3.8 shows the puff duration based on the dosage, the right-hand side shows the puff duration based on q_t. Although a difference is apparent, it is not as strong as for the whole dataset shown in figure 3.7 and may well be explained by the slightly different definitions of the puff duration rather than uncertainties in the result. We find that, whereas the average puff duration (but not the standard deviation) is almost independent of the ensemble size for the dosage-based method, there is an increase in the puff duration based on q_t with the ensemble size. This can be explained by the fact that q_t computed for an entire time series by definition puts more weight on stronger signals. Beyond an ensemble size of about 20 the value of q_t only changes minimally, so this can be considered the minimum acceptable ensemble size.

We would like to establish an objective method that does not require any thresholds or filtering. Therefore we need to compare ensembles of all (i.e. high and low-quality) measurements to ensembles of only high-quality signals. Figure 3.9 shows a comparison of the puff duration computed from ensembles taken from all measurements (fat dashed line) to the puff duration based on ensembles of the high-quality measurements only (solid line). Again, the left-hand side shows the puff duration based on the dosage, whereas the right-hand side shows the puff duration based on q_t. For the dosage-based puff duration we find a striking difference between the datasets. In no case is the average puff duration based on all measurements even within the uncertainty range of the puff duration based

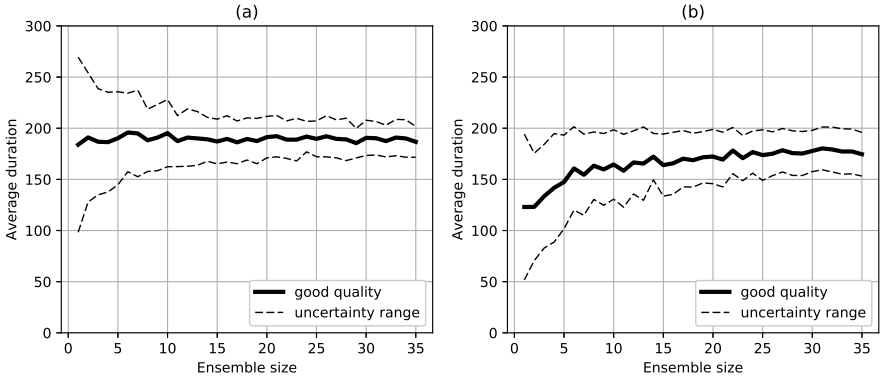

FIGURE 3.8: Comparison of average puff durations for different ensemble sizes based on (a) dosage and (b) q_t. Only concentration measurements marked as high quality are considered. The dashed lines show the standard deviation.

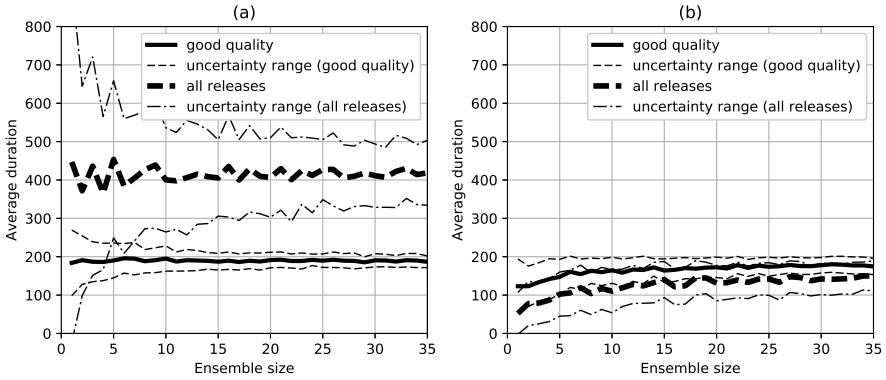

FIGURE 3.9: Comparison of average puff durations for different ensemble sizes based on dosage (left column) and q_t (right column). Results for ensembles taken out of a pool of high quality measurements only are shown as a solid line. Results for ensembles taken out of all measurements, both good and low quality, are shown as a fat dashed line. The thin dashed and dot-dashed lines show the corresponding standard deviations.

on the high-quality signals. The random uncertainty of the puff duration based on q_t is higher, but the result for all measurements vs. high-quality measurements is much closer. This suggests that q_t might be the better, more reliable, choice for evaluating field data.

To get a better idea of the quality of ensembles of all measurements, we take the uncertainty range of the best available prediction of the correct value (i.e. the puff duration from an ensemble of all 35 high-quality puffs) and plot the puff duration computed from ensembles taken from all measurements over it (see figure 3.10). It can be seen that, wheras small ensembles underpredict the puff duration, the result is within the uncertainty range for ensemble sizes of 60 or more.

For validation purposes it is desirable to reduce the uncertainty of measurements as far as possible. Figure 3.11 compares the normalised standard deviation for different ensemble sizes between the dosage-based method (thin dashed line) and the q_t-based approach, (a)

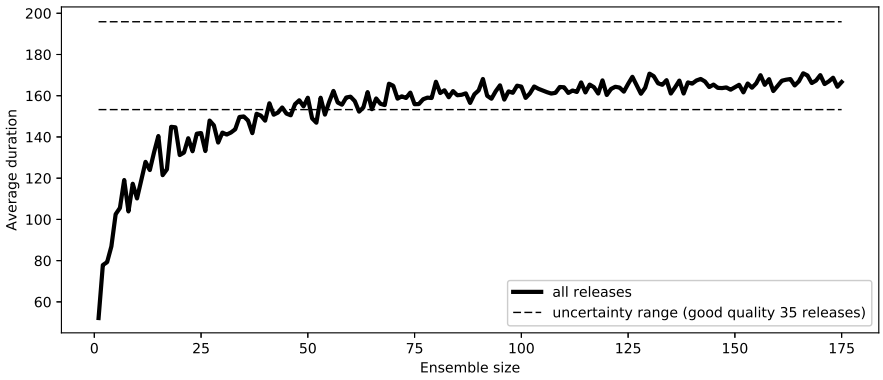

FIGURE 3.10: Average puff durations for different ensemble sizes based on q_t for ensembles of all measurements. The dashed lines indicate the range of uncertainty of the best result (i.e. biggest ensemble size) for the high quality measurements. It can be seen that ensembles of about 60 are sufficient to lie within this uncertainty range.

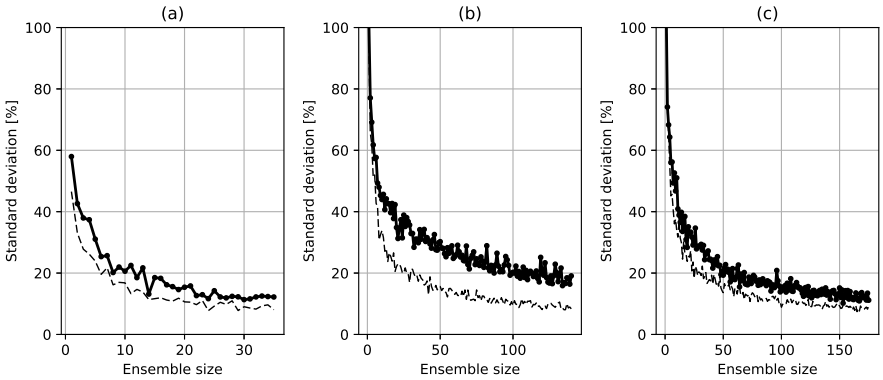

FIGURE 3.11: Standard deviations of the puff duration based on q_t (fat line) and based on dosage (thin dashed line) for (a) only high quality measurements (b) only low quality measurements and (c) combinations of all measurements

for the high-quality ensembles, (b) for the low-quality ensembles and (c) for ensembles taken from all measurements. In all cases the standard deviation is lower for the dosage-based approach, which would suggest that this method is better for validation purposes. However this is misleading given the large systematic error contained in the puff durations based on this method when using low-quality measurements (compare Figure 3.9; see also Table 3.1). The standard deviation of the q_t-based approach is higher, but the systematic error (in this case as a function of the ensemble size) vanishes for large enough ensembles.

So far discussion of the results has focused on applying our method to a well-established quantity, the puff duration. However it would be desirable to use q_t itself as a validation quantity, because it describes short time scales, which are (at least to our knowledge) not quantified by established validation measures.

The top part of figure 3.12 shows a comparison of average q_t computed for the largest available ensemble of high-quality measurements (solid line) and for the largest available

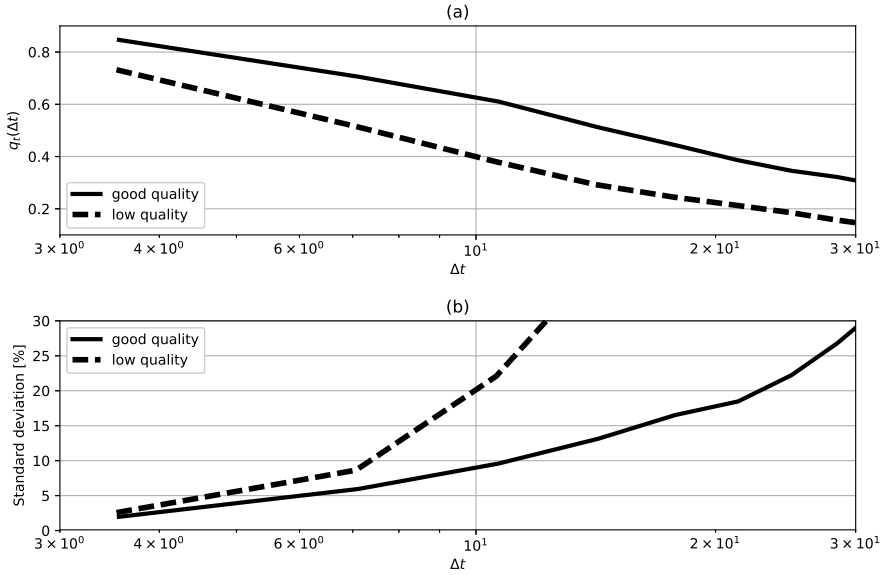

FIGURE 3.12: (a) Average q_t and (b) corresponding normalised standard deviation for the biggest ensemble of high quality signals (solid line) and the biggest ensemble of low quality signals (dashed line).

ensemble of low-quality measurements (dashed line) at small time scales. The corresponding normalised standard deviation is shown in the bottom part of the same figure. Firstly it can be observed that q_t can be clearly distinguished between the two sets (see also figure 3.5 for the behaviour of q_t for different types of signals). Secondly we find that the normalised standard deviation is only about 3 % at the smallest time step, but rapidly increases with Δt as the signal at the two times becomes less and less correlated. This suggests that q_t is more appropriate as a validation quantity for small Δt.

Figure 3.13 (a) shows $q_t(\Delta t \approx 3.5\,s)$ based on high-quality and low-quality ensembles. Figure 3.13 (b) shows the same for $q_t(\Delta t \approx 35\,s)$. It can be seen that q_t becomes independent of ensemble size at comparatively low values (about 7 for $q_t(\Delta t \approx 3.5\,s)$ and about 15 for $q_t(\Delta t \approx 35\,s)$. This makes it very attractive as a validation quantity for atmospheric dispersion modelling, because a meaningful result can be obtained from a small number of measurements, i.e. under similar meteorological conditions.

When comparing the puff durations based on q_t and the dosage, as shown in figure 3.14, the difference regarding low dosages already observed for wind tunnel data is confirmed for field measurements. We selected a puff release from the puff dispersion field experiment in a desert location in Nevada [63] mentioned section 3. Figure 3.14 (a) shows the dosage at each detector, (b) the puff duration based on q_t and (c) the puff duration based on the dosage. The size of the circles is proportional to each quantity respectively. It can be seen that q_t results in relevant puff durations only at detectors with a significant observed dosage, whereas the puff duration based on the dosage results in a longer puff duration at some of the detectors where there is no significant observed dosage. The exact results are shown in table 3.2. At detectors with strong signals the durations from

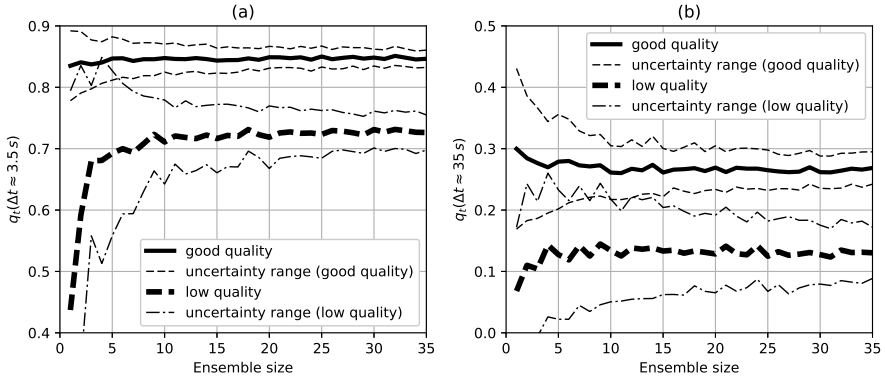

FIGURE 3.13: q_t as a function of ensemble size for two different times. (a) $q_t(\Delta t \approx 3.5\,s)$ and (b) $q_t(\Delta t \approx 35\,s)$. Ensembles based on high quality measurements are shown by a solid line, ensembles based on low quality measurements are shown by a dashed line.

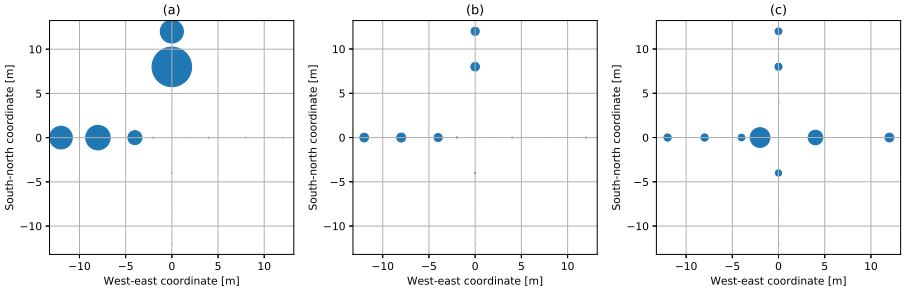

FIGURE 3.14: (a) Dosages (b) puff duration based on q_t (c) puff duration based on dosages. Each quantity is represented by the size of the circles.

both methods are very similar. The results for low dosages suggest that q_t recognises sudden spikes as noise, whereas without pre-processing the dosage approach results in a high duration when there is more than one spike in the detected noise.

Figure 3.15 shows an example of q_t (left-hand side) and $q_{\mathbf{x},t}$ (right-hand side) applied to a series of 240 puff releases (two hours with 30 seconds per release). q_t shows the already familiar shape up to the order of 10 seconds. But for larger times it quantifies the relation between the signals resulting from consecutive releases. $q_{\mathbf{x},t}$ shows a behaviour similar to what has been predicted by theory in Section 3.

The resulting travelling times, computed by deriving Gaussian fits to the results for $q_{\mathbf{x},t}$ shown in Figure 3.15, are shown in figure 3.16. A more detailed evaluation will follow in a future publication.

Detector	Dosage (ppm s)	Duration (dosage) (s)	Duration (q_t) (s)
1	45.05	4.60	4.65
2	52.37	4.70	4.90
3	17.12	3.90	4.05
4	0.05	34.05	0.10
5	0.00	0.00	0.00
6	0.00	0.00	0.00
7	0.05	18.65	0.05
8	0.03	0.00	0.00
9	0.01	6.80	0.05
10	0.00	0.00	0.00
11	0.00	0.00	0.00
12	0.01	3.45	0.05
13	0.00	0.00	0.00
14	137.31	4.40	4.55
15	46.88	4.05	4.10

TABLE 3.2: Comparison of dosages and of puff durations based on dosages and q_t.

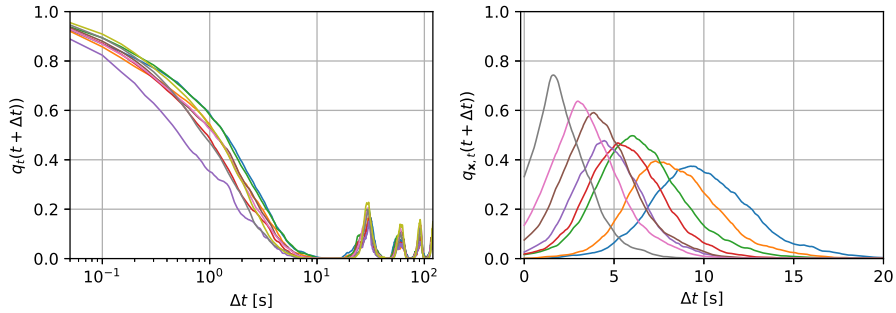

FIGURE 3.15: Example of q_t and $q_{\mathbf{x},t}$ between detectors along the streamwise axis. Detectors at positions $-12\,m$, $-8\,m$, $-4\,m$, $-2\,m$, $0\,m$, $2\,m$, $4\,m$, $8\,m$, $12\,m$, source at $40\,m$. $q_{\mathbf{x},t}$ is relative to the detector nearest to the source.

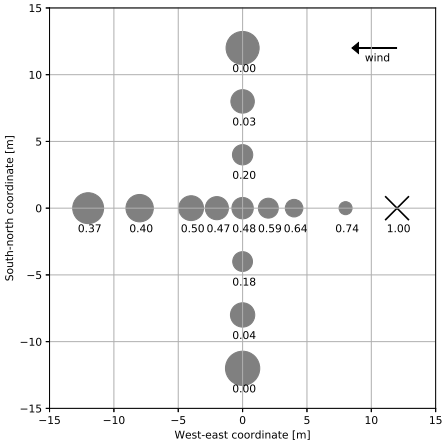

FIGURE 3.16: Marker sizes represent the travelling time from the detector marked with a cross, whereas the numbers correspond to the peak correlation of the signal at each detector to the signal at the detector marked with a cross.

3.5 Summary and discussion

In this chapter a new method for evaluating puff dispersion field experiments on based on generalised distance functions has been presented. It has been shown that characteristic properties of the puff releases, like puff duration, streamwise and spanwise puff size and convection velocity can be derived using this method.

When applied to wind tunnel data, our method shows similar characteristics to a dosage-based approach when estimating the puff duration for high-quality, i.e. sufficiently high-signal, data. For low-quality data, the puff durations derived by our method are more consistent with those derived from the high-quality releases compared to the dosage-based approach, but the standard deviation is significantly higher. For a data set consisting of both low-quality and high-signal data our method retrieves the puff duration of the high-signal releases, whereas the dosage-based method results in an average of puff durations from low-quality and high-signal releases. In this case, the standard deviations of the puff duration derived with both methods are comparable.

First tests on field measurement data show that the distance-neighbour function approach distinguishes between noise and an actual signal when determining puff durations in a detector array, whereas a dosage-based approach needs further input, specifically setting a threshold or similar. This means that the distance-neighbour function method is self-contained and independent of user input (and is therefore less subjective).

It has been shown analytically that the distance-neighbour function method enables much more information about puffs to be obtained by relating signals measured at different locations to each other, in particular the puff size and convection velocity of puffs.

Finally the generalised distance functions themselves can be used as validation quantities for dispersion models. The standard deviation is particularly low at small time scales, which distinguishes them from validation quantities used so far. This means that it is possible to validate the behaviour of large-eddy simulations at the smallest resolved scales or, depending on the resolution of the concentration measurements, even allow for a validation of the subgrid model.

Chapter 4

Preferential concentration of small inertial particles in homogeneous isotropic turbulence

Parts of this chapter have been published under the title 'Explanation of differences in experimental and computational results for the preferential concentration of inertial particles' [131].

4.1 Numerical method

PANDORA as used in this chapter has been developed Stephen John Scott [104] and Aditya Uday Karnik [67]. It is a pseudospectral direct numerical simulation code that is parallelised in 1-D (slab decomposition) and contains a Lagrangian point-particle implementation [104]. The particles are associated to the various slabs (corresponding to different MPI processes) and therefore fluid halos are necessary in order to obtain the fluid velocity from all neighbouring gridpoints necessary for the interpolation scheme applied [104].

This leads to a reduced scalability and high memory consumption when using many processes, as necessary at high Reynolds numbers [128].

4.1.1 Fluid simulation

In PANDORA the following Fourier space equivalents of the rotation form of the Navier-Stokes equation and of the continuity equation are solved [104]:

Stage 1:	$U_1 = U_n$
	$G_1 = F(U_n, t_n)$
Stage 2:	$U_2 = U_1 + \frac{1}{3}\Delta t G_1$
	$G_2 = -\frac{5}{9}G_1 + F(U_2, t_n + \frac{1}{3}\Delta t)$
Stage 3:	$U_3 = U_2 + \frac{15}{16}\Delta t G_1$
	$G_3 = -\frac{153}{128}G_2 + F(U_3, t_n + \frac{3}{4}\Delta t)$
Stage 4:	$U_{n+1} = U_2 + \frac{8}{15}G_3$

TABLE 4.1: Runge-Kutta scheme used in PANDORA [128]

$$\frac{\partial \hat{\boldsymbol{u}}(\boldsymbol{k})}{\partial t} = -\nu \boldsymbol{k}^2 \hat{\boldsymbol{u}}(\boldsymbol{k}) - \widehat{\boldsymbol{\omega} \times \boldsymbol{u}}(\boldsymbol{k}) + \frac{\boldsymbol{k}}{|\boldsymbol{k}|^2}\left[\boldsymbol{k} \cdot \left(\widehat{\boldsymbol{\omega} \times \boldsymbol{u}}\right)(\boldsymbol{k})\right] \tag{4.1}$$

$$\boldsymbol{k} \cdot \hat{\boldsymbol{u}}(\boldsymbol{k}) = 0. \tag{4.2}$$

No separate pressure equation needs to be solved, which is one of the big advantages of spectral methods [104].

4.1.2 Particle simulation

The particle equation described in 2.2.1 is solved in PANDORA, neglecting the terms that are expected to be small in order of magnitude, thus leaving the inertia, drag and gravity terms. Assuming that the particles are small and a have a density much higher than the fluid, the gravity term is also simplified. The resulting particle equation reads

$$m_p \frac{\mathrm{d}u_{p,i}}{\mathrm{d}t} = m_p \frac{1}{\tau_p}\left(u_{f,i} - u_{p,i}\right) + m_p g_i \tag{4.3}$$

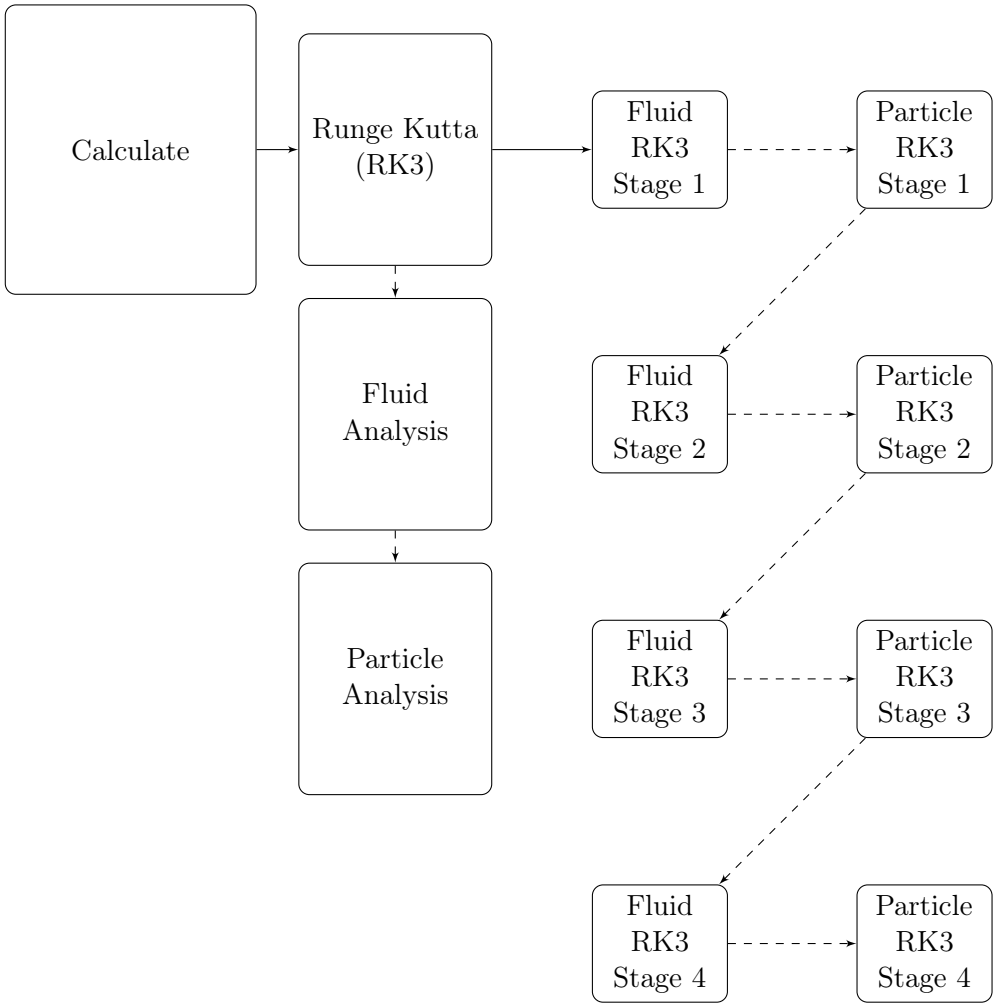

FIGURE 4.1: Flowchart of a timestep in PANDORA. In each timestep a Runge-Kutta scheme is performed, followed by fluid and particle analysis. The Runga-Kutta scheme consists of four stages, each of which is composed of a fluid calculation followed by a particle calculation [128].

4.1.3 Numerical solution

Figure 4.1 gives an overview of the flow of PANDORA during one timestep. The numerical solution of the fluid and particle equations is followed by a computation of fluid and particle statistics.

The third-order Runge-Kutta scheme implemented in PANDORA is shown in table 4.1. It was published by Williamson [126] and has been chosen due to a good balance between accuracy and memory consumption [104]. In each of the four stages the fluid computation is followed by a particle computation.

In the four stages of the fluid computation (see figure 4.2) the Runge-Kutta terms $U1$ to U_{n+1} (see table 4.1) are formed and then the vorticity is computed. The velocity and vorticity components are then transformed into wavespace using the library FFTW [44].

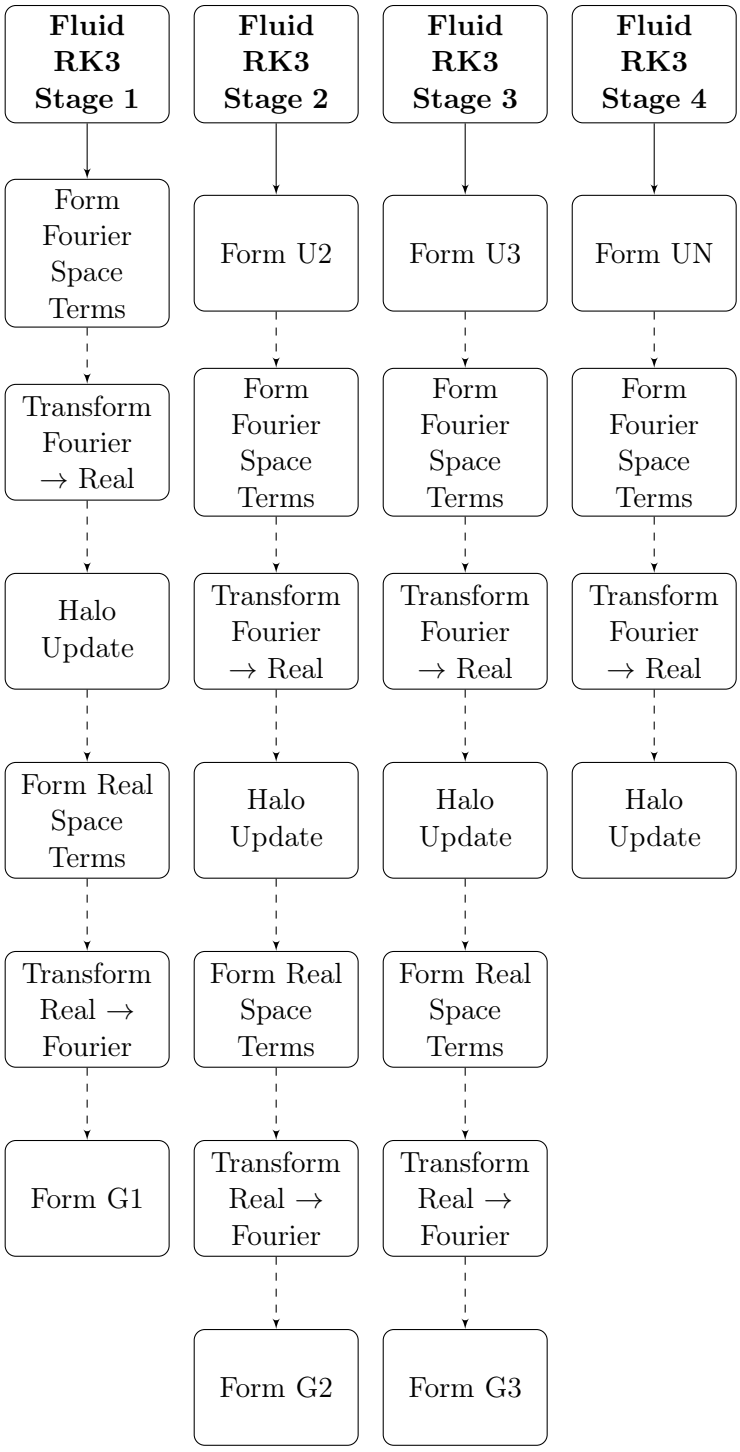

FIGURE 4.2: Flowchart for the different fluid Runge-Kutta stages. The essential program flow starts in Fourier space, continues in real space and ends in Fourier space, with Fast Fourier transforms in between [128].

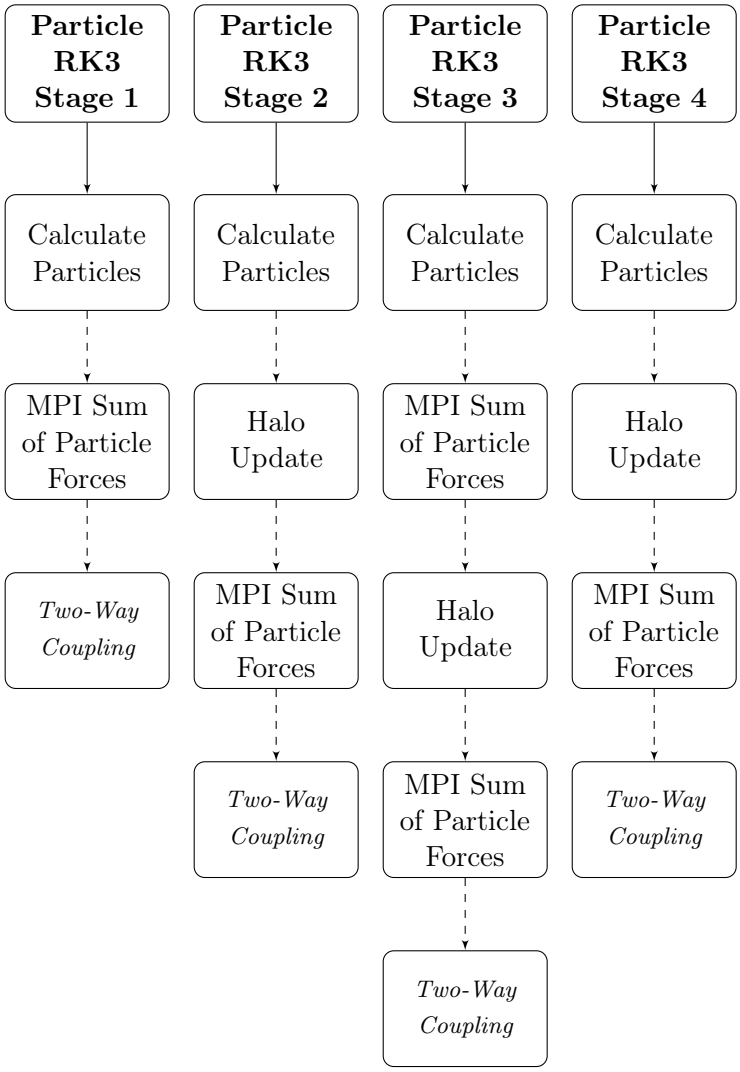

FIGURE 4.3: Flowchart for the different particle Runge-Kutta stages of the particle part [128].

At this point the halos, which are only needed to supply the fluid information for interpolating the fluid velocity at the particle location, are updated. The real space velocities and vorticities are multiplied to form the non-linear term, which is then transformed back into Fourier space. Now the forces in the Navier-Stokes equation can be computed, followed by an enforcing of continuity. Finally the Runge-Kutta terms $G1$ to $G3$ (see table 4.1), or in the last step, the final velocity, are formed.

The particle routines are shown in figure 4.3. For one-way coupled simulations as used in this work only the first step, the particle calculation, is strictly necessary, which consists of interpolating the fluid velocity at the position of the particle and then solving the particle equation of motion.

4.1.4 Forcing scheme

The forcing scheme of PANDORA is based on the stochastic scheme developed by Eswaran and Pope [35] and consists of the following implementation of an Ornstein-Uhlenbeck process [104]:

$$\hat{\boldsymbol{b}}\left(\boldsymbol{k}, t+\Delta t\right) = \hat{\boldsymbol{b}}\left(\boldsymbol{k}, t\right)\left(1-\frac{\Delta t}{T_F}\right) + \hat{\boldsymbol{\theta}}\left(\frac{2\sigma_F^2 \Delta t}{T_F}\right)^{\frac{1}{2}} \tag{4.4}$$

where $\hat{\boldsymbol{b}}(\boldsymbol{k}, t)$ is the forcing acceleration, T_F the forcing time scale, σ_f^2 the forcing amplitude and $\hat{\boldsymbol{\theta}}$ a complex random vector $\hat{\boldsymbol{\theta}}$.

The forcing time scale and forcing amplitude are related through the forcing dissipation $\epsilon^* = \sigma_f^2 T_F$ [35].

4.2 Direct numerical simulations of homogeneous isotropic turbulence at high Reynolds numbers

Direct numerical simulations of homogeneous isotropic turbulence were performed in order to investigate the dispersion of Lagrangian point particles with and without gravity. Prior to inserting particles however it was necessary to achieve a reliable turbulence simulation. A choice of forcing parameters is required in order to compensate for energy loss due to the lack of energy production.

In past PhD theses using PANDORA ([104], [67]) a set of forcing parameters for simulations on grid sizes between 32^3 and 256^3 was used, achieving Taylor-scale Reynolds numbers up to about 150. These forcing parameters were used as a starting point. However, since realistic atmospheric turbulence simulations are expected to require significantly higher Reynolds numbers, it was necessary to extend the forcing to higher grid sizes. An analysis of the memory requirements ofPANDORA showed that the biggest grid size currently achievable is 1024^3, a size at which other workers (e.g. [66], [134], [78]) have successfully simulated turbulent flows at Re_λ up to almost 500.

The simulations by Scott [104] and Karnik [67] are all using a fixed value of the kinematic viscosity ν, regardless of the grid size. In consequence, the dissipation rate rapidly increases when trying to obtain a more turbulent flow at higher Re_λ. Furthermore it was found that guessing adequate forcing parameters, even using an empirical prediction method as described by Eswaran and Pope [35], is a non-trivial task. On the other hand a comparison to more recent publications showed that many workers decrease the kinematic viscosity, hence keeping the dissipation rate constant. A comparison between constant viscosity and constant dissipation simulations is shown in figure 4.4. The data points

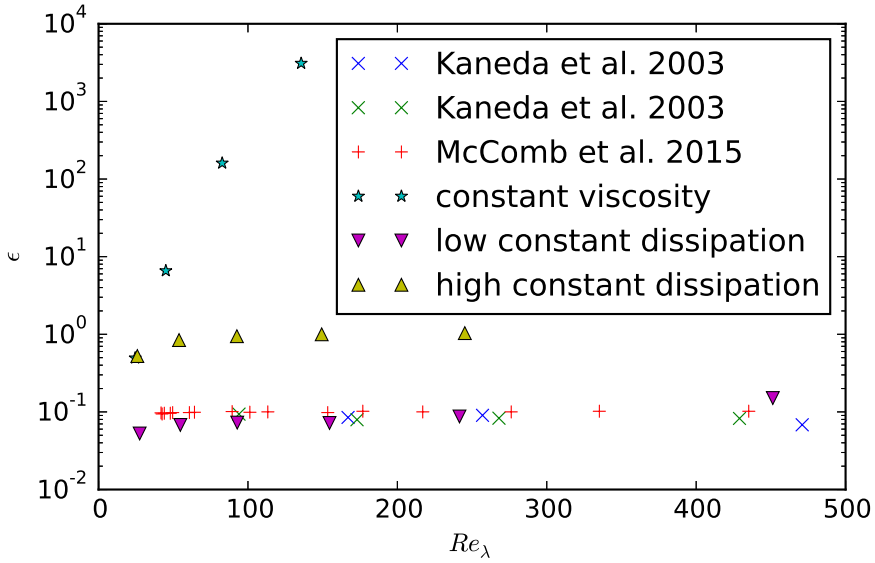

FIGURE 4.4: Dissipation rate ϵ as a function of Taylor scale Reynolds number Re_λ. Own results are compared to results from [66] and [78].

constant viscosity are from own simulations using the forcing parameters documented in [67]. As can be seen, the first data point of the series *high constant dissipation* coincides with the first *constant viscosity* data point. Assuming an approximately linear relation between forcing dissipation ϵ^* and dissipation rate ϵ, the simulations were extended towards higher Reynolds number on grids up to 512^3 by adapting the viscosity while keeping the forcing dissipation constant. It can be seen that the dissipation increases from the first data point, corresponding to a 32^3 grid, to the second data point, corresponding to a 64^3 grid, and then stays fairly constant. The data points denominated *low constant dissipation* are based on the same principle, simply by choosing a lower dissipation rate.

Whilst the forcing dissipation ϵ^* seems to show a fairly clear correlation to the dissipation rate, it does not fully describe the forcing. A forcing time scale T_L and a forcing amplitude σ_F need to be chosen. Rosa et al. investigated the influence of the forcing time scale on the turbulent flow. Own simulations varying the forcing time scale showed no clear results, with little differences regardless of the forcing time scale. However for higher Reynolds numbers it was found that stronger fluctuations can be expected, which leads to potential difficulties of the forcing scheme in combination with the adaptive timestep. If the forcing time scale is chosen too small, larger timesteps can lead to a negative autocorrelation part of the forcing. On the other hand larger forcing time scales can lead to potential problems when the timestep is reduced during higher-energy fluctuations, since the autocorrelation part can then approach 1 and hence prolong the forcing of these high-energy phases.

The resolution $k_{max}\eta$ of all simulations (shown in figure 4.5) is on the order of 1 or

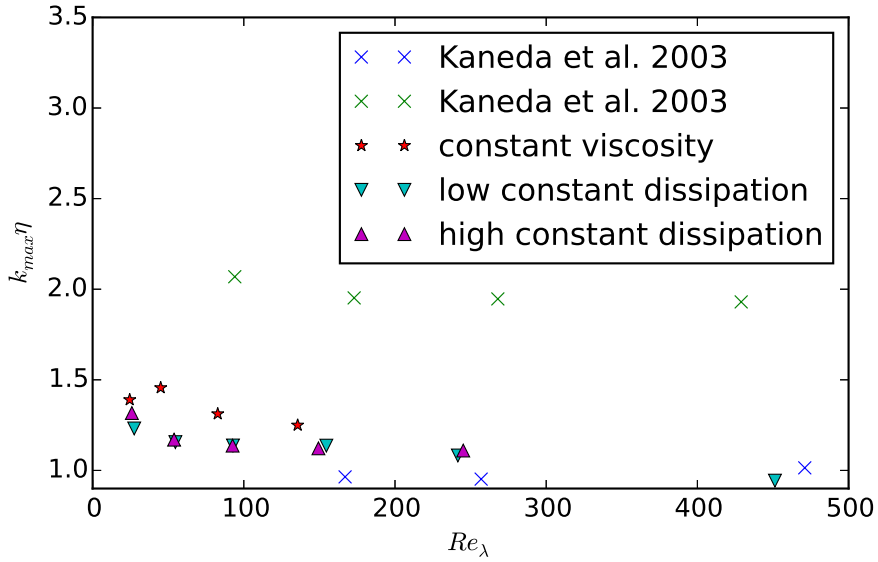

FIGURE 4.5: Resolution $k_{max}\eta$ as a function of Taylor scale Reynolds number Re_λ. Own results are compared to results from [66].

higher and therefore the simulations can be considered sufficiently resolved. Comparing between the original series of simulations and the new approach, it seems that the new parameters produce more consistent results. However, the resolution seems to go down with increasing Reynolds number. Although this is still acceptable for the results presented here, for future simulations on larger grids it should be considered to correct, i.e. reduce, the forcing dissipation. The Taylor Reynolds numbers achieved at a given resolution are somewhat below the ones produced by Kaneda et al. [66], which might be due to more optimised dealiasing and forcing schemes used by these authors.

Both the dissipation constant C_ϵ (figure 4.6) and the ratio of integral length scale and Taylor length scale L/λ (figure 4.7) are in fairly good agreement with published results from other workers, which suggests that the turbulence statistics are correct. C_ϵ is slightly lower compared to other results, which could be an additional indication that the forcing scheme might need to be modified, as discussed above.

4.3 Reynolds number, Stokes number and volume fraction effects

One-way coupled simulations of particles in homogeneous isotropic simulations have been performed over a range of Taylor-scale Reynolds numbers up to ~ 450. The Stokes number St_η, the Reynolds number Re_λ and the number of particles have been varied.

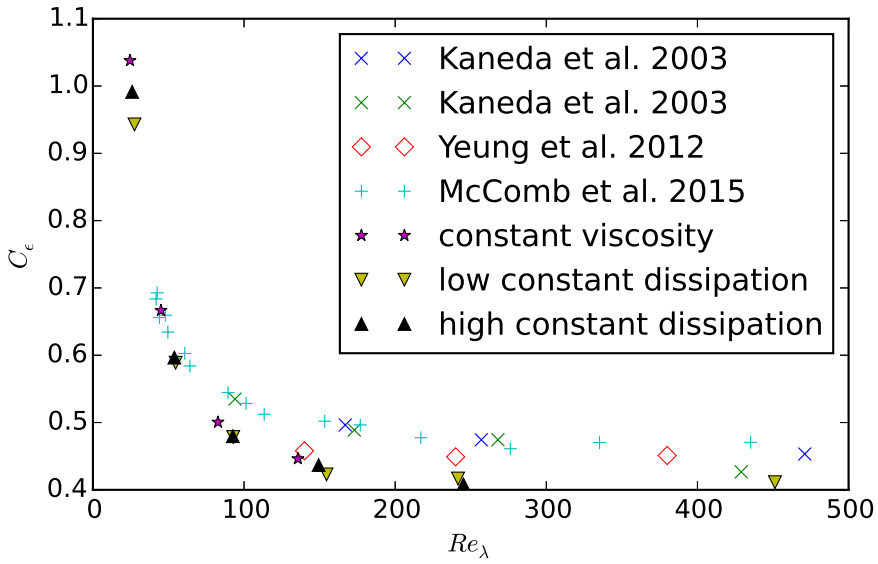

FIGURE 4.6: Dissipation constant C_ϵ as a function of Taylor scale Reynolds number Re_λ. Own results are compared to results from [66], [134] and [78].

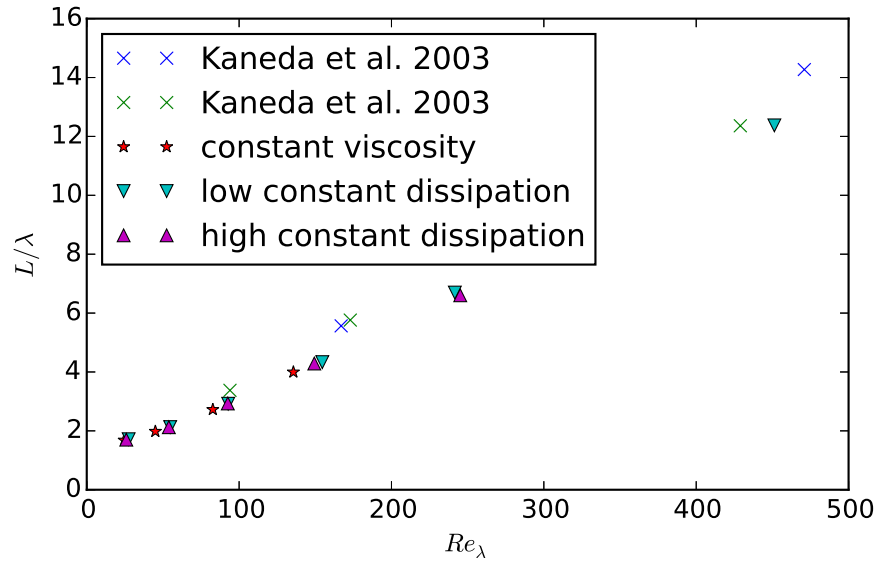

FIGURE 4.7: Ratio between integral length scale and Taylor length scale L/λ as a function of Taylor scale Reynolds number Re_λ. Own results are compared to results from [66], [134] and [78].

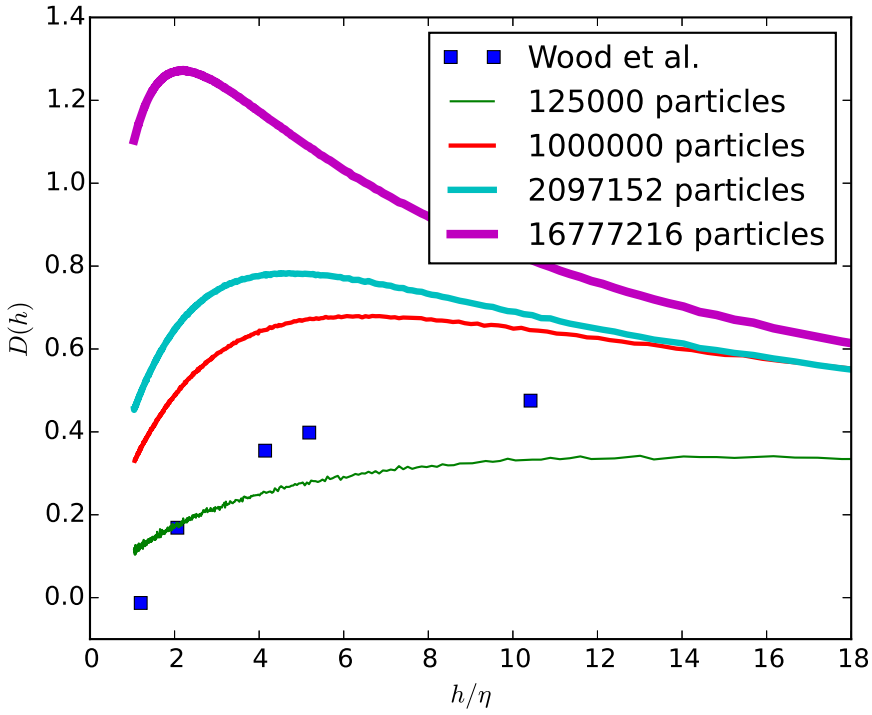

FIGURE 4.8: D measure over normalised bin size h/η at $St_\eta = 1$ and $Re_\lambda \approx 250$ for different total numbers of particles. The results of own simulations are compared to measured results from [132].

It was attempted to reproduce experimental results from Wood et al. [132] that were performed in a turbulence chamber at Reynolds numbers of $Re_\lambda \approx 230$ for Stokes numbers St_η between 0.57 and 8.1. A comparison of simulation results and experimental results for the D measure at $St \approx 1$ are shown in figure 4.8. The number of particles has been varied between 125,000 and 16,777,216, and it can be seen that it has a strong effect on D. D increases with the number of particles, while its peak shifts towards smaller bin sizes.

In order to be able to investigate a broad range of Stokes numbers and numbers of particles within reasonable computing time, simulations at a comparatively low Reynolds number of $Re_\lambda = 45$ were performed for Stokes numbers between 0.4 and 8, using between 4,096 and 2,097,152 particles. The results are shown in figure 4.9. D is highest at $St_\eta = 1$. However, this peak is far less pronounced in the simulations with less particles. The results show that the dependence of D on the number of particles is stronger for smaller St_η and weaker for higher St_η.

The radial distribution function $g(r)$ shows no systematic dependence on the number of particles, as can be seen from figure 4.10 for the same simulations as discussed above. Differences are more likely to be explained with uncertainties, in particular for the simulations with only few particles.

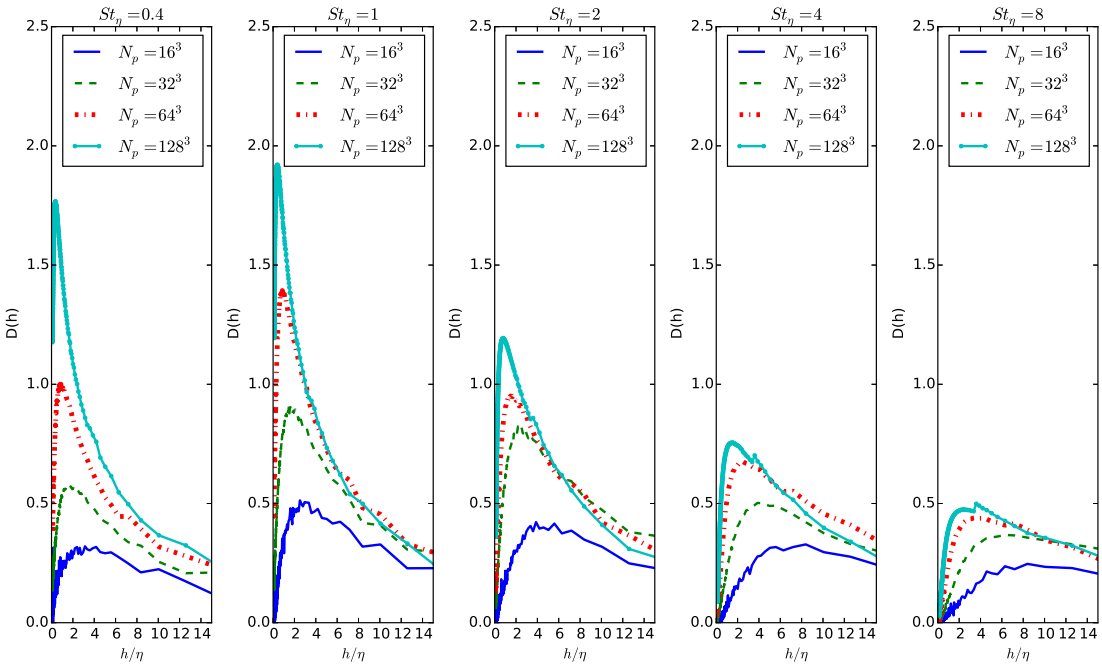

FIGURE 4.9: D measure over normalised bin size h/η for St_η between 0.4 and 8 (from left to right) at $Re_\lambda \approx 45$. The number of particles N_p is varied from $16^3 = 4096$ particles to $128^3 = 2097152$ particles.

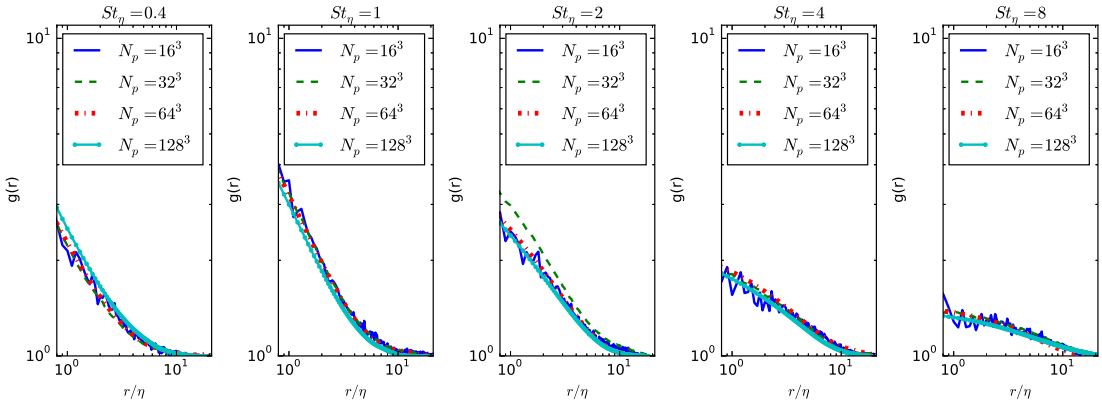

FIGURE 4.10: Radial distribution function $g(r)$ over normalised particle distance r/η for St_η between 0.4 and 8 (from left to right) at $Re_\lambda \approx 45$. The number of particles N_p is varied from $16^3 = 4096$ particles to $128^3 = 2097152$ particles.

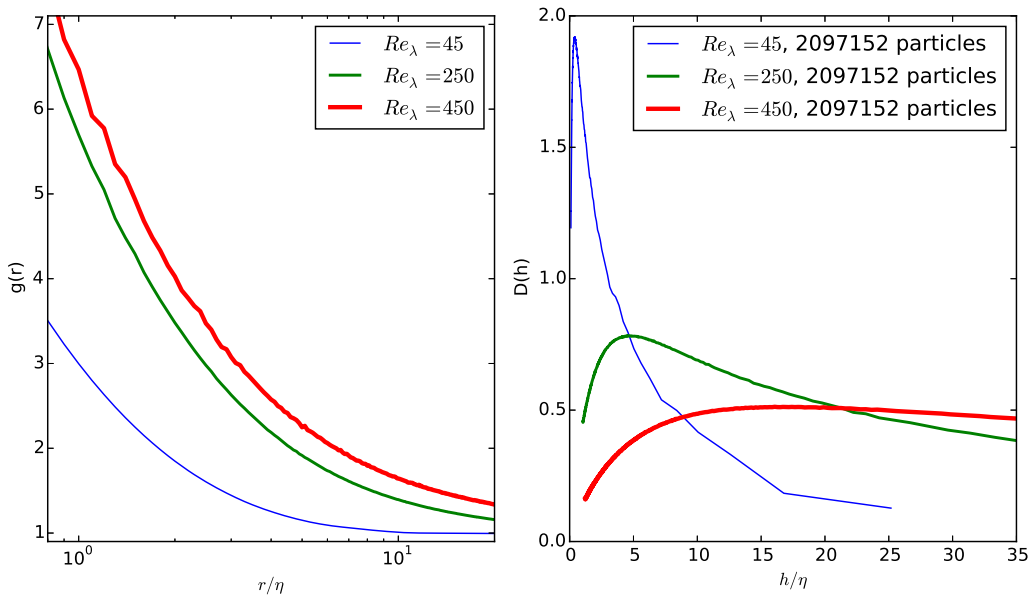

FIGURE 4.11: Left: radial distribution function $g(r)$ over normalised particle distance r/η for $Re_\lambda \approx 45$, $Re_\lambda \approx 250$ and $Re_\lambda \approx 450$. Right: D measure over normalised bin size h/η for the same Reynolds numbers.

The Reynolds number dependence of preferential concentration was investigated comparing simulations for $St_\eta = 1$ at Reynolds numbers up to $Re_\lambda \approx 450$. The results for $Re_\lambda \approx 45$, $Re_\lambda \approx 250$ and $Re_\lambda \approx 450$ are shown in figure 4.11. For the radial distribution function $g(r)$ the results show a significant change between $Re_\lambda \approx 45$ and $Re_\lambda \approx 250$, but very similar values of $g(r)$ for the two highest Reynolds numbers. This agrees well with the results of other workers (e.g. Ireland et al. [58]) that suggest that $g(r)$ becomes independent of Re_λ at sufficiently high Reynolds number. D on the other hand shows a more complex behaviour when maintaining the number of particles. The results for the Reynolds numbers investigated here show that D decreases with increasing Reynolds number.

By varying the number of particles it was found that a scaling behaviour with the Reynolds number similar to that exhibited by $g(r)$ can be achieved for D when using the same number of particles per control volume (at the same resolution $k_max\eta$ - compare figure 4.5). The D measure for $(1/8)^3$ particles per control volume and $(1/4)^3$ particles per control volume is shown in figure 4.12. As for $g(r)$, there is a significant change between $Re_\lambda \approx 45$ and $Re_\lambda \approx 250$, but only a small change between $Re_\lambda \approx 250$ and $Re_\lambda \approx 450$.

Using the definition of the highest resolved wavenumber, it can be stated that D seems to become independent of the Reynolds number at sufficiently high Reynolds number if $N_p^{(1/3)}\eta$ is kept constant where N_p is the number of particles and η is the Kolmogorov length. To the author's knowledge, this is a new result. This scaling law, first published

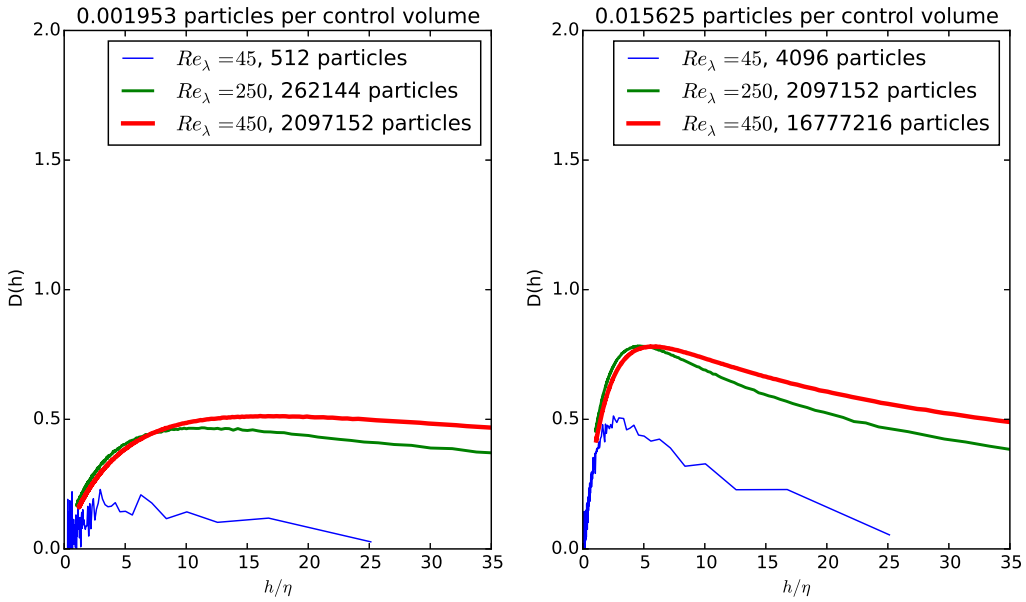

FIGURE 4.12: D measure over normalised bin size h/η at $Re_\lambda \approx 45$, $Re_\lambda \approx 250$ and $Re_\lambda \approx 450$ with constant number of particles per control volume. The graphs on the left and right are for different numbers of particles per control volume (left: $(1/8)^3$, right: $(1/4)^3$).

in [131], has been independently tested by Mora et al. [84] using Voronoi analysis on DNS data.

For small Stokes numbers preferential concentration becomes much less pronounced, but at $St_\eta \approx 0.1$, which according to the estimates for atmospheric aerosols in the previous chapter is within a realistic range, there is still detectable clustering, as shown in figure 4.13. For the same simulations, the Schmidt numbers have been evaluated (figure 4.14). Whereas for St_η between 0.5 and 1 the Schmidt numbers are higher than 1, indicating higher fluid point than solid particle dispersal, for the smaller Stokes numbers the Schmidt numbers are below 1. This would suggest that these small particles do not behave like a gas, but show slightly stronger dispersion due to interaction with the turbulent flow.

4.4 Discontinuous effects

Simulations were carried out to understand how the preferential concentration develops over time. This becomes increasingly important with higher Reynolds number, because the computing times are significantly larger for these bigger simulations. Therefore it is desirable to understand how long a simulation needs to be in order to obtain a valid result.

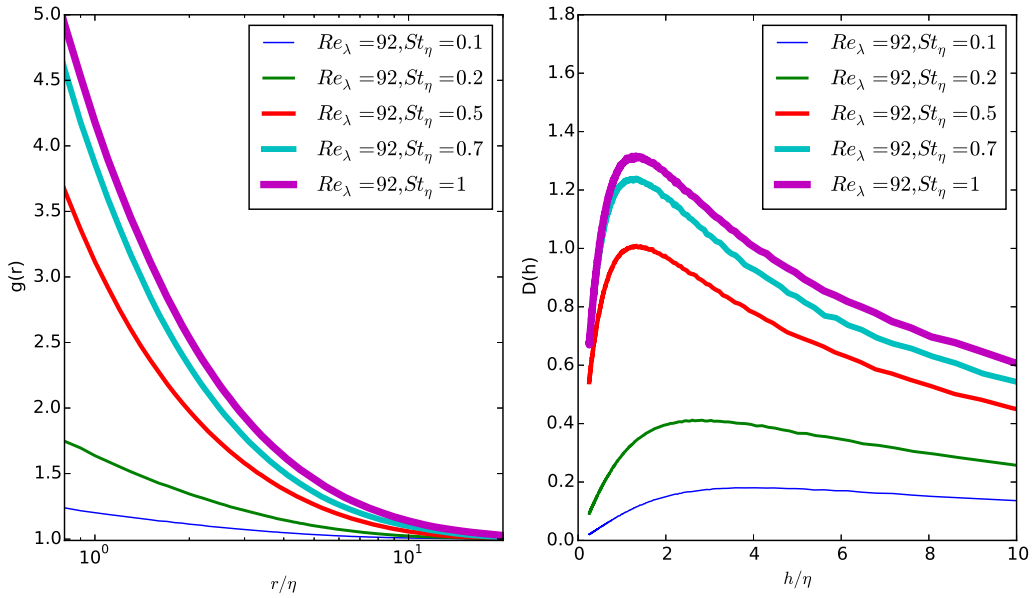

FIGURE 4.13: Radial distribution function $g(r)$ (left) and D measure (right) at $Re_\lambda \approx 92$, Stokes numbers ranging from $St_\eta = 0.1$ to $St_\eta = 1$.

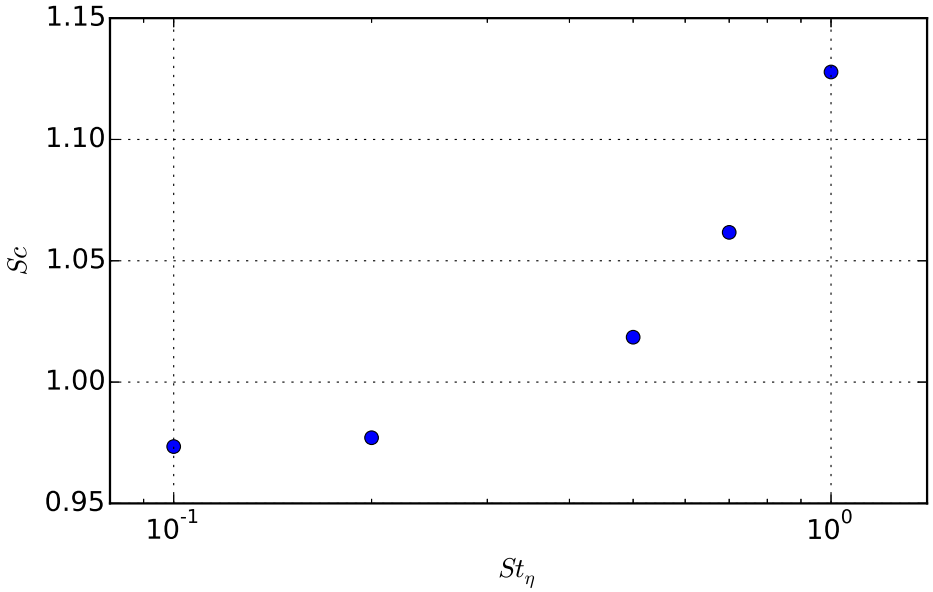

FIGURE 4.14: Schmidt number Sc as a function of Stokes number St_η at $Re_\lambda \approx 92$.

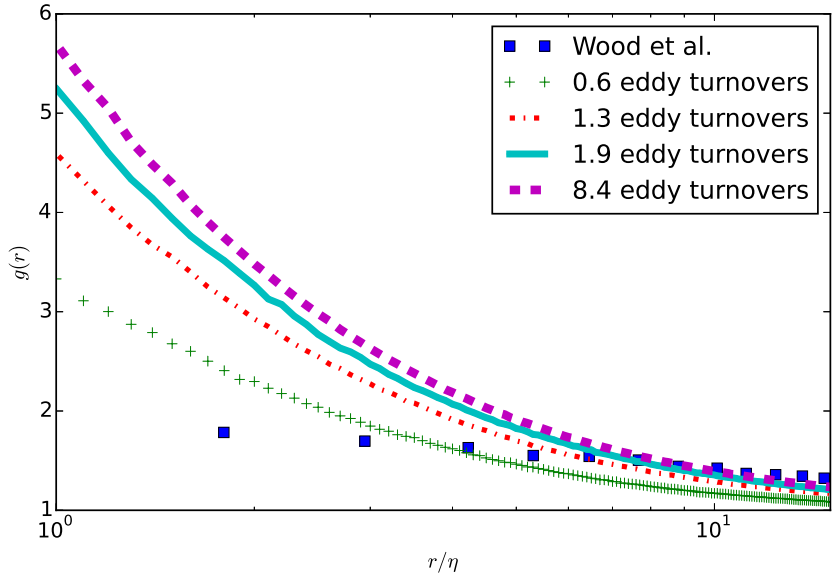

FIGURE 4.15: Radial distribution function $g(r)$ over normalised particle distance r/η for $Re_\lambda \approx 250$ and $St_\eta = 1$. Snapshots between 0.6 and 8.4 large-eddy turnovers after insertion of particles. The results are compared to experimental results from [132].

Furthermore, in the future it is planned to simulate shear flows, which in contrast to homogeneous isotropic turbulence are not stationary. Therefore only a limited simulation time after the particle initialisation is available. This could mean that the initialisation will have a stronger influence on the results than is the case in isotropic turbulence.

Finally the time development of preferential concentration can help to understand better the results from experiments. In contrast to the direct numerical simulations carried out here, experiments cannot have periodic boundary conditions and usually, but in particular in grid turbulence in a wind tunnel, only a limited time is available to investigate the particle behaviour.

In a first numerical experiment, simulations at $Re_\lambda \approx 250$ have been carried out for $St_\eta = 1$ particles. The radial distribution function $g(r)$ is compared to the experimental results by Wood et al. [132] in figure 4.15. The radial distribution function obtained after 1.3 large eddy turnovers is significantly higher than $g(r)$ after 0.6 large eddy turnovers. There is still a slight increase after 1.9 large eddy turnovers and a rather marginal increase after 8.4 large eddy turnovers. These results suggest that preferential concentration has mostly developed after one or two large eddy turnovers. The radial distribution function obtained from the experiment is lower than any of the numerical results for small distances. For larger distances the experimental results are closer to the numerical results after several large eddy turnovers. This could be an indication that the differences between the numerical and experimental results cannot be explained, at least not fully, with non-stationary effects.

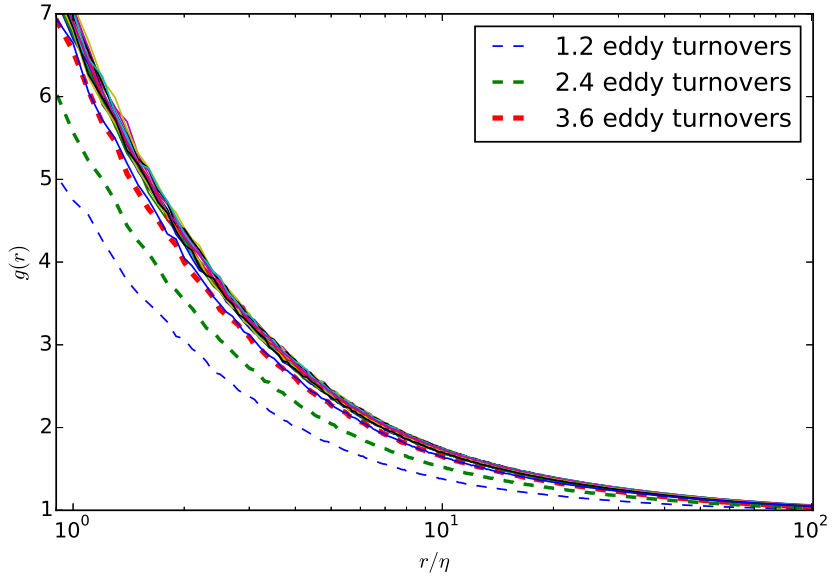

FIGURE 4.16: Radial distribution function $g(r)$ over normalised particle distance r/η at $Re_\lambda \approx 450$ and $St_\eta = 1$. Snapshots between 1.2 and 27 large-eddy turnovers after insertion of particles.

A long-term numerical experiment at $Re_\lambda \approx 450$ over ~ 27 large-eddy turnovers (figure 4.16) shows that after about 4 large-eddy turnovers the radial distribution function is fully developed and variations in the following results are very small.

The time development of local concentrations follows the same pattern, as indicated by D shown in figure 4.17. Only marginal differences can be seen for the results for more than 3.6 large-eddy turnovers.

4.5 Influence of gravity

To investigate the influence of gravity, simulations have been carried out over a range of Froude numbers between $Fr_\eta = 0.01$ and $Fr_\eta = 0.65$ at $Re_\lambda \approx 250$ and $St_\eta = 1$. The resulting radial distribution function $g(r)$ is shown in comparison with numerical results from Ireland et al. [59] and experimental results from Wood et al. [132] in figure 4.18. Gravity reduces $g(r)$, an effect that becomes more dominant with decreasing Froude number. Whereas $g(r)$ at $Fr_\eta = 0.65$ is almost identical to $g(r)$ without gravity, at $Fr_\eta = 0.01$ the radial distribution function is significantly reduced.

In comparison to the simulation result from Ireland et al. [59], $g(r)$ at $Fr_\eta = 0.05$ is smaller. This is probably not due to the gravity term in particular, since it can be seen as well when comparing results without gravity from the corresponding publication [58] to own results. In both publications, Ireland et al. used simulations at a higher resolution $k_{max}\eta \sim 1.6 \ldots 1.6$. They also put considerable effort into a highly accurate

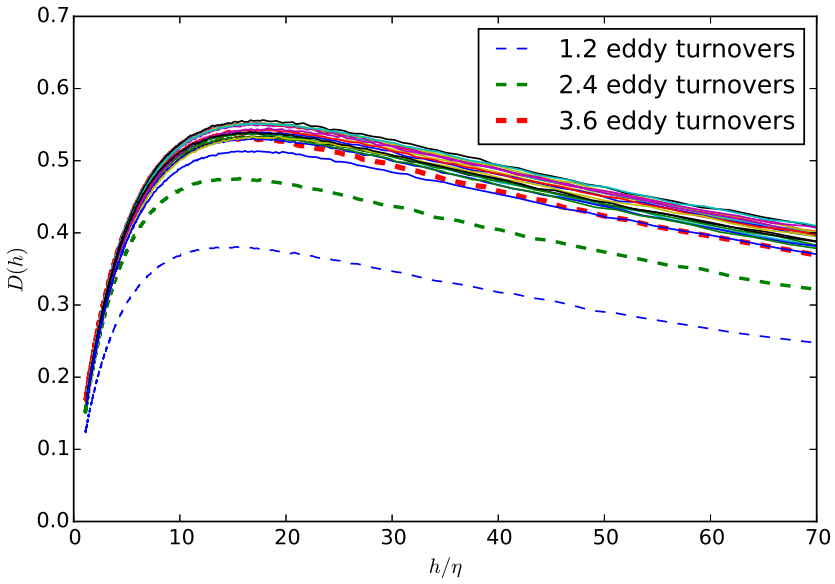

FIGURE 4.17: D measure over normalised bin size h/η at $Re_\lambda \approx 450$ and $St_\eta = 1$. Snapshots between 1.2 and 27 large-eddy turnovers after insertion of particles..

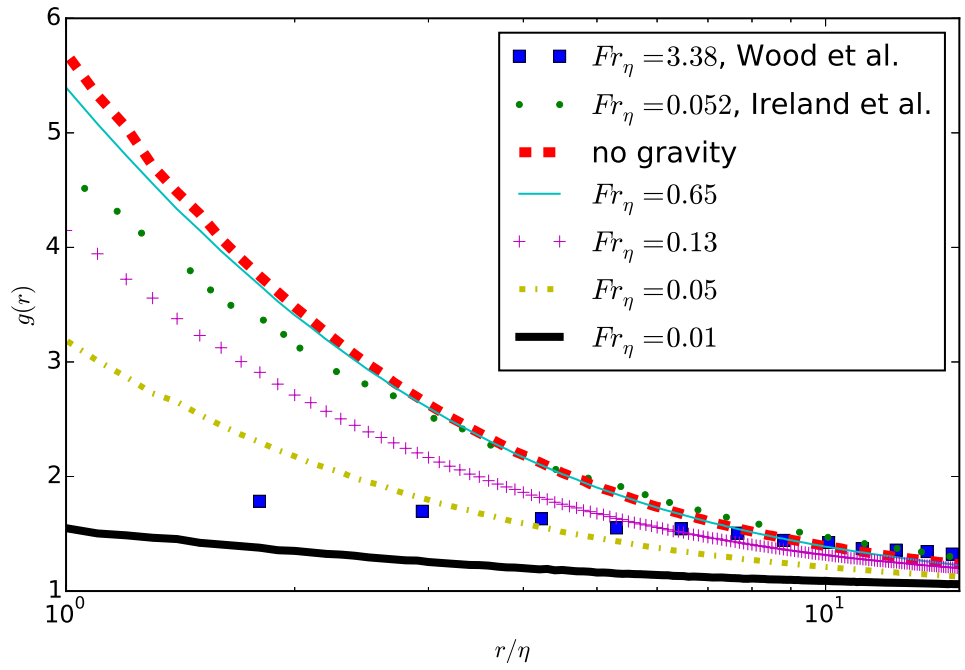

FIGURE 4.18: Radial distribution function $g(r)$ over normalised particle distance r/η for $Re_\lambda \approx 250$, $St_\eta = 1$ and Froude numbers between $Fr_\eta = 0.01$ and $Fr_\eta = 0.65$. The results are compared to experimental results from [132] and DNS results from [59].

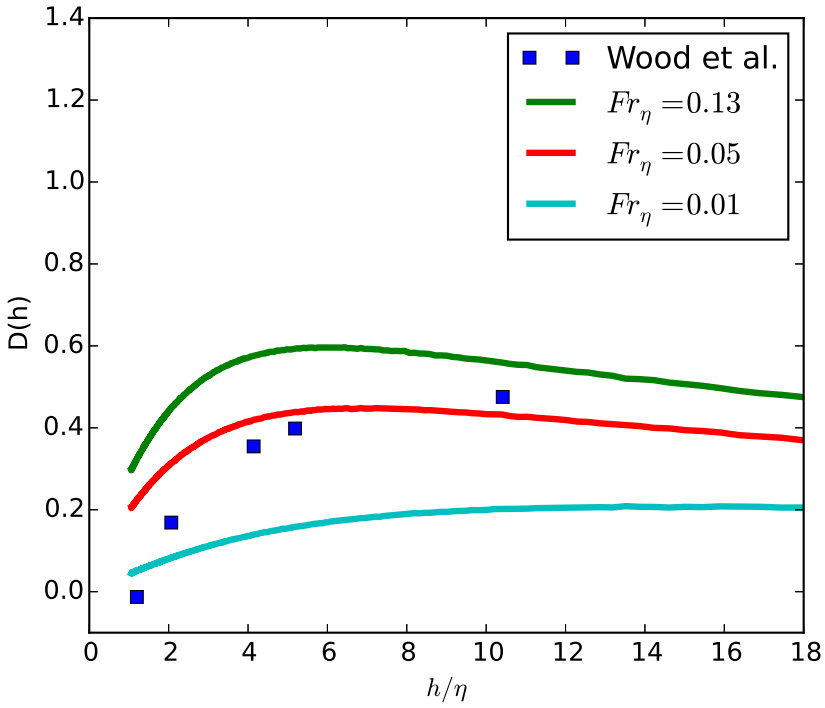

FIGURE 4.19: D measure over normalised bin size h/η for $Re_\lambda \approx 250$, $St_\eta = 1$ and Froude numbers $Fr_\eta = 0.01$, $Fr_\eta = 0.13$ and $Fr_\eta = 0.65$ using 2097152 particles. The results are compared to experimental results from [132].

interpolation scheme, as described in [60]. Whereas a resolution of $k_{max}\eta > 1$ cannot be expected to significantly improve the computed velocity field, it will certainly lead to a more accurate fluid velocity at the position of the particle. Effectively the additional gridpoints correspond to a spectral interpolation. Whilst high accuracy is certainly desirable, the results presented here can nevertheless be considered acceptable, since they are consistent amongst each other and hence allow the study of the various input parameters.

The results of Wood et al. [132] lie between the own results for $Fr_\eta = 0.05$ and $Fr_\eta = 0.01$, despite a Froude number of $Fr_\eta = 3.38$ (estimated from the published flow characteristics). The D measure using 2,097,152 particles (shown in figure 4.19) again shows similarity between own simulation results at $Fr_\eta = 0.05$ and the experimental results. Both using $g(r)$ and D, the Froude number seems not adequate to explain the difference. However, the particles were inserted through a tube at the top of the turbulence chamber [132], which might have given the particles an initial velocity significant enough to modify the results. This could be investigated in the future by simulations that start with an initial particle velocity in gravity direction.

A comparison of simulations at Stokes numbers between ~ 0.5 and ~ 8 (figure 4.20) shows that gravity reduces preferential concentration for low Stokes numbers, but enhances it for higher Stokes numbers. Whereas for $Fr_\eta = 0.65$ the lower Stokes number results

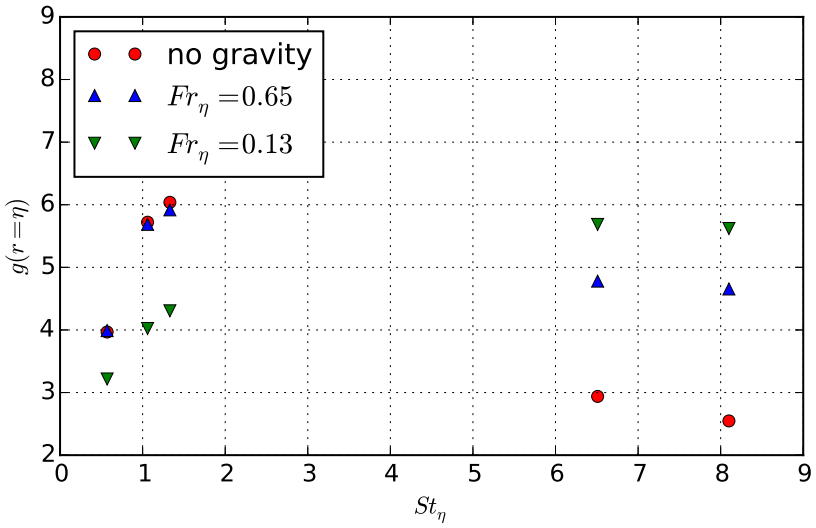

FIGURE 4.20: Radial distribution function $g(r)$ at distance $r = \eta$ over Kolmogorov scale Stokes number St_η for Kolmogorov scale Froude numbers $Fr_\eta = 0.13$ and $Fr_\eta = 0.65$ and without gravity. The Reynolds number is $Re_\lambda \approx 250$.

show little difference to the simulations without gravity, at $St_\eta \approx 6.5$ and $St_\eta \approx 8$ there is a clear difference. At $Fr_\eta = 0.13$, i.e. stronger gravity, the difference can be clearly seen for all Stokes numbers. Whereas for $Fr_\eta = 0.65$ the peak preferential concentration occurs at $St_eta \sim 1$, $g(r)$ is bigger for $St_\eta \approx 6.5$ and $St_\eta \approx 8$ for $Fr_\eta = 0.13$.

Simulations at a lower Reynolds number have been performed to investigate the influence of the number of particles and of the Stokes number when a gravity force is present. The results for the radial distribution function $g(r)$ are shown in figure 4.21. Whereas, similar to the results without gravity discussed above, the number of particles does not influence $g(r)$ for the lower Stokes numbers, there are some differences at $St_\eta = 8$ that are not present without gravity. The differences do not seem to follow a trend. Therefore it can be speculated that they are either due to uncertainties or to the way particles interact with turbulent structures.

As opposed to particle-particle distances, local concentrations show a more complex behaviour as shown in figure 4.22. Gravity enhances preferential concentration at high Stokes numbers and reduces it at low Stokes numbers. On the other hand the number of particles leads to bigger differences at low Stokes numbers than at intermediate Stokes numbers and, as opposed to the investigations of these effects without gravity, larger differences again at the highest St_η. For the highest numbers of particles there is a clear peak preferential concentration at $St_\eta = 1$ and a second, smaller peak at $St_\eta = 8$. For $32^3 = 32768$ particles the pattern is similar to simulations without gravity, with a peak at $St_\eta = 1$ and a decrease with higher Stokes numbers. For $16^3 = 4096$ particles there is an increase from D at $St_\eta = 0.4$ to $St_\eta = 1$, but little change for higher Stokes numbers.

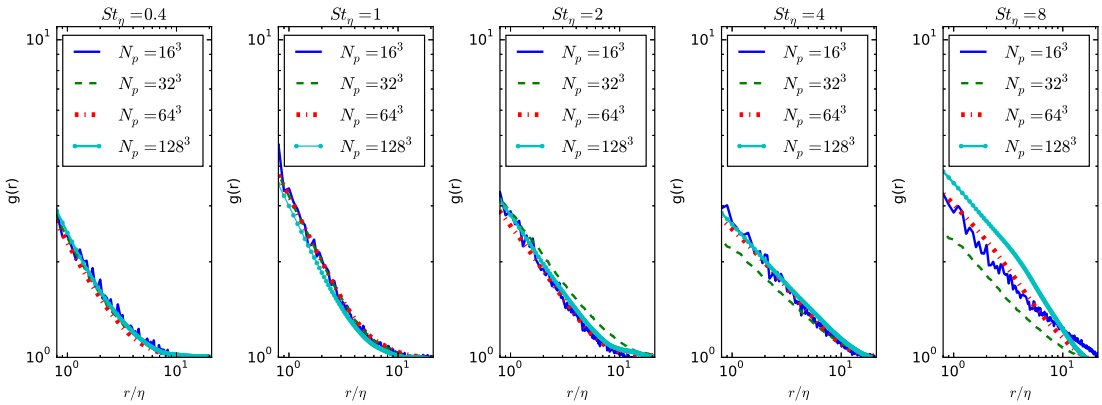

FIGURE 4.21: Radial distribution function $g(r)$ over normalised particle distance r/η for St_η between 0.4 and 8 (from left to right) at $Re_\lambda \approx 45$ and $Fr_\eta = 1$. The number of particles N_p is varied from $16^3 = 4096$ particles to $128^3 = 2097152$ particles.

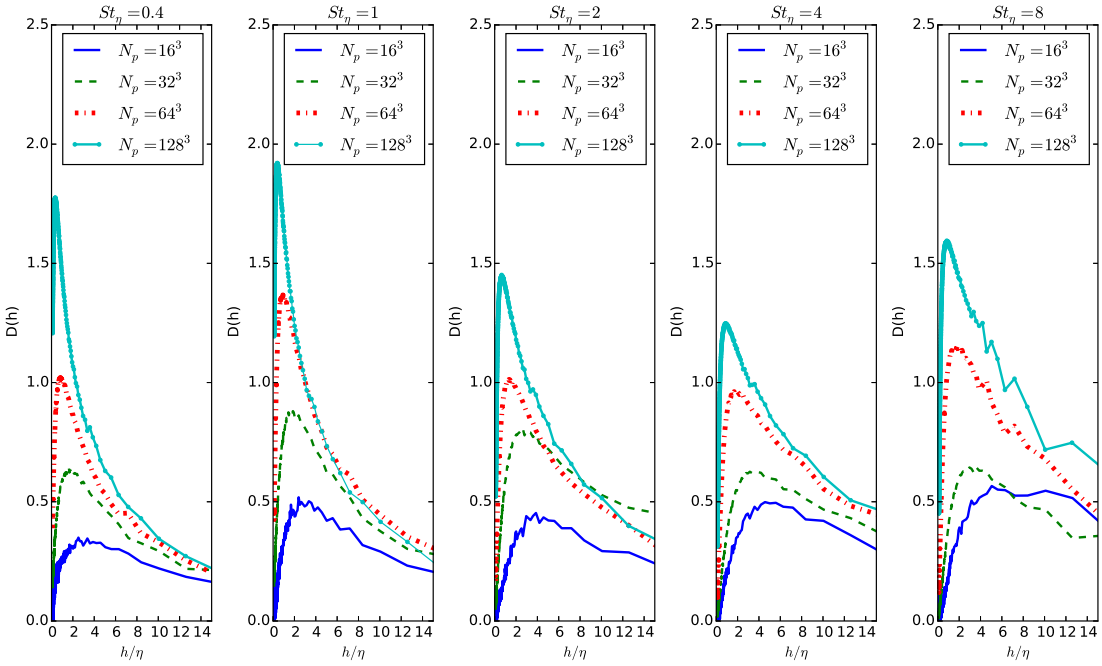

FIGURE 4.22: D measure over normalised bin size h/η for St_η between 0.4 and 8 (from left to right) at $Re_\lambda \approx 45$ and $Fr_\eta = 1$. The number of particles N_p is varied from $16^3 = 4096$ particles to $128^3 = 2097152$ particles.

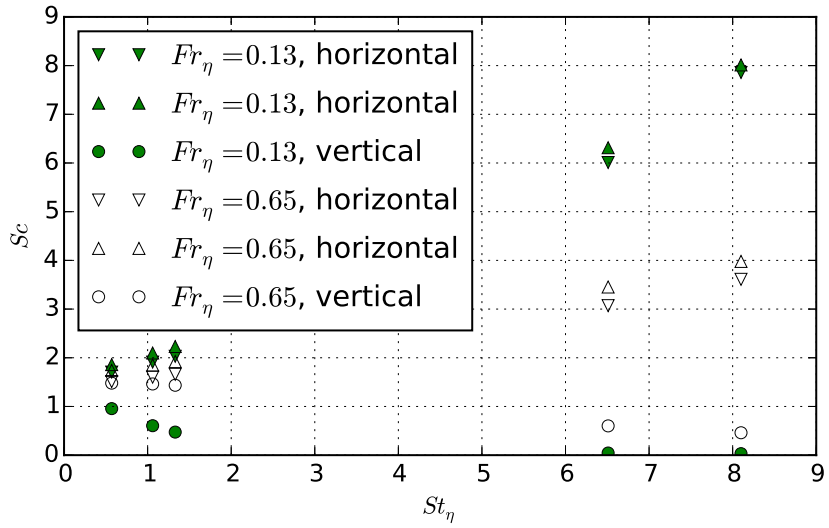

FIGURE 4.23: Vertical and horizontal Schmidt numbers over Kolmogorov scale Stokes number St_η for Kolmogorov scale Froude numbers $Fr_\eta = 0.13$ and $Fr_\eta = 0.65$ and without gravity. The Reynolds number is $Re_\lambda \approx 250$..

To understand the difference between particle and gas dispersion under the influence of gravity, The vertical (i.e. in gravity direction) and horizontal Schmidt numbers have been evaluated for simulations at $Fr_\eta = 0.13$ and $Fr_\eta = 0.65$, $Re_\lambda = 250$. The Stokes numbers are between ~ 0.5 and ~ 8. Whereas for $Fr_\eta = 0.13$ there is a difference between horizontal and vertical Schmidt numbers over the whole range of Stokes numbers, the influence disappears at the smallest Stokes numbers for $Fr_\eta = 0.65$. The Schmidt numbers in gravity direction are below 1 for all Stokes numbers at $Fr_\eta = 0.13$ and for $St_\eta \approx 6.5$ and $St_\eta \approx 8$ at $Fr_\eta = 0.65$, indicating stronger dispersion than for a gas and hence an influence of gravity. For the Stokes numbers around 1 at $Fr_\eta = 0.65$ however, the vertical Schmidt numbers are above 1, indicating smaller dispersion compared to a fluid point. This would suggest that under these conditions inertial effects are more relevant for particle dispersion than gravity effects (compare figure 4.14 and the discussion of atmospheric aerosols in chapter 2.4).

4.6 Summary and discussion

The results presented here for the radial distribution function $g(r)$ confirm the well-established Stokes-number dependence of preferential concentration with a peak at $St_\eta \approx 1$ [132]. $g(r)$ is enhanced by gravity for higher Stokes numbers and decreased for lower Stokes numbers, similar to the results by other workers [59], leading to a second peak in preferential concentration at higher Stokes numbers.

In agreement with the literature ([28, 58]) $g(r)$ appears to converge at high Reynolds numbers.

Results on the D measure reproduce the non-linear dependence of local concentrations on the global particle loading observed by Monchaux et al. [82]. This has a significant physical meaning, because in one-way coupled simulations of point-particles any complex explanations like two-way particle-turbulence interactions or particle-particle collisions can be excluded as an explanation.

The complex dependence of preferential concentrations on both global particle loading and Reynolds number as observed in recent experimental work based on concentration-based measures [82, 87, 114] has been reduced to the finding that D seems to become independent of the Reynolds number at sufficiently high Reynolds number if $N_p^{(1/3)}\eta$ is kept constant where N_p is the number of particles and η is the Kolmogorov length. This scaling law has a similarity to the convergence of the particle-distance based radial distribution function with Re_λ. Since publication in [131] it has been independently tested by Mora et al. [84] using Voronoi analysis on DNS data.

Contradicting recent findings on the Stokes number dependence of preferential concentration in experiments using concentration-based measures [87, 114] have been explained with the particle loading dependence and gravity effects. Whereas for sufficiently high global particle loadings and without gravity D shows a similar Stokes number dependence as $g(r)$ with a peak at $St_\eta \approx 1$, reducing the number of particles can lead to a shift in Stokes number dependence due to the fact that the local concentrations change more with the global particle loading at low Stokes numbers and less at high Stokes numbers. When gravity is include, this is further complicated. Therefore, depending on global particle loading and gravity, it is possible to observe peak preferential concentration at a peak other than $St_\eta \approx 1$ or even a near-independence of the Stokes number.

Simulations for small Stokes numbers showed that preferential concentration is clearly measurable at $St = 0.1$, with an expected influence on particle dispersion in the atmospheric boundary layer, particularly in windy situations (see the previous chapter for expected Stokes numbers).

Experimental results by Wood et al. [132] for D and $g(r)$ could be qualitatively, but not quantitatively reproduced, with the numerical results being significantly higher. Possible explanations are an influence of the injection of particles or the non-stationary conditions of a typical experiment. The fact that in the simulations a periodic boundary conditions are used, whereas the experiment is delimited by solid walls, might contribute to the differences.

The results presented here for $g(r)$ show some quantitative differences to those published by Ireland et al. ([58, 59]), with the published results having a higher value of $g(r)$ at $St_\eta = 1$. A possible explanation is the higher resolution and higher-order interpolation scheme used by these authors. This could have implications when using large-eddy simulations, since a literature search (2.7.3) showed that there is not yet an overall satisfying subgrid model for particles, in particular for small particles.

Chapter 5

DNS code development

5.1 PANDORA 2.0 - performance improvements during the eCSE 11-1 project

A new version of PANDORA based on the libraries FFTW and PETSc was developed within the eCSE project 'PANDORA Upgrade : Particle Dispersion in Bigger Turbulent Boxes'. All of the results presented in this section were obtained during this project and are published in a final project report [130]. This work was funded under the embedded CSE programme of the ARCHER UK National Supercomputing Service (http://www.archer.ac.uk).

The aim of the eCSE project was to overcome the limitations of the previous code in terms of memory use and efficiency. The parallelisation was changed from a 1D ('slab') decomposition to a 2D ('pencil') decomposition. All of the parallelisation was implemented using distributed arrays as provided by PETSc. The global transforms that are necessary to perform FFT in all three directions have been implemented using the parallel transpose functions of FFTW.

The main goal of the project was to reduce the memory use of PANDORA to allow for bigger simulations with more particles. This was achieved by storing only the data

Grid size (real space)	1024^3	2048^3	4096^3	2048^3
ARCHER nodes	32	64	128	64
Cores	512	1024	2048	1536
Particles	-	-	-	8,589,934,592
Memory/node in PANDORA (estimate)	20 GB	80 GB	-	-
Memory/node in PANDORA 2.0 (target)	3.5 GB	14 GB	54 GB	25 GB
Memory/node in PANDORA 2.0 (achieved)	1.9 GB	6.3 GB	23.8 GB	32.5 GB

Table 5.1: Memory improvements in PANDORA 2.0

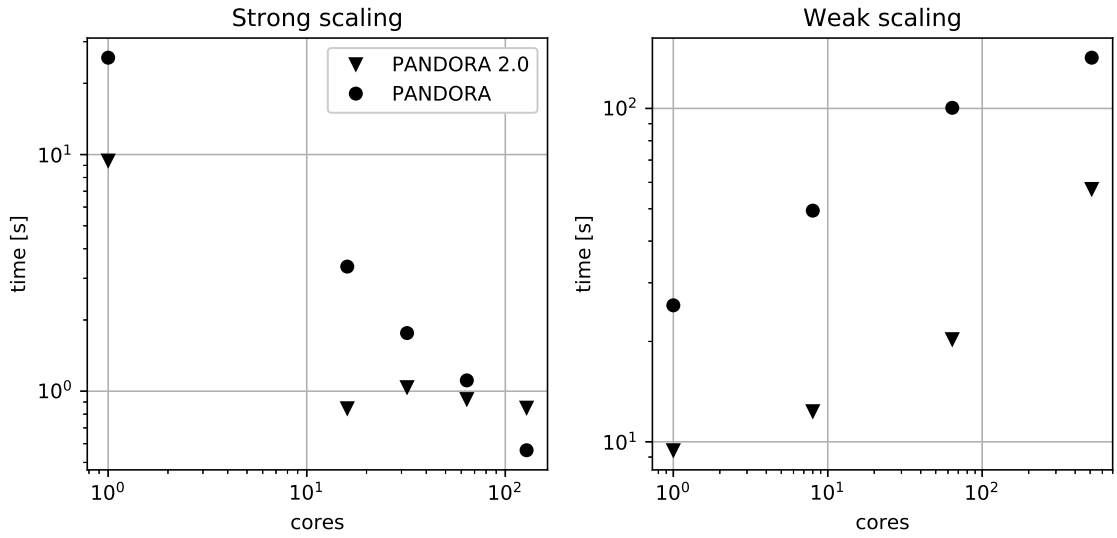

FIGURE 5.1: Strong scaling (left) and weak scaling (right) of fluid simulations on ARCHER using PANDORA and PANDORA 2.0. The left-hand side shows the computing time for 10 time steps on a 128^3 domain. The right-hand side shows the computing time for 10 time steps on 128^3, 256^3, 512^3 and 1024^3 domains.

strictly necessary. Splitting MPI communicators in each of the two parallelised directions makes it possible to perform the main work on Fourier transforms and global transpose on two-dimensional slices in parallel. Therefore less memory is needed for buffer arrays.

Since the 2/3 rule for dealiasing is used in PANDORA, it was attempted to avoid real-space data wherever possible. Applying the 2/3 rule in all three dimensions it can be seen that in wave-space only $(2^3)/(3^3) = 8/27$ of memory is needed compared to the corresponding real-space data.

A combination of the above principles led to a significant memory improvement compared to the previous PANDORA code as summed up in table 5.1. It can be seen that PANDORA 2.0 uses only about a 10th of memory for fluid simulations compared to the previous version.

For simulations with particles the target was not entirely achieved. This is due to the fact that, as opposed to the original planning, it was decided to use threedimensional real-space velocity arrays for the interpolation of fluid velocities at the particle position. The original idea to use ghost particles rather than fluid halos turned out to be to difficult to implement. It also needs to be emphasised that for many particles (more than one per control volume) fluid halos are more memory saving.

The program flow has been slightly modified, mainly to make better use of data already available in memory, as shown in figures 5.4 and 5.5 as well as table 5.2.

Finally the particle code has been modified to allow for passive particles as well as inertial particles.

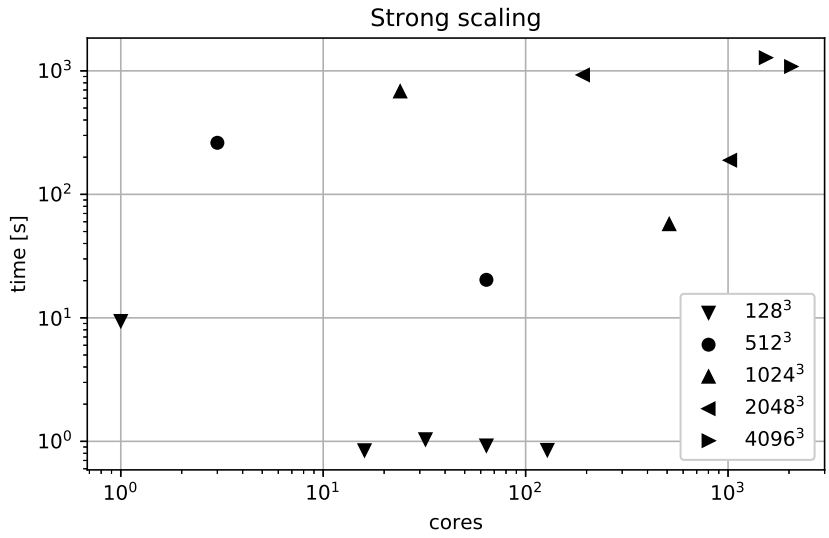

FIGURE 5.2: Strong scaling of PANDORA 2.0 for different domain sizes.

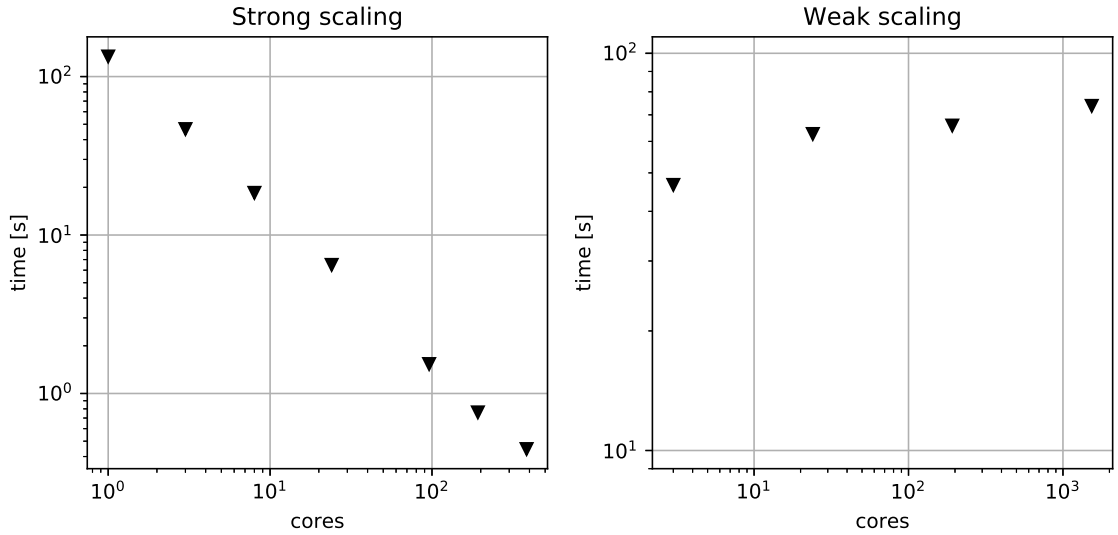

FIGURE 5.3: Strong and weak scaling of PANDORA 2.0 for one time step with one particle per control volume. The strong scaling simulations were performed on a 256^3 domain, the weak scaling tests on 256^3, 512^3, 1024^3 and 2048^3 domains.

5.2 Implementation of the Rogallo transform in PANDORA 2.0

5.2.1 Simulation of linear shear flows

Simulations of homogeneous turbulence have been performed by many workers (e.g. [101], [9], [19]. Many of them used the Rogallo transform[101] to solve the Navier-Stokes equation in a moving coordinate system. Rogallo [101] used a coordinate transform to simulate linear shear flows in a moving frame with periodic boundary conditions. An

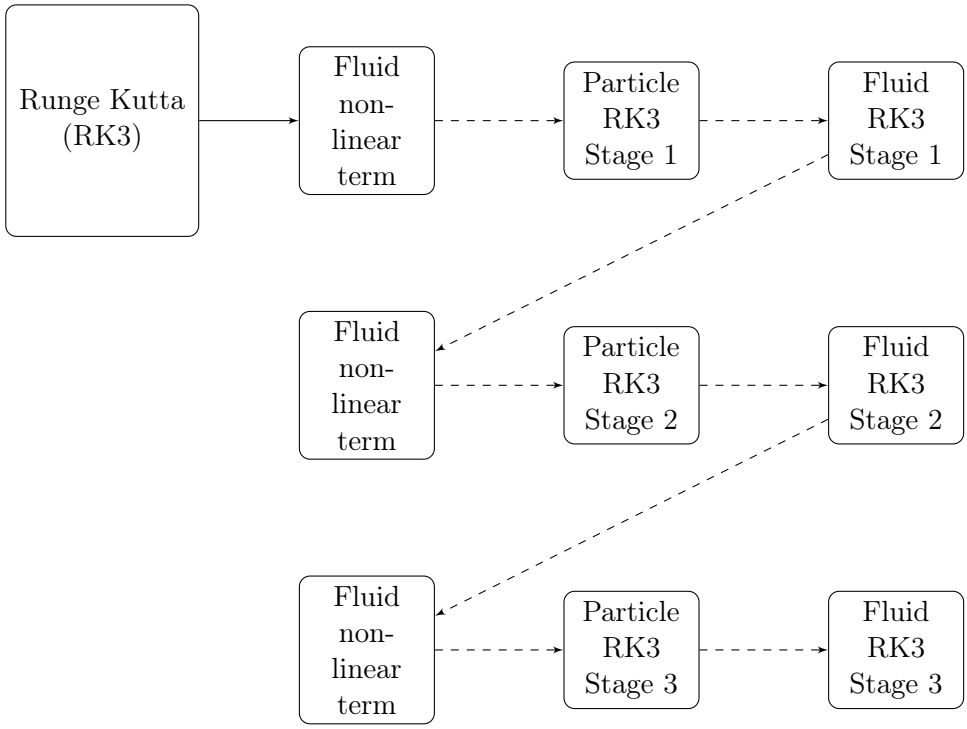

FIGURE 5.4: Flowchart of a timestep in PANDORA 2.0. In each timestep a Runge-Kutta scheme is performed, followed by fluid and particle analysis. The Runga-Kutta scheme consists of three stages. As opposed to the previous PANDORA code, the particle Runge-Kutta routines are performed after calculating the non-linear term and before solving the Navier-Stokes equation.

Stage 1:	$U_1 = U_n$
	$G_1 = F(U_n, t_n)$
	$U_2 = U_1 + \frac{1}{3}\Delta t G_1$
Stage 2:	$G_2 = -\frac{5}{9}G_1 + F(U_2, t_n + \frac{1}{3}\Delta t)$
	$U_3 = U_2 + \frac{15}{16}\Delta t G_1$
Stage 3:	$G_3 = -\frac{153}{128}G_2 + F(U_3, t_n + \frac{3}{4}\Delta t)$
	$U_{n+1} = U_2 + \frac{8}{15}G_3$

TABLE 5.2: Runge-Kutta scheme used in PANDORA 2.0. The scheme is essentially the same as in the old PANDORA code, but organised differently to directly use information that already is in memory.

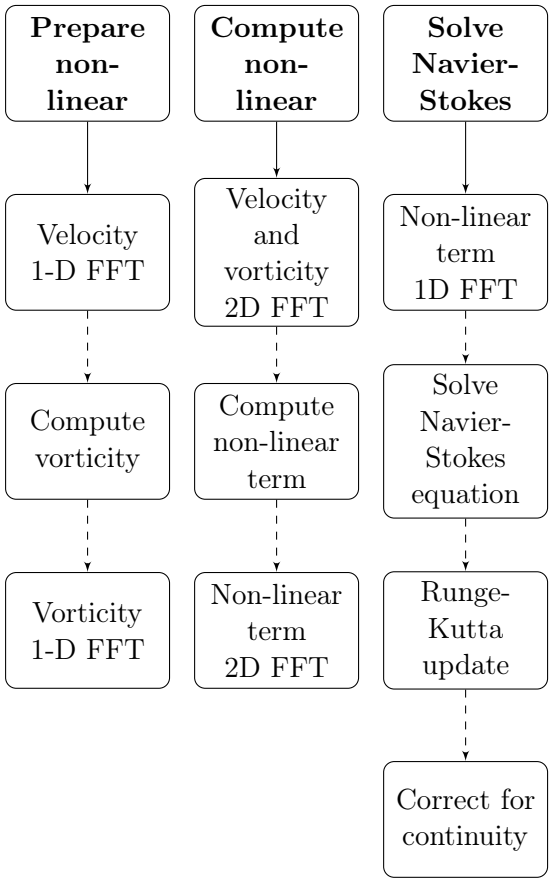

FIGURE 5.5: Flowchart for the different steps in solving the fluid equations.

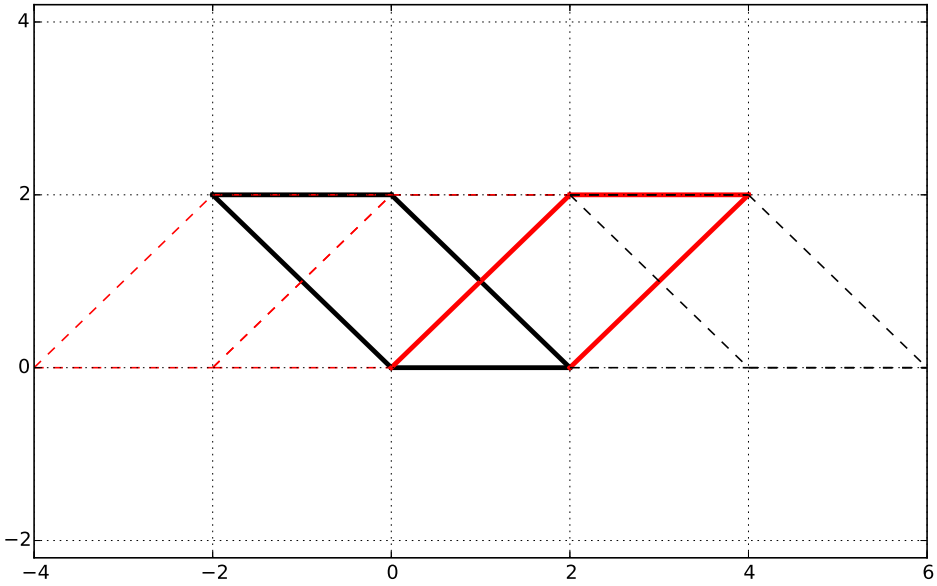

FIGURE 5.6: Illustration of a moving mesh for the simulation of linear shear flows.

illustration of a moving mesh at a uniform shear rate for two different times is shown in figure 5.6. A coordinate transform between a system at rest x_j and a moving system x_i' can be expressed by [101]

$$x_i' = B_{ij}(t)x_j \tag{5.1}$$

where the transformation tensor B_{ij} is given by [9]

$$B_{ij}(t) = \begin{bmatrix} 1 & -St & 0 \\ 0 & 1 & 0 \\ 0 & 0 & 1 \end{bmatrix} \tag{5.2}$$

As the computational domain moves with the shear flow, the computational grid is distorted and the mesh aspect ratio grows [101]. At some point the computational domain will be smaller than the turbulent structures in some direction and the simulation will no longer be accurate [9]. This problem is mitigated by remeshing the domain, which is best performed at $St = 0.5$, because then a transform to a grid skewed in exactly the opposite direction is possible on exactly the same grid points due to the periodic boundary conditions [21].

Although this process is straightforward in real space, it leads to aliasing in Fourier space, which need to be corrected through dealiasing [101]. The dealising leads to a sudden loss in turbulent kinetic energy and dissipation [19]. The energy losses are typically in the order of $1 \ldots 5\,\%$ for weak shear up to $40\,\%$ at high shear rates [72]. In a comparison between a Rogallo code and a code that works in a fixed laboratory system, Brucker et al. [19] observed very small differences in energy and dissipation at dimensionless shear rates $S^* = 5$, but their results for $S^* = 30$ show energy losses in the order of $\sim 15\,\%$ and dissipation losses in the order of $\sim 25\,\%$.

Brucker et al. [19] developed an algorithm that works without remeshing and thus avoids the energy loss described above. Sukheswalla et al. [112] performed simulations with this code up to $Re_\lambda = 500$ and $S^* = 5.67$. A numerical issue they faced were Gibbs oscillation (see 2.6.3 for a further discussion) when resolving thin vortical structures. These oscillations grow non-linearly and distort the high-wavenumber region of the spectrum.

The Navier-Stokes equation as implemented by Rogallo [101] reads

$$\begin{aligned} &\frac{\partial \hat{u}_i}{\partial t} + \mathcal{F}\left(B_{kj}\frac{\partial u_i}{\partial x_k}u_j\right) + A_{rj}\hat{u}_k \\ &-\frac{B_{ji}k_j}{k_m B_{mr} B_{jr} k_j}\left(k_m B_{mr}\mathcal{F}\left(B_{kj}\frac{\partial u_r}{\partial x_k}u_j\right) + k_m B_{mr} A_{rj}\hat{u}_j\right) = -\nu B_{lj} B_{nj} k_l k_n \hat{u}_i \end{aligned} \tag{5.3}$$

5.2.2 Separation of the mean and fluctuating flow

With the advantages of the rotational form of the Navier-Stokes equation in mind, in particular its conservation properties and economical use of memory, the equations are derived in the following with references to existing work (the main steps are based on [101], [9] and [19]) wherever possible.

We begin with the Navier-Stokes equation in the rotational form [21] and the continuity equation for incompressible flows. (Note that a capital letter T is used for the time in the laboratory system.)

$$\frac{\partial \mathbf{u}}{\partial T} + \omega \times \mathbf{u} = -\nabla \left(p + \frac{1}{2}\mathbf{u}^2 \right) + \nu \Delta \mathbf{u} \tag{5.4}$$

$$\nabla \cdot \mathbf{u} = 0 \tag{5.5}$$

Following [19] we use the well-known Reynolds decomposition to separate mean and fluctuating velocity, vorticity and pressure:

$$\mathbf{u} = \mathbf{U} + \mathbf{u}' \qquad \omega = \mathbf{\Omega} + \omega' \qquad p = P + p' \tag{5.6}$$

Substituting for $\mathbf{u}$ and averaging equation 5.5 yields:

$$\nabla \cdot \mathbf{U} = 0 \tag{5.7}$$

Subtracting **??** from 5.5:

$$\nabla \cdot \mathbf{u}' = 0 \tag{5.8}$$

Substituting 5.6 on the left-hand side of 5.4:

$$\frac{\partial \left(\mathbf{U} + \mathbf{u}' \right)}{\partial T} + \left(\mathbf{\Omega} + \omega' \right) \times \left(\mathbf{U} + \mathbf{u}' \right) = \frac{\partial \mathbf{U}}{\partial T} + \frac{\partial \mathbf{u}'}{\partial T} + \mathbf{\Omega} \times \mathbf{U} + \mathbf{\Omega} \times \mathbf{u}' + \omega' \times \mathbf{U} + \omega' \times + \mathbf{u}' \tag{5.9}$$

Substituting 5.6 on the right-hand side of 5.4:

$$-\nabla \left(\left(P + p' \right) + \frac{1}{2} \left(\mathbf{U} + \mathbf{u}' \right)^2 \right) + \nu \Delta \left(\mathbf{U} + \mathbf{u}' \right) = -\nabla P - \nabla p' + \frac{1}{2} \left(\mathbf{UU} + 2\mathbf{U}\mathbf{u}' + \mathbf{u}'\mathbf{u}' \right) + \nu \Delta \mathbf{U} + \nu \Delta \mathbf{u}' \tag{5.10}$$

Combining 5.9 and 5.10 and averaging:

$$\frac{\partial \mathbf{U}}{\partial T} + \mathbf{\Omega} \times \mathbf{U} + \left\langle \omega' \times \mathbf{u}' \right\rangle = -\nabla P - \frac{1}{2}\nabla \left(\mathbf{U}^2 + \left\langle \mathbf{u}'^2 \right\rangle \right) + \nu \Delta \mathbf{U} \tag{5.11}$$

Subtracting 5.11 from 5.4 we obtain

$$\frac{\partial \mathbf{u}'}{\partial T} + \mathbf{\Omega} \times \mathbf{u}' + \omega' \times \mathbf{U} + \omega' \times \mathbf{u}' - \left\langle \omega' \times \mathbf{u}' \right\rangle = -\nabla p' - \nabla \left(\mathbf{U}\mathbf{u}' \right) - \frac{1}{2}\nabla \left(\mathbf{u}'\mathbf{u}' - \left\langle \mathbf{u}'\mathbf{u}' \right\rangle \right) + \nu \Delta \mathbf{u}' \tag{5.12}$$

Using continuity it can be shown that

$$- \left\langle \omega' \times \mathbf{u}' \right\rangle = \nabla \left\langle \mathbf{u}'\mathbf{u}' \right\rangle \tag{5.13}$$

and therefore, as [19], we obtain the final result

$$\begin{aligned} &\frac{\partial \mathbf{u}'}{\partial T} + \mathbf{\Omega} \times \mathbf{u}' + \omega' \times \mathbf{U} + \omega' \times \mathbf{u}' = \\ &-\nabla p' - \nabla \left(\mathbf{U}\mathbf{u}' \right) - \frac{1}{2}\nabla \left(\mathbf{u}'\mathbf{u}' \right) + \nu \Delta \mathbf{u}' \end{aligned} \tag{5.14}$$

or in tensor notation (note that we use capital letters - X_i to denote the fixed coordinate system)

$$\frac{\partial u_i'}{\partial T} + \epsilon_{ijk}\Omega_j u_k' + \epsilon_{ijk}\omega_j' U_k + \epsilon_{ijk}\omega_j' u_k' = -\frac{\partial p'}{\partial X_i} - \frac{\partial}{\partial X_i}\left(U_j u_j' \right) - \frac{1}{2}\frac{\partial}{\partial X_i}u'^2 + \nu \frac{\partial^2}{\partial X_j^2}u_i' \tag{5.15}$$

Any homogeneous flow follows the linear relation for the mean velocity field [9]

$$U_i = A_{ij} X_j \tag{5.16}$$

where A_{ij} is a deformation tensor and X_j is the coordinate vector. The homogeneous and fluctuating vorticities are then

$$\Omega_i = \epsilon_{ijk} A_{kj} \qquad \omega_i = \epsilon_{ijk} \partial u_k' \partial X_j \tag{5.17}$$

We also substitute the dynamic pressure

$$p^* = p' + \frac{1}{2}u'^2 \tag{5.18}$$

The Navier-Stokes equation for the fluctuating part of homogeneous turbulence can then be written as

$$\frac{\partial u_i'}{\partial T}+\epsilon_{ijk}\epsilon_{jmn}A_{nm}u_k'+\epsilon_{ijk}\epsilon_{jmn}\frac{\partial u_n'}{\partial X_m}U_k+\epsilon_{ijk}\omega_j'u_k' = -\frac{\partial p^*}{\partial X_i}-A_{jk}X_k\frac{\partial u_j'}{\partial X_i}-u_j'\frac{\partial A_{jk}X_k}{\partial X_i}+\nu\frac{\partial^2 u_i'}{\partial X_j^2} \tag{5.19}$$

which can be rewritten as

$$\frac{\partial u_i'}{\partial T}+A_{ik}u_k'-A_{ki}u_k'+\frac{\partial u_i'}{\partial X_k}A_{kj}X_j-\frac{\partial u_k'}{\partial X_i}A_{kj}X_j+\epsilon_{ijk}\omega_j'u_k' = -\frac{\partial p^*}{\partial X_i}-A_{kj}X_j\frac{\partial u_k'}{\partial X_i}-u_j'A_{ji}+\nu\frac{\partial^2 u_i'}{\partial X_j^2} \tag{5.20}$$

Eliminating terms:

$$\frac{\partial u_i'}{\partial T}+A_{ik}u_k'+A_{kj}X_j\frac{\partial u_i'}{\partial X_k}+\epsilon_{ijk}\omega_j'u_k' = -\frac{\partial p^*}{\partial X_i}+\nu\frac{\partial^2 u_i'}{\partial X_j^2} \tag{5.21}$$

5.2.3 Transformation to a moving coordinate system

We now transform 5.21 into a coordinate system that moves with the homogeneous velocity. The coordinates x_m, t of the moving system are related to those of the fixed system X_m, T by the relations [9] [101]

$$x_m = B_{mn}(t)X_n \qquad t = T \tag{5.22}$$

The fixed velocity component u_m' can then be substituted by the moving velocity component u_n using [9]

$$u_m' = B_{mn}^{-1}(t)u_n \tag{5.23}$$

We use the chain rule to obtain the derivatives

$$\frac{\partial}{\partial X_m} = B_{nm}(t)\frac{\partial}{\partial x_n} \tag{5.24}$$

in space and

$$\frac{\partial}{\partial T} = \frac{\partial}{\partial t}+X_m\frac{dB_{nm}}{dt}\frac{\partial}{\partial x_n} \tag{5.25}$$

in time.

We can now transform each term of 5.21 into the moving coordinate system as follows:

$$\frac{\partial u_i'}{\partial T} = \frac{\partial B_{ik}^{-1}(t)u_k}{\partial t} + X_m \frac{dB_{nm}}{dt}\frac{\partial B_{ik}^{-1}(t)u_k}{\partial x_n} = B_{ik}^{-1}(t)\frac{\partial u_k}{\partial t} + u_k\frac{dB_{ik}^{-1}(t)}{dt} + X_j\frac{dB_{nj}}{dt}B_{ik}^{-1}(t)\frac{\partial u_k}{\partial x_n} \tag{5.26}$$

$$A_{ij}u_j' = A_{ij}B_{jk}^{-1}(t)u_k \tag{5.27}$$

$$A_{lj}X_j\frac{\partial u_i'}{\partial X_l} = A_{lj}X_jB_{nl}B_{ik}^{-1}\frac{\partial u_k'}{\partial x_n} \tag{5.28}$$

$$\epsilon_{ijk}\omega_j'u_k' = \epsilon_{ijk}\omega_j'B_{km}^{-1}u_m \tag{5.29}$$

$$\frac{\partial p^*}{\partial X_i} = B_{ji}\frac{\partial p^*}{\partial x_j} \tag{5.30}$$

$$\nu\frac{\partial^2 u_i'}{\partial X_j^2} = \nu B_{lj}B_{nj}\frac{\partial^2\left(B_{ik}^{-1}u_k\right)}{\partial x_l\partial x_n} = \nu B_{lj}B_{nj}B_{ik}^{-1}\frac{\partial^2\left(u_k\right)}{\partial x_l\partial x_n} \tag{5.31}$$

We then obtain the final result

$$\begin{aligned} &B_{ik}^{-1}(t)\frac{\partial u_k}{\partial t} + B_{ik}^{-1}\frac{dB_{nj}}{dt}X_j\frac{\partial u_k}{\partial x_n} + \frac{dB_{ik}^{-1}(t)}{dt}u_k \\ &+\epsilon_{ijk}\omega_j'B_{km}^{-1}u_m + B_{ik}^{-1}B_{nl}A_{lj}X_j\frac{\partial u_k'}{\partial x_n} + A_{ij}B_{jk}^{-1}(t)u_k \\ &= -B_{ji}\frac{\partial p^*}{\partial x_j} + \nu B_{ik}^{-1}B_{lj}B_{nj}\frac{\partial^2\left(u_k\right)}{\partial x_l\partial x_n} \end{aligned} \tag{5.32}$$

Note that the same naming convention as in [9] is used to show the similarities. As intended, except for the non-linear term we obtain the same result.

Multiplying by B_{ri} [9] we obtain

$$\begin{aligned} &\left(B_{ri}B_{ik}^{-1}\right)\frac{\partial u_k}{\partial t} + \left(B_{ri}B_{ik}^{-1}\right)\frac{dB_{nj}}{dt}X_j\frac{\partial u_k}{\partial x_n} + B_{ri}\frac{dB_{ik}^{-1}(t)}{dt}u_k \\ &+B_{ri}\epsilon_{ijk}\omega_j'B_{km}^{-1}u_m + \left(B_{ri}B_{ik}^{-1}\right)B_{nl}A_{lj}X_j\frac{\partial u_k'}{\partial x_n} + B_{ri}A_{ij}B_{jk}^{-1}(t)u_k \\ &= -B_{ri}B_{ji}\frac{\partial p^*}{\partial x_j} + \nu\left(B_{ri}B_{ik}^{-1}\right)B_{lj}B_{nj}\frac{\partial^2\left(u_k\right)}{\partial x_l\partial x_n} \end{aligned} \tag{5.33}$$

Simplifying and reordering yields

$$\begin{aligned} &\frac{\partial u_i}{\partial t} + B_{ir}\epsilon_{rjk}\omega'_j B^{-1}_{km} u_m + \left(\frac{dB_{nj}}{dt} + B_{nl}A_{lj}\right) X_j \frac{\partial u_k}{\partial x_n} \\ &+B_{ir}\left(\frac{dB^{-1}_{rk}}{dt} + A_{rj}B^{-1}_{jk}\right) u_k = -B_{ir}B_{jr}\frac{\partial p^*}{\partial x_j} + \nu B_{lj}B_{nj}\frac{\partial^2 (u_i)}{\partial x_l \partial x_n} \end{aligned} \tag{5.34}$$

Using the differential equations for the moving coordinate system [101]

$$\left(\frac{dB_{nj}}{dt} + B_{nl}A_{lj}\right) = 0 \tag{5.35}$$

and [9]

$$\left(\frac{dB^{-1}_{rk}}{dt} - A_{rj}B^{-1}_{jk}\right) = 0 \tag{5.36}$$

we finally obtain

$$\begin{aligned} &\frac{\partial u_i}{\partial t} + B_{ir}\epsilon_{rjk}\omega'_j B^{-1}_{km} u_m + 2B_{ir}A_{rj}B^{-1}_{jk}u_k \\ &\qquad = -B_{ir}B_{jr}\frac{\partial p^*}{\partial x_j} + \nu B_{lj}B_{nj}\frac{\partial^2 u_i}{\partial x_l \partial x_n} \end{aligned} \tag{5.37}$$

Transformation into Fourier space is straightforward:

$$\begin{aligned} &\frac{\partial \hat{u}_i}{\partial t} + B_{ir}\epsilon_{rjk}\widehat{\omega'_j B^{-1}_{km}} u_m + 2B_{ir}A_{rj}B^{-1}_{jk}\hat{u}_k \\ &\qquad = -B_{ir}B_{jr}\mathbf{i}k_j\hat{p}^* - \nu B_{lj}B_{nj}k_l k_n \hat{u}_i \end{aligned} \tag{5.38}$$

To substitute the pressure term we multiply 5.38 with $\mathbf{i}k_i$ and obtain (the first and last terms disappear due to continuity):

$$\begin{aligned} &+\mathbf{i}k_i B_{ir}\epsilon_{rjk}\widehat{\omega'_j B^{-1}_{km}} u_m + 2\mathbf{i}k_i B_{ir}A_{rj}B^{-1}_{jk}\hat{u}_k \\ &\qquad = \mathbf{i}k_i B_{ir}B_{jr}\mathbf{i}k_j\hat{p}^* \end{aligned} \tag{5.39}$$

Then the pressure term becomes

$$-B_{ir}B_{jr}\mathbf{i}k_j\hat{p}^* = B_{ir}B_{jr}k_j\frac{k_i B_{ir}\epsilon_{rjk}\widehat{\omega'_j B^{-1}_{km}} u_m + 2k_i B_{ir}A_{rj}B^{-1}_{jk}\hat{u}_k}{k_i B_{ir}B_{jr}k_j} \tag{5.40}$$

Substituting into 5.38:

$$\begin{aligned} &\frac{\partial \hat{u}_i}{\partial t} + B_{ir}\epsilon_{rjk}\widehat{\omega'_j B^{-1}_{km}}u_m + 2B_{ir}A_{rj}B^{-1}_{jk}\hat{u}_k \\ -\frac{B_{ir}B_{jr}k_j}{k_i B_{ir}B_{jr}k_j}&\left(k_i B_{ir}\epsilon_{rjk}\widehat{\omega'_j B^{-1}_{km}}u_m + 2k_i B_{ir}A_{rj}B^{-1}_{jk}\hat{u}_k\right) = -\nu B_{lj}B_{nj}k_l k_n \hat{u}_i \end{aligned} \tag{5.41}$$

The vorticity in the laboratory system ω'_j is expressed in terms of the velocity in the moving system as

$$\omega'_i = \epsilon_{ijk}\frac{\partial u'_k}{\partial X_j} = \epsilon_{ijk}B_{mj}B^{-1}_{kn}\frac{\partial u_n}{\partial x_m} \tag{5.42}$$

The transformation into Fourier space is straightforward and we obtain

$$\hat{\omega}'_i = \epsilon_{ijk}B_{mj}B^{-1}_{kn}\mathbf{i}k_m\hat{u}_n \tag{5.43}$$

5.2.4 Equations for the transformation matrices

The transformation matrix B_{ij} is obtained from the differential equation

$$\frac{dB_{ij}}{dt} + B_{ij}A_{kj} = 0 \tag{5.44}$$

For homogeneous shear flows with one shear component an analytical solution is easily obtained. In particular for

$$A = \begin{bmatrix} 0 & 0 & S \\ 0 & 0 & 0 \\ 0 & 0 & 0 \end{bmatrix} \tag{5.45}$$

with the initial condition at $t = 0$

$$B = \begin{bmatrix} B_1 & 0 & 0 \\ 0 & B_2 & 0 \\ 0 & 0 & B_3 \end{bmatrix} \tag{5.46}$$

the solution is

$$B = \begin{bmatrix} B_1 & 0 & -B_1 S \cdot t \\ 0 & B_2 & 0 \\ 0 & 0 & B_3 \end{bmatrix} \tag{5.47}$$

Inversion is straightforward and we get

$$B^{-1} = \begin{bmatrix} 1/B_1 & 0 & S \cdot t/B_3 \\ 0 & 1/B_2 & 0 \\ 0 & 0 & 1/B_3 \end{bmatrix} \tag{5.48}$$

For the general case, the differential equation is solved numerically using the Runge-Kutta scheme implemented for the rest of the code.

5.2.5 Remeshing

For the reasons described in chapter 5.2.1, it is necessary to remesh the coordinate system at regular intervals. Despite being more intuitive in real space, it is more convenient and efficient to do this in wave space. The standard procedure established by other authors, in particular [101], is implemented in PANDORA 2.0 in one shear direction. As the domain is decomposed in two directions, it is only possible to avoid parallel communication in the direction that is not decomposed.

5.2.6 Homogeneous turbulence at the rapid distortion limit

The RDT equations (see [61] for a discussion of viscous and inviscid RDT applied to shear flows) follow directly from the full Navier-Stokes equations without any difficulties.

The viscous RDT equation reads

$$\frac{\partial \hat{u}_i}{\partial t} + 2B_{ir}A_{rj}B_{jk}^{-1}\hat{u}_k - \frac{B_{ir}B_{jr}k_j}{k_iB_{ir}B_{jr}k_j}2k_iB_{ir}A_{rj}B_{jk}^{-1} = -\nu B_{lj}B_{nj}k_lk_n\hat{u}_i \tag{5.49}$$

and the inviscid RDT equation becomes

$$\frac{\partial \hat{u}_i}{\partial t} + 2B_{ir}A_{rj}B_{jk}^{-1}\hat{u}_k - \frac{B_{ir}B_{jr}k_j}{k_iB_{ir}B_{jr}k_j}2k_iB_{ir}A_{rj}B_{jk}^{-1}\hat{u}_k = 0 \tag{5.50}$$

5.3 Verification and validation of the Rogallo code

5.3.1 Decaying Taylor-Green vortex

The decaying Taylor-Green vortex is one of the most commonly studied test cases for Navier-Stokes solvers due to its clearly defined symmetric initial condition. Taylor and

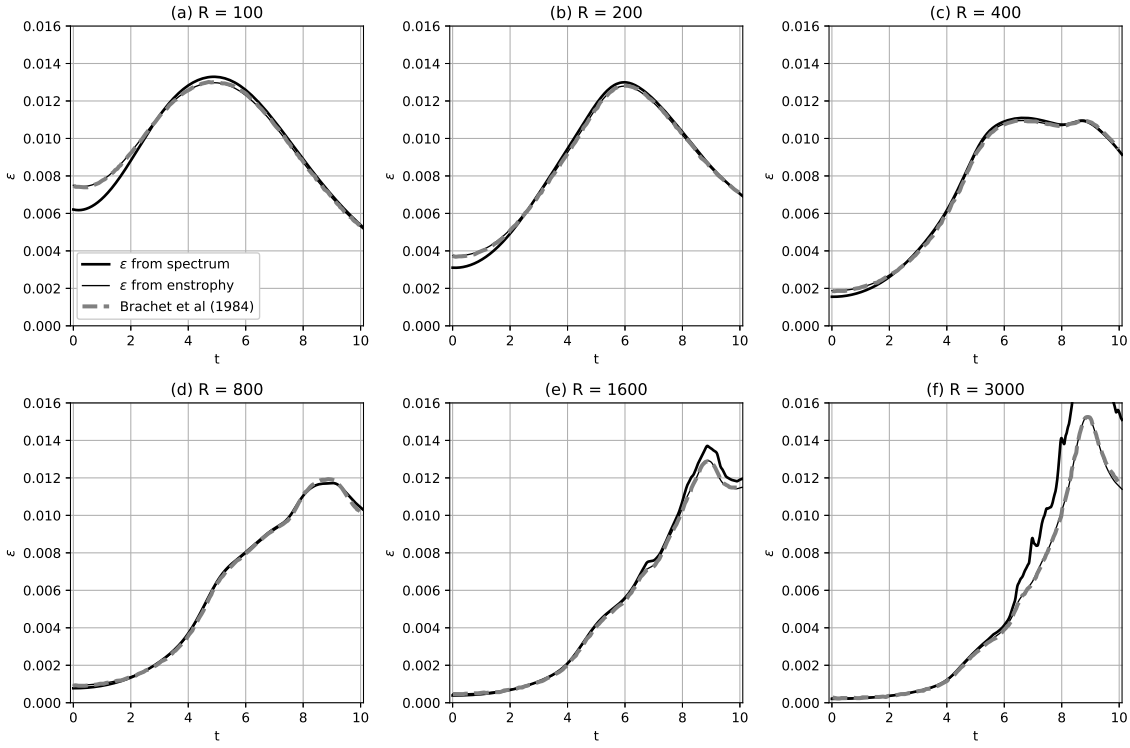

FIGURE 5.7: Dissipation of the Taylor-Green vortex for various large-scale Reynolds numbers $R = 1/\nu$. Dashed line: published results from Brachet et al. [17], thin line $\epsilon = \nu|\omega^2|$, thick line spectral dissipation. The spectral dissipation is different at initialisation because of the discretisation of the integral.

Green [118] presented a short-time solution using series development. The first numerical solution of the general Taylor-Green vortex problem was published by Orszag [88], followed by a more extensive solution by Brachet et al [17].

The solutions presented here are compared against the published results by Brachet et al [17]. Two different calculations of dissipation are presented here, the first based on the spectral evaluation [93] (equation 6.191) as implemented in the PANDORA 2.0 code by default, the second based on the assertion that in homogeneous turbulence $\epsilon = \nu\omega^2$, i.e. the dissipation is proportional to the enstrophy [30].

Following [17] we use the definition of the large-scale Reynolds number

$$R = 1/\nu \tag{5.51}$$

and perform calculations of the viscous decaying Taylor-Green vortex at $R = 100$, $R = 200$, $R = 400$, $R = 800$, $R = 1600$ and $R = 3000$. A 256^3 computational grid is used for all calculations.

The dissipation for all Reynolds numbers is shown in figure 5.7. It can be seen that there is an excellent agreement at all Reynolds numbers for the dissipation based on the

enstrophy definition. This indicates that the PANDORA 2.0 code is correct. This is further confirmed by the energy spectra compared to published results by Brachet et al [17] as shown in figure 5.8. Differences are likely to be due to reading out the figures from the publication.

As for the dissipation based on a spectral calculation, it can be seen that the initial values differ substantially from the enstrophy based evaluation. This can be explained from the discretisation of the energy spectrum in whole-wavenumber steps, wheres the definition is only strictly valid for infinitely thin spheres in wave space. For the initialisation that only contains very few non-zero wave modes this leads to a difference from the enstrophy-based dissipation. At later stages the discrete Fourier series approaches the real value due to more non-zero wave modes.

For the highest Reynolds numbers, in particular $R = 3000$, dissipation calculations based on the different definitions differ at later times. This is likely to be due to the highest wave numbers that are not truncated by the 2/3 rule. To further investigate this, additional calculations were performed. In these calculations, in addition to the default 2/3 rule, the highest wavenumbers $> 1/3N$ have been truncated in all directions (further referred to as spherical truncation). The results are shown in figure 5.9.

While these results seem to suggest that a spherical truncation leads to better results, it needs to be observed that the highest wave numbers deviate from the results obtained using the 2/3 rule, as shown in the spectra in figure 5.10. Therefore the spherical truncation cannot replace a sufficiently high resolution where the highest wave numbers are needed, which is usually the case for small inertial particles.

5.3.2 Turbulence statistics from shear flow simulations

Homogeneous shear flows have been simulated by a number of authors (e.g. [72], [19], [61], [112]). For the purpose of validation it is desirable to select a publication using a similar numerical method. It should also be based on a clearly defined initial condition and include extensive statistics. This limits the choice considerably and for this work the validation data base published by Matsumoto et al [77] was chosen despite the relatively poor resolution of those computations. To show the effect of the resolution, additional simulations on larger grid sizes have been performed. Furthermore the effect of the exact formulation of the transformed Navier-Stokes equation, the influence of the aspect ratio of the computing domain and the impact of remeshing were investigated.

An overview of the several simulations performed is given in table 5.3. The smallest grid size 64^3 corresponds to the grid used by Matsumoto et al [77]. Whereas the dealiasing scheme in PANDORA 2.0 is based on the 2/3 rule, the published results are based on a combination of truncation and random shifts.

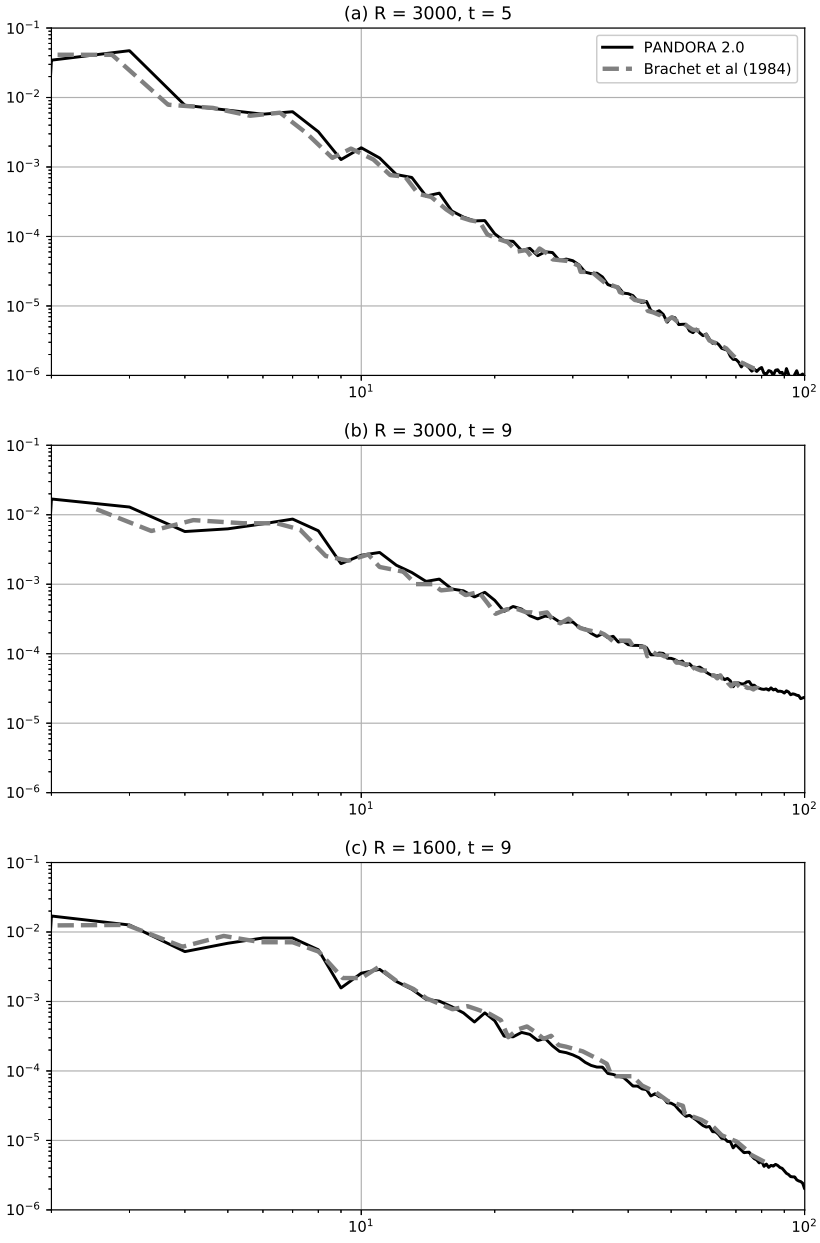

FIGURE 5.8: Energy spectra of the decaying Taylor-Green vortex. Dashed line: published results from Brachet et al. [17], thin line $\epsilon = \nu|\omega^2|$, thick line spectral dissipation. (a) R = 3000, t = 5 (b) R = 3000, t=9 (c) R = 1600, t=9.

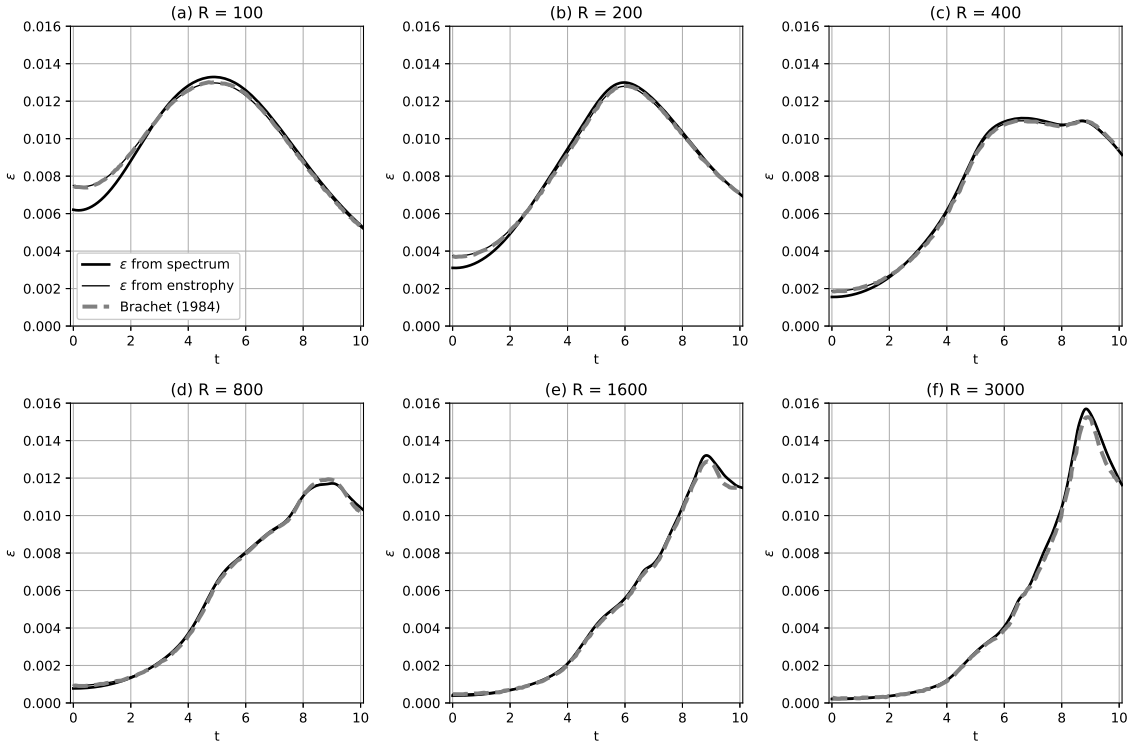

FIGURE 5.9: Same as fig. 5.7, but in addition to the 2/3 rule dealiasing a spherical truncation of all wavenumbers $> k_{max}$ has been performed.

Grid	Navier-Stokes implementation	Remesh	Dealiasing
64^3	Equation 5.41	$St = 0.5$	2/3 rule
96^3	Equation 5.41	$St = 0.5$	2/3 rule
128^3	Equation 5.41	$St = 0.5$	2/3 rule
256^3	Equation 5.41	$St = 0.5$	2/3 rule
64^3	Equation 5.41	$St = 0.5$	spherical
96^3	Equation 5.41	$St = 0.5$	spherical
128^3	Equation 5.41	$St = 0.5$	spherical
256^3	Equation 5.41	$St = 0.5$	spherical
64^3	Equation 5.3	$St = 0.5$	2/3 rule
128^3	Equation 5.3	$St = 0.5$	2/3 rule
256^3	Equation 5.3	$St = 0.5$	2/3 rule
64^3	Equation 5.3	$St = 0.5$	spherical
128^3	Equation 5.3	$St = 0.5$	spherical
256^3	Equation 5.3	$St = 0.5$	spherical
256×128^2	Equation 5.41	$St = 1$	2/3 rule
256×128^2	Equation 5.41	$St = 1$	spherical
64^3	Equation 5.41	$St = 0.5$	2/3 rule
128^3	Equation 5.41	$St = 0.5$	2/3 rule
256^3	Equation 5.41	$St = 0.5$	2/3 rule
64^3	Equation 5.41	$St = 0.5$	spherical
128^3	Equation 5.41	$St = 0.5$	spherical
256^3	Equation 5.41	$St = 0.5$	spherical

TABLE 5.3: Overview of the shear-flow simulations

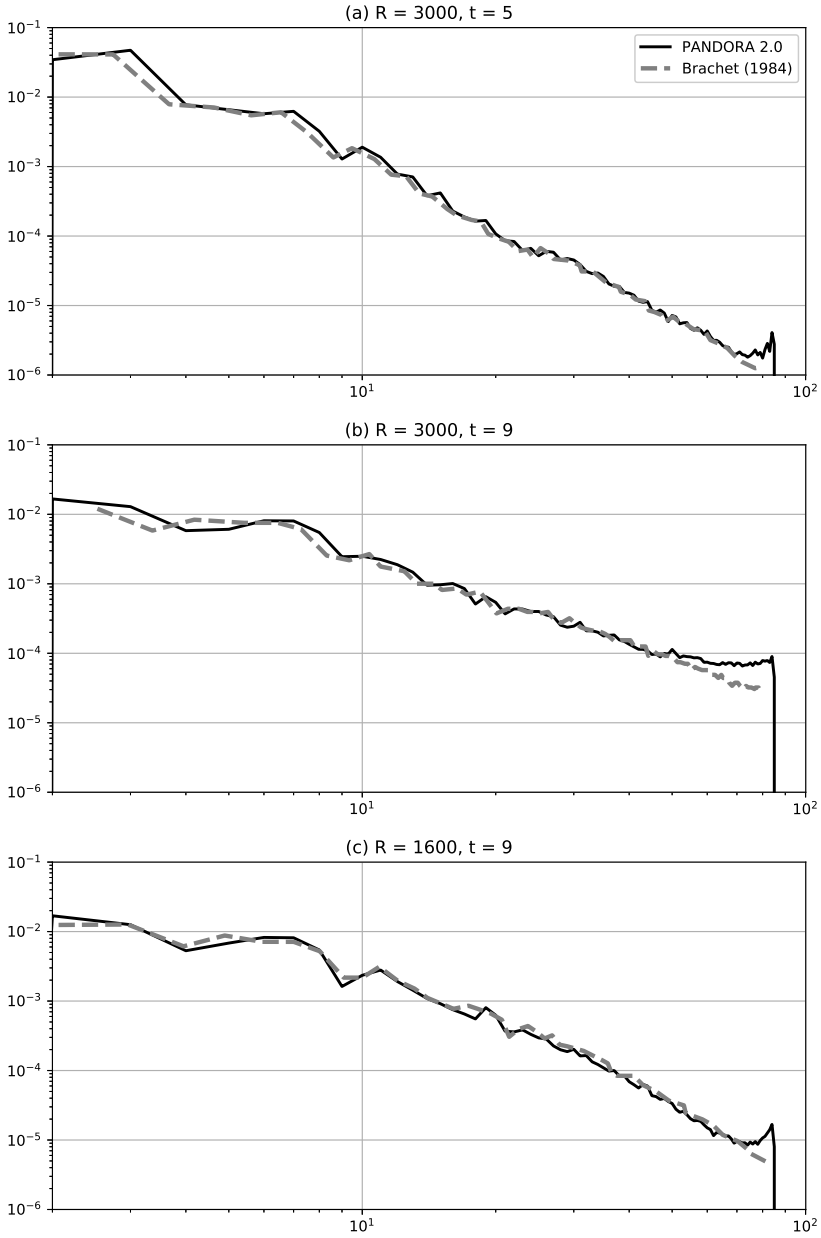

FIGURE 5.10: Same as fig. 5.8, but in addition to the 2/3 rule dealiasing a spherical truncation of all wavenumbers $> k_{max}$ has been performed.

Results for the turbulence kinetic energy and dissipation are commonly represented as theory predicts exponential growth [61]. Figure 5.11 shows the energy, dissipation and production based on equation 5.41 compared to the published results by Matsumoto et al [77]. In the upper row, the results using the 2/3 rule for dealiasing are shown, the lower row shows the results based on spherical truncation. As expected, a significant impact of the remeshing on the energy and more so on dissipation can be seen that decreases with increasing resolution. Comparison of the two dealiasing schemes shows that the wave numbers affected by this are outside the $k = 1/3N$ sphere. Energy and production agree well with the published results, in particular for times $< St = 10$. The dissipation

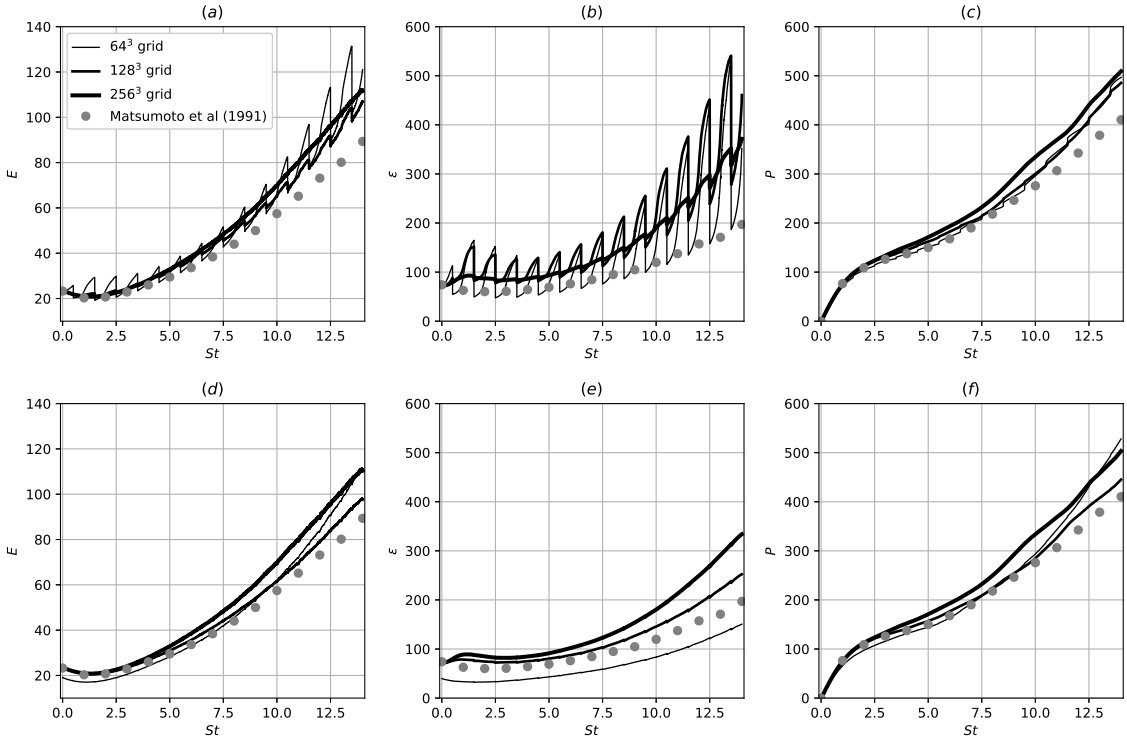

FIGURE 5.11: Comparison of energy, dissipation and production from own simulations and published results by Matsumoto et al. [77]. The results in the top row are from simulations with a dealiasing scheme based on the 2/3 rule, the results on the bottom row have been additionally spherically truncated. (a) and (d) energy (b) and (e) dissipation (c) and (f) production.

shows a dependence on the computing grid as well as remeshing, so a comparison to the results by Matsumoto et al [77] is not straightforward. However the published results are in between the results based on spherical truncation on the 64^3 and 128^3 grids, which is plausible.

The energy components in streamwise, spanwise and shear directions are shown in figure 5.12. It is evident that the lowest resolution simulations show a tendency to overestimate energy in streamwise direction and underestimate energy in the spanwise and shear directions. The higher resolution simulations show a good agreement with the published results.

One significant difference between the calculations presented here and those performed by Matsumoto et al [77] is the dealiasing scheme. While the present computations are based on the 2/3 rule, Matsumoto et al [77] used the same dealiasing scheme as Rogallo [101] based on random phase shifts. The latter scheme keeps higher wave modes, but also some aliasing errors remain. To show the influence of the higher wave modes, additional computations on a 96^3 grid were performed, which maintain the same number of wave modes as the Matsumoto et al [77] computations. Figure 5.13 shows energy, dissipation

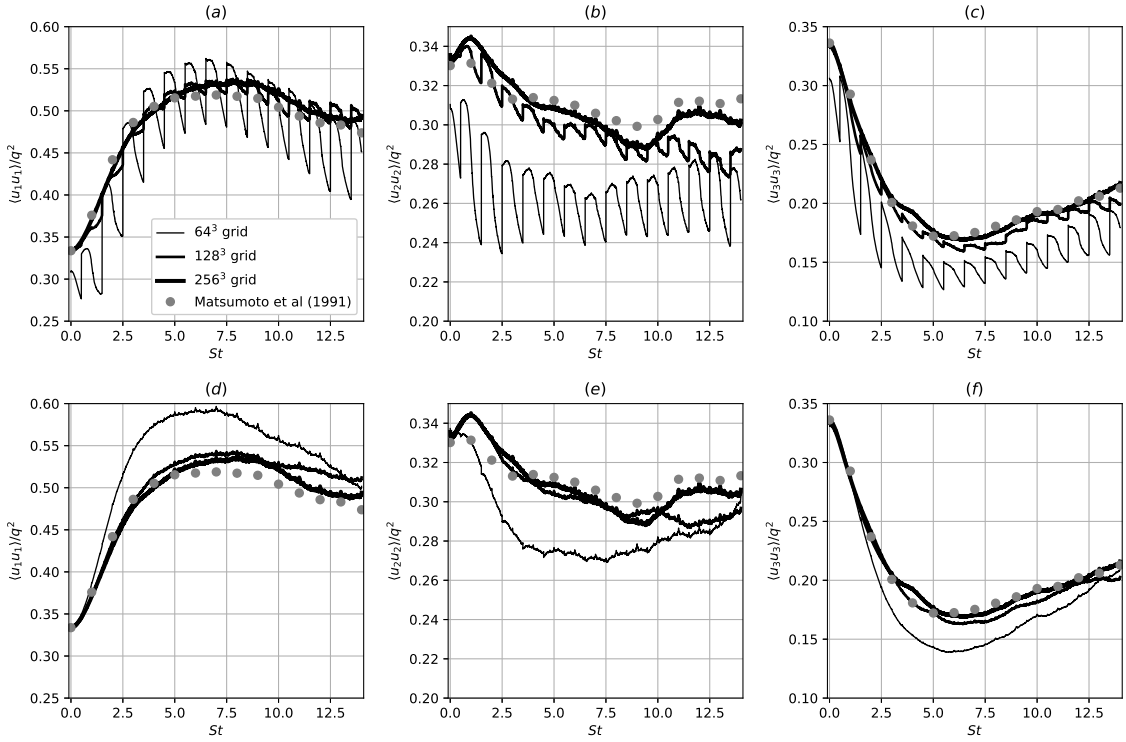

FIGURE 5.12: Energy components (a) and (d) streamwise (b) and (e) spanwise (c) and (f) in shear direction.

and production for these simulations. A very good agreement can be found, confirming what has been said about dealiasing.

Figures 5.14 and 5.15 show the same quantities as figures 5.11 and 5.12, but computed using the convective Rogallo formulation of the transformed Navier-Stokes equation (equation 5.3). The results are almost exactly identical. However it can be seen from the energy components (figure 5.15) that the Rogallo formulation is impacted by the remeshing, even using a spherical truncation, for which the Bardino/Ferziger rotational formulation (equation 5.41) is unaffected.

Figures 5.16 and 5.17 show the same quantities as figures 5.11 and 5.12, but computed on a $4\pi \times 2\pi \times 2\pi$ domain. There is almost perfect agreement between the simulations. Differences occur due to the different remeshing times and are mostly visible for the dissipation in the simulations without spherical dealiasing.

Finally the effect of remeshing is investigated. The loss in energy and dissipation at remesh, which is due to different resolution of the computing domain in different directions, has been discussed by many authors. Some workers (e.g. Lee et al [72]) have come to the conclusion that energy loss is so significant, in particular at high shear rates, that it would be better not to remesh at all.

Figure 5.18 show the same quantities as figure 5.11 with the only difference being that no remeshing was performed. It can be seen that all simulations show a significant increase

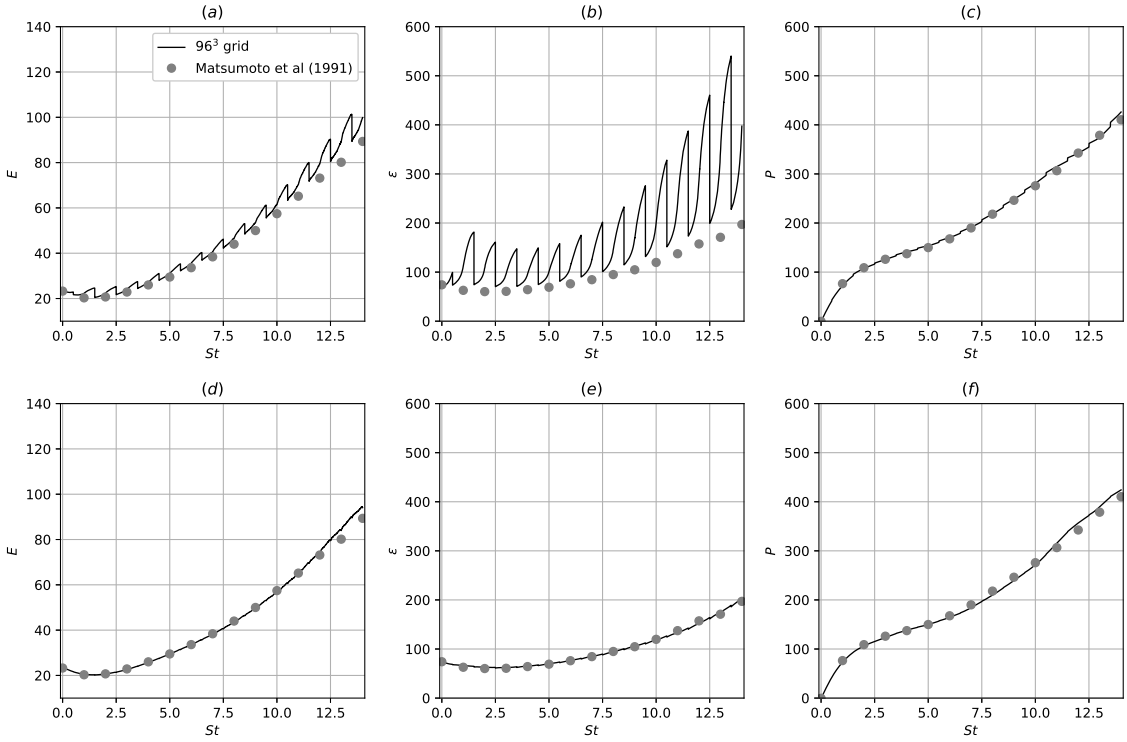

FIGURE 5.13: Comparison of energy, dissipation and production from own simulations and published results by Matsumoto et al. [77]. The results in the top row are from simulations with a dealiasing scheme based on the 2/3 rule, the results on the bottom row have been additionally spherically truncated. (a) and (d) energy (b) and (e) dissipation (c) and (f) production.

in energy and dissipation that becomes smaller with increasing grid resolution. The production agrees well with the published results of Matsumoto et al [77] on the smallest grid, but shows a stronger increase on finer grids.

The energy components (figure 5.19 without remesh vs figure 5.12 with remesh) decrease substantially and do not result in a sum of 1 as would be expected from conservation of energy. This would suggest that the results without remesh are not correct, although they become better with increasing grid resolution.

A look at the energy spectra reveals an unphysical growth in the high-wavenumber part of the spectrum. The spectra of the three energy components are shown at two times, $St = 2$ and $St = 5$, for the simulations with remesh (figures 5.20 and 5.22 respectively) and without remesh (figures 5.22 and 5.26 respectively). The spectra for the computations with remesh all show a fairly good agreement amongst each other. For the lowest grid resolutions, including the published results by Matsumoto et al [77] there is a deviation from the better resolved simulations in the highest wavenumbers. A further disagreement between simulations can also be found in the lowest wave number, in particular in spanwise direction (at $St = 5$, figure 5.22). While the difference in the highest wave numbers is likely numerical and due to the limited resolution, it seems

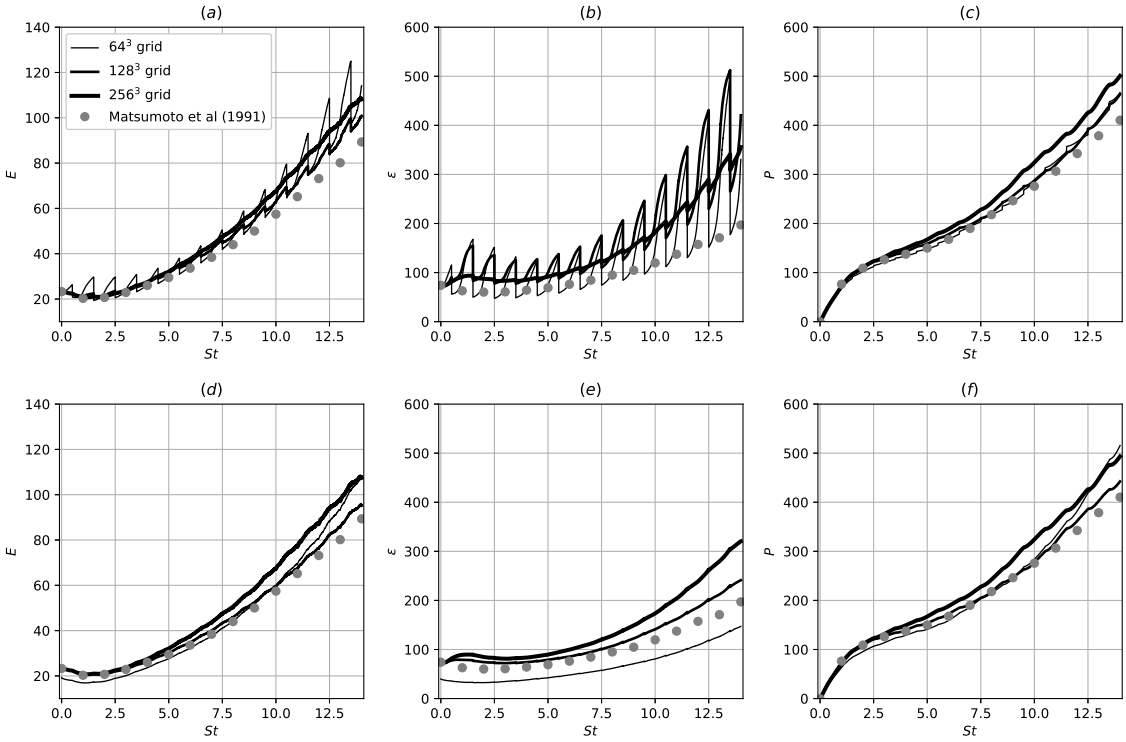

FIGURE 5.14: Same as 5.11, but computed using the convective Rogallo formulation [101].

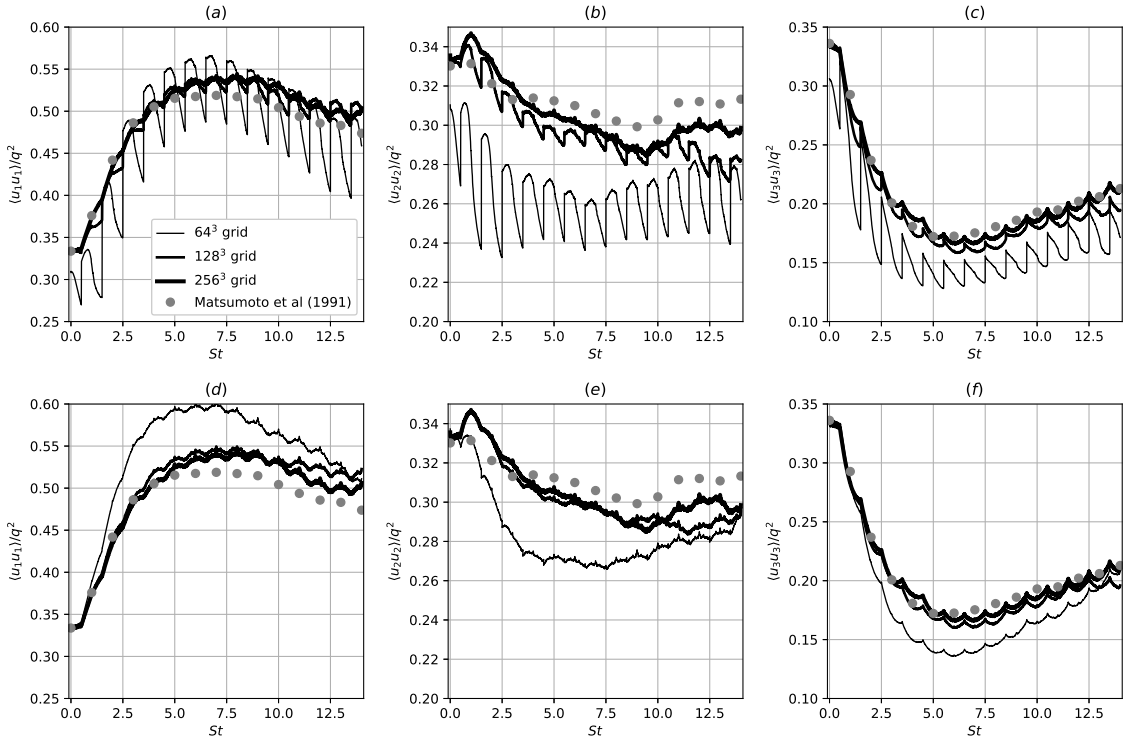

FIGURE 5.15: Same as 5.12, but computed using the convective Rogallo formulation [101].

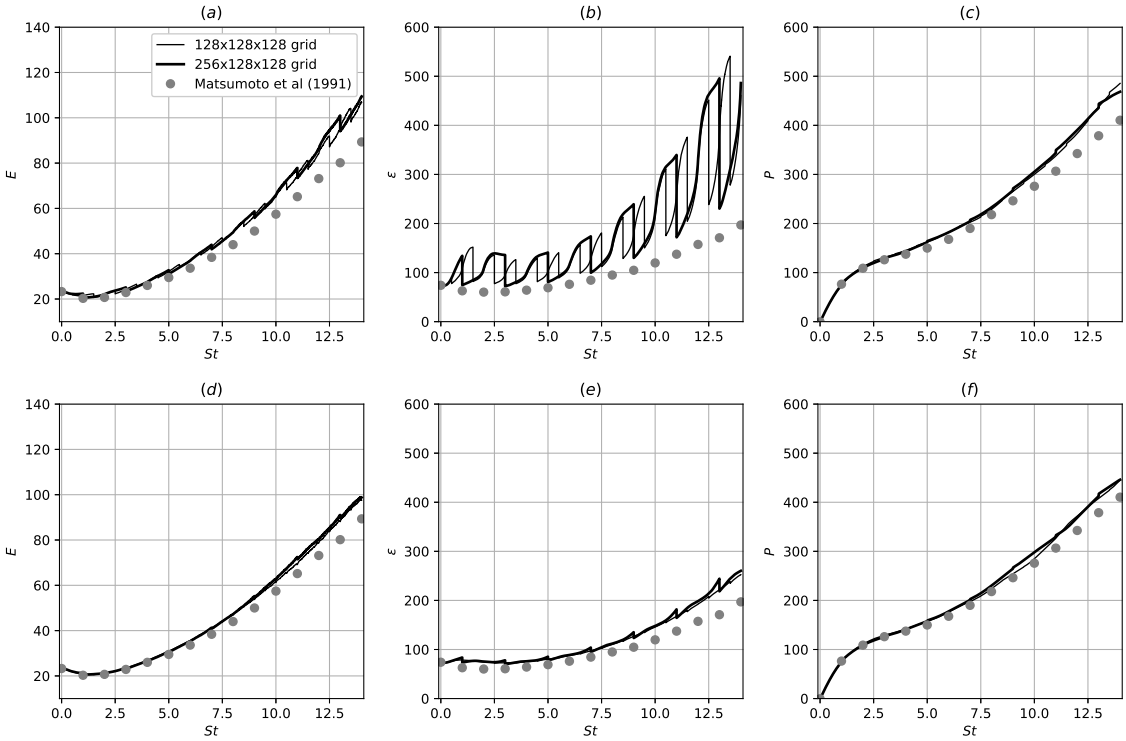

FIGURE 5.16: Same as 5.11, but computed using an elongated computing domain.

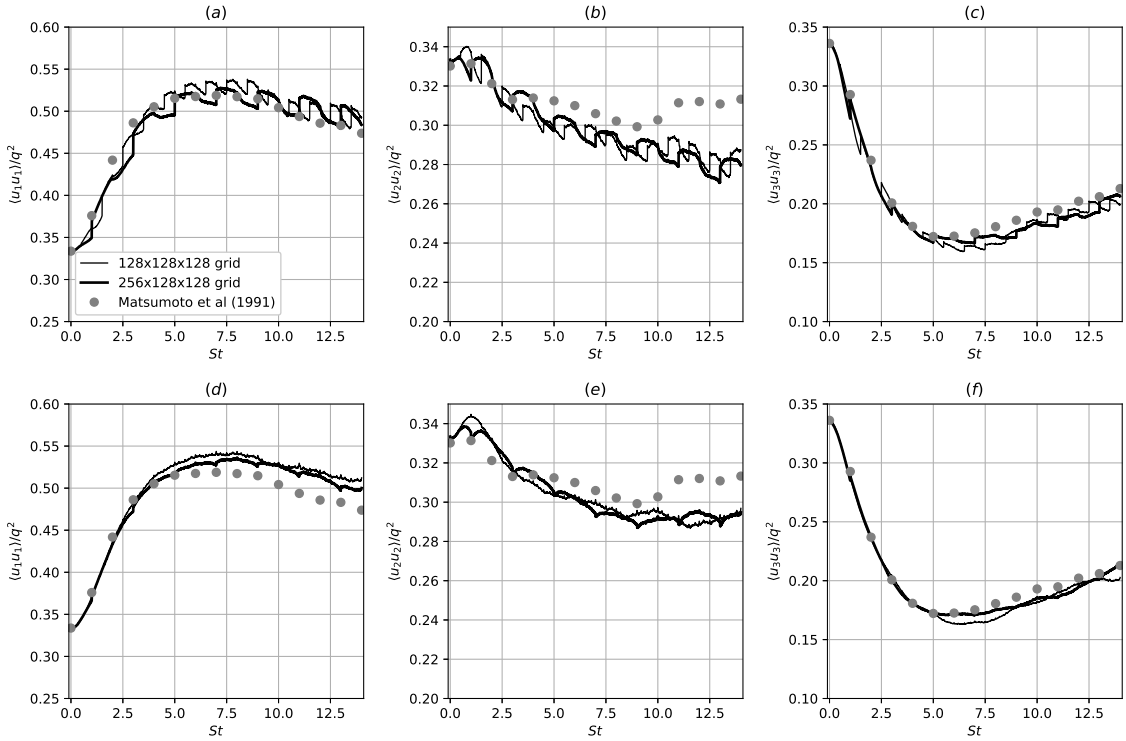

FIGURE 5.17: Same as 5.12, but computed using an elongated computing domain.

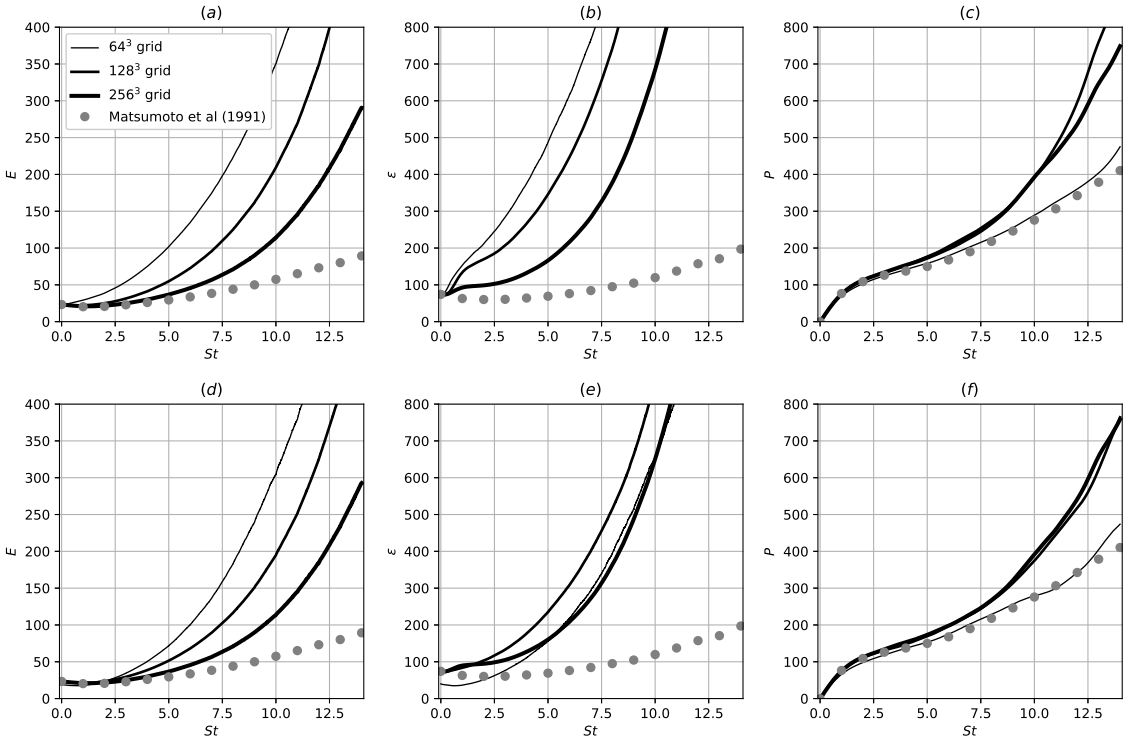

FIGURE 5.18: Same as 5.11, but computed without remeshing.

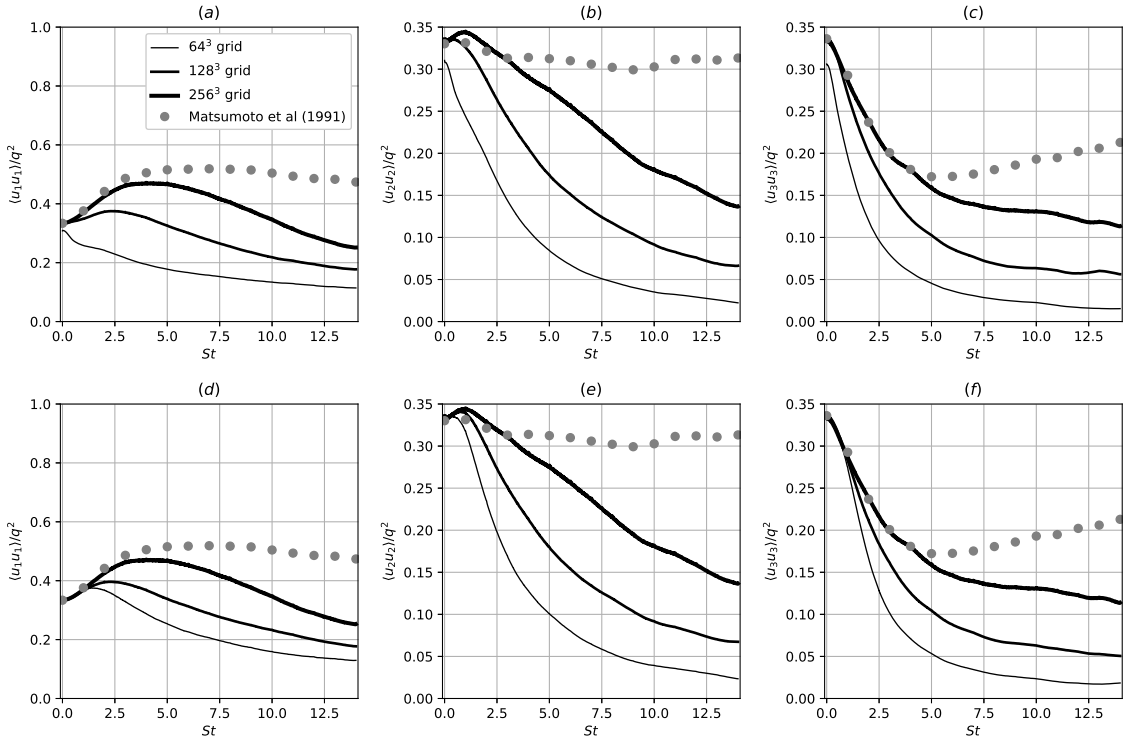

FIGURE 5.19: Same as 5.12, but computed without remeshing.

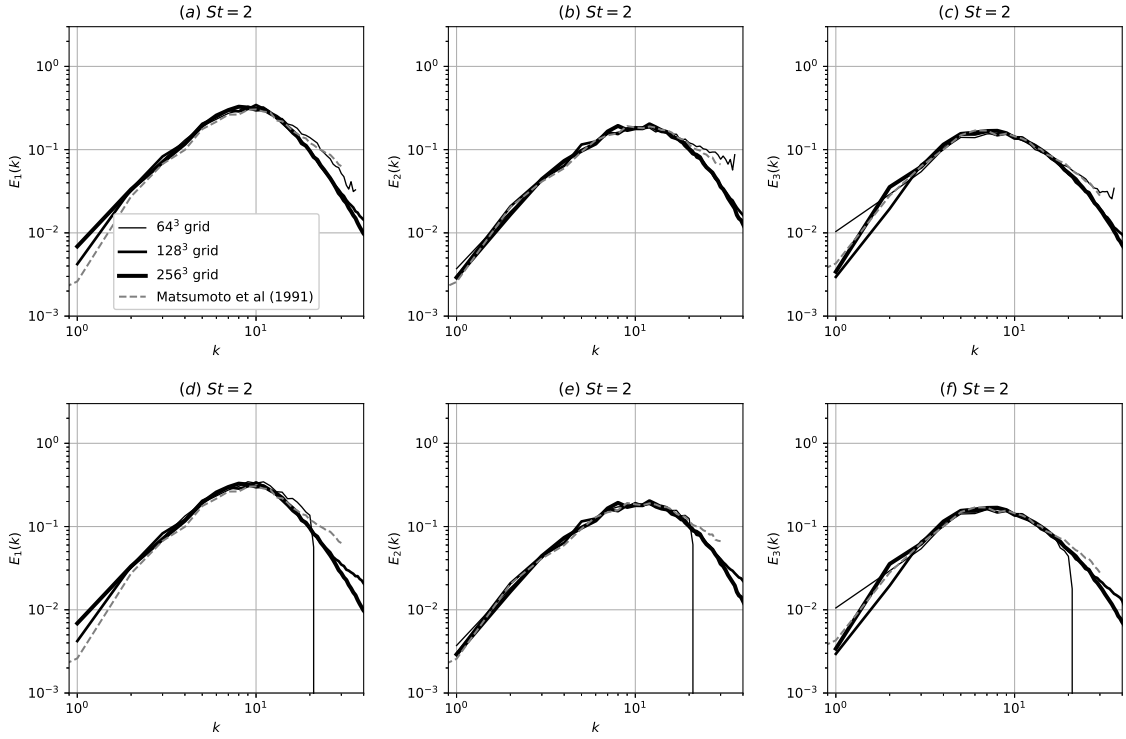

FIGURE 5.20: Spectra of the energy components in (a)(d) streamwise (b)(e) spanwise (c)(f) shear direction at time $S \cdot t = 2$.

plausible that the lowest wave number simply differs due to the turbulent nature of the flow, which does not average out well in the lowest wave number range with only few wave modes per wave number.

The spectra of the computations without remesh show a significant increase in high wave number content. This increase is stronger for the coarsest grid and less visible for the best-resolved grid. Although the spectral truncation influences the spectral shape at cutoff, it does not prevent this effect from occurring.

A similar unphysical increase in high-wavenumber energy has been observed by Sukheswalla et al [112], who used a different numerical algorithm that replaces the remeshing with an interpolation. The occurrence of spurious high wave modes was explained by those authors with Gibbs oscillations and a spectral filter was introduced as a remedy for this problem. Based on the results shown in the present work, it can be concluded that the remeshing procedure, rather than distorting the results, introduces stability into the computations and the Rogallo [101] algorithm is therefore still appropriate for the computation of homogeneous shear flows, especially when characterised properly. The publications by Brucker et al. [19] and Sukheswalla et al [112] indicate that while an alternative spectral algorithm is possible, it needs to address the unphysical growth of energy and dissipation that is naturally being dealt with during remesh in the Rogallo algorithm.

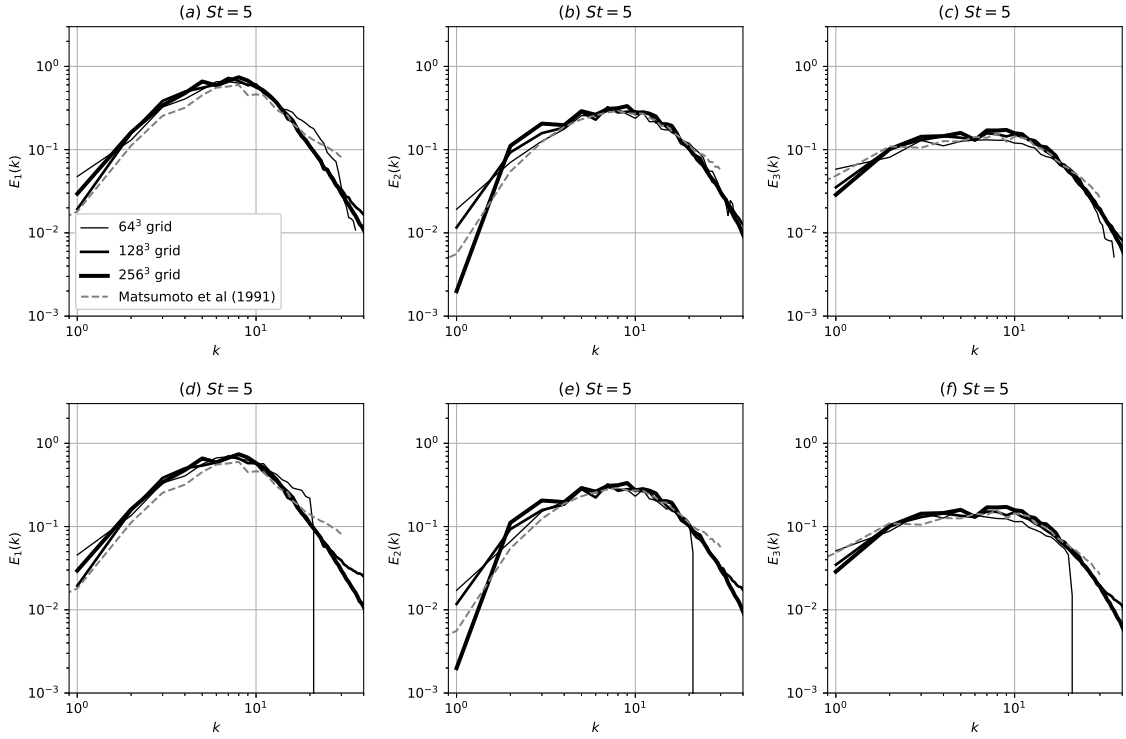

FIGURE 5.21: Spectra of the energy components in (a)(d) streamwise (b)(e) spanwise (c)(f) shear direction at time $S \cdot t = 5$.

FIGURE 5.22

5.3.3 Passive particles in shear flow

As the main purpose of PANDORA 2.0 is to perform computations of passive and inertial particle movement in turbulent flows, another validation test case is needed for the dispersion of particles. This limits the choice of available publications even further compared to the criteria for a fluid validation test case as discussed in the previous section. A publication by Ahmed and Elghobashi [2] was selected, which contains extensive fluid and particle statistics. While the numerical algorithm used for the fluid simulations was different, the initial conditions are well documented, enabling a comparison. However an exact agreement based on the described initialisation was not easy to achieve. In particular a slightly higher maximum wavenumber was necessary in order to achieve the same integral length scale.

The initial conditions are summarised in tables 5.4 and 5.5. These cases differ by their different shear parameter at the same shear-rate and correspond to the fluid test cases I and II in the publication [2].

Figure 5.27 shows the development of energy and dissipation. There is an excellent agreement in energy growth and dissipation for the higher shear parameter simulation. The lower shear parameter simulation shows a good agreement in dissipation until $St = 8$

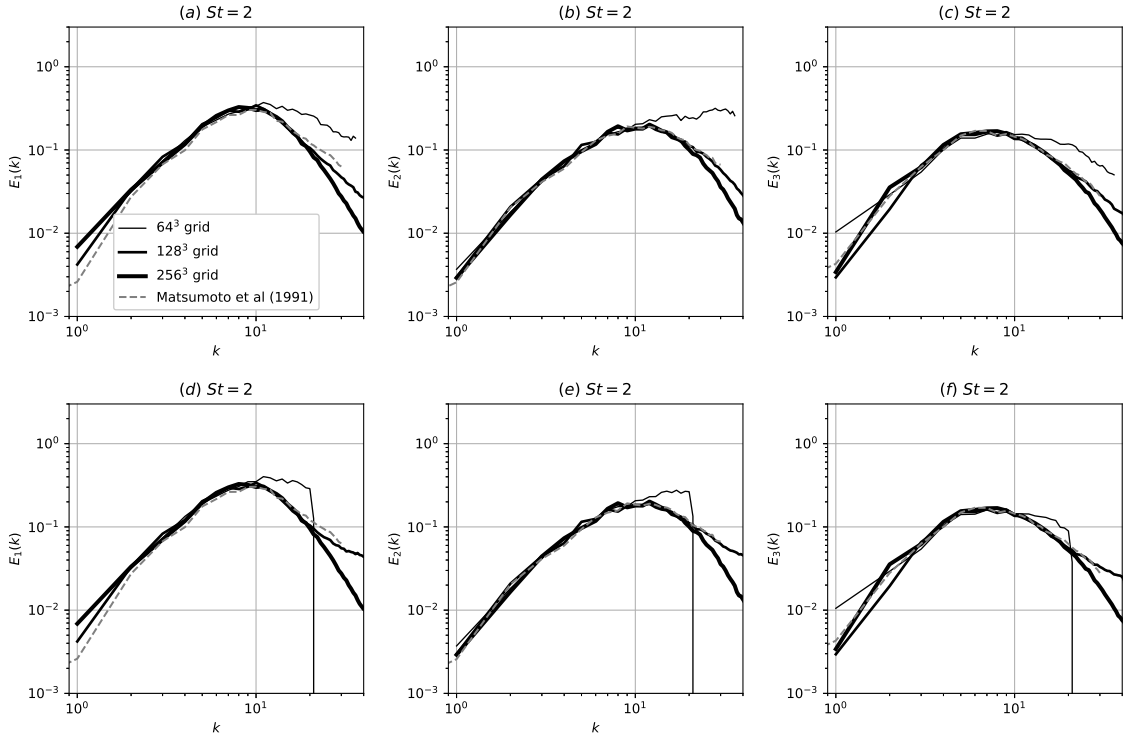

FIGURE 5.23: Same as 5.11, but computed without remeshing.

FIGURE 5.24

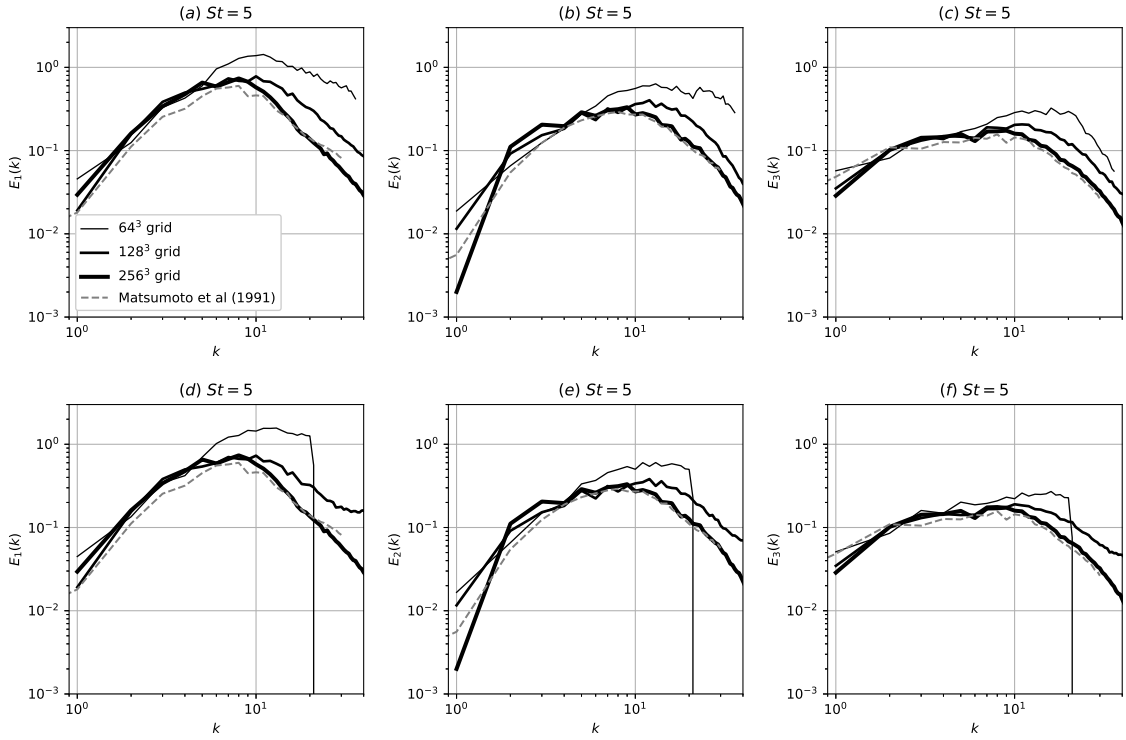

FIGURE 5.25: Same as 5.12, but computed without remeshing [101].

FIGURE 5.26

Shear rate	S	0.96		
Grid		256×128^2		
Taylor Reynolds number	Re_λ	20.0		
Peak wave number	k_p/k_{min}	5.3		
Turbulent intensity	u'	0.219772	$u'/(2\pi)$	0.034978
Viscosity	ν	0.004145	$\nu/(2\pi)^2$	0.000105
Dissipation	ϵ	0.021152	$\epsilon/(2\pi)^2$	0.0005358
Energy	E	0.072450	$E/(2\pi)^2$	0.001835
Integral length scale	l_{int}	0.476626	$l_{int}/(2\pi)$	0.075857
Taylor scale	λ	0.376796	$\lambda/(2\pi)$	0.059969
Kolmogorov scale	η	0.042836	$\eta/(2\pi)$	0.0068175
Large-eddy turnover time	T_E	2.16873		2.16873

TABLE 5.4: Initial conditions of the simulations for Case I. Values normalised by the length scale 2π have been provided to allow a direct comparison with the simulations of Ahmed and Elghobashi [2].

Shear rate	S	0.96		
Grid		256×128^2		
Taylor Reynolds number	Re_λ	19.9		
Peak wave number	k_p/k_{min}	5.3		
Turbulent intensity	u'	0.112393	$u'/(2\pi)$	0.017887
Viscosity	ν	0.002133	$\nu/(2\pi)^2$	0.000054
Dissipation	ϵ	0.002846	$\epsilon/(2\pi)^2$	0.000072
Energy	E	0.018948	$E/(2\pi)^2$	0.000480
Integral length scale	l_{int}	0.476626	$l_{int}/(2\pi)$	0.075857
Taylor scale	λ	0.376796	$\lambda/(2\pi)$	0.059969
Kolmogorov scale	η	0.042964	$\eta/(2\pi)$	0.006838
Large-eddy turnover time	T_E	4.24069		

TABLE 5.5: Initial conditions of the simulations for Case II. Values normalised by the length scale 2π have been provided to allow a direct comparison with the simulations of Ahmed and Elghobashi [2].

and a good agreement in energy until about $St = 6$, at which point the energy in our own simulations grows significantly faster.

The growth of velocity components is shown in figure 5.28. For the higher shear parameter simulation all components agree well with slightly faster growth from $St = 8$. No preference for any one of the velocity components, other than in the simulations in the previous section, can be found. At the lower shear parameter the streamwise component grows significantly faster in our own simulations compared to the published results from about $St = 6$, with good agreement before that time.

The shear stress is commonly normalised by the variances in streamwise and shear directions and is also known as shear-stress correlation [112]. To make efficient use of the parallelisation of PANDORA 2.0, shear is used in the third direction, i.e. $A_{13} = S$, and therefore in the context of this work the shear-stress correlation is defined as

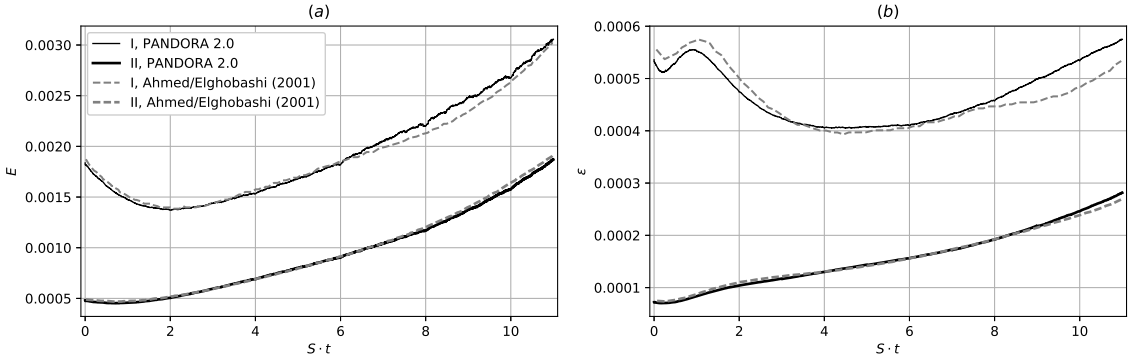

FIGURE 5.27: Energy and dissipation of the simulations. Dashed line from Ahmed and Elghobashi [2]

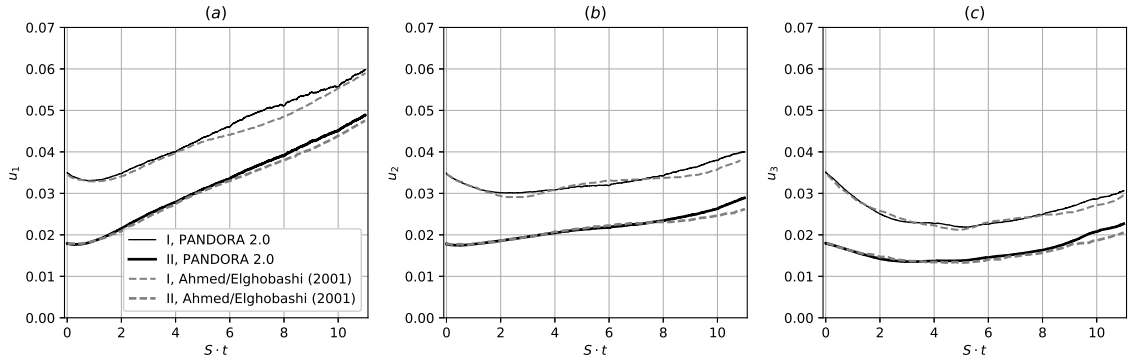

FIGURE 5.28: Velocity components. Dashed line from Ahmed and Elghobashi [2]

$$\rho_{uv} = \frac{u_1' u_3'}{\sqrt{{u_1'}^2 {u_3'}^2}} \tag{5.52}$$

The normalised shear stress components are shown in figure 5.29. There is a good agreement in all stress components. The Reynolds stress component in shear direction approximates, both in the published results and own simulations, the expected value of around -0.6 to -0.4 (as discussed by [112]).

A good agreement has been achieved in the energy spectra as shown in figure 5.30 for $St = 2$ and $St = 10$. Differences are mainly to be found in the lowest wave number, which is likely due to the higher peak wave number at initialisation. At the highest wave numbers the energy density from our own simulations is also lower than the published spectra, however the reason for this is more likely due to the higher resolution of our simulations, as discussed in the previous section about fluid simulations.

The dissipation spectra (figure 5.31) show an equivalent tendency to the energy spectra. As expected for higher-order statistics, the differences are slightly more pronounced. In particular the above said about the highest wavenumbers is more pronounced for the dissipation.

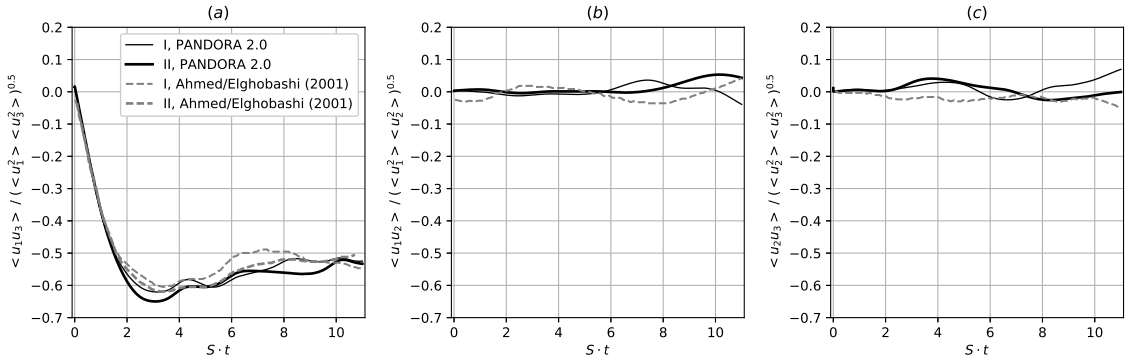

FIGURE 5.29: Reynolds stress components. Dashed line from Ahmed and Elghobashi [2]

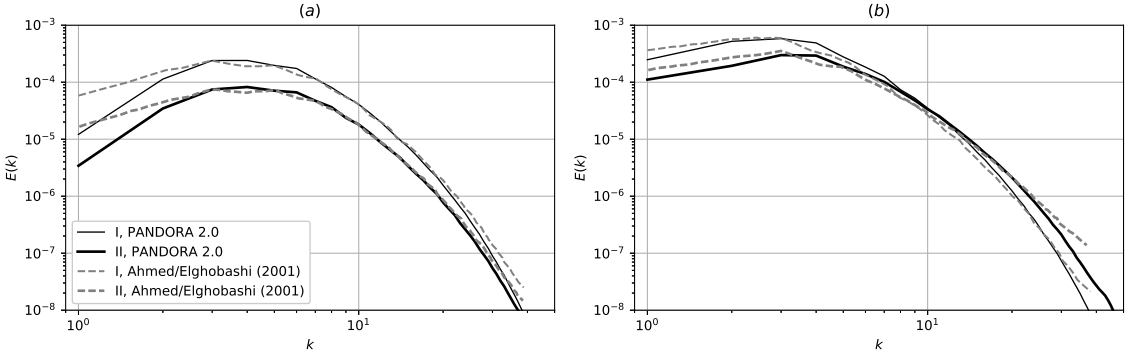

FIGURE 5.30: Energy spectra at (a) $S \cdot t = 2$ and (b) $S \cdot t = 10$. Dashed line from Ahmed and Elghobashi [2]

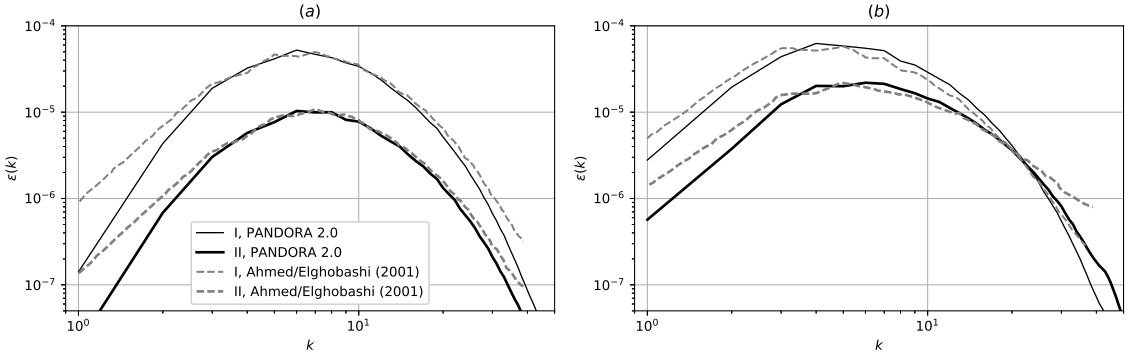

FIGURE 5.31: Dissipation spectra at (a) $S \cdot t = 2$ and (b) $S \cdot t = 10$. Dashed line from Ahmed and Elghobashi [2]

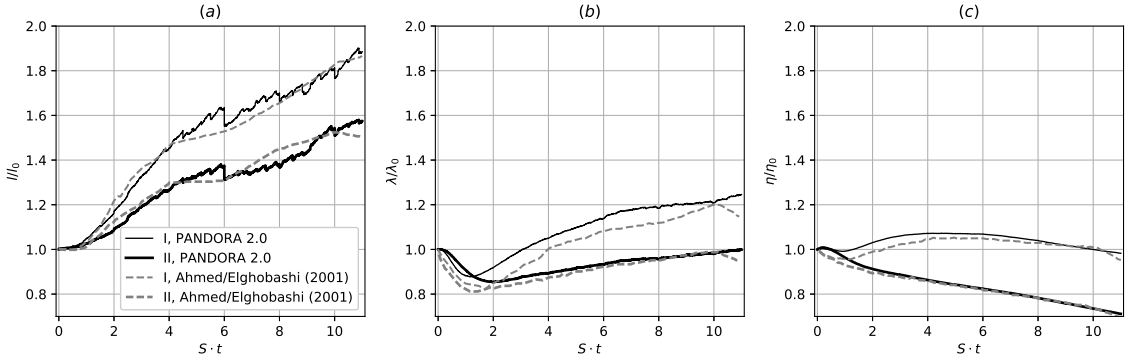

FIGURE 5.32: (a) Integral length scale (b) Taylor scale (c) Kolmogorov scale. Dashed line from Ahmed and Elghobashi [2]

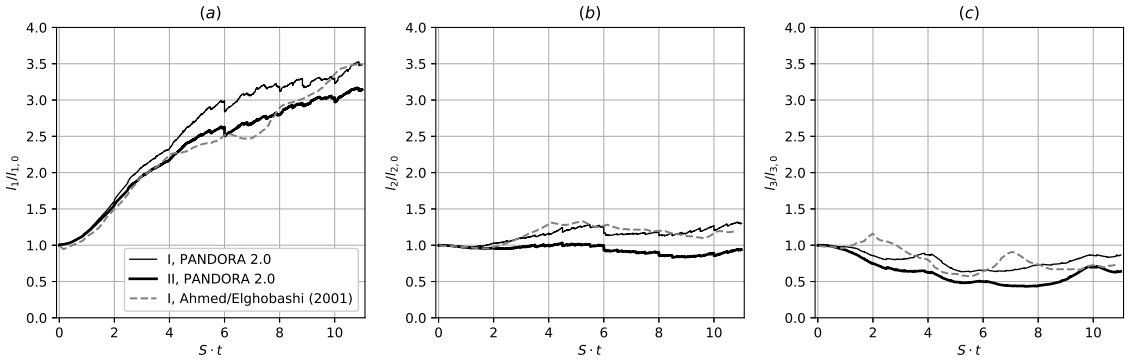

FIGURE 5.33: Components of the integral length scale (a) streamwise (b) spanwise (c) shear direction. Dashed line from Ahmed and Elghobashi [2]

From the spectra it can already be predicted that there is a better agreement in the smallest length scales than in the largest scales. This can also be seen from the results for the integral length scale, the Taylor scale and the Kolmogorov scale shown in figure 5.32. The Kolmogorov length in particular shows good agreement throughout the simulation, whereas the growth in the integral length scale differs for both shear parameters at intermediate times between $St = 4$ and $St = 8$. The Taylor length scale grows stronger in our own simulations, corresponding to more energy in the inertial range.

A further investigation of the development of the integral length scale can be seen in figure 5.33, where it is shown componentwise. While the components in spanwise and shear direction remain constant for both published and own results, for the streamwise component a stronger growth can be seen than for that published by Ahmed and Elghobashi [2]. Judging by the common expectation of continous growth [112], the present results are closer to the expected behaviour.

Finally the shear parameter and resolution are discussed as shown in figure 5.34. The resolution of the present results is higher and therefore would be expected to be more exact. The shear parameter, both based on the large-eddy turnover time and based on the energy-dissipation ratio, shows better agreement with the published results for

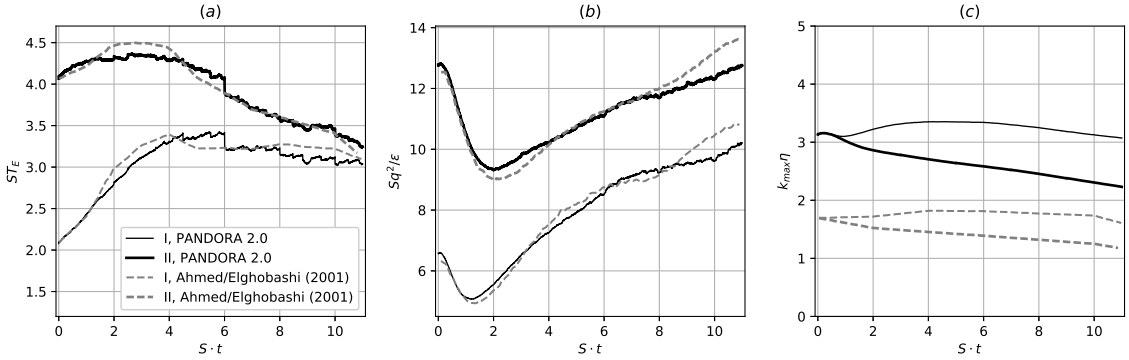

FIGURE 5.34: (a) Shear parameter (b) resolution of the simulations. Dashed line from Ahmed and Elghobashi [2]

Particle case		A	B	C	I	II
Fluid case		I	I	II	I	II
Passive particles					x	x
Inertial particles		x	x	x		
Particle diameter	d_p/η	0.0356	0.0356	0.0366	-	-
Particle density	ρ_p/ρ_f	3312	33124	1696	-	-
Particle Reynolds number	Re_p	0.00086	0.00086	0.00058	-	-
Kolmogorov-scale Stokes number	St_η	0.233	2.330	0.126	-	-
Stokes number based on large-eddy turnover time	St_{T_E}	0.040	0.402	0.023	-	-

TABLE 5.6: Initial conditions at injection time $St = 1$ of the inertial (A, B, C) and passive (I, II) particle simulations

the higher shear-parameter simulations than at the lower shear parameter. For the lower shear parameter simulations the shear parameter based on the large-eddy turnover time shows a significantly different development compared to the published results from about $St = 4$, whereas differences in the energy-dissipation ratio are particularly evident at times $St = 6$ until about $St = 10$. This suggests a different development of turbulent structures in the simulations.

In the context of this work, both passive and inertial particle statistics are relevant, because passive particles allow for a comparison with atmospheric tracer gas experiments, whereas time-resolved inertial particle measurements under realistic atmospheric conditions are difficult to obtain. In the following, results for passive particles are discussed, followed by inertial particle simulations.

An overview of the initial conditions for all particle simulations are given in table 5.6. As in the publication [2], passive particles have been introduced in both fluid cases. For the lower shear parameter inertial particles have been simulated at two different Stokes numbers, whereas at the higher shear parameter only one Stokes number has been simulated.

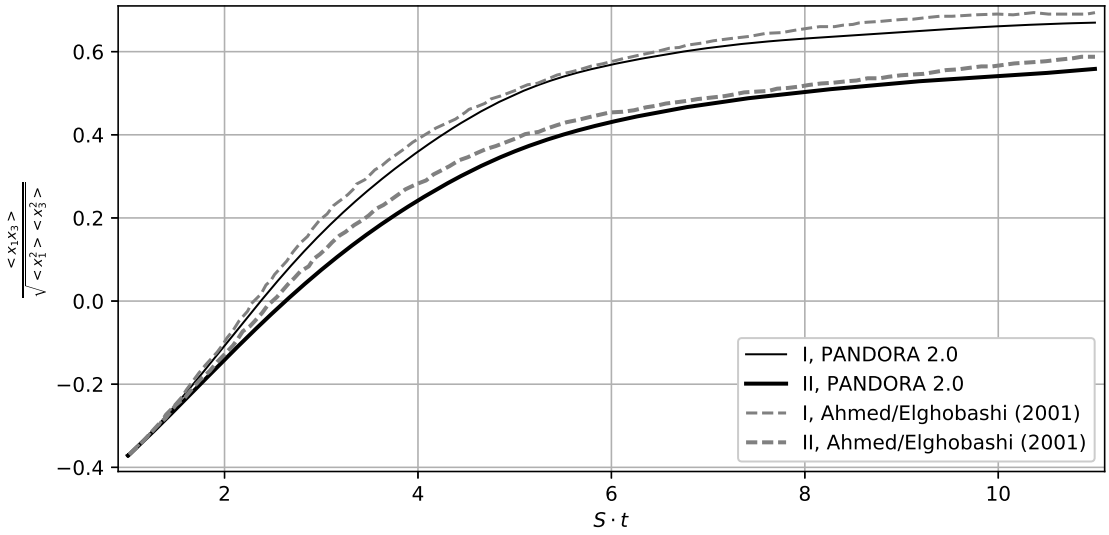

FIGURE 5.35: Dispersion cross correlation for passive particles. Dashed line from Ahmed and Elghobashi [2]

The dispersion cross correlation in shear direction is very similar to the shear stress correlation discussed earlier (see figure 5.29). It reaches a plateau from about $St = 4$ as shown in figure 5.35. While the final value in our own simulations agrees well with the published results, the initial increase is slightly steeper in our own simulations.

While the dispersion (figure 5.36) in streamwise and spanwise directions shows a good agreement between own and published [2] results, there is a larger difference in shear direction (only available from the published results for the lower shear parameter simulation). However it is useful to take the different shear rate compared to the published results into account by a normalisation as suggested by Squires and Eaton [108]. This normalised dispersion shows a better agreement between own and published results, which is plausible as the normalisation is based on a short-term rapid distortion prediction. Notably the normalised dispersion in spanwise and shear directions collaps well for all simulations, our own and the published results, at both shear parameters until about $St = 6$ to $St = 8$. For the streamwise dispersion this is only the case for the initial time until around $St = 3$. Additional published results from Squires and Eaton [108], named cases 1 to 3, have been added to illustrate this point. These results have been moved to start at $St = 1$, the time at which the particles were introduced in our simulations as well as those of Ahmed and Elghobashi [2], for better comparison.

Finally the diffusivity of passive particles (figure 5.38) is discussed. The best agreement can be seen in the streamwise and spanwise direction. In shear direction the relative difference between our own simulations and the published results (only available for the lower shear parameter) is bigger. However it needs to be emphasised that this is also due to the fact that diffusivity is significantly smaller in shear direction than in streamwise direction. In absolute terms a similar difference can be found in the streamwise direction.

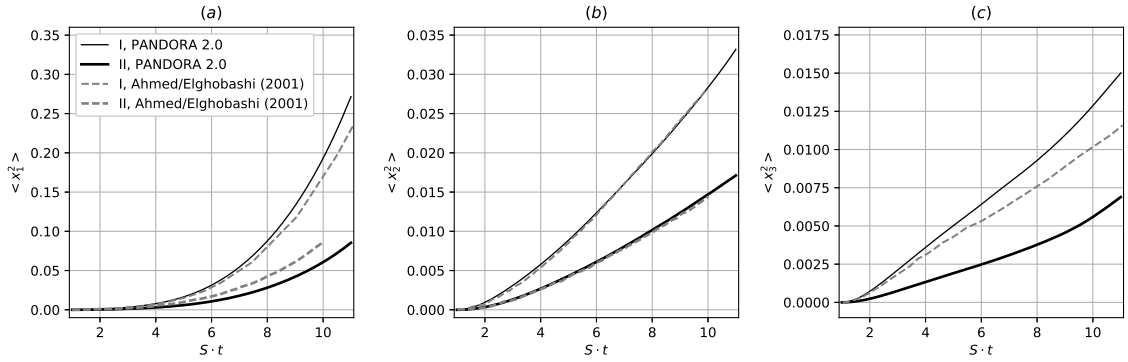

FIGURE 5.36: (a) Streamwise dispersion (b) spanwise dispersion and (c) dispersion in shear direction of passive particles. Dashed line from Ahmed and Elghobashi [2].

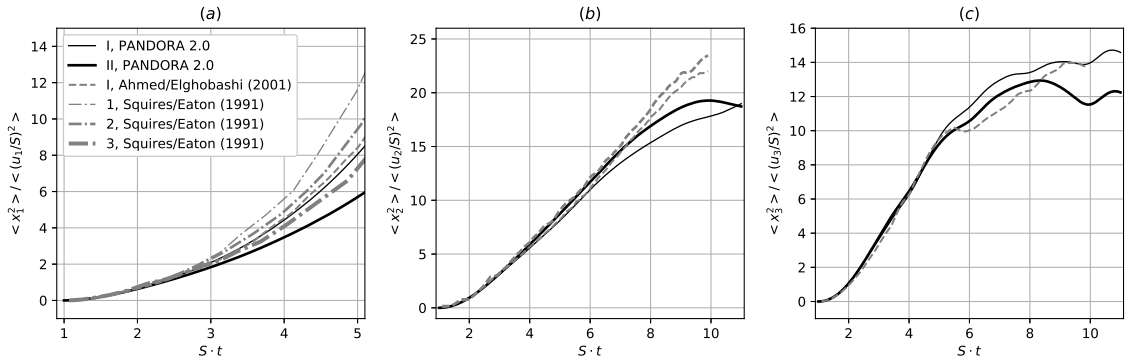

FIGURE 5.37: Same as figure 5.36, but normalised by u_i^2/S^2. Dashed line from Ahmed and Elghobashi [2]. Dash-dotted line from Squires and Eaton [109].

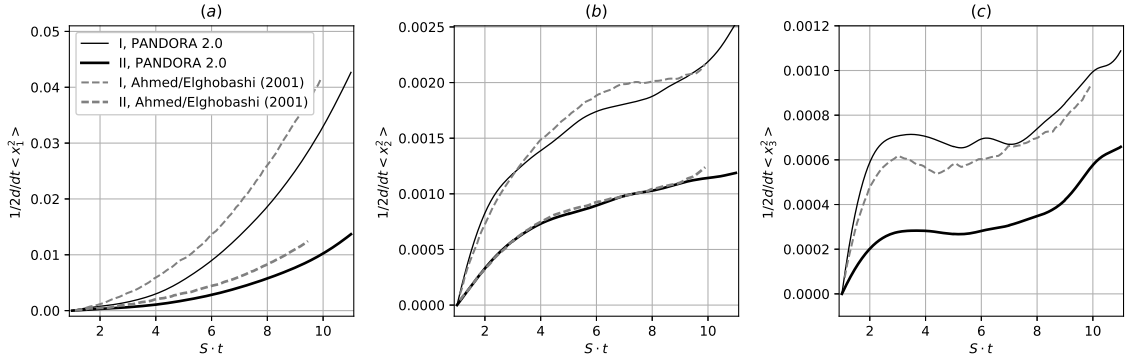

FIGURE 5.38: Diffusivity of passive particles in (a) streamwise (b) spanwise (c) shear direction. Dashed line from Ahmed and Elghobashi [2]

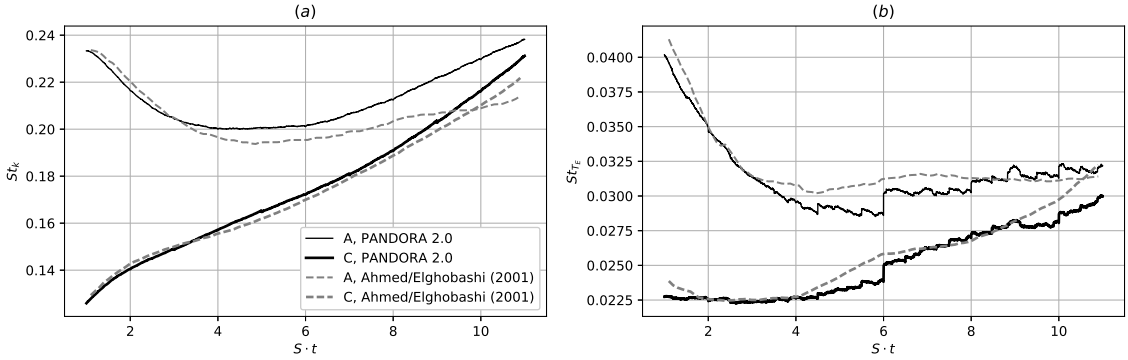

FIGURE 5.39: (a) Kolmogorov-scale Stokes number for cases A and C (b) Stokes number based on large-eddy turnover time for cases A and C. Dashed line from Ahmed and Elghobashi [2]

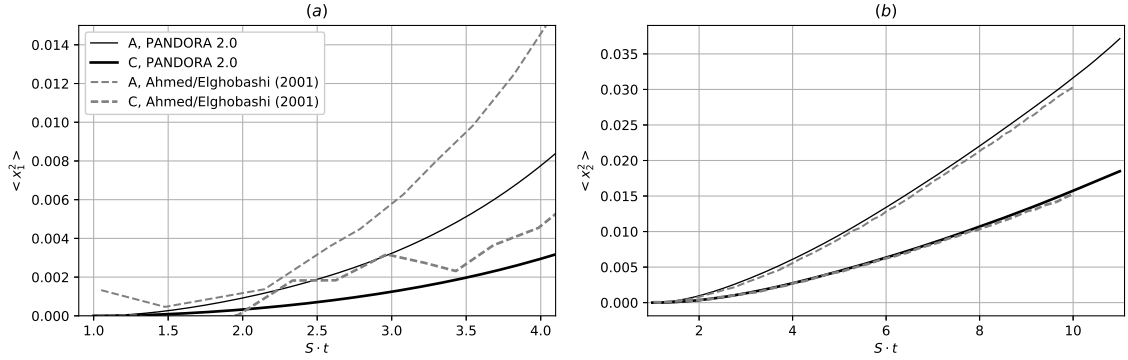

FIGURE 5.40: Dispersion of $St_\eta = 0.23$ particles in (a) streamwise (b) spanwise direction. Dashed line from Ahmed and Elghobashi [2]

5.3.4 Inertial particles in shear flow

The dispersion of $St_k = 0.23$ particles (figure 5.40) is in reasonably good agreement in both the streamwise and spanwise direction. Results for the shear directions are not available from [2] and can therefore not be compared. When applying a normalisation by turbulent intensity and shear rate (figure 5.41), similar results as for passive particles are obtained.

A similar result as that for passive particles is also obtained for the diffusivity shown in figure 5.42. While there is good agreement in spanwise direction, larger differences are found in streamwise direction.

In addition to the previous statistics, for inertial particles the relative velocity between particles and fluid can be investigated as shown in figure 5.43 for the streamwise and spanwise directions. Our own results for the relative velocity components reach a plateau, whereas the results published by Ahmed and Elghobashi [2] indicate a continuously growing relative velocity. The development in Stokes numbers both on Kolmorov time scales and on the large-eddy turnover time 5.39 shows a similar trend to the development

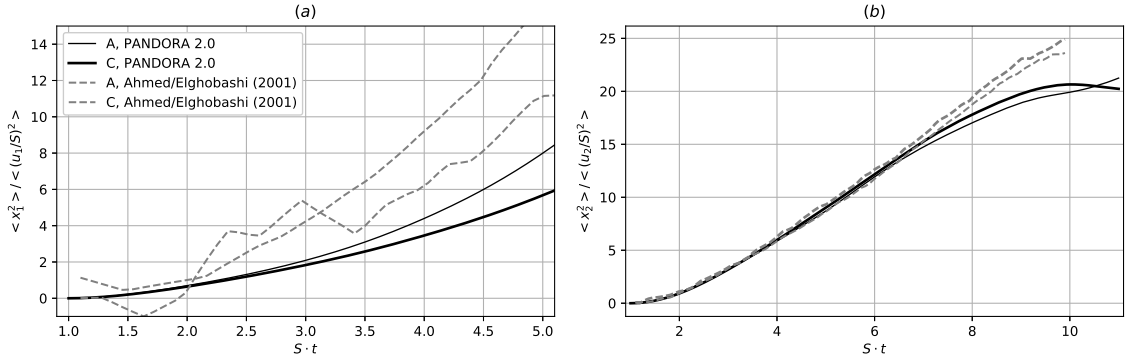

FIGURE 5.41: Same as figure 5.40, but normalised by u_i^2/S^2. Dashed line from Ahmed and Elghobashi [2]

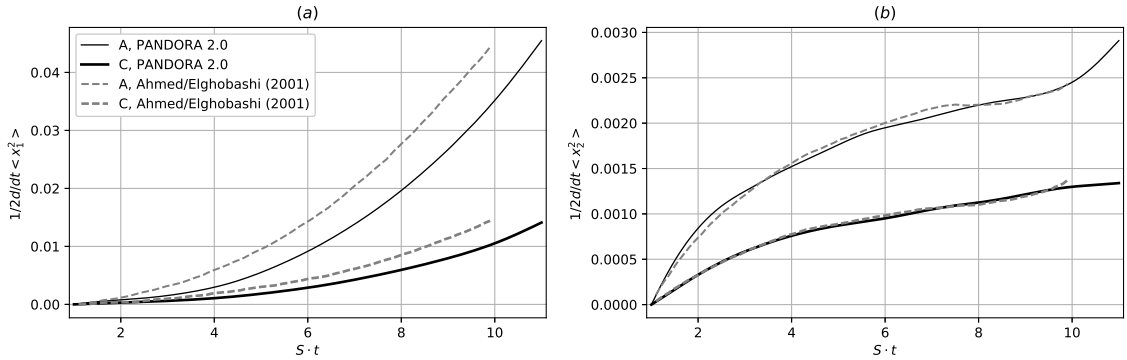

FIGURE 5.42: Diffusivity of $St_\eta = 0.23$ particles in (a) streamwise (b) spanwise direction. Dashed line from Ahmed and Elghobashi [2]

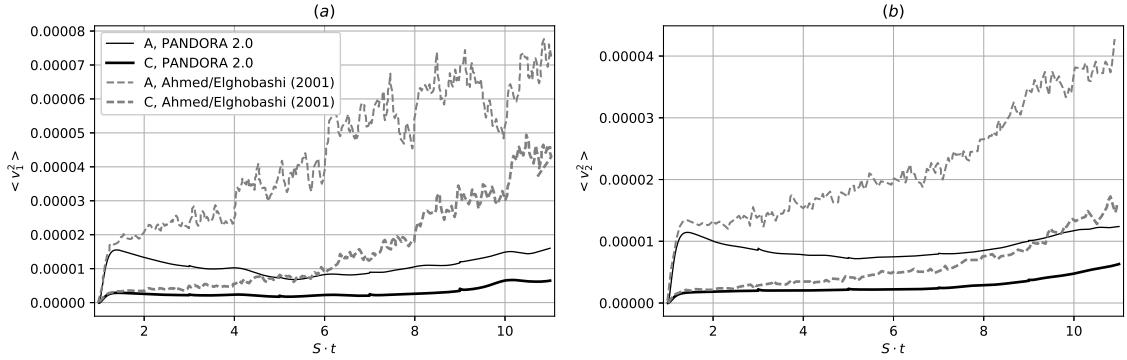

FIGURE 5.43: Relative velocity of $St_\eta = 0.23$ particles in (a) streamwise (b) spanwise direction. Dashed line from Ahmed and Elghobashi [2]

in relative particle velocity in our own simulations, whereas in the published results the relative velocity shows a significant growth that does not correspond to the Stokes number. In the author's view a similar behaviour of relative velocity and Stokes number seems more plausible. The increase in the published results in relative velocity could be due to sharp gradients or insufficient resolution in space and/or time.

For $St_k = 2.3$ particles both normalised (figure 5.46) and unnormalised (figure 5.45)

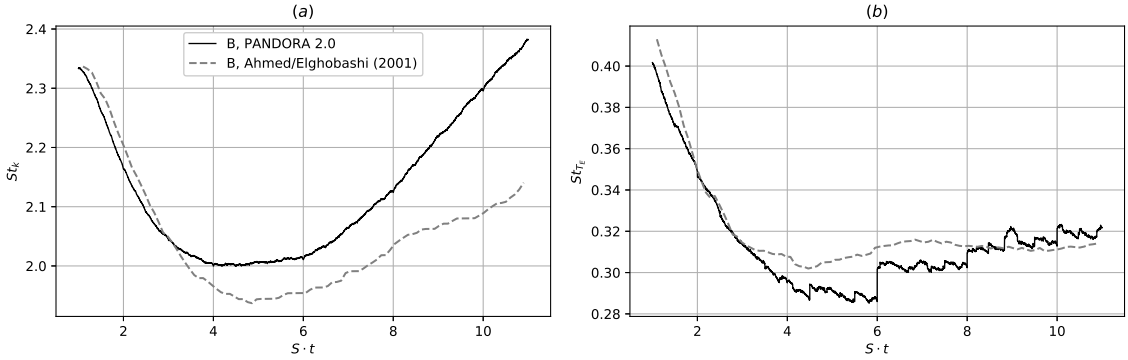

FIGURE 5.44: (a) Kolmogorov-scale Stokes number for case B (b) Stokes number based on large-eddy turnover time for case B. Dashed line from Ahmed and Elghobashi [2]

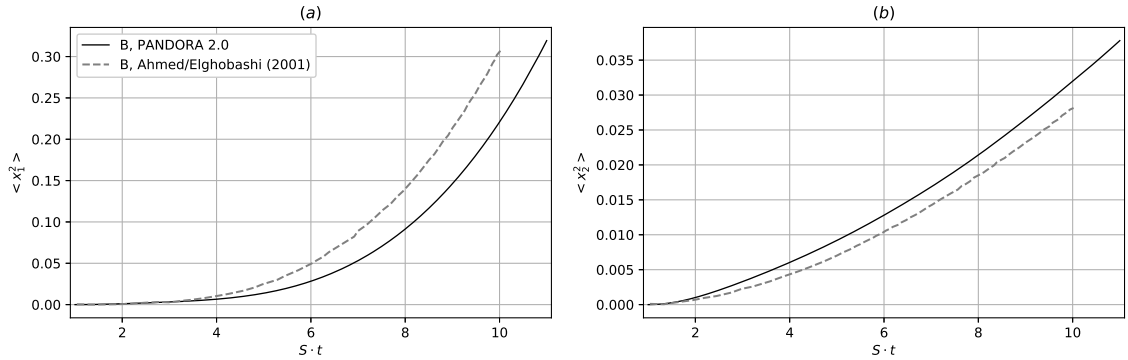

FIGURE 5.45: Dispersion of $St_\eta = 2.3$ particles in (a) streamwise (b) spanwise direction. Dashed line from Ahmed and Elghobashi [2]

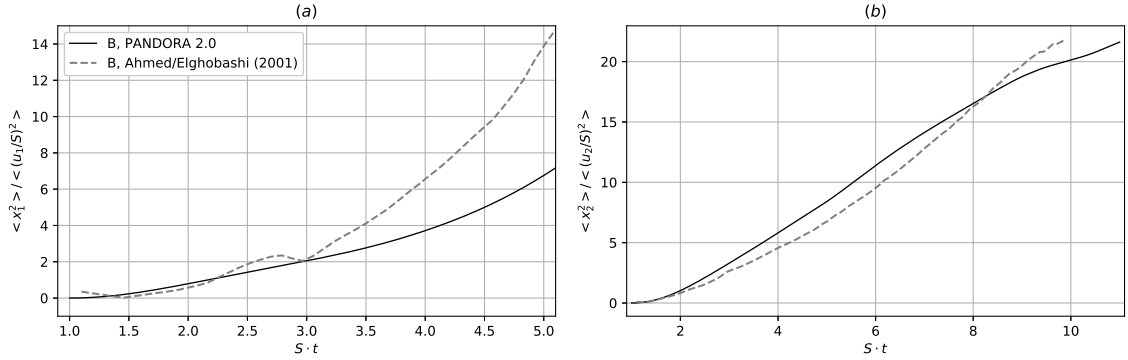

FIGURE 5.46: Same as figure 5.40, but normalised by u_i^2/S^2. Dashed line from Ahmed and Elghobashi [2]

dispersion show a significant deviation between own and published results in streamwise direction, whereas there is an acceptable agreement in spanwise direction.

The diffusivity 5.46 shows opposite trends in streamwise and spanwise directions. While the streamwise diffusivity is smaller in our own simulations compared the published results, the opposite is true for the spanwise diffusivity. The spanwise diffusivity agrees

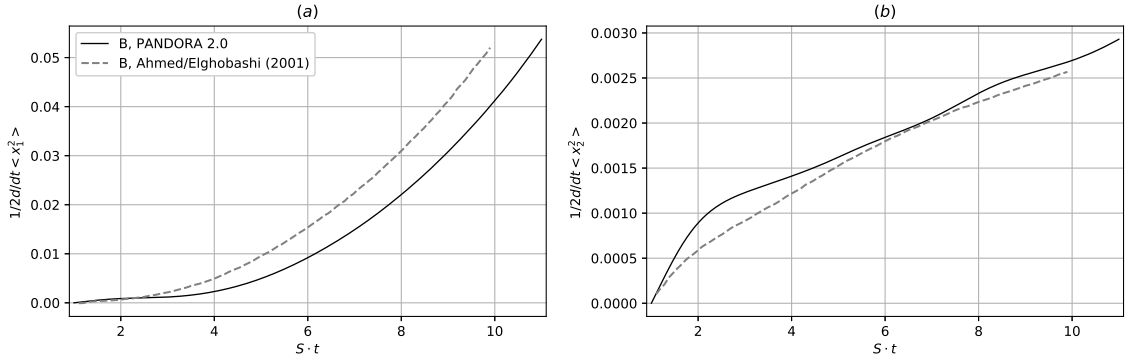

FIGURE 5.47: Diffusivity of $St_\eta = 2.3$ particles in (a) streamwise (b) spanwise direction. Dashed line from Ahmed and Elghobashi [2]

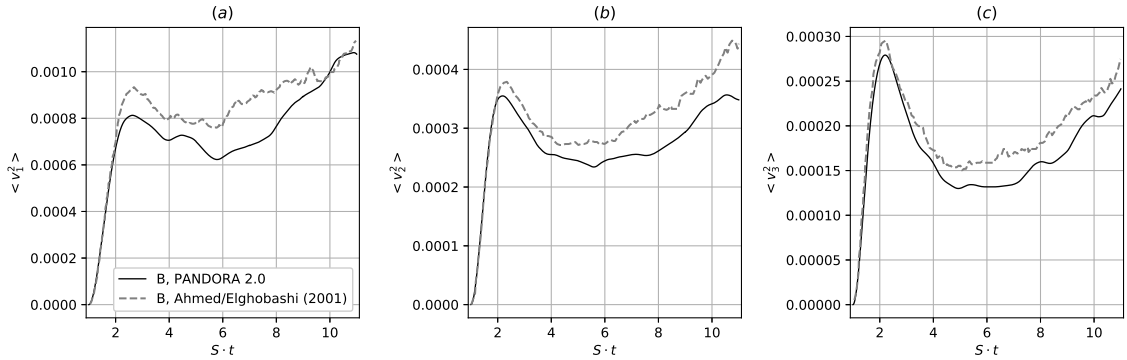

FIGURE 5.48: Relative velocity of $St_\eta = 2.3$ particles in (a) streamwise (b) spanwise (c) shear direction. Dashed line from Ahmed and Elghobashi [2]

better, indicating that differences are mostly related to the shear and less to the small-scale turbulence.

Finally the relative particle-fluid velocity is discussed. As opposed to the $St_k = 0.23$ simulations, for the higher-inertia simulations a qualitative agreement in the temporal development can be found. However, in all directions the relative velocity from our own calculations is still slightly lower compared to the results by Ahmed and Elghobashi [2]. The better overall agreement at higher particle inertia enforces the above argument that differences might be due to sharp gradients at the smallest scales in the published results.

From the above discussion it can be seen that there is good agreement in both fluid and particle simulations compared to published results. Differences can be associated with differences in initial conditions and numerical method. Additionally it has been found that the grid resolution significantly influences the development of energy and dissipation.

Particle case		D	E	F	G
Fluid case		I	I	I	I
Particle diameter	d_p/η	0.015	0.015	0.015	0.015
Particle density	ρ_p/ρ_f	3143	6286	3143	6286
Particle Reynolds number	Re_p	0.0009	0.0009	0.0009	0.0009
Kolmogorov-scale Stokes number	St_η	0.221	0.442	0.221	0.442
Stokes number based on large-eddy turnover time	St_{T_E}	0.038	0.762	0.038	762
Gravity direction		x_1	x_1	x_3	x_3
Settling velocity	v_s/u'	-1.57	-3.14	-1.57	-3.14

TABLE 5.7: Initial conditions at injection time $St = 1$ of the inertial particle simulations with gravity (D, E, F and G).

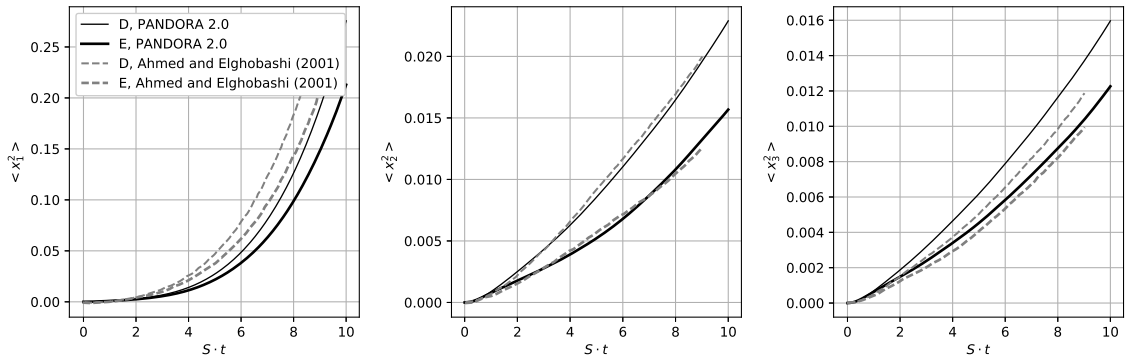

FIGURE 5.49: Dispersion in (a) streamwise (b) spanwise (c) shear direction with gravity in streamwise direction. Dashed line from Ahmed and Elghobashi [2]

5.3.5 Effects of gravity

In this section the effects of gravity are included. The published results by Ahmed and Elghobashi [2] include two simulations, D and E with gravity in streamwise direction and two cases with gravity in shear directions, F and G. An overview of the initial conditions for our corresponding simulations are given in table 5.7. The simulations D and F as well as E and G are identical except for the direction of gravity. The difference between D and E and F and G respectively lies in a different Stokes number. Both increased inertia and gravity effects can be expected at higher Stokes numbers.

The effects of gravity in streamwise direction on the dispersion of particles are shown in figure 5.49. A comparison between the published results and our own simulations show the same relation between the dispersion in different directions. Both the order of magnitude of the results and the Stokes number effects are similar. While there is a good quantitative agreement in spanwise direction, larger differences can be seen in streamwise direction, especially at longer simulation times.

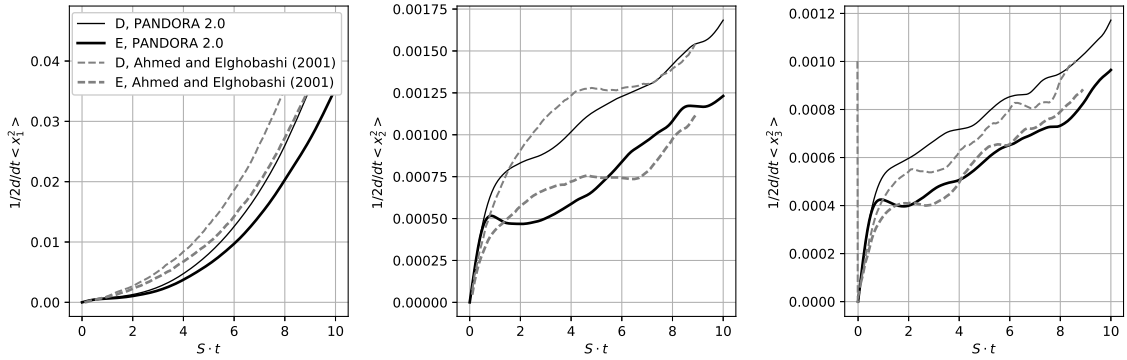

FIGURE 5.50: Diffusivity in (a) streamwise (b) spanwise (c) shear direction with gravity in streamwise direction. Dashed line from Ahmed and Elghobashi [2]

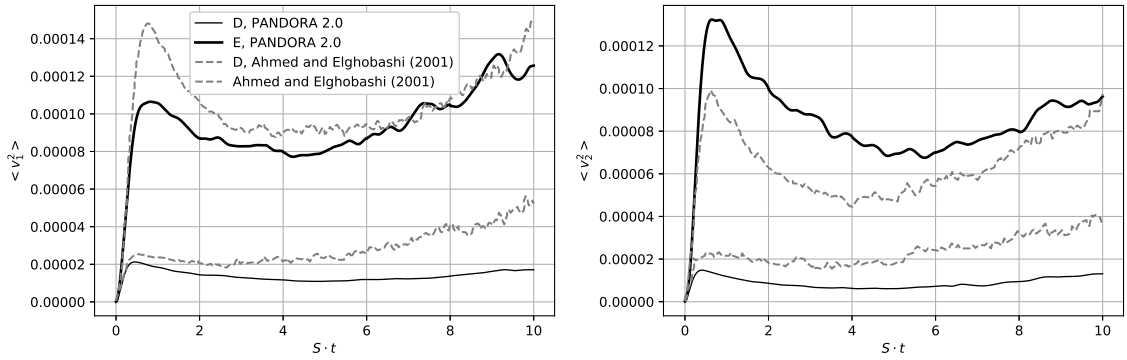

FIGURE 5.51: Relative velocity in (a) streamwise (b) spanwise direction with gravity in streamwise direction. Dashed line from Ahmed and Elghobashi [2]

Similar observations can be made about the diffusivity, shown in figure 5.50. The order of magnitude of the different simulations agrees well, as does the trend. Both from our own simulations and from the published results it can be seen that diffusivity in streamwise direction increases exponentially, whereas in the other directions a sharp increase is followed by a linear increase at a slower rate.

The relative velocities from our own and the published results [2] are in better agreement than for the inertial particles without gravity at lower Stokes numbers.

Gravity in shear direction, shown in figure 5.53, seems to lead to a bigger disagreement between own and published results than in streamwise direction. This can be seen especially for the streamwise and shear components, for both of which the simulations presented here show higher dispersion. However, the orders of magnitude agree as does the overall effect of the Stokes number.

Equivalently to the dispersion, the diffusivity (figure 5.53) in streamwise and shear directions is higher than from the published results. It can also be noted that the diffusivity in streamwise direction shows significant oscillations.

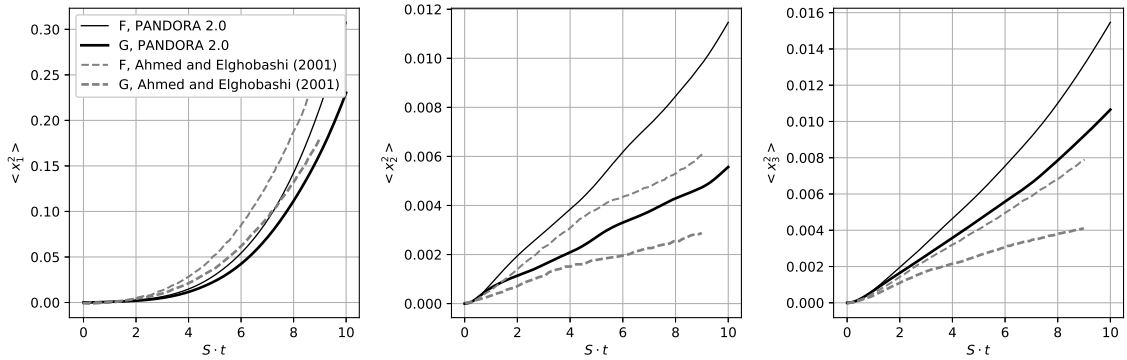

FIGURE 5.52: Dispersion in (a) streamwise (b) spanwise (c) shear direction with gravity in shear direction. Dashed line from Ahmed and Elghobashi [2]

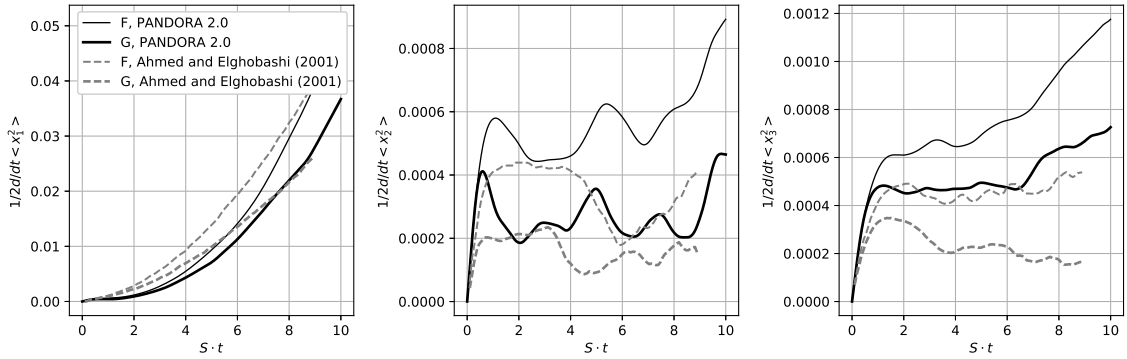

FIGURE 5.53: Diffusivity in (a) streamwise (b) spanwise (c) shear direction with gravity in shear direction. Dashed line from Ahmed and Elghobashi [2]

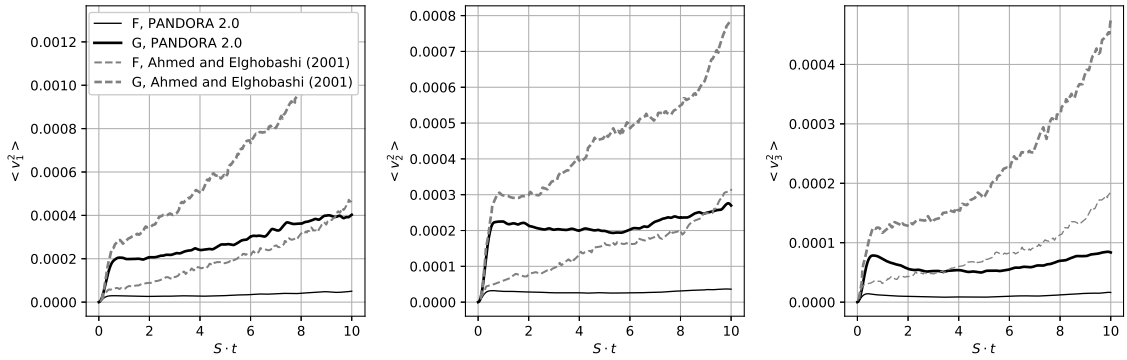

FIGURE 5.54: Relative velocity in (a) streamwise (b) spanwise (c) shear direction with gravity in shear direction. Dashed line from Ahmed and Elghobashi [2]

Finally the relative particle velocity (figure 5.54) shows similar behaviour with gravity in shear direction as it does without gravity. While there is a significant increase in the relative velocity in the published results, the relative velocity from our own simulations stays at a relatively constant level after the initial sharp increase.

5.4 Summary and discussion

The PANDORA 2.0 code has been extended to include simulations of homogeneous turbulence in a moving coordinate system using the Rogallo transform [101]. In order to stay consistent with the existing code for isotropic turbulence this has been done for the Navier-Stokes equation in its rotational form. To the author's knowledge this has not yet been done by other workers, therefore a full derivation of the equation has been given.

Both the isotropic and the Rogallo code have been verified with the decaying Taylor-Green vortex, showing good agreement with the results published by Brachet et al [17]. Except for the highest wave numbers of the spectra, the results of the isotropic and Rogallo formulation are exactly identical. Differences at the highest wave numbers are in the order of rounding errors and to be expected due to the different formulation.

Initial simulations of shear flows show reasonable agreement with published results by Matsumoto et al [77]. Strict verification runs using analytical solutions at the rapid distortion limit should be performed as well as simulations at higher Reynolds numbers with a fully developed inertial range.

Simulations of passive and inertial particles in shear flows have been performed and compared to published results by Ahmed and Elghobashi. While there is good agreement for passive particles, some discrepancies remain for inertial particles, mostly for the relative velocities. These are potentially due to sharp gradients or resolution issues at the smallest scales in the published results, since there is a better agreement in the development of relative velocity and Stokes numbers in our own results, which were also performed at a higher grid resolution.

When gravity is taken into account, the results are similar to those of inertial particles. While the order of magnitude as well as the effect of the Stokes number agrees between own and published results, the quantitative agreement is not always good. This is not necessary an indication of discrepancies in either code, since the simulations with gravity also include far more uncertainties. In particular it can be seen that gravity in shear direction leads to larger differences than gravity in streamwise direction. Here more complex interactions between shear, gravity and turbulent structures can take place. Especially the interaction between dispersion in shear direction and transport by the

mean flow means that even small differences in the settling velocity might already lead to bigger differences in the results.

Chapter 6

Particles in homogeneous shear flows at high Reynolds numbers

While the results of the previous chapter show the successful application of PANDORA 2.0 for dispersion simulations at modest Reynolds numbers, the characteristic Reynolds numbers of the atmospheric boundary layer are significantly higher. Therefore simulations were performed using larger computing domains in order to achieve high-Reynolds number simulations. Part of the simulations were performed on the national supercomputer ARCHER within the EPSRC project 'Dispersion of Small Heavy Particles in Linear Shear Turbulence' (e639).

6.1 Simulation strategy

Simulation were performed starting from the initialisation scheme used by Ahmed and Elghobashi [2]. Initially a decaying turbulence simulation was performed, the initial conditions of which are summarised in table 6.1. The restart file was then used to precompute shear turbulence on a 1536×768^2 grid for a time up to $S \cdot t = 4$. Then particles were introduced at a higher grid resolution of 3072×1536^2. Due to computational limitations, but also with the goal of developing a subgrid model for atmospheric large-eddy simulations in mind, a comparatively brief simulation time from injection time $S \cdot t = 4$ until $S \cdot t = 4.2$ was chosen. The grid sizes and shear rates of these simulations are summarised in tables 6.2 and 6.3. Shear rates range from $S \approx 1$ to $S \approx 5$.

6.2 Fluid statistics

Figures 6.1 to 6.4 show selected fluid statistics for the cases 1, 2, 4 and 6 respectively. For the lowest shear rate cases, 1 and 6, the energy decreases a bit further initially until

Simulation		I1 / A1	I2 / A2	I4	I6
Grid		512×256^2	512×256^2	512×256^2	512×256^2
Taylor Reynolds number	Re_λ	575	1817	3616	287
Peak wave number	k_p/k_{min}	6.0	6.0	3.0	6.0
Turbulent intensity	u'	0.17259	0.54577	0.54447	0.17259
Viscosity	ν	0.00010	0.00010	0.00010	0.00020
Dissipation	ϵ	0.00004	0.00403	0.00101	0.00081
Energy	E	0.04468	0.44680	0.44468	0.04468
Integral length scale	l_{int}	0.41994	0.41994	0.84505	0.41994
Taylor scale	λ	0.33296	0.33296	0.66407	0.33296
Kolmogorov scale	η	0.00706	0.00397	0.00561	0.00998
Large-eddy turnover time	T_E	2.43319	0.76944	1.55205	2.43319

TABLE 6.1: Initial conditions of the initial decaying turbulence simulations.

Simulation		I1	I2	I4	I6
Grid (Fluid simulation)		1536×768^2	1536×768^2	1536×768^2	1536×768^2
Grid (Particle simulation)		3072×1536^2	3072×1536^2	3072×1536^2	3072×1536^2
Shear rate	S	1.070887	4.6263	2.0259	1.00672

TABLE 6.2: Parameters of the shear flow simulations.

Simulation		A1	A1b	A2	A2b
Grid		1024×512^2	2048×1024^2	1024×512^2	2048×512^2

TABLE 6.3: Parameters of the additional computations for cases I1 and I2 at different resolution.

a simulation time of about $S \cdot t = 1$, when it begins the expected exponential increase. At higher shear rates, cases 2 and 4, the energy increase sets in at the beginning of the shear flow simulation. As can be seen from the velocity components, the energy increase takes place mainly in streamwise direction (d) and spanwise direction (e), whereas the velocity component in shear direction (f) shows comparatively little change, although in all simulations it decreases slightly until a simulation time of about $S \cdot t = 3$, before increasing. The simulations reach Reynolds numbers at particle injection time $S \cdot t = 4$ (shown in figures 6.1 to 6.4 (c)) between about 80 and 250. All simulations show good growth in energy and dissipation.

The effect of remeshing is almost not visible in the turbulent energy (a) for the lowest Reynolds number cases, 1 and 6 (figures 6.1 and 6.4), but shows clearly in the other two simulations, especially case 2 (figure 6.2), where energy losses of up to 10% take place. Remeshing effects show much stronger in the dissipation (b).Here, in all cases but the lowest Reynolds number simulation, case 6, significant drops are visible. While this would limit the usefulness of the simulations for, especially high order, fluid statistics, this is expected and acceptable behaviour within the purpose of these simulations, i.e. initialisation of a shear flow simulation for particle dispersion, which then takes places at a higher resolution.

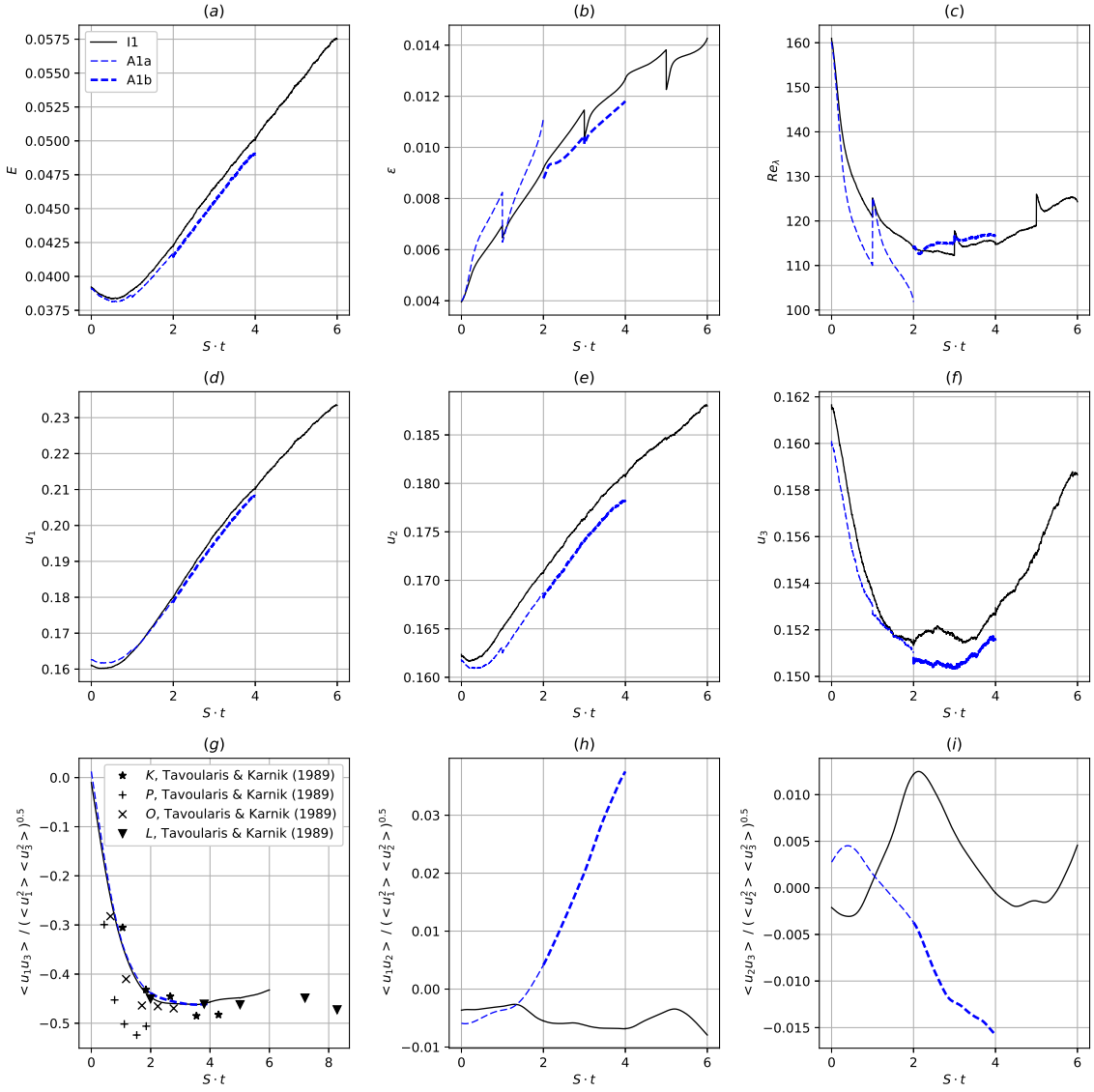

FIGURE 6.1: Fluid statistics for case 1. (a) energy (b) dissipation (c) Taylor-scale Reynolds number (d)-(f) velocity components (g)-(i) normalised shear stress components. Reference data from Tavoularis and Korrsin [117].

For the normalised shear stress (figures 6.1(g) to 6.4(g)) the results are compared with measured reference data from Tavoularis and Korrsin [117]. All simulations show reasonable agreement with the measured shear stresses and converge to a value of about -0.5. The other components of the Reynolds tensor only fluctuate to a comparatively small extent, as is expected.

To assess the quality of the fluid simulation towards the end of each particle simulation, longitudinal spectra (a) are shown in figures 6.5 to 6.8 and compared to measured spectra from Ferchichi and Tavoularis [37]. The energy spectra normalised by the Kolmogorov scales $E_{11}/(\epsilon\nu^5)^{1/4}$ can be used to assess the overall quality of the simulation over the entire spectrum. They show reasonably good agreement with the measured data in the inertial range. Notably the lowest Reynolds number simulation (case 6, figure 6.8) does

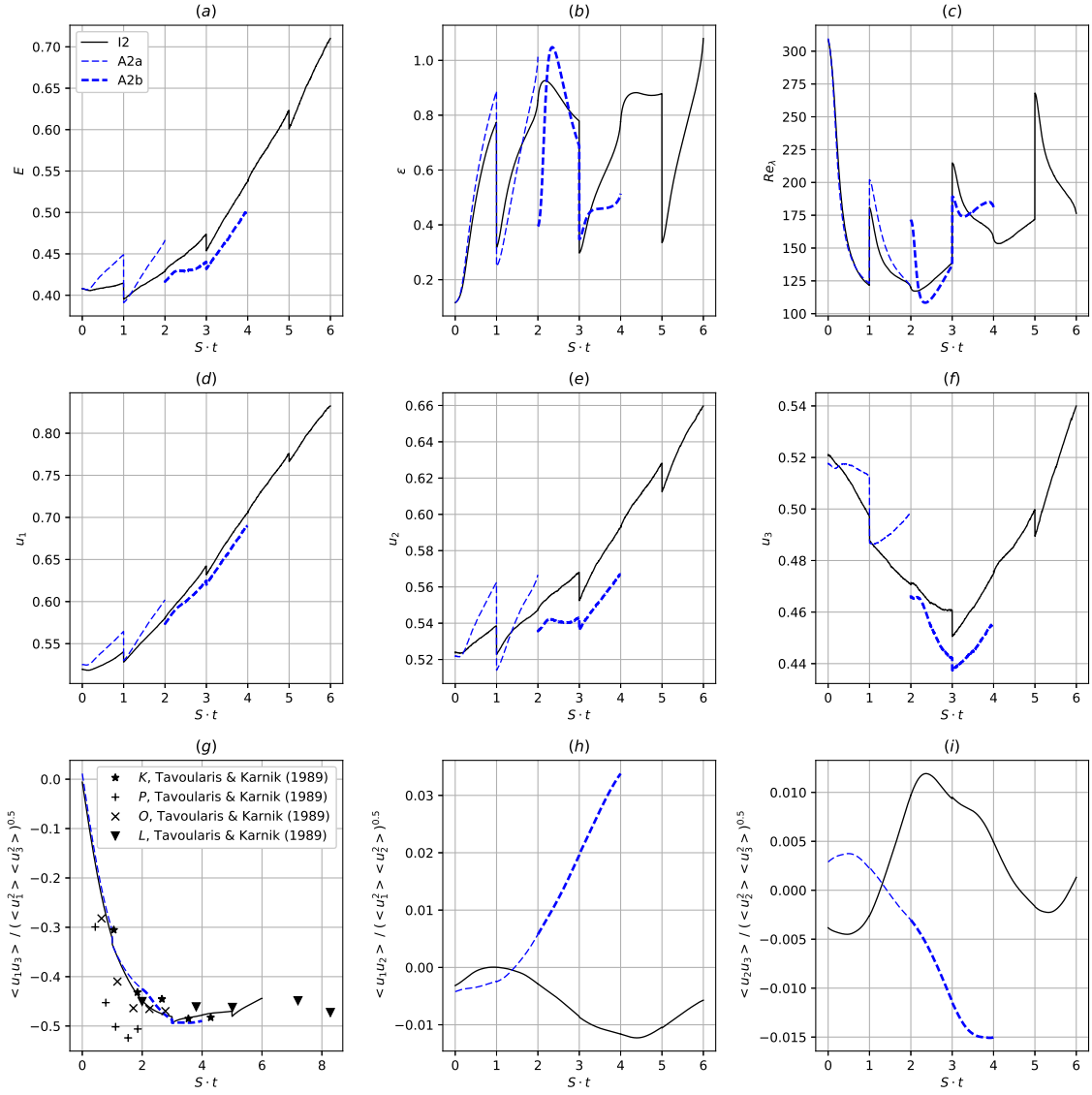

FIGURE 6.2: Fluid statistics for case 2. (a) energy (b) dissipation (c) Taylor-scale Reynolds number (d)-(f) velocity components (g)-(i) normalised shear stress components. Reference data from Tavoularis and Korrsin [117]

not exhibit a fully developed inertial range, whereas the other simulations come closer. The measured spectra represent a broad range of Taylor-scale Reynolds numbers from $Re_\lambda = 170$ to $Re_\lambda = 660$, all of which agree well in the inertial range and into the dissipative range. While the higher Re_λ simulations, i.e. cases 1, 2 and 4, collapse with the measured data at lower wave numbers, a gradual underestimate towards the higher wave numbers can be observed, with a significant drop in the dissipative range.

A more detailed view of the inertial range can be obtained from the compensated spectra $E_{11}/(\epsilon\nu^5)^{1/4}$ (part (b) of the figures). While the spectra show differences to the measured spectra, the inertial range lies within the typical range of the Kolmogorov constant, as is expected [37]. As expected, the Kolmogorov constant is highest for the lowest Reynolds number (case 6, figure 6.8). In figure 6.8 it can be seen yet more clearly that for this

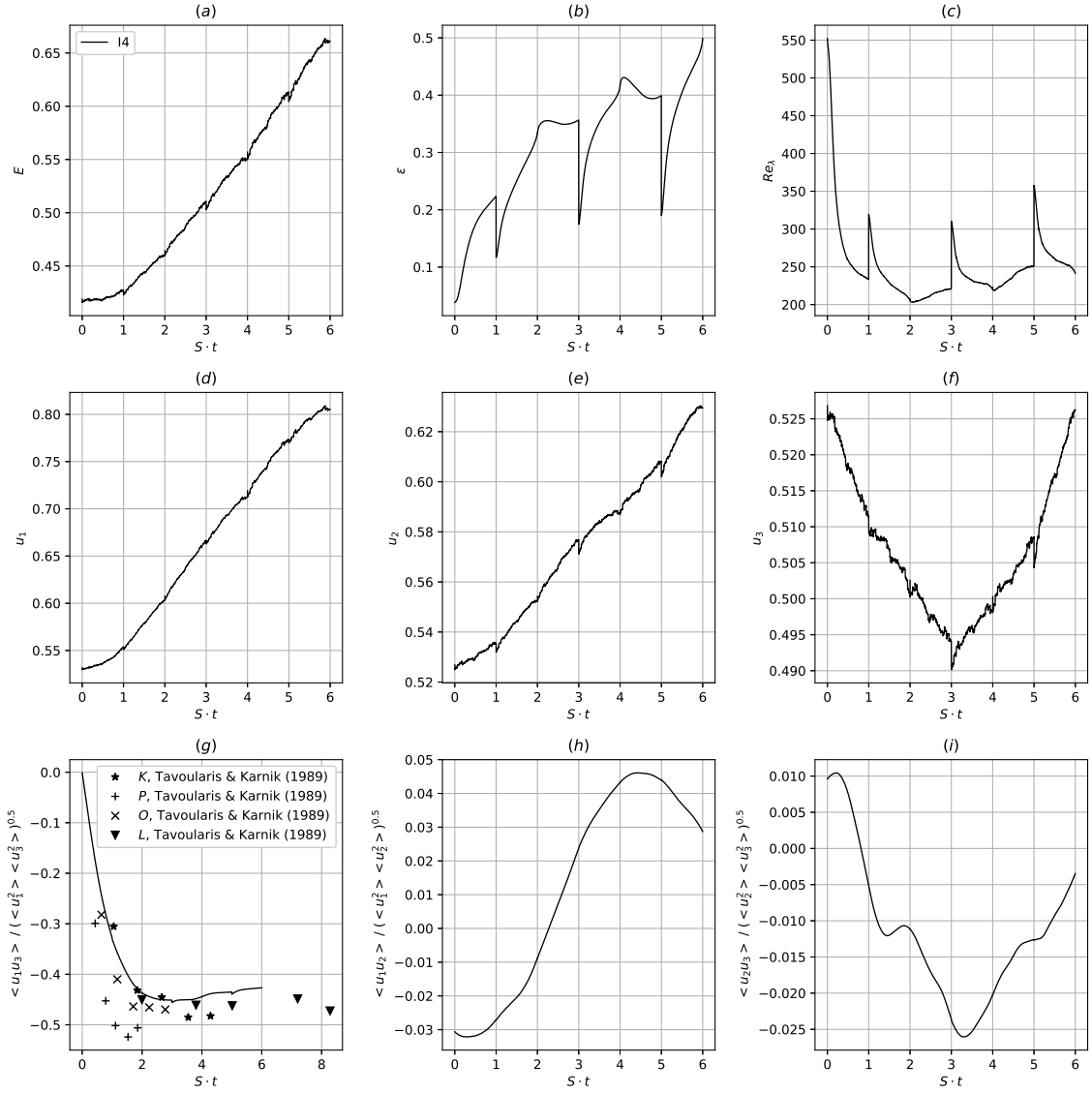

FIGURE 6.3: Fluid statistics for case 4. (a) energy (b) dissipation (c) Taylor-scale Reynolds number (d)-(f) velocity components (g)-(i) normalised shear stress components. Reference data from Tavoularis and Korrsin [117]

case the inertial range is not fully developed. Comparing the compensated spectra, this suggests while there is a computational limit as to which Reynolds numbers can be reached, it is at least possible to obtain spectra with a sufficiently developed inertial range to be considered a turbulent flow.

None of the dissipation spectra $E_{11}/(\epsilon\nu^5)^{1/4}$ are fully developed at higher wave numbers, which is within the expectations given the simulations were performed at the resolution limit. Here again there is a clear distinction between the first three cases at higher Reynolds numbers (cases 1, 2 and 4, figures 6.5 (c), 6.6 (c) and 6.7) and case 6 (figure 6.8 (c)). While for the higher Reynolds-number simulations the peak of the dissipation spectrum is below that of the measured spectra, for case 6 the peak is higher than

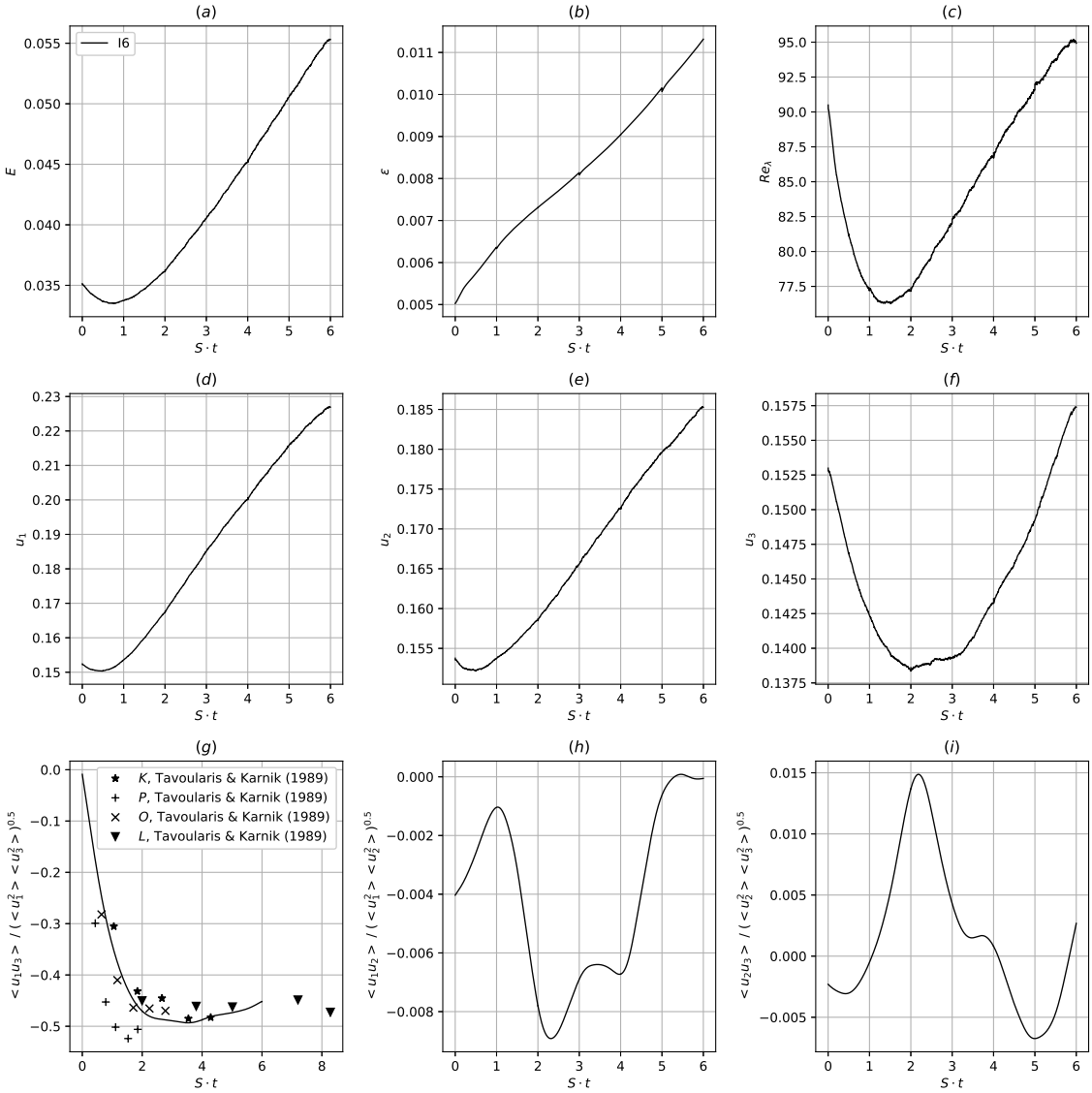

FIGURE 6.4: Fluid statistics for case 6. (a) energy (b) dissipation (c) Taylor-scale Reynolds number (d)-(f) velocity components (g)-(i) normalised shear stress components. Reference data from Tavoularis and Korrsin [117]

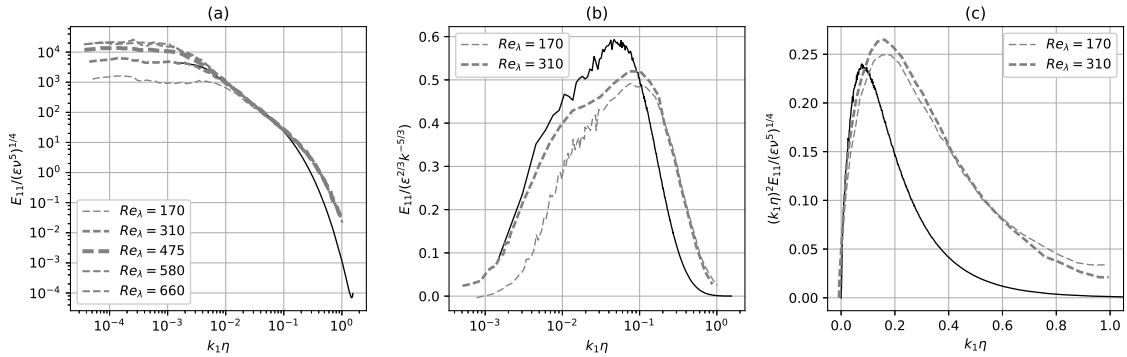

FIGURE 6.5: Longitudinal spectra for case I1p at $S \cdot t \approx 4.197$. (a) Energy spectrum normalised by Kolmogorov scales (b) Compensated energy spectrum (c) Dissipation spectrum. Dashed line: reference data from Ferchichi and Tavoularis [37]

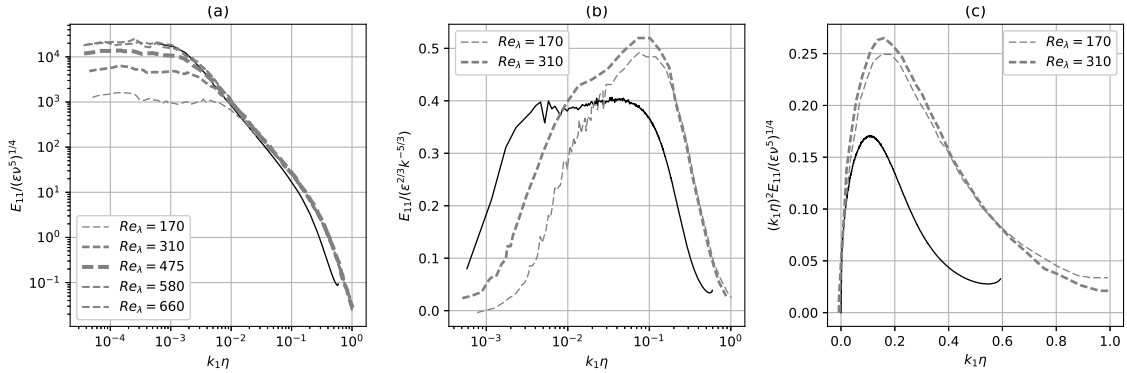

FIGURE 6.6: Longitudinal spectra for case I2p at $S \cdot t \approx 4.197$. (a) Energy spectrum normalised by Kolmogorov scales (b) Compensated energy spectrum (c) Dissipation spectrum. Dashed line: reference data from Ferchichi and Tavoularis [37]

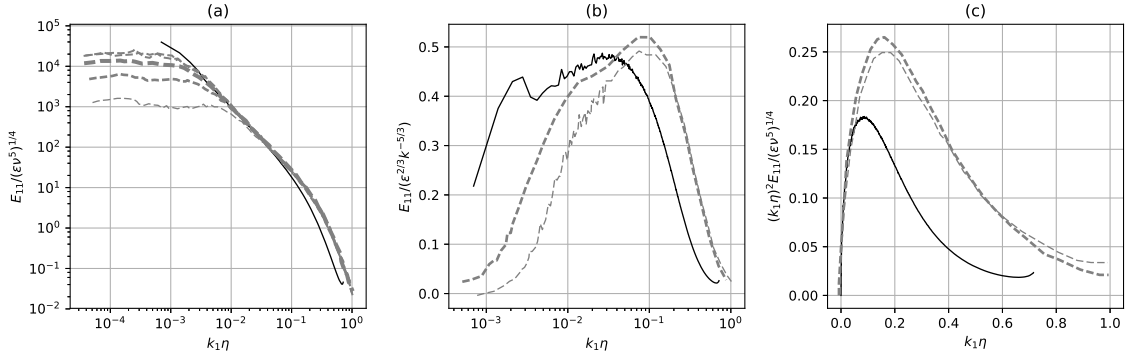

FIGURE 6.7: Longitudinal spectra for case I4p at $S \cdot t \approx 4.197$. (a) Energy spectrum normalised by Kolmogorov scales (b) Compensated energy spectrum (c) Dissipation spectrum. Dashed line: reference data from Ferchichi and Tavoularis [37]

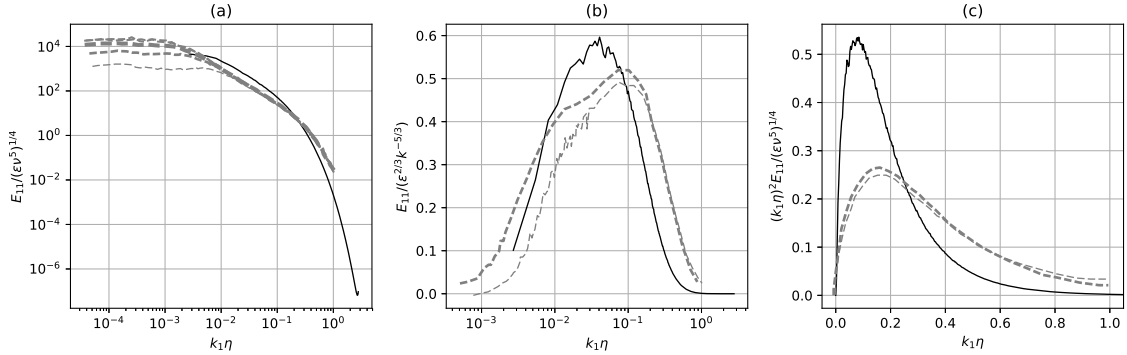

FIGURE 6.8: Longitudinal spectra for case I6p at $S \cdot t \approx 4.197$. (a) Energy spectrum normalised by Kolmogorov scales (b) Compensated energy spectrum (c) Dissipation spectrum. Dashed line: reference data from Ferchichi and Tavoularis [37]

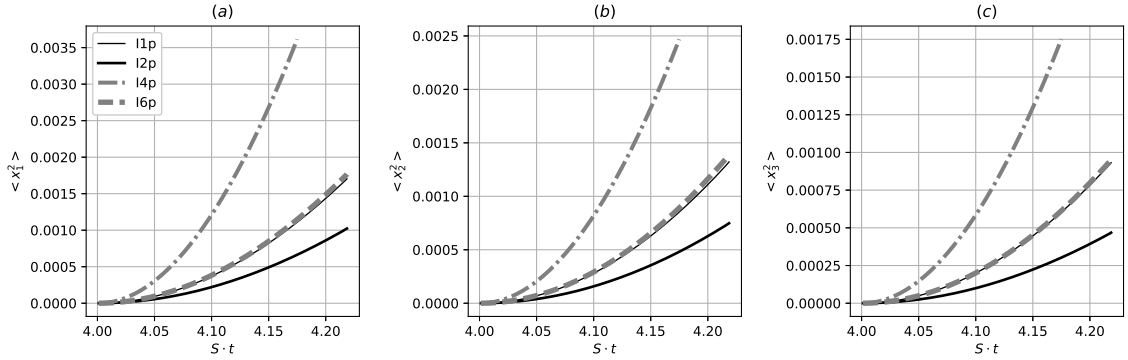

FIGURE 6.9: Dispersion in (a) streamwise (b) spanwise and (c) shear directions.

in the experimental data, suggesting that the flow does not represent fully developed turbulence.

6.3 Dispersion of passive particles

Passive particles were introduced at higher grid resolutions at time $S \cdot t = 4$ for simulations I1, I2, I4 and I6.

The dispersion of the simulations is shown in figure 6.9. All simulations show, as expected, the greatest dispersion in streamwise direction, followed by the spanwise direction. Differences in growth can be explained with the different shear numbers of the simulations. Growth is exponential growth as would be expected for shear flows.

When normalising as introduced in section 5.3.3, all results for the dispersion agree well, including for the shear direction (figure 6.10). This indicates the simulation time is short enough for the dispersion to be dominated by the turbulent velocities. In the context of the goal of this thesis, the investigation of subgrid-scale particle dispersion in atmospheric large-eddy simulations, the effect of turbulence on these scales is what needs to be focused on, since the larger scales are available to the extent that the shear rate is known. These results show that a dependence on the Reynolds number cannot be found, which is an important result for the usefulness of shear flow simulations at lower Reynolds numbers for particle statistics. Due to the significantly lower computational effort needed for the latter, it is useful to know that statistics can be obtained from them, e.g. through the derivation of empirical models or through machine learning.

Figure 6.11 shows the dispersion cross correlation for these simulations. All simulations show a similar development, which is similar to the initial phase of the results shown for particle dispersion in the chapter on validation. Physically the dispersion of particles in shear flows are influenced by both the transport through small-scale turbulence and the mean flow. At this initial stage the dispersion by turbulence is still dominant, which can

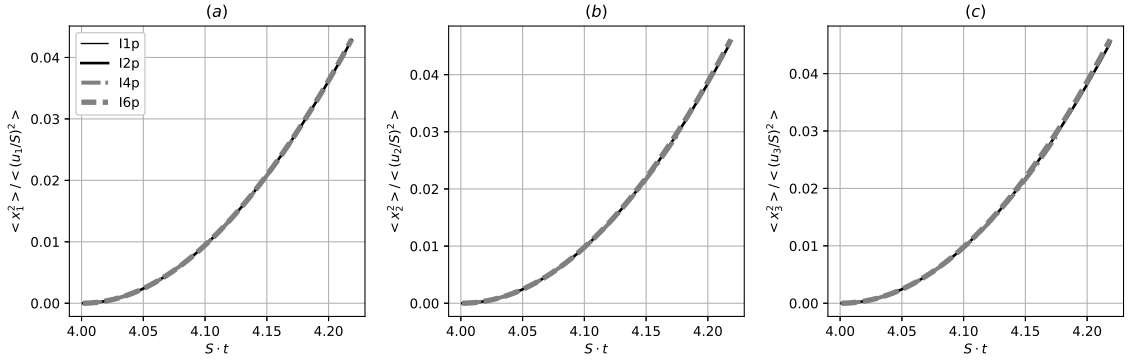

FIGURE 6.10: Normalised dispersion in (a) streamwise (b) spanwise and (c) shear directions.

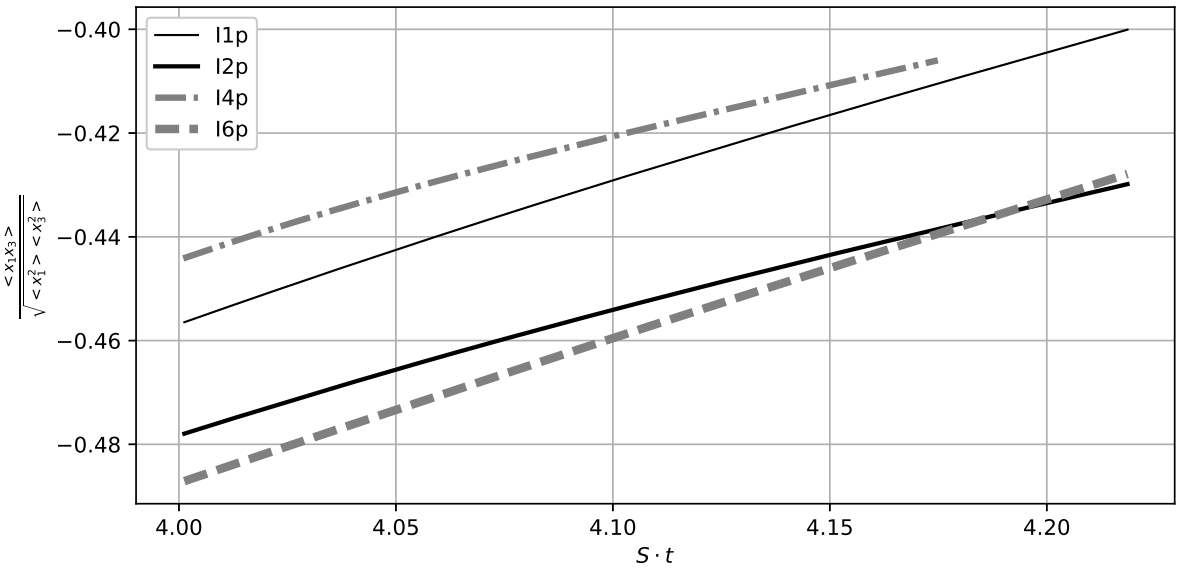

FIGURE 6.11: Dispersion cross correlation for the simulations.

also seen by the fact that the initial values of the dispersion cross correlation correspond to the shear stress at particle injection time.

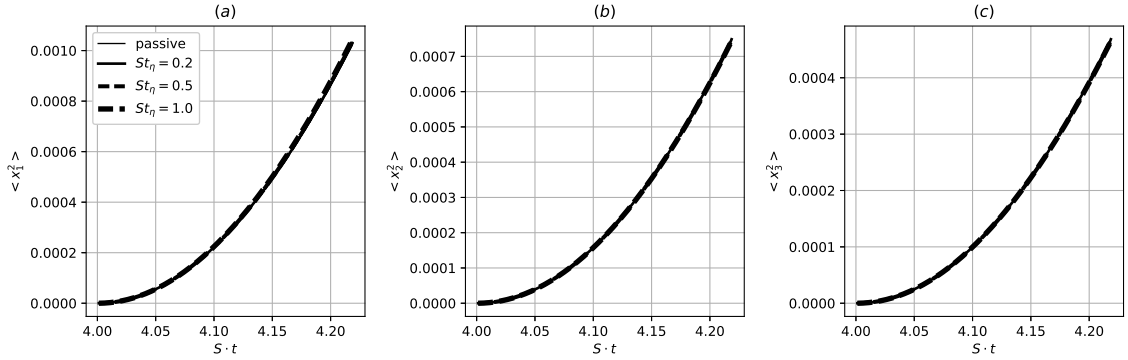

FIGURE 6.12: Dispersion in (a) streamwise (b) spanwise and (c) shear directions for case 2 for passive particles and inertial particles at Kolmogorov-scale Stokes number $St_\eta = 0.2$, $St_\eta = 0.5$ and $St_\eta = 1.0$

6.4 Dispersion of inertial particles

Further simulations for inertial particles at Stokes numbers $St_\eta = 0.2$, $St_\eta = 0.5$ and $St_\eta = 1.0$ have been performed.

A comparison of the dispersion (figure 6.14) shows an agreement between all simulations. However, when computing the ratio between inertial particle dispersion and passive particle dispersion, as shown in figure 6.13, it can be seen that the streamwise dispersion grows faster with increasing Stokes number. For high Stokes numbers this corresponds to the results of Ahmed and Elghobashi [2] for low-Reynolds number flows. On the other hand Ahmed and Elghobashi [2] observed an initially smaller dispersion compared to fluid particles for small Stokes numbers. The results in the validation chapter would indicate that this might be due to fluctuations in the published results, which could be due to the low resolution or the interpolation scheme used for the published simulations. For the spanwise component a very moderately reduced dispersion compared to passive particles can be observed in particular for the highest Stokes number simulation, which agrees with the results of Ahmed and Elghobashi [2]. In shear direction the differences in dispersion are similar to the spanwise direction.

Figure 6.14 shows the dispersion cross correlation for simulation I2. A systematic Stokes number dependence can be seen. With increasing Stokes number the dispersion cross correlation grows more slowly, which is likely due to the inertia reducing acceleration by the mean flow.

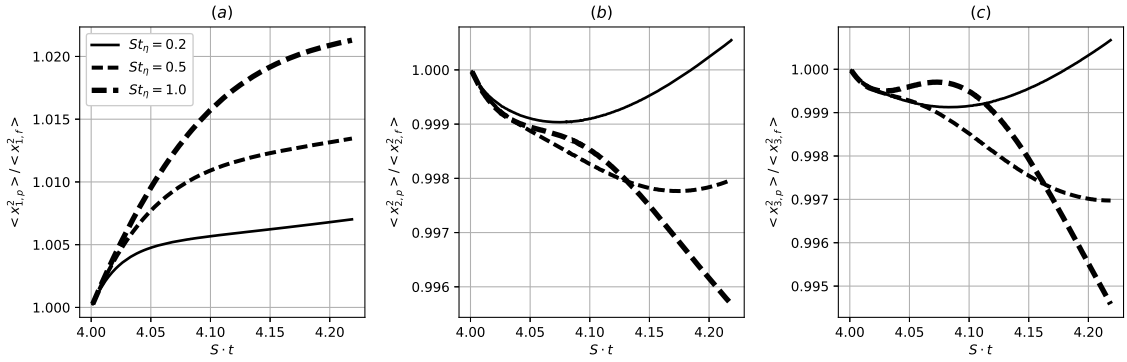

FIGURE 6.13: Normalised dispersion in (a) streamwise (b) spanwise and (c) shear directions for case 2 for passive particles and inertial particles at Kolmogorov-scale Stokes number $St_\eta = 0.2$, $St_\eta = 0.5$ and $St_\eta = 1.0$

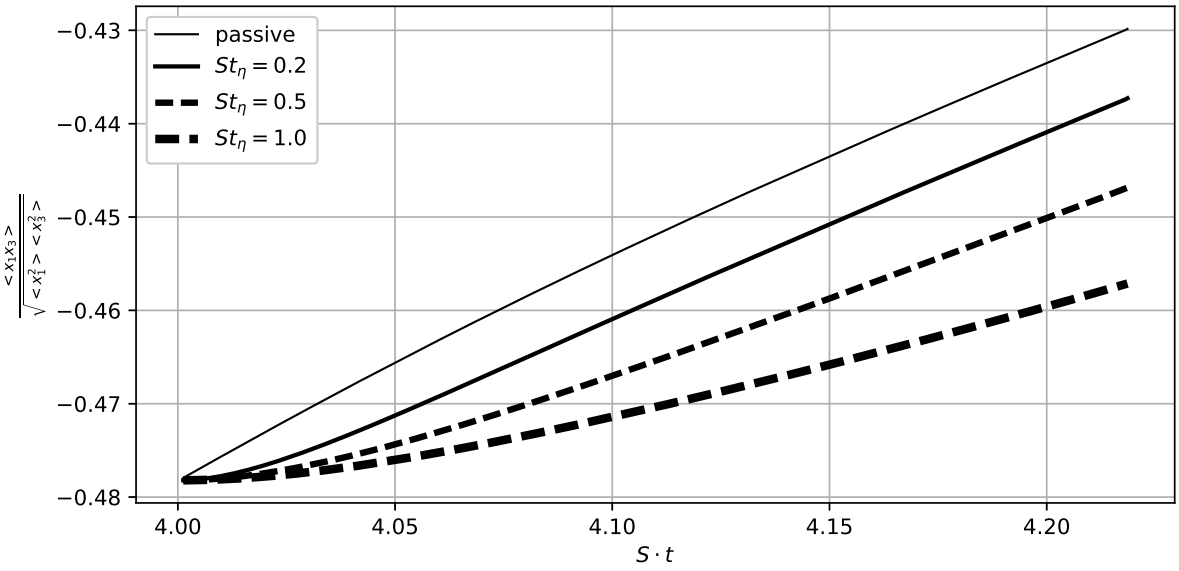

FIGURE 6.14: Dispersion cross correlation for case 2 for passive particles and inertial particles at Kolmogorov-scale Stokes number $St_\eta = 0.2$, $St_\eta = 0.5$ and $St_\eta = 1.0$.

6.5 Summary and discussion

In this chapter homogeneous shear flow simulations at Reynolds numbers between $Re_\lambda \approx 80$ and $Re_\lambda \approx 250$ were discussed. The normalised shear stress from the simulations was compared with measured reference data from Tavoularis and Korrsin [117]. All simulations show reasonable agreement with the measured shear stresses.

Measured spectra from Ferchichi and Tavoularis [37] were used for further validation of the results. The energy spectra show good agreement with the measured data in the inertial range. The lowest Reynolds number simulation does not exhibit a fully developed inertial range, whereas this can be identified in the other simulations. While the higher Re_λ simulations collapse with the measured data at lower wave numbers, a gradual underestimate towards the higher wave numbers can be observed, with a significant drop in the dissipative range.

A comparison of several simulations shows little indication of a Reynolds number dependence of the dispersion of passive particles, which is an important result for the usefulness of shear flow simulations at lower Reynolds numbers for particle statistics. However, from simulations of inertial particles a Stokes number dependence of dispersion even at the comparatively short simulation times used in the simulations could be seen.

Chapter 7

Approximations for the dispersion of particles

In this chapter two different approaches are used to investigate the potential for suitable subgrid models for particle dispersions. The simulations from the chapter on the validation of the PANDORA 2.0 code for particle dispersion (sections 5.3.3, 5.3.4 and 5.3.5) were reproduced using a simple large-eddy approach using a spectral cutoff filter as well as inviscid and viscous rapid distortion theory (as described in section 5.2.6). An emphasis will be put on the latter, as the difference of scales between the grid resolution of typical large-eddy simulations and the scales needed to resolve particle dispersion (see section 2.3.4) makes the application of standard LES approaches difficult and justifies the use of a more complete model.

7.1 Fluid statistics from large-eddy simulations

A simple spectral cutoff filter was implemented to investigate the effects of filtering on fluid and particle statistics. To this end the velocity field for all wavenumbers $k_c > 0.2\,k_{max}$ (further referred to as '0.2') and $k_c > 0.5\,k_{max}$ ('0.5') was set to zero. No subgrid-model was used.

Figure 7.1 shows the energy spectra at times $S \cdot t = 2$ and $S \cdot t = 10$. Using the cutoff at $k_c > 0.5\,k_{max}$, most of the energy spectrum is preserved. At $k_c > 0.2\,k_{max}$ the energy-containing range as well as the lower end of the inertial range are maintained. A numerical artefact at the spectral cutoff can be clearly seen, where the energy increases above the DNS result up to the cutoff wave number. This can be attributed to the incomplete energy transfer in this wavenumber range. At time $S \cdot t = 10$ the lower-resolution simulation also shows some disagreements with the DNS results in the energy-containing range.

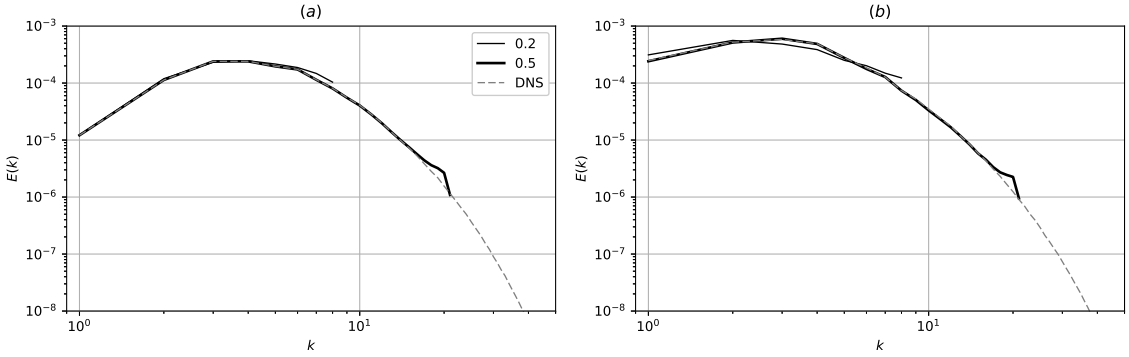

FIGURE 7.1: Energy spectra at (a) $S \cdot t = 2$ and (b) $S \cdot t = 10$ for case I (table 5.4). Dashed line direct numerical simulation, thin line $k_c > 0.2, k_{max}$, thick line $k_c > 0.5, k_{max}$.

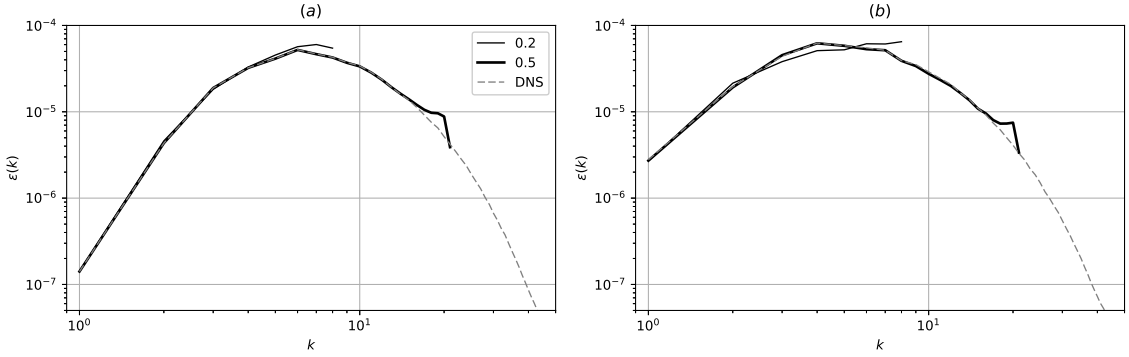

FIGURE 7.2: Dissipation spectra at (a) $S \cdot t = 2$ and (b) $S \cdot t = 10$ for case I (table 5.4). Dashed line direct numerical simulation, thin line $k_c > 0.2, k_{max}$, thick line $k_c > 0.5, k_{max}$.

These effects are yet more prominent in the dissipation spectra (figure 7.2). In particular the increase in dissipation towards the cutoff wavenumber is stronger than the increase in energy.

The energy and dissipation of the simulations for Case I are shown in figure 7.3. As already evident from the spectra discussed above, the energy at a cutoff $k_c > 0.5\,k_{max}$ is only slightly underestimated, whereas at a cutoff $k_c > 0.2\,k_{max}$ significantly more energy is missing. This lack of energy in the higher wave number range shows yet more prominently in the dissipation. Both simulations correctly reproduce the initial loss of energy and later increase, although the lower-resolved simulation underestimates the energy throughout the simulation time. The more complex behaviour of dissipation over time is approximated reasonably well at a cutoff $k_c > 0.5\,k_{max}$. On the other hand when filtering the wavenumbers above $k_c > 0.2\,k_{max}$ the temporal development development changes significantly and more than a third of dissipation is lost compared to the direct numerical simulation.

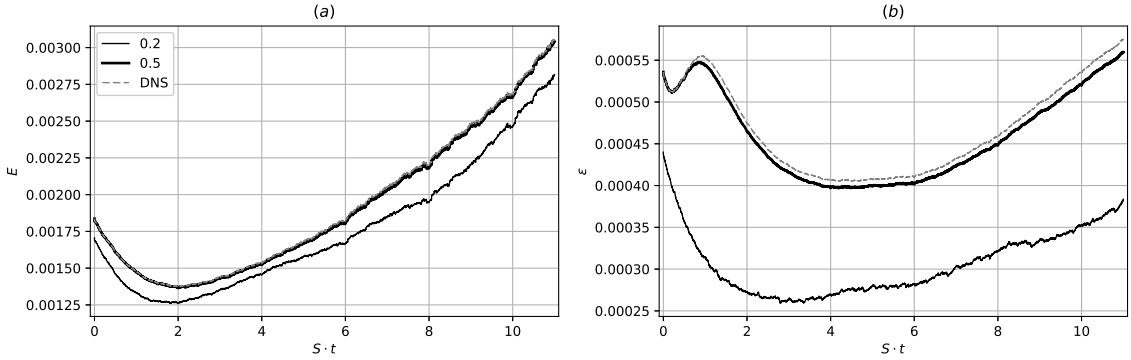

FIGURE 7.3: (a) Energy and (b) dissipation of the simulations for case I (table 5.4). Dashed line direct numerical simulation, thin line $k_c > 0.2, k_{max}$, thick line $k_c > 0.5, k_{max}$.

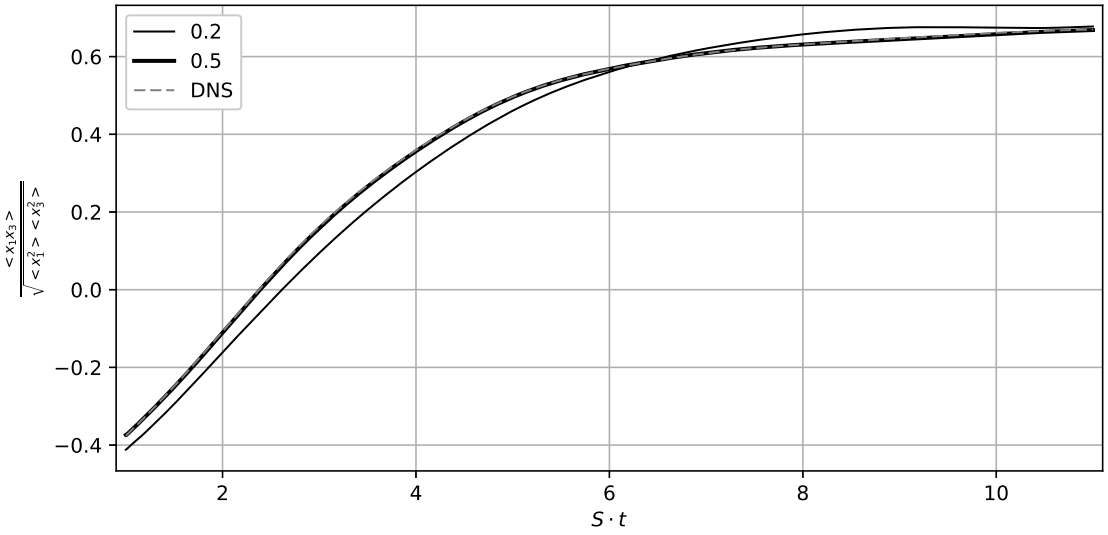

FIGURE 7.4: Dispersion cross correlation for passive particles for passive particles for case I (table 5.6). Dashed line direct numerical simulation, thin line $k_c > 0.2, k_{max}$, thick line $k_c > 0.5, k_{max}$.

7.2 Particle statistics from large-eddy simulations

The dispersion cross correlation is shown in figure 7.4. At a cutoff wavenumber of $k_c > 0.5\, k_{max}$ the dispersion cross correlation is reproduced well. At a lower resolution, the dispersion cross correlation is lower than the DNS results up to a time of about $S \cdot t = 2$ and overpredicted subsequently until converging to the correct value towards the end of the simulation. This indicates that the interaction of turbulent structures and the mean flow in the transport of particles and consequently the spatial distribution of dispersion on the shear plane is not correctly predicted.

The main components of diffusivity are shown in figure 7.5. While the results of the $k_c > 0.5\, k_{max}$ simulations match all components almost exactly, at $k_c > 0.2\, k_{max}$ the results

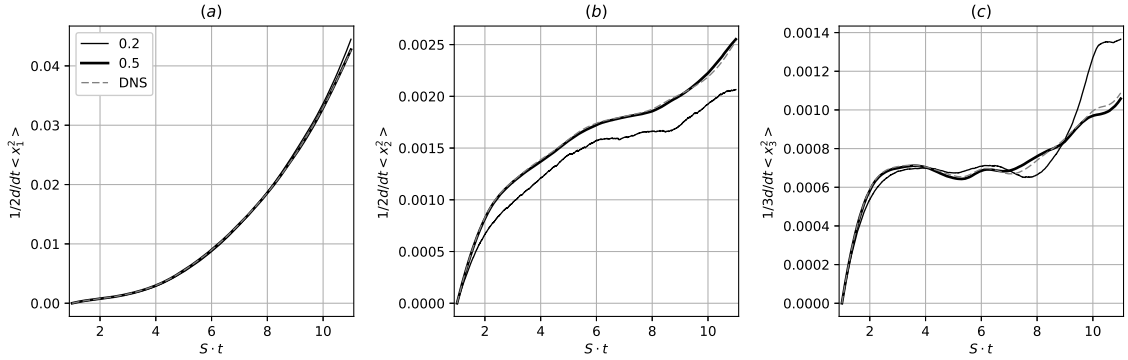

FIGURE 7.5: Diffusivity of passive particles in (a) streamwise (b) spanwise (c) shear direction for passive particles for case I (table 5.6). Dashed line direct numerical simulation, thin line $k_c > 0.2, k_{max}$, thick line $k_c > 0.5, k_{max}$.

show some deviations from direct numerical simulation. The streamwise component, which is dominated by transport through the mean flow, is predicted well, although a slight overestimation can be seen towards the end of the simulation. The diffusivity in spanwise direction is underestimated, indicating an insufficient buildup of and transport by turbulence. The shear component shows stronger fluctuations compared to the direct numerical simulation. A sudden increase can be seen starting at about $S \cdot t = 8$, which might be attributed to acceleration by larger structures that are moderated by smaller-scale turbulence in the higher-resolution simulations.

7.3 Fluid statistics from inviscid and viscous rapid-distortion theory approximations

Both viscous and inviscid rapid-distortion theory have been implemented in PANDORA 2.0. A detailed description is given in section 5.2.6. All simulations from sections 5.3.3, 5.3.4 and 5.3.5 were reproduced using viscous rapid distortion theory ('vRDT') and inviscid rapid distortion theory ('iRDT') using exactly the same grid and input conditions.

All results are shown for the entire simulation time as well as in a closer view for the first part of the simulation from $S \cdot t = 0$ till $S \cdot t = 2$.

The energy and dissipation from case I is shown in figure 7.6. It can be seen that the inviscid rapid distortion theory significantly overestimates both quantities. This is an expected result, as the production of energy by the shear is not balanced by energy loss through the viscous term. When the viscous term is taken into account, the results are far more accurate, especially for shorter times. While viscous rapid distortion theory does not exactly match the DNS results, it stays fairly close. The temporal development of the energy is slightly different compared to the DNS results, with a higher increase in energy between about $S \cdot t = 1$ and $S \cdot t = 7$, at which point it stagnates, whereas the energy from the direct numerical simulation increases further. Dissipation is slightly underestimated by viscous RDT, although the overall agreement is good.

Figure 7.7 shows the energy and dissipation from case II. It can be seen that the agreement is better at a higher shear rate used in this simulation. Inviscid rapid distortion theory overestimates both energy and dissipation, but to a lesser extent. Viscous RDT matches the energy fairly closely up to a simulation time of $S \cdot t = 6$, when the energy stagnates compared to DNS. A similar picture can be seen for dissipation, but the agreement lasts only until about $S \cdot t = 4$.

The velocity components for cases I and II (shown in figures 7.8 and 7.10) are, as can be expected from the energy, reproduced reasonably well by viscous rapid distortion theory with stronger deviations from DNS when neglecting the viscous term. Both inviscid and viscous RDT are qualitatively correct when it comes to the distribution of energy between the different components, where most energy is in the streamwise component and least in shear direction. Inviscid RDT significantly overestimates the streamwise and spanwise velocity components. In shear direction initially the velocity is overestimated, but underestimated from times $S \cdot t = 5$ (case I, figure 7.8) and $S \cdot t = 3$ (case II, figure7.8). Viscous RDT agrees reasonably well with the DNS results for the streamwise velocity. The agreement for the spanwise and shear components is also good for short times up to about $S \cdot t = 2$, but eventually these velocity components are underestimated.

Figures 7.11 (case I) and 7.12 (case II) show the energy spectra at times $S \cdot t = 2$ and $S \cdot t = 10$. Compared to the direct numerical simulations, too much energy is produced

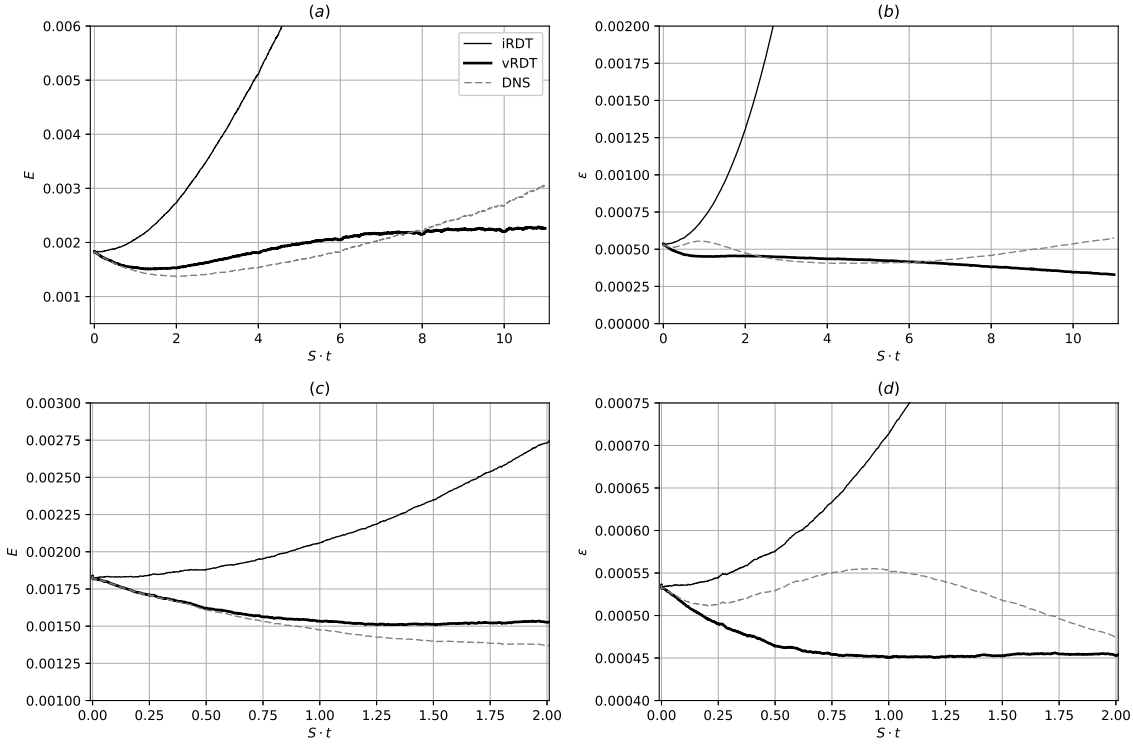

FIGURE 7.6: (a) Energy and (b) dissipation of the simulations for case I (table 5.4) between $S \cdot t = 0$ and $S \cdot t = 10$. (c)(d) same as (a) and (b) between $S \cdot t = 0$ and $S \cdot t = 2$. Dashed line direct numerical simulation, thin line inviscid rapid distortion theory, thick line viscous rapid distortion theory.

at high wavenumbers using the inviscid approximation. The high-wavenumber range is significantly overestimated at $S \cdot t = 10$, while the energy also increases beyond the correct energy in the low-wavenumber range. Including the viscous term results in an underestimation of high-wavenumber energy that is comparable to the application of a spectral filter. The lower wave numbers correspond well to those from direct numerical simulations at both times, although they are slightly underestimated at $S \cdot t = 10$, in particular for the high shear number simulation (case II, figure 7.12).

This can also be seen in the dissipation spectra for cases I and II (figures 7.13 and 7.14). The direct numerical simulation results are reproduced fairly well in the lower wave-number range by viscous rapid distortion theory. The strong energy build-up at high wavenumbers predicted by inviscid rapid distortion theory manifests strongly in the dissipation as well. Similarly, viscous RDT matches the dissipation fairly well, with an appearance comparable to the application of a spectral filter.

An important indicator of the quality of a model are the Reynolds stress components, which are shown in figures 7.15 and 7.16. The Reynolds stress component on the shear plane $< u_1 u_3 > / < u_1^2 u_3^2 >^{0.5}$ is reproduced well by both inviscid and viscous rapid distortion theory for short times, but the shear stress is overestimated at longer simulation

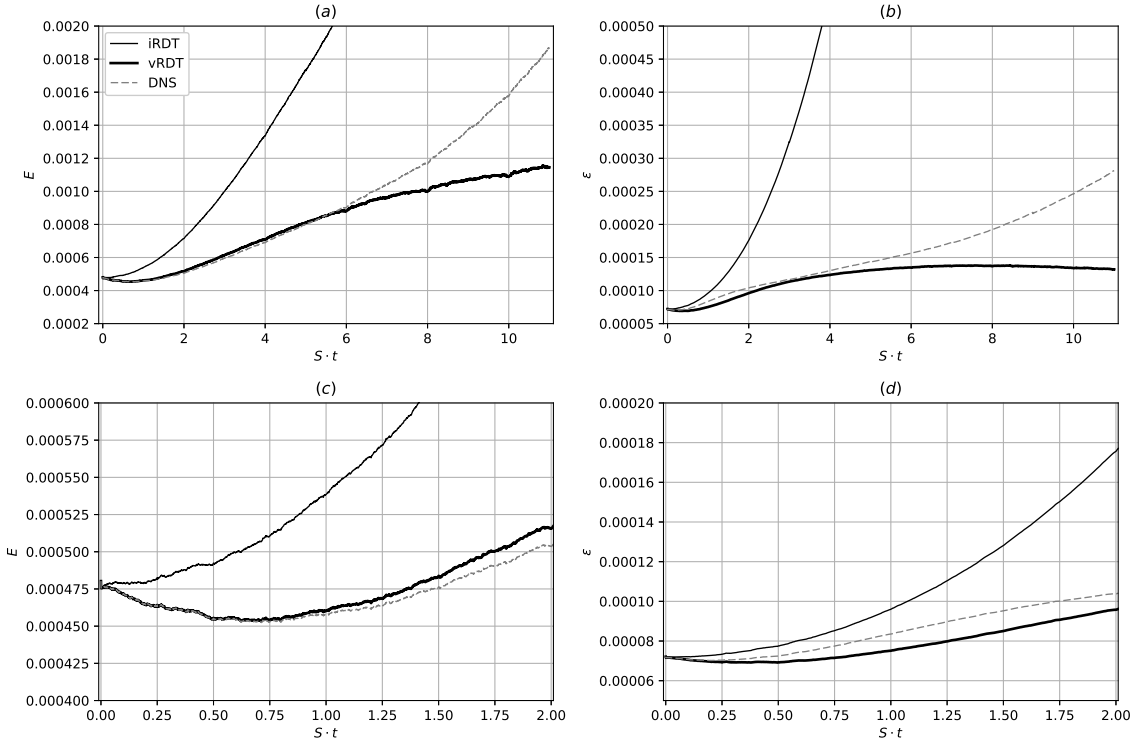

FIGURE 7.7: (a) Energy and (b) dissipation of the simulations for case II (table 5.5) between $S \cdot t = 0$ and $S \cdot t = 10$. (c)(d) same as (a) and (b) between $S \cdot t = 0$ and $S \cdot t = 2$. Dashed line direct numerical simulation, thin line inviscid rapid distortion theory, thick line viscous rapid distortion theory.

times. Shear stresses in other directions stay near the limit of direct numerical simulations for viscous rapid distortion theory, but are significantly larger when the viscous term is neglected. They are however still small compared to the component in shear direction and in this sense still within acceptable limits.

7.4 Particle statistics from inviscid and viscous rapid-distortion theory approximations

7.4.1 Passive particles

Figure 7.17 shows the dispersion cross correlation for passive particles (case I). While both rapid distortion theory implementations show qualitatively the same behaviour as DNS, inclusion of the viscous term leads to better quantitative agreement. Both viscous and inviscid rapid distortion theory underestimate the dispersion cross correlation to some degree, although at larger times from about $S \cdot t = 8$ the viscous RDT result approaches the DNS result again.

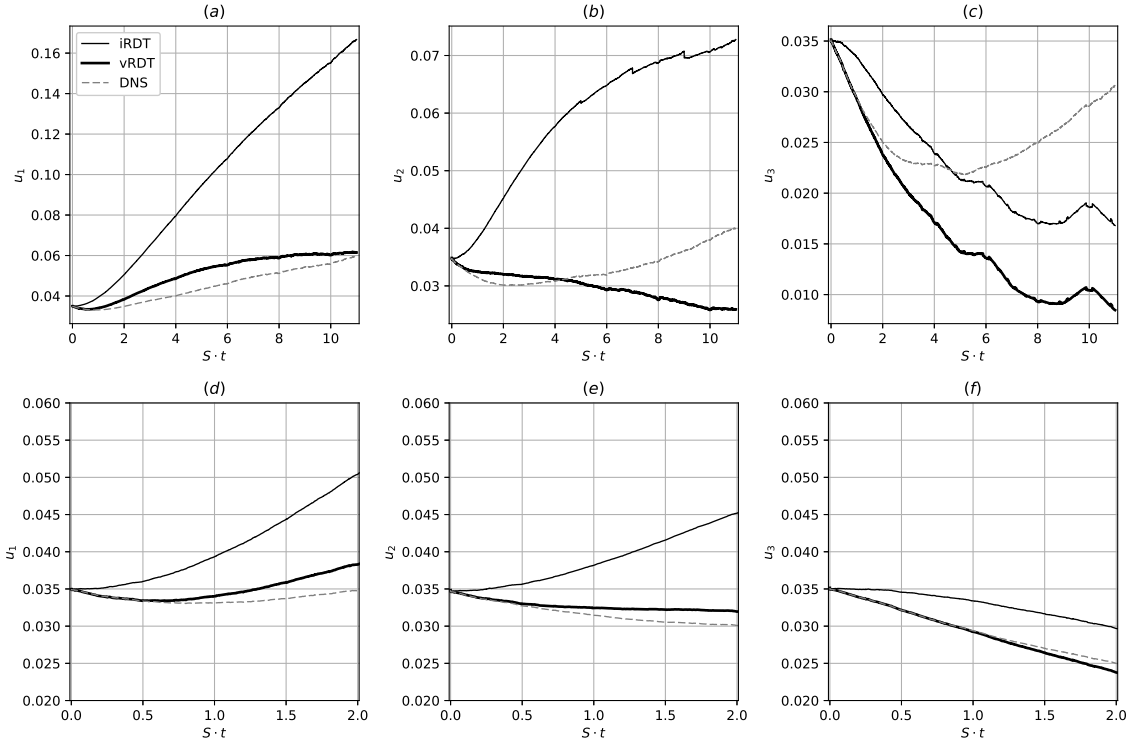

FIGURE 7.8: Velocity components in (a) streamwise (b) spanwise and (c) shear direction for case I (table 5.4) between $S \cdot t = 0$ and $S \cdot t = 10$. (d) to (f) same as (a) to (c) between $S \cdot t = 0$ and $S \cdot t = 2$. Dashed line direct numerical simulation, thin line inviscid rapid distortion theory, thick line viscous rapid distortion theory.

Dispersion (figure 7.18) is overestimated by the inviscid rapid distortion theory at short times, whereas the viscous simulations come reasonably close to the DNS results. For longer time periods rapid distortion theory, both inviscid and viscous, diverges from the dispersion computed using DNS. Viscous rapid distortion theory increasingly underestimates the spanwise and shear components of dispersion, yet agrees reasonably well with the streamwise dispersion component. For inviscid the opposite occurs: while streamwise dispersion is increasingly overestimated, in spanwise and shear directions the agreement is fairly good.

7.4.2 Inertial particles

Inertial particles have been investigated at Stokes numbers $St_\eta = 0.23$ (case A; table 5.6) and $St_\eta = 2.3$ (case B; table 5.6). At low inertia, the results for the dispersion as well as dispersion cross correlation (figures 7.19 and 7.20) show a similar behaviour as for passive particles. Viscous rapid distortion theory comes reasonably close to the DNS results at short times. Compared to passive particles (see figure 7.17) it can be seen that, while the agreement between viscous RDT and DNS is similar for $St_\eta = 0.23$ and passive particles, inviscid rapid distortion theory performs worse for $St_\eta = 0.23$ particles. This

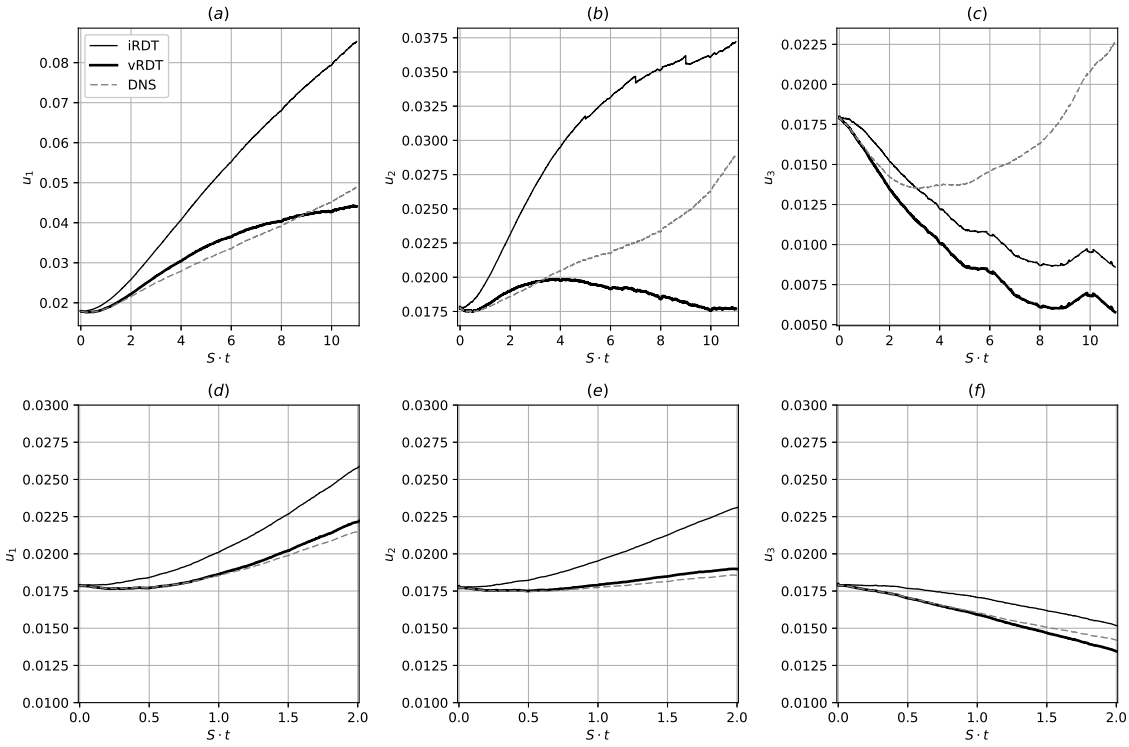

FIGURE 7.9: Velocity components for case II (table 5.5). Dashed line direct numerical simulation, thin line inviscid rapid distortion theory, thick line viscous rapid distortion theory.

FIGURE 7.10: Velocity components in (a) streamwise (b) spanwise and (c) shear direction for case II (table 5.5) between $S \cdot t = 0$ and $S \cdot t = 10$. (d) to (f) same as (a) to (c) between $S \cdot t = 0$ and $S \cdot t = 2$. Dashed line direct numerical simulation, thin line inviscid rapid distortion theory, thick line viscous rapid distortion theory.

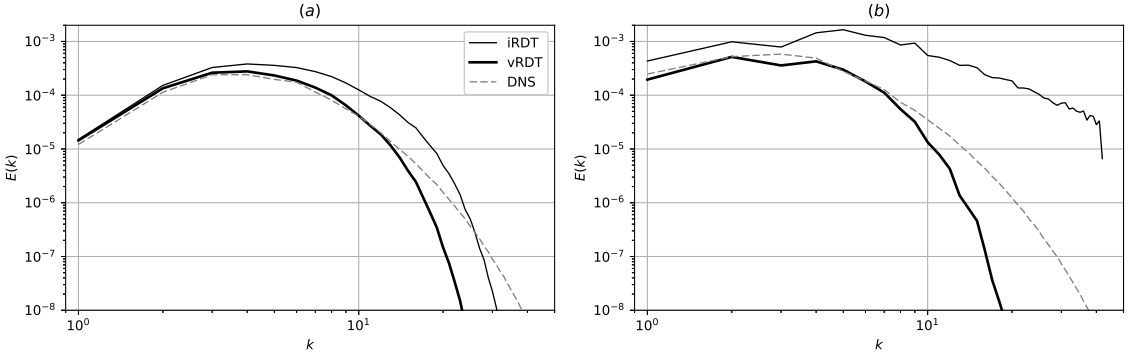

FIGURE 7.11: Energy spectra at (a) $S \cdot t = 2$ and (b) $S \cdot t = 10$ for case I (table 5.4). Dashed line direct numerical simulation, thin line inviscid rapid distortion theory, thick line viscous rapid distortion theory.

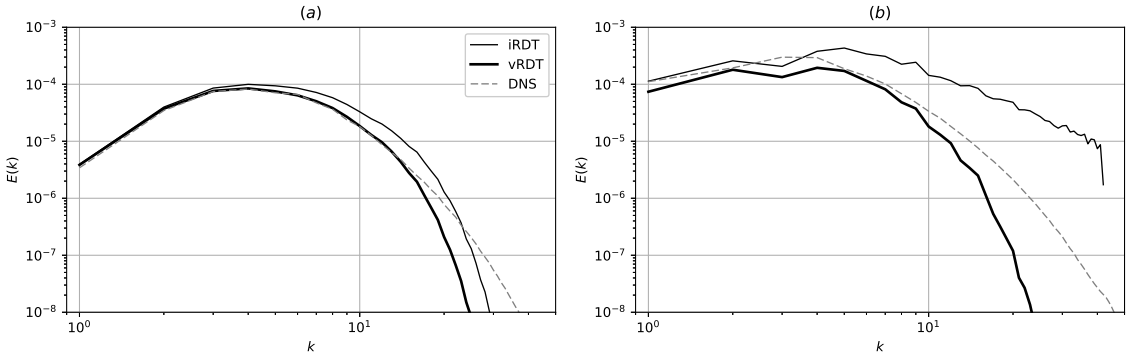

FIGURE 7.12: Energy spectra at (a) $S \cdot t = 2$ and (b) $S \cdot t = 10$ for case II (table 5.5). Dashed line direct numerical simulation, thin line inviscid rapid distortion theory, thick line viscous rapid distortion theory.

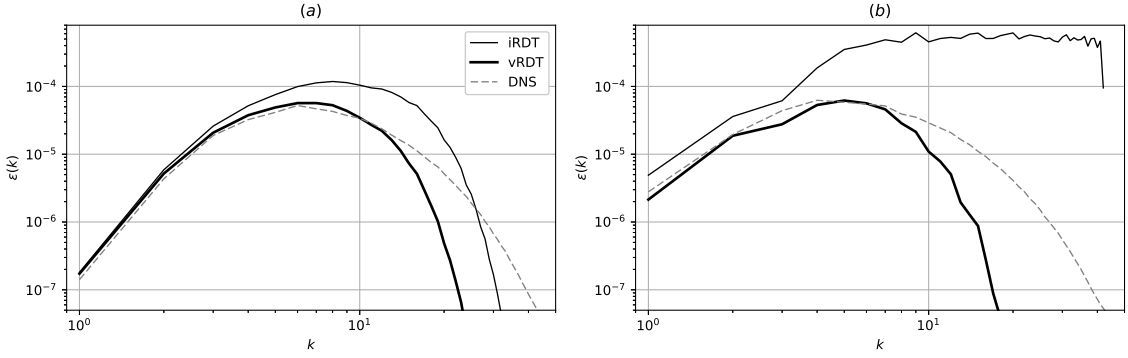

FIGURE 7.13: Dissipation spectra at (a) $S \cdot t = 2$ and (b) $S \cdot t = 10$ for case I (table 5.4). Dashed line direct numerical simulation, thin line inviscid rapid distortion theory, thick line viscous rapid distortion theory.

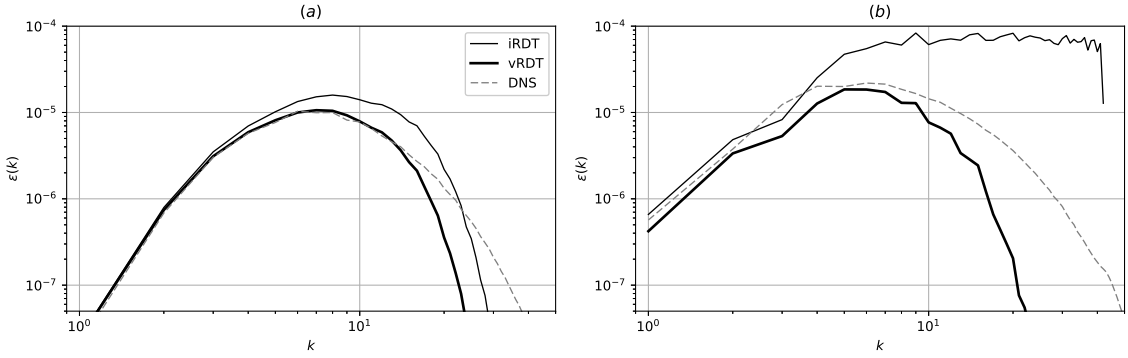

FIGURE 7.14: Dissipation spectra at (a) $S \cdot t = 2$ and (b) $S \cdot t = 10$ for case II (table 5.5). Dashed line direct numerical simulation, thin line inviscid rapid distortion theory, thick line viscous rapid distortion theory.

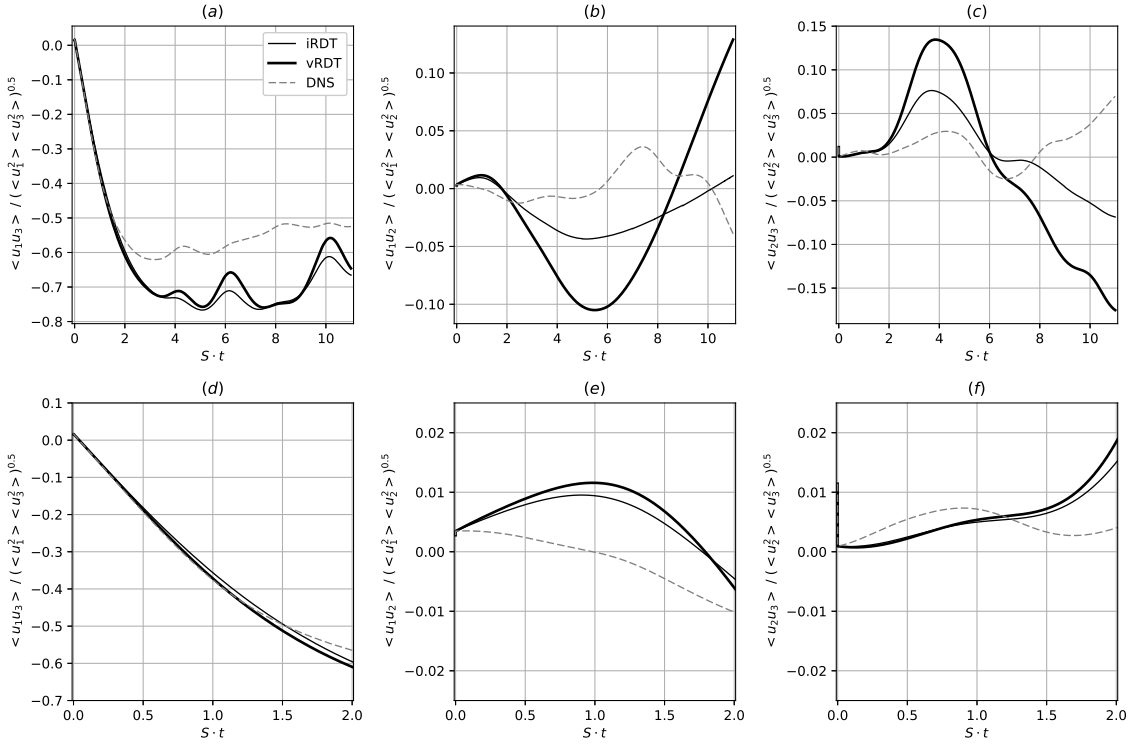

FIGURE 7.15: Reynolds stress components for case I (table 5.4) between $S \cdot t = 0$ and $S \cdot t = 10$. (a) $< u_1u_3 > / < u_1^2u_3^2 >^{0.5}$, (b) $< u_1u_2 > / < u_1^2u_2^2 >^{0.5}$, (c) $< u_2u_3 > / < u_2^2u_3^2 >^{0.5}$. (d) to (f) same as (a) to (c) between $S \cdot t = 0$ and $S \cdot t = 2$. Dashed line direct numerical simulation, thin line inviscid rapid distortion theory, thick line viscous rapid distortion theory.

could be related to the interaction between particle inertia and turbulent structures at the smallest scales, which are significant due the small particle relaxation times.

The results for the dispersion components (figure 7.18) show very little difference to those obtained for passive particles, in particular for viscous RDT. Slight differences can be seen in the inviscid RDT prediction of the spanwise and shear components at longer simulation times.

The inviscid approximation does not show convincing results for the relative particle velocity (figure 7.21). The behaviour of the particle velocity follows closely that of the fluid velocity (figure 7.8) with a significant overestimation of the streamwise and spanwise velocities. The viscous rapid distortion theory are closer to the DNS results than the agreement between own simulations and published results shown in section 5.3.4. This result effectively suggests that the uncertainty from the input conditions and numerical setup could be bigger than the error through neglecting the nonlinear term.

For the higher Stokes number ($St_\eta = 2.3$) simulation, the agreement between both rapid distortion theory implementations and DNS regarding the dispersion cross correlation (figure 7.22) improves slightly, especially at short times. This can be understood by the larger particle relaxation times, which mean that the particle motion is less sensitive to

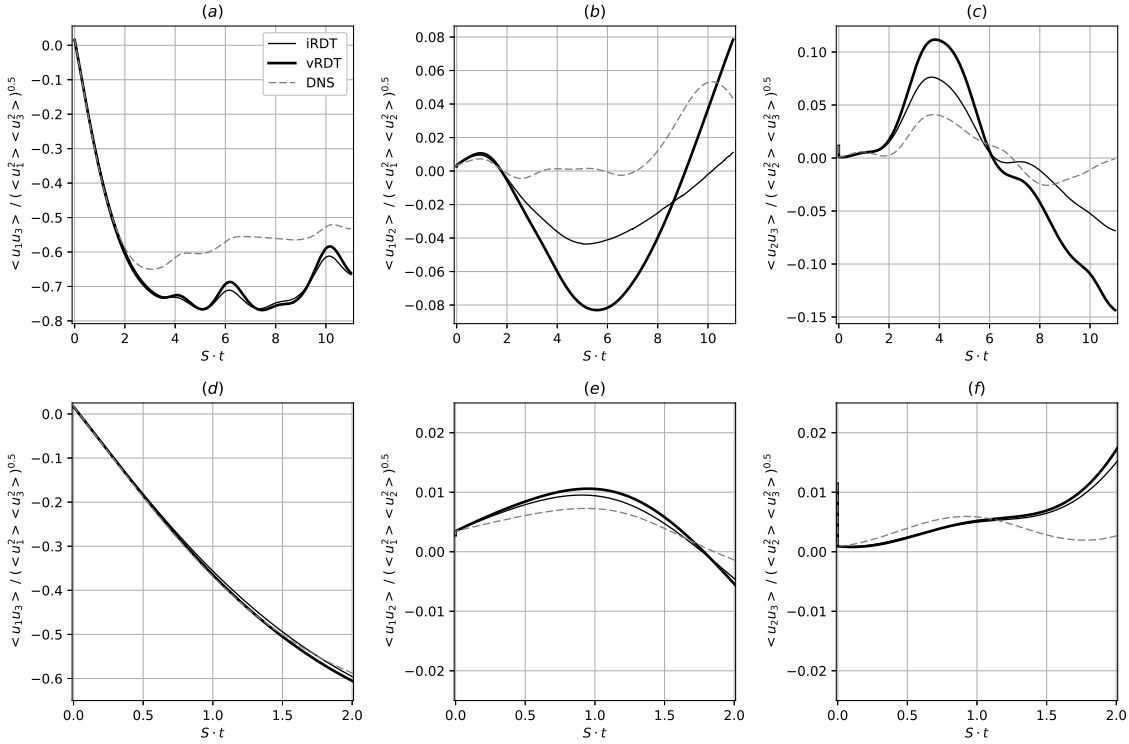

FIGURE 7.16: Reynolds stress components for case II (table 5.5) between $S \cdot t = 0$ and $S \cdot t = 10$. (a) $< u_1u_3 > / < u_1^2u_3^2 >^{0.5}$, (b) $< u_1u_2 > / < u_1^2u_2^2 >^{0.5}$, (c) $< u_2u_3 > / < u_2^2u_3^2 >^{0.5}$. (d) to (f) same as (a) to (c) between $S \cdot t = 0$ and $S \cdot t = 2$. Dashed line direct numerical simulation, thin line inviscid rapid distortion theory, thick line viscous rapid distortion theory.

smaller-scale turbulence that is not available in the flow field (in the case of viscous rapid distortion theory) or overpredicted (in the case of inviscid rapid distortion theory), as can be seen from the energy spectra (figure 7.11).

For the dispersion, shown in figure 7.23, again the viscous rapid distortion theory leads to good agreement with DNS at short times, while neglection of the viscous term leads to an overestimation.

Finally the relative particle velocity at higher Stokes number (figure 7.24) is discussed. The inviscid rapid distortion theory results are in significant disagreement with direct numerical simulation except for the velocity component in shear direction. For the simulations including the viscous term again an agreement not far off the comparison between DNS and published results (section 5.3.4) can be seen.

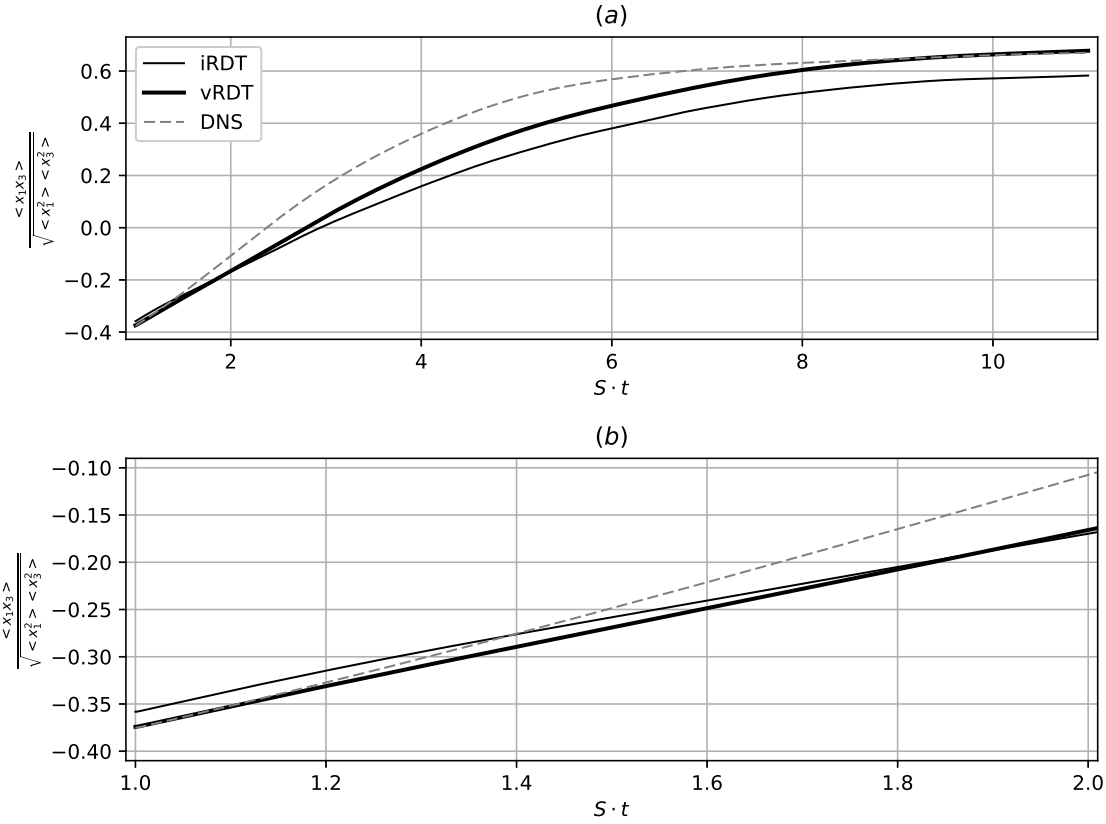

FIGURE 7.17: (a) Dispersion cross correlation for passive particles for case I (table 5.6). (b) same as (a) between $S \cdot t = 0$ and $S \cdot t = 2$. Dashed line direct numerical simulation, thin line inviscid rapid distortion theory, thick line viscous rapid distortion theory.

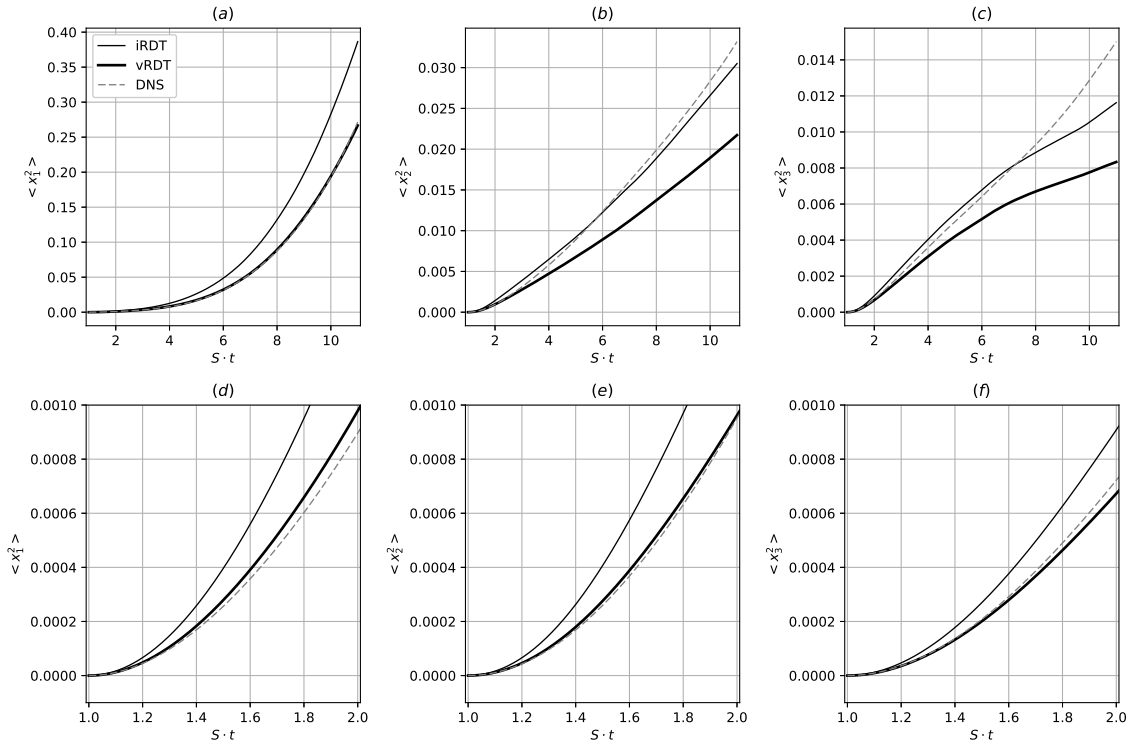

FIGURE 7.18: (a) Streamwise dispersion (b) spanwise dispersion and (c) dispersion in shear direction for passive particles for case I (table 5.6) between $S \cdot t = 0$ and $S \cdot t = 10$. (d) to (f) same as (a) to (c) between $S \cdot t = 0$ and $S \cdot t = 2$. Dashed line direct numerical simulation, thin line inviscid rapid distortion theory, thick line viscous rapid distortion theory.

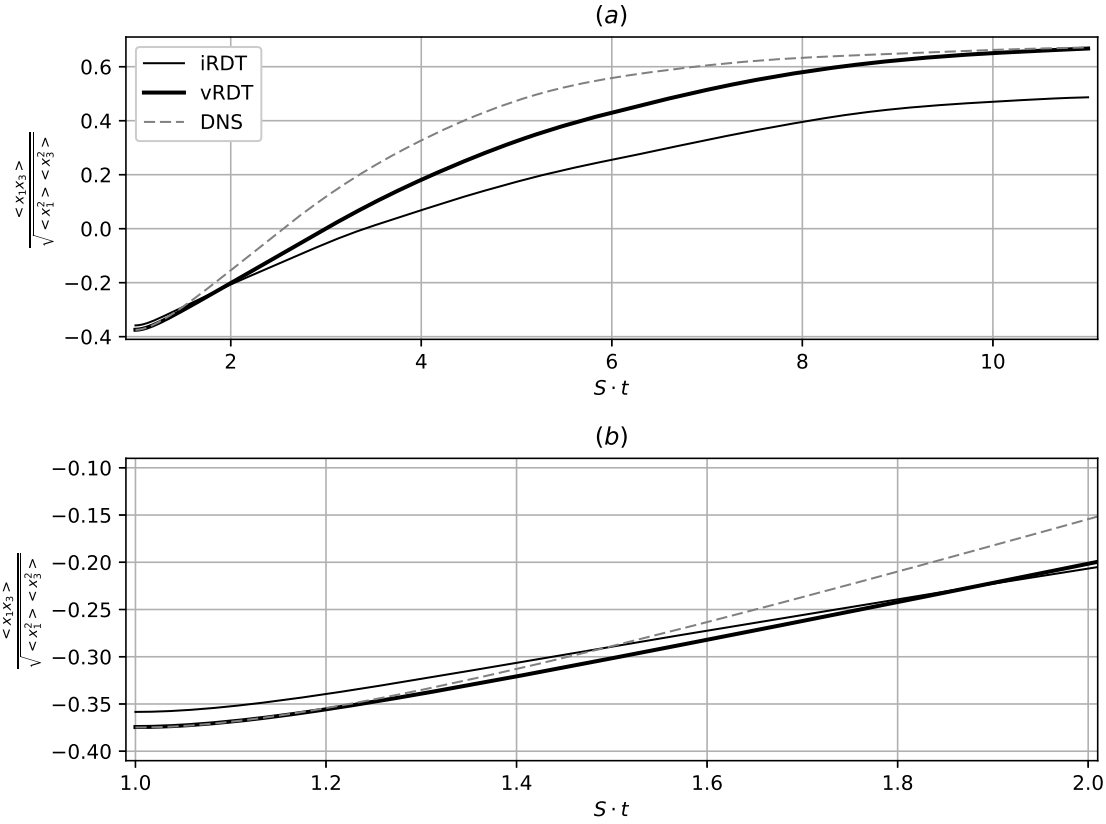

FIGURE 7.19: (a) Dispersion cross correlation of $St_\eta = 0.23$ particles (case A; table 5.6) between $S \cdot t = 0$ and $S \cdot t = 10$. (b) same as (a) between $S \cdot t = 0$ and $S \cdot t = 2$. Dashed line direct numerical simulation, thin line inviscid rapid distortion theory, thick line viscous rapid distortion theory.

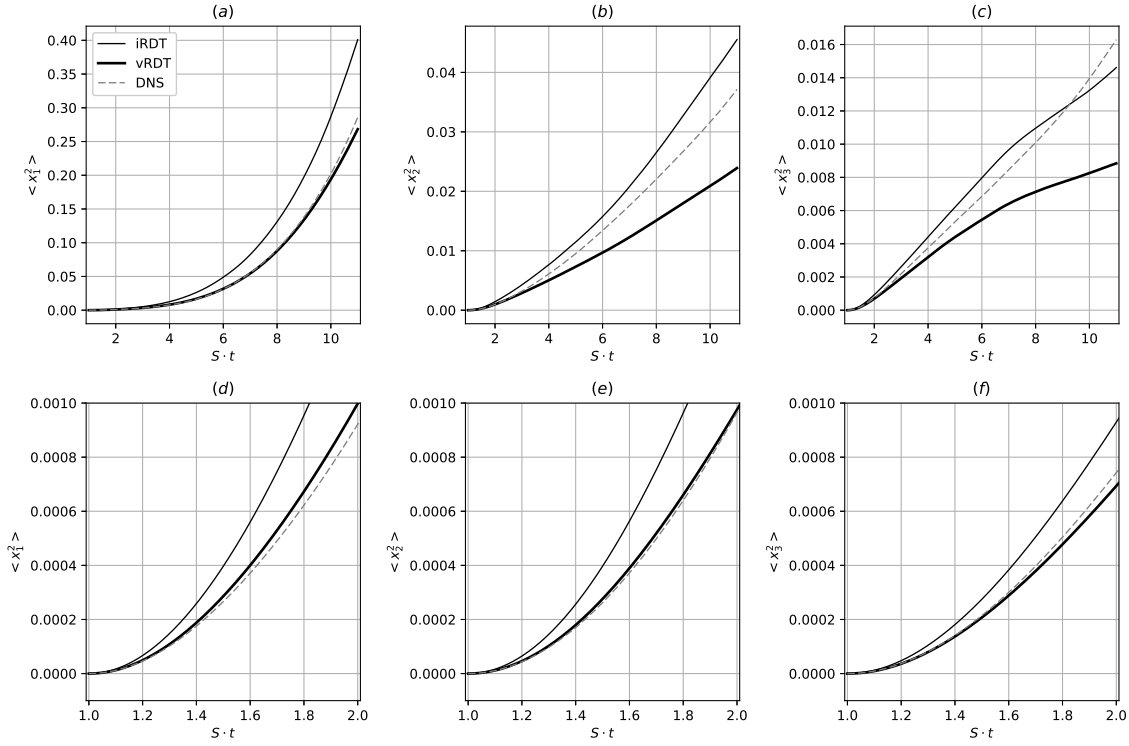

FIGURE 7.20: Dispersion of $St_\eta = 0.23$ particles in (a) streamwise (b) spanwise (c) shear direction (case A; table 5.6) between $S \cdot t = 0$ and $S \cdot t = 10$. (d) to (f) same as (a) to (c) between $S \cdot t = 0$ and $S \cdot t = 2$. Dashed line direct numerical simulation, thin line inviscid rapid distortion theory, thick line viscous rapid distortion theory.

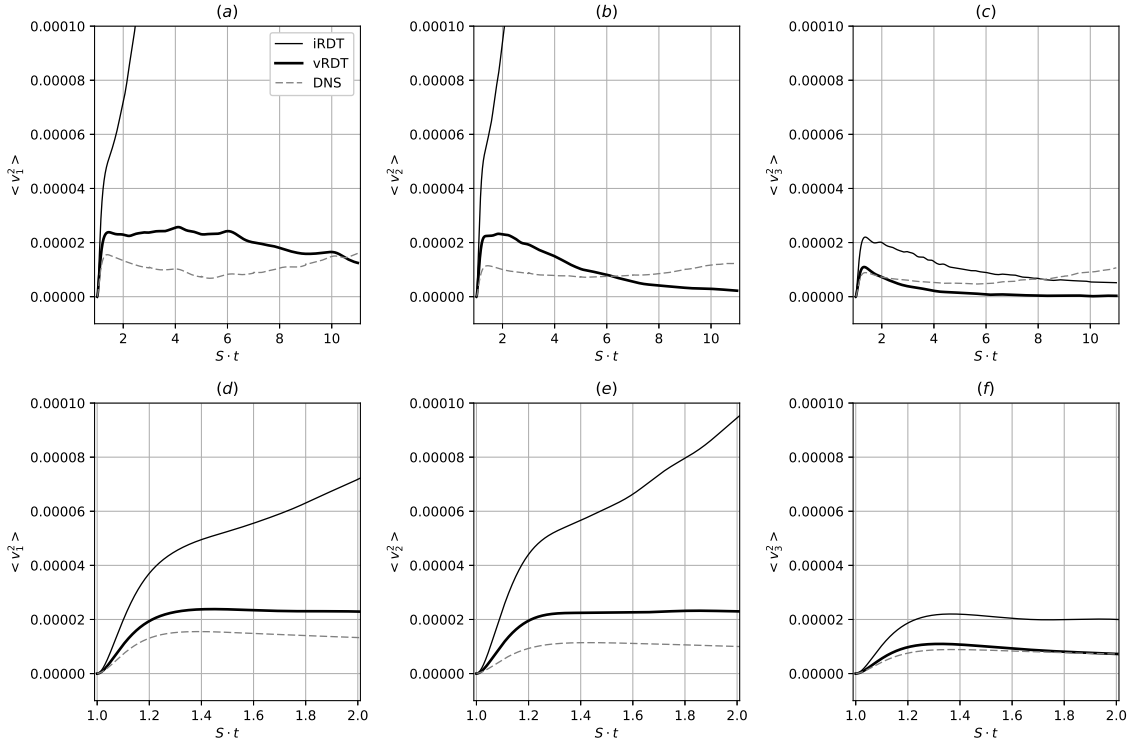

FIGURE 7.21: Relative velocity of $St_\eta = 0.23$ particles in (a) streamwise (b) spanwise (c) shear direction (case A; table 5.6) between $S \cdot t = 0$ and $S \cdot t = 10$. (d) to (f) same as (a) to (c) between $S \cdot t = 0$ and $S \cdot t = 2$. Dashed line direct numerical simulation, thin line inviscid rapid distortion theory, thick line viscous rapid distortion theory.

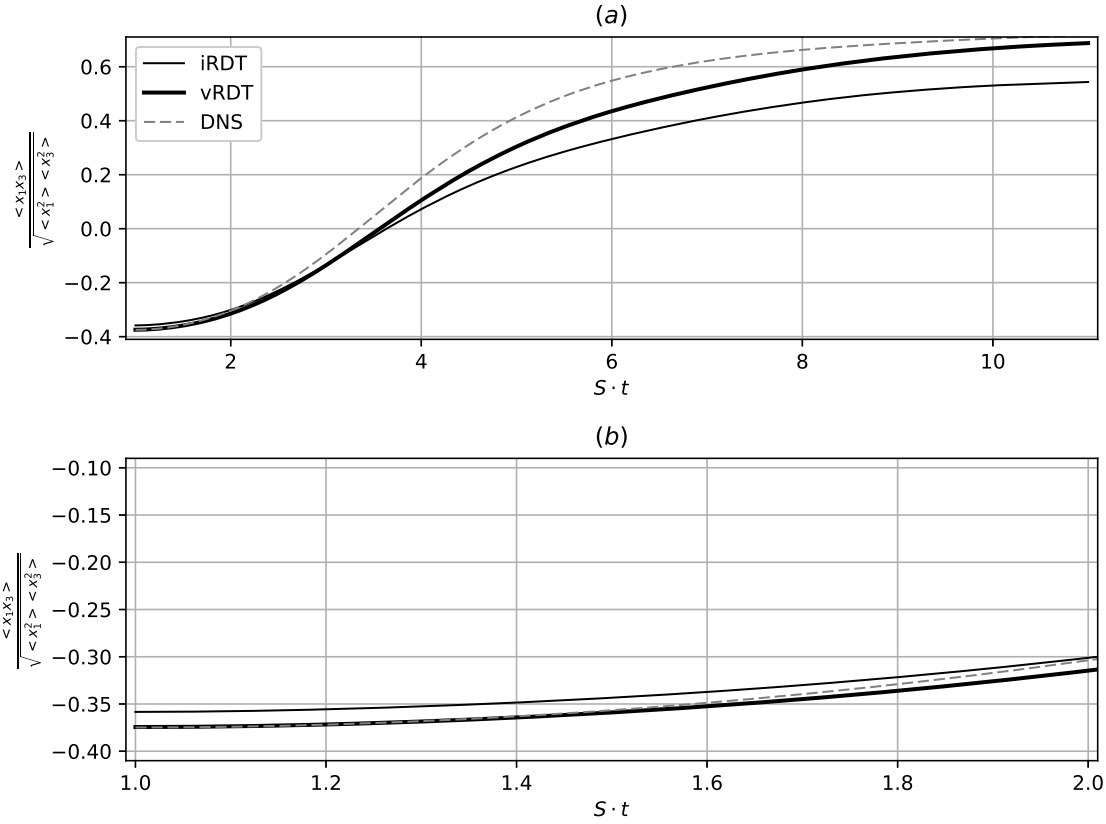

FIGURE 7.22: (a) Dispersion cross correlation of $St_\eta = 2.3$ particles (case B; table 5.6) between $S \cdot t = 0$ and $S \cdot t = 10$. (b) same as (a) between $S \cdot t = 0$ and $S \cdot t = 2$. Dashed line direct numerical simulation, thin line inviscid rapid distortion theory, thick line viscous rapid distortion theory.

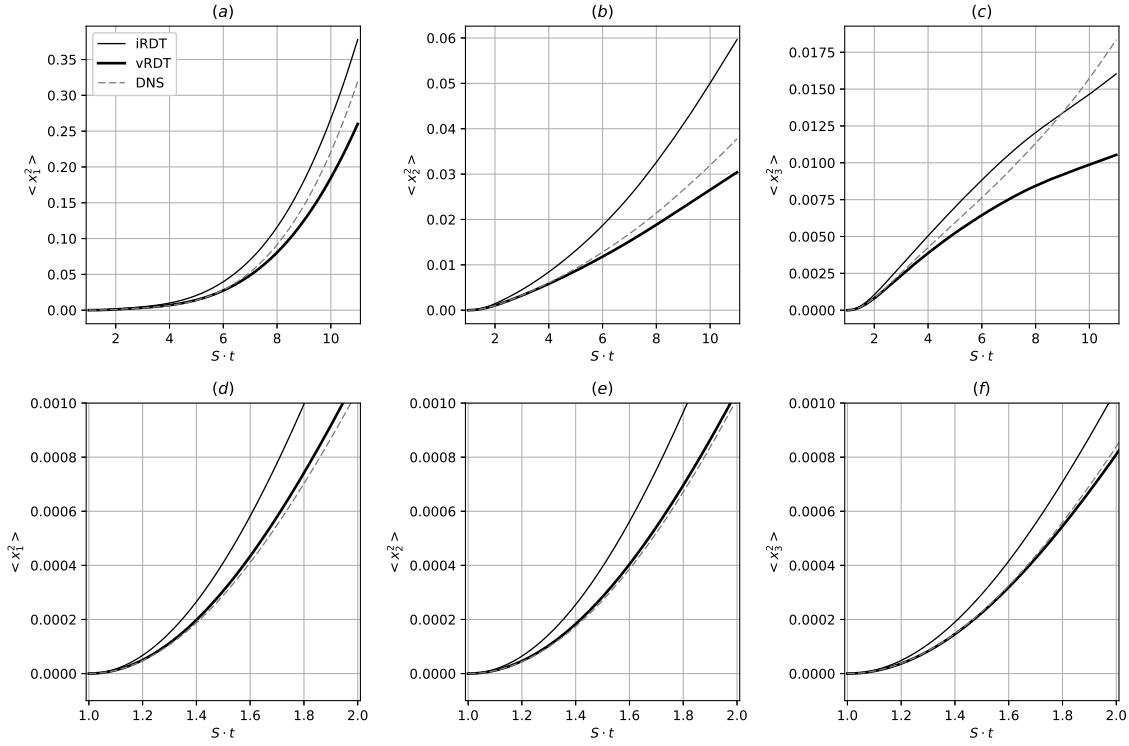

FIGURE 7.23: Dispersion of $St_\eta = 2.3$ particles in (a) streamwise (b) spanwise direction (c) shear direction (case B; table 5.6) between $S \cdot t = 0$ and $S \cdot t = 10$. (d) to (f) same as (a) to (c) between $S \cdot t = 0$ and $S \cdot t = 2$. Dashed line direct numerical simulation, thin line inviscid rapid distortion theory, thick line viscous rapid distortion theory.

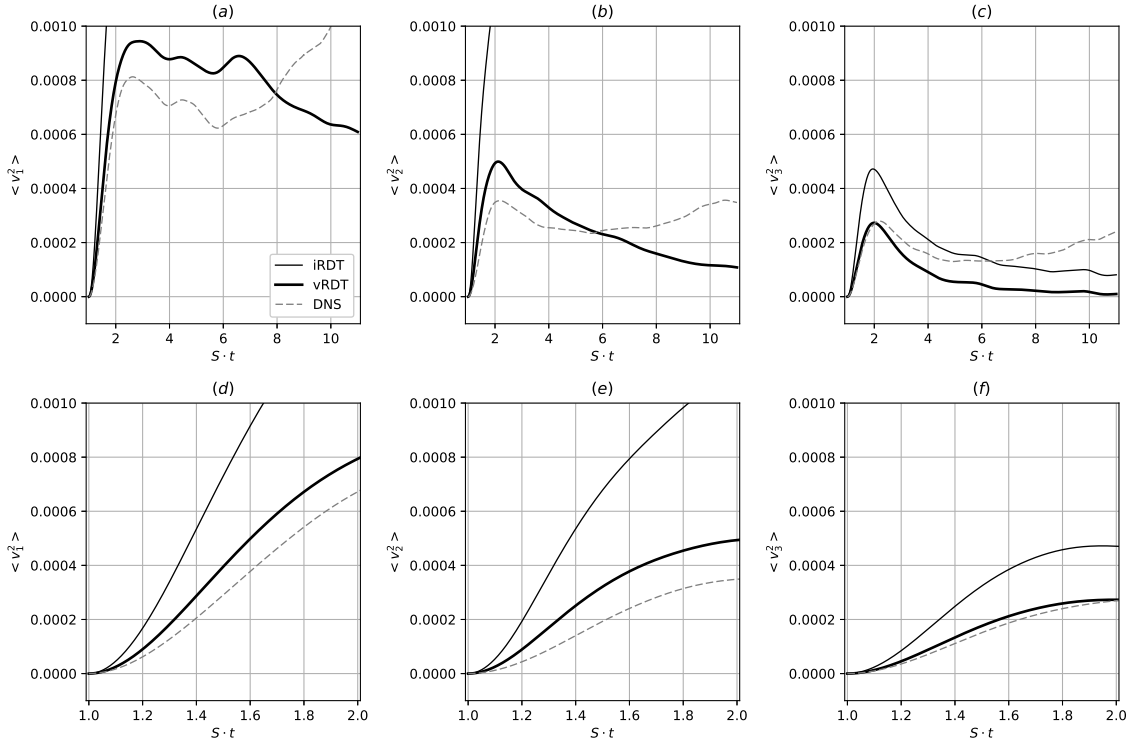

FIGURE 7.24: Relative velocity of $St_\eta = 2.3$ particles in (a) streamwise (b) spanwise (c) shear direction (case B; table 5.6) between $S \cdot t = 0$ and $S \cdot t = 10$. (d) to (f) same as (a) to (c) between $S \cdot t = 0$ and $S \cdot t = 2$. Dashed line direct numerical simulation, thin line inviscid rapid distortion theory, thick line viscous rapid distortion theory.

7.5 Summary and discussion

The results in this chapter have shown that particle dispersion in homogeneous shear flows, both for passive and inertial particles, can be modelled reasonably well at short times of about $S \cdot t = 1$ from injection of the particles using viscous rapid distortion. Not only is there a fair agreement in dispersion results, but also the relative particle velocity can be approximated using this approach. This suggests rapid distortion theory as a potential candidate for a subgrid model for atmospheric large-eddy simulations. Apart from a numerical solution of the equations for rapid distortion theory as used here, analytical solutions are available, e.g. in [102]. While the analytical solutions mentioned were derived for passive particles, the simulations presented in this chapter have shown that rapid distortion theory is capable of predicting the dispersion of inertial particles. It might be possible to extend analytical solutions to inertial particles. To this end it could be possible to make use of the equilibrium Euler method [38].

Inviscid rapid distortion theory does not seem sufficient except for qualitative results. While large-eddy simulations showed good agreement with the DNS results, it has to be noted that typical grid resolutions of atmospheric LES are still big compared to the LES results presented here.

Chapter 8

Conclusions and future work

The goal of this work was to improve the accuracy of atmospheric dispersion modelling for small heavy particles with an ultimate outcome in the form of a suitable subgrid-scale model that can be used in large-eddy simulations.

A new method for the evaluation of field experiments was presented in **chapter 3**. Using this method reliable validation quantities at the shortest measurable time scales can be obtained from tracer gas releases in the atmospheric boundary layer. The new method for the evaluation of field experiments developed in this work makes it possible to understand tracer release experiments under real atmospheric conditions at time resolutions that have not been available so far.

Chapter 4 contains the results of direct numerical simulations of particles in homogeneous isotropic turbulence and gives a first idea about the behaviour of typical atmospheric aerosols. An estimate of atmospheric aerosol properties has shown that small particles with diameters in the order of $1\,\mu m$ can be expected to show almost gas-like dispersion behaviour, whereas larger particles of approximately $d_p > 5\,\mu m$ are increasingly influenced by inertia and gravity effects. Inertia effects including clustering can be expected in windy situations, whereas in calm situation gravity can become relevant. Preliminary simulations of idealised atmospheric particles in homogeneous isotropic turbulence confirm this observation.

For larger particles a strong clustering behaviour near walls (in practical terms the ground as well as building walls) can be expected, which means that correct near-wall concentrations are of significance for the dispersion modelling of fine particulate matter. This near-wall behaviour can be expected to be extremely weather-dependent, which poses an additional challenge. Simulations of small inertial particles in homogeneous isotropic turbulence have shown that both particle-particle distance and local concentrations appear to follow a clear scaling law with Reynolds number. This implies that it is likely not necessary to perform simulations at typical atmospheric Reynolds numbers in order to understand the small-scale behaviour of particles.

In order to progress from isotropic simulations to more complex flows, in particular homogeneous shear flows, a new improved version of the pseudospectral direct numerical simulation code PANDORA was developed. **Chapter 5** introduces the modified code. The improved version PANDORA 2.0 is described and the development of additional code for homogeneous turbulence using the Rogallo transform was presented. The new PANDORA 2.0 has been validated against the Taylor-Green vortex as well as published results from homogeneous shear-flow simulations with and without particles. A reasonable agreement within the limits of uncertainties due to the initialisation and numerical method has been observed.

While the validation simulations show the usability of the code for homogeneous shear flows at low Reynolds numbers, in **chapter 6** additional simulations were performed at higher Reynolds numbers. The fluid statistics are in good agreement with measured results from the literature. Passive particle simulations at different Reynolds numbers do not seem to show a significant Reynolds number dependence, which suggests that for particles in homogeneous shear flows lower Reynolds numbers might lead to sufficient results. On the other hand a comparison of inertial and passive particle simulations shows a Stokes number dependence in streamwise direction even at short simulation times.

In addition to the direct numerical simulations, the PANDORA code in its current form contains both inviscid and viscous rapid distortion theory. This approach has been tested in **chapter 7** as a potential candidate for a subgrid-scale model. While the inviscid rapid distortion theory approach seems to be limited to qualitative analysis, a reasonably good agreement between viscous rapid distortion theory and direct numerical simulations for both passive and inertial particle has been found.

8.1 Future work and outlook

With the final goal of developing a fully functional subgrid particle model for atmospheric large-eddy simulations in mind, this thesis has shown some requirements and a potential candidate for such a model. All simulations for homogeneous shear flows indicate that for complex flows an isotropic dispersion model seems insufficient.

The new method for the evaluation of field experiments developed in this work makes it possible to understand tracer release experiments under real atmospheric conditions at time resolutions that have not been available so far. At the same time the DNS code PANDORA has been further developed to allow simulations at higher Reynolds numbers, getting close to realistic turbulence. The simulation of shear flows and further homogeneous deformed flows is possible.

The new experimental method and the code developed here could be combined to obtain insight into the small-scale behaviour of passive and inertial particles. To this end,

field experiments consisting of puff releases and of continuous releases of a tracer gas could be evaluated. Based on shear rates and other turbulence data obtained from the measurements, it could then be attempted to match the small-scale characteristics of the tracer gas using passive particles. The same fluid simulations can also be performed with inertial particles in order to understand the difference between the tracer gas and the inertial particles under the given atmospheric conditions.

The results have shown that particle dispersion in homogeneous shear flows, both for passive and inertial particles, can be modelled reasonably well at short times of about $S \cdot t = 1$ from injection of the particles using viscous rapid distortion. Not only is there a fair agreement in dispersion results, but also the relative particle velocity can be approximated using this approach. This suggests rapid distortion theory as a potential candidate for a subgrid model for atmospheric large-eddy simulations. Apart from a numerical solution of the equations for rapid distortion theory as used here, analytical solutions are available, e.g. in [102]. While the analytical solutions mentioned were derived for passive particles, the simulations presented in chapter 7 have shown that rapid distortion theory is capable of predicting the dispersion of inertial particles. It might be possible to extend analytical solutions to inertial particles. To this end it could be possible to make use of the equilibrium Euler method [38].

All the above work takes into account shear effects, but not the direct influence (blocking) of the surface. This could also be investigated using rapid distortion theory.

Appendix A

Preliminary results for atmospheric particle dispersion

Using the estimates for characteristic atmospheric aerosols properties discussed in chapter 2.4, simulations of particles in homogeneous isotropic turbulence at $Re_\lambda \approx 250$ have been performed. An overview of the simulation parameters is given in table A.1. The fluid simulations use the same input parameters as the other simulations at $Re_\lambda \approx 250$ presented throughout this chapter.

As can be seen from figure A.1, there is some particle clustering at the highest Stokes number $St_\eta = 0.1$, but both $g(r)$ and D disappear for $St_\eta = 0.01$. However, the Schmidt numbers (shown in figure A.2) suggest that there are still some minimal inertia effects at $St_\eta = 0.01$. The simulations corresponding to $10\,\mu m$ particles show that at high atmospheric dissipation rates, both the vertical and horizontal Schmidt numbers are below 1 and therefore particles are stronger dispersed than fluid particles. For the simulation corresponding to the lowest atmospheric dissipation rate, the vertical Schmidt number is below 1 and the horizontal Schmidt number is above 1, which is a typical characteristic of gravity effects, where the particles are accelerated in the gravity direction whilst dispersion in the horizontal direction is reduced compared to fluid particles. The simulation

particle diameter (atmosphere)	$10\,\mu m$	$10\,\mu m$	$10\,\mu m$	$10\,\mu m$	$1\,\mu m$
St_η	10^{-4}	10^{-3}	10^{-2}	10^{-1}	10^{-3}
Fr_η	$5 \cdot 10^-5$	$2 \cdot 10^{-3}$	$5 \cdot 10^{-2}$	1.65	1.65
ϵ (atmosphere)	10^{-6}	10^{-4}	10^{-2}	10^0	10^0

TABLE A.1: Stokes numbers St_η and Froude numbers Fr_η as well as the corresponding particle diameters and typical atmospheric dissipation rates for direct numerical simulations of particles in homogeneous isotropic turbulence at $Re_\lambda \approx 250$. Both the diameter and the atmospheric dissipation rates are **not** identical to the quantities used in the simulations.

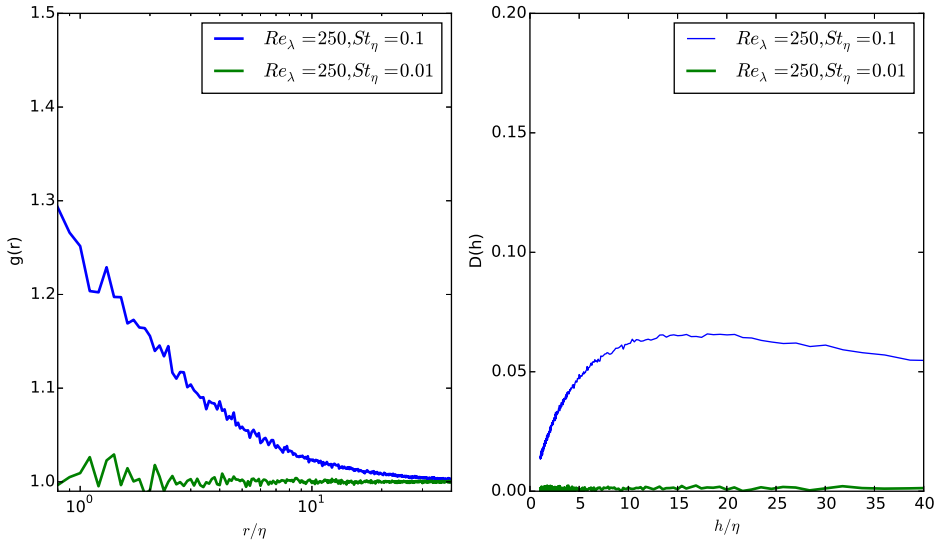

FIGURE A.1: Radial distribution function $g(r)$ (left) and D measure (right) at $Re_\lambda \approx 250$ and Stokes numbers $St_\eta = 0.1$ and $St_\eta = 0.01$.

corresponding to an atmospheric dissipation rate of $10^{-4}\, m^2/s^3$ results in Schmidt numbers very close to 1. However the vertical Schmidt number is slightly below 1 and the horizontal Schmidt number is slightly above 1. This would indicate a minimal gravity effect.

For particles corresponding to atmospheric $1\,\mu m$ particles, only one simulation was performed. The Schmidt numbers are almost exactly 1. Therefore it can be expected that for this particle size the dispersion behaviour is almost identical to that of a gas.

These simulations only cover a small range of particle sizes and atmospheric conditions. Furthermore the Reynolds number $Re_\lambda \approx 250$ is moderate and homogeneous isotropic turbulence is an idealised model. Nevertheless these results give an idea of expected dispersion behaviour of atmospheric aerosols. Whereas the smallest particles can be expected to behave similar to a gas, for larger particles inertial behaviour can be expected in windy, more turbulent, situations. In calm situations and at greater heights the dispersion behaviour of these larger particles can be expected to be influenced by gravity. In all cases, these effects are moderate. This might suggest that it is feasible to use simple models and introduce correction terms without losing much accuracy.

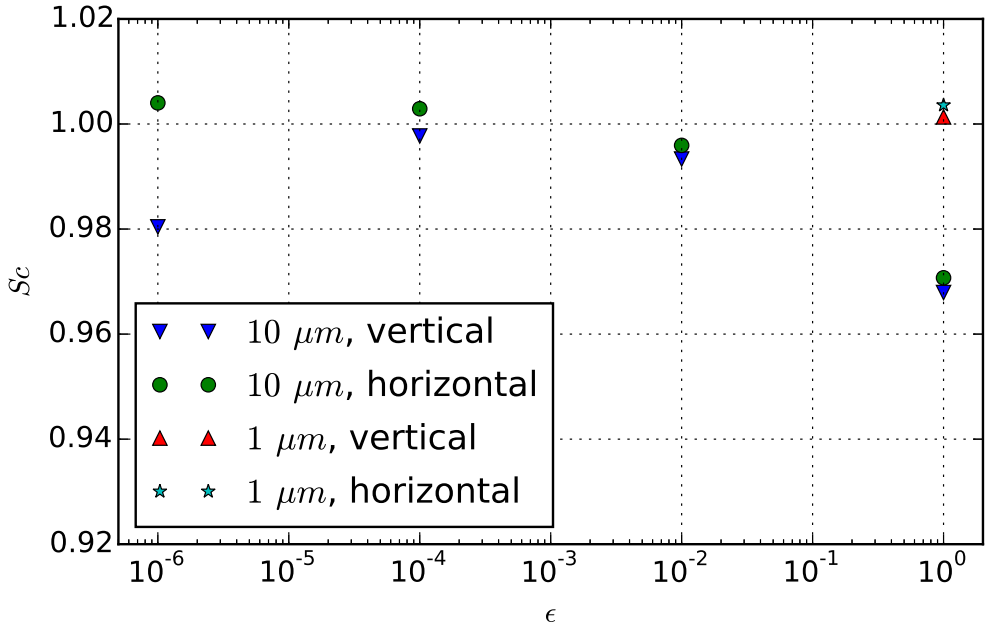

FIGURE A.2: Estimate of Schmidt numbers for 10 μm and 1 μm particles over a range of atmospheric dissipation rates (in m^2/s^3) based on numerical simulations at $Re_\lambda \approx 250$.

References

[1] CEDVAL-LES, 2011. Compilation of Experimental Data for Validation of Microscale Dispersion Models. *Meteorological Institute, University of Hamburg, Germany, www.mi.uni-hamburg.de/cedval-les.*

[2] A. M. Ahmed and S. Elghobashi. Direct numerical simulation of particle dispersion in homogeneous turbulent shear flows. *Physics of Fluids*, 13(11):3346–3364, 2001.

[3] A. Aliseda, A. Cartellier, F. Hainaux, and J. C. Lasheras. Effect of preferential concentration on the settling velocity of heavy particles in homogeneous isotropic turbulence. *Journal of Fluid Mechanics*, 468:77–105, 2002.

[4] V. Armenio, U. Piomelli, and V. Fiorotto. Effect of the subgrid scales on particle motion. *Physics of Fluids*, 11(10):3030–3042, 1999.

[5] Callum Atkinson, Nicolas Alexander Buchmann, and Julio Soria. An experimental investigation of turbulent convection velocities in a turbulent boundary layer. *Flow, Turbulence and Combustion*, 94(1):79–95, 2015.

[6] Sean CC Bailey, Marcus Hultmark, Joerg Schumacher, Victor Yakhot, and Alexander J Smits. Measurement of local dissipation scales in turbulent pipe flow. *Physical review letters*, 103(1):014502, 2009.

[7] S. Balachandar and J. K. Eaton. Turbulent dispersed multiphase flow. *Annual Review of Fluid Mechanics*, 42:111–133, 2010.

[8] S Balachandar and MR Maxey. Methods for evaluating fluid velocities in spectral simulations of turbulence. *Journal of Computational Physics*, 83(1):96–125, 1989.

[9] J Bardino, JH Ferziger, and WC Reynolds. Improved turbulence models based on large eddy simulation of homogeneous, incompressible turbulent flows. 1983.

[10] Ilona Bastigkeit, R Fischer, B Leitl, and M Schatzmann. Fundamental quality requirements for the generation of les-specific validation data sets from systematic wind tunnel model experiments. *Proceedings of CWE2010. Chapel-Hill, NC, USA*, 2010.

[11] GK Batchelor. Diffusion in a field of homogeneous turbulence: II. The relative motion of particles. In *Mathematical Proceedings of the Cambridge Philosophical Society*, volume 48, pages 345–362. Cambridge University Press, 1952.

[12] Robert J Beare, Malcolm K Macvean, Albert AM Holtslag, Joan Cuxart, Igor Esau, Jean-Christophe Golaz, Maria A Jimenez, Marat Khairoutdinov, Branko Kosovic, David Lewellen, et al. An intercomparison of large-eddy simulations of the stable boundary layer. *Boundary-Layer Meteorology*, 118(2):247–272, 2006.

[13] Jérémie Bec, Holger Homann, and Samriddhi Sankar Ray. Gravity-driven enhancement of heavy particle clustering in turbulent flow. *Physical review letters*, 112(18): 184501, 2014.

[14] Eva Berbekar, Frank Harms, and Bernd Leitl. Dosage-based parameters for characterization of puff dispersion results. *Journal of hazardous materials*, 283:178–185, 2015.

[15] Bert Blocken, Rob Vervoort, and Twan van Hooff. Reduction of outdoor particulate matter concentrations by local removal in semi-enclosed parking garages: a preliminary case study for eindhoven city center. *Journal of Wind Engineering and Industrial Aerodynamics*, 159:80–98, 2016.

[16] T Bouvet, JD Wilson, and A Tuzet. Observations and modeling of heavy particle deposition in a windbreak flow. *Journal of applied meteorology and climatology*, 45 (9):1332–1349, 2006.

[17] Marc E Brachet, D Meiron, S Orszag, B Nickel, R Morf, and Uriel Frisch. The taylor-green vortex and fully developed turbulence. *Journal of Statistical Physics*, 34(5-6):1049–1063, 1984.

[18] Gary A Briggs. Final results of the condors convective diffusion experiment. *Boundary-Layer Meteorology*, 62(1-4):315–328, 1993.

[19] Kyle A Brucker, Juan C Isaza, T Vaithianathan, and Lance R Collins. Efficient algorithm for simulating homogeneous turbulent shear flow without remeshing. *Journal of Computational Physics*, 225(1):20–32, 2007.

[20] ORH Buxton, R de Kat, and B Ganapathisubramani. The convection of large and intermediate scale fluctuations in a turbulent mixing layer. *Physics of Fluids*, 25 (12):125105, 2013.

[21] C Canuto, MY Hussaini, A Quarteroni, and TA Zang. *Spectral methods: evolution to complex domains and applications to fluid dynamics*. Springer, New York, 2007.

[22] Ian P Castro. Dissipative distinctions. *Journal of Fluid Mechanics*, 788:1–4, 2016.

[23] Ian P Castro, Zheng-Tong Xie, Vladimir Fuka, Alan G Robins, M Carpentieri, P Hayden, D Hertwig, and O Coceal. Measurements and computations of flow in an urban street system. *Boundary-Layer Meteorology*, 162(2):207–230, 2017.

[24] SJ Caughey, JC Wyngaard, and JC Kaimal. Turbulence in the evolving stable boundary layer. *Journal of the Atmospheric Sciences*, 36(6):1041–1052, 1979.

[25] Matthew J Cernick, SW Tullis, and MF Lightstone. Particle subgrid scale modelling in large-eddy simulations of particle-laden turbulence. *Journal of Turbulence*, 16(2):101–135, 2015.

[26] Marcelo Chamecki, Charles Meneveau, and Marc B Parlange. Large eddy simulation of pollen transport in the atmospheric boundary layer. *Journal of Aerosol Science*, 40(3):241–255, 2009.

[27] CFM Coimbra and RH Rangel. General solution of the particle momentum equation in unsteady stokes flows. *Journal of Fluid Mechanics*, 370:53–72, 1998.

[28] L. R. Collins and A. Keswani. Reynolds number scaling of particle clustering in turbulent aerosols. *New Journal of Physics*, 6, 2004.

[29] POAL Davies, MJ Fisher, and MJ Barratt. The characteristics of the turbulence in the mixing region of a round jet. *Journal of Fluid Mechanics*, 15(3):337–367, 1963.

[30] DA Donzis, PK Yeung, and KR Sreenivasan. Dissipation and enstrophy in isotropic turbulence: resolution effects and scaling in direct numerical simulations. *Physics of Fluids*, 20(4):045108, 2008.

[31] JC Doran and TW Horst. An evaluation of gaussian plume-depletion models with dual-tracer field measurements. *Atmospheric Environment (1967)*, 19(6):939–951, 1985.

[32] Philippe Drobinski, Pierre Carlotti, Rob K Newsom, Robert M Banta, Ralph C Foster, and Jean-Luc Redelsperger. The structure of the near-neutral atmospheric surface layer. *Journal of the atmospheric sciences*, 61(6):699–714, 2004.

[33] S. Elghobashi and G. C. Truesdell. Direct simulation of particle dispersion in a decaying isotropic turbulence. *Journal of Fluid Mechanics*, 242:655–700, 1992.

[34] S Elghobashi and GC Truesdell. Direct simulation of particle dispersion in a decaying isotropic turbulence. *Journal of Fluid Mechanics*, 242:655–700, 1992.

[35] V. Eswaran and S. B. Pope. An examination of forcing in direct numerical simulations of turbulence. *Computers & Fluids*, 16(3):257–278, 1988.

[36] P. Fede and O. Simonin. Numerical study of the subgrid fluid turbulence effects on the statistics of heavy colliding particles. *Physics of Fluids*, 18(4):045103, 2006.

[37] M Ferchichi and S Tavoularis. Reynolds number effects on the fine structure of uniformly sheared turbulence. *Physics of Fluids*, 12(11):2942–2953, 2000.

[38] Jim Ferry and S Balachandar. Equilibrium expansion for the eulerian velocity of small particles. *Powder Technology*, 125(2):131–139, 2002.

[39] J. Ferziger and M. Peric. *Computational Methods for Fluid Dynamics*. Springer Verlag, 1996.

[40] J. R. Fessler, J. D. Kulick, and J. K. Eaton. Preferential concentration of heavy-particles in a turbulent channel flow. *Physics of Fluids*, 6(11):3742–3749, 1994.

[41] Rasmus Fischer, Ilona Bastigkeit, Bernd Leitl, and Michael Schatzmann. Generation of spatio-temporally high resolved datasets for the validation of les-models simulating flow and dispersion phenomena within the lower atmospheric boundary layer. In *Proc. 5th International Symposium on Computational Wind Engineering (CWE2010), Chapel Hill, North Carolina, USA*, 2010.

[42] MJ Fisher and POAL Davies. Correlation measurements in a non-frozen pattern of turbulence. *Journal of fluid mechanics*, 18(1):97–116, 1964.

[43] Rod Frehlich, Yannick Meillier, Michael L Jensen, and Ben Balsley. A statistical description of small-scale turbulence in the low-level nocturnal jet. *Journal of the atmospheric sciences*, 61(9):1079–1085, 2004.

[44] M. Frigo and S. G. Johnson. The design and implementation of FFTW3. In *Proceedings of the IEEE*, volume 93, pages 216–231, 2005.

[45] Vladimír Fuka and Josef Brechler. Large eddy simulation modelling of the dispersion of radioactive particulate matter. *International Journal of Environment and Pollution*, 48(1-4):156–163, 2012.

[46] M Germano. Turbulence: the filtering approach. *Journal of Fluid Mechanics*, 238: 325–336, 1992.

[47] VW Goldschmidt, MF Young, and ES Ott. Turbulent convective velocities (broadband and wavenumber dependent) in a plane jet. *Journal of Fluid Mechanics*, 105: 327–345, 1981.

[48] Susumu Goto and JC Vassilicos. Local equilibrium hypothesis and Taylor's dissipation law. *Fluid Dynamics Research*, 48(2):021402, 2016.

[49] RF Griffiths, I Mavroidis, and CD Jones. The development of a fast-response portable photo-ionization detector: a model of the instrument's response and validation tests in air. *Measurement Science and Technology*, 9(9):1369, 1998.

[50] F Harms, B Leitl, M Schatzmann, and G Patnaik. Validating LES-based flow and dispersion models. *Journal of Wind Engineering and Industrial Aerodynamics*, 99 (4):289–295, 2011.

[51] R Jason Hearst and Philippe Lavoie. Decay of turbulence generated by a square-fractal-element grid. *Journal of Fluid Mechanics*, 741:567–584, 2014.

[52] WC Hinds. Aerosol technology: Properties, behavior, and measurement of airborne particles. *New York, Wiley-Interscience, 1982. 442 p.*, 1982.

[53] Nicholas S Holmes and Lidia Morawska. A review of dispersion modelling and its application to the dispersion of particles: an overview of different dispersion models available. *Atmospheric environment*, 40(30):5902–5928, 2006.

[54] JR Holton. An introduction to dynamic meteorology. *International geophysics series (USA). v. 23.*, 1979.

[55] JCR Hunt and Pierre Carlotti. Statistical structure at the wall of the high reynolds number turbulent boundary layer. *Flow, Turbulence and Combustion*, 66(4):453–475, 2001.

[56] Julian CR Hunt and Jonathan F Morrison. Eddy structure in turbulent boundary layers. *European Journal of Mechanics-B/Fluids*, 19(5):673–694, 2000.

[57] W. T. Hwang and J. K. Eaton. Homogeneous and isotropic turbulence modulation by small heavy (St similar to 50) particles. *Journal of Fluid Mechanics*, 564:361–393, 2006.

[58] Peter J Ireland, Andrew D Bragg, and Lance R Collins. The effect of reynolds number on inertial particle dynamics in isotropic turbulence. part 1. simulations without gravitational effects. *Journal of Fluid Mechanics*, 796:617–658, 2016.

[59] Peter J Ireland, Andrew D Bragg, and Lance R Collins. The effect of reynolds number on inertial particle dynamics in isotropic turbulence. part 2. simulations with gravitational effects. *Journal of Fluid Mechanics*, 796:659–711, 2016.

[60] Peter J Ireland, T Vaithianathan, Parvez S Sukheswalla, Baidurja Ray, and Lance R Collins. Highly parallel particle-laden flow solver for turbulence research. *Computers & Fluids*, 76:170–177, 2013.

[61] Juan C Isaza and Lance R Collins. On the asymptotic behaviour of large-scale turbulence in homogeneous shear flow. *Journal of Fluid Mechanics*, 637:213–239, 2009.

[62] Guodong Jin and Guo-Wei He. A nonlinear model for the subgrid timescale experienced by heavy particles in large eddy simulation of isotropic turbulence with a stochastic differential equation. *New Journal of Physics*, 15(3):035011, 2013.

[63] C. D. Jones. Report on puff structure field experiments. *Nevada, USA, October/November 2001, DSTL*, unpublished, 2001.

[64] CD Jones and RF Griffiths. Full-scale experiments on dispersion around an isolated building using an ionized air tracer technique with very short averaging time. *Atmospheric Environment (1967)*, 18(5):903–916, 1984.

[65] D Kaftori, G Hetsroni, and S Banerjee. Particle behavior in the turbulent boundary layer. i. motion, deposition, and entrainment. *Physics of Fluids*, 7(5):1095–1106, 1995.

[66] Yukio Kaneda, Takashi Ishihara, Mitsuo Yokokawa, Ken'ichi Itakura, and Atsuya Uno. Energy dissipation rate and energy spectrum in high resolution direct numerical simulations of turbulence in a periodic box. *Physics of Fluids*, 15(2):L21, 2003.

[67] Aditya U Karnik. *Direct numerical investigations of dilute dispersed flows in homogeneous turbulence*. PhD thesis, University of Southampton, 2012.

[68] Aditya U Karnik and John S Shrimpton. Mitigation of preferential concentration of small inertial particles in stationary isotropic turbulence using electrical and gravitational body forces. *Physics of Fluids*, 24(7):073301, 2012.

[69] A. N. Kolmogorov. Local structure of turbulence in an incompresible fluid at very high reynolds numbers. *C. R. Acad. Sci. USSR*, 30:201, 1941.

[70] JGM Kuerten. Subgrid modeling in particle-laden channel flow. *Physics of Fluids (1994-present)*, 18(2):025108, 2006.

[71] JGM Kuerten. Point-particle dns and les of particle-laden turbulent flow-a state-of-the-art review. *Flow, Turbulence and Combustion*, 97(3):689–713, 2016.

[72] Moon Joo Lee, John Kim, and Parviz Moin. Structure of turbulence at high shear rate. *Journal of Fluid Mechanics*, 216:561–583, 1990.

[73] A Leonard. Energy cascade in large-eddy simulations of turbulent fluid flows. *Advances in geophysics*, 18:237–248, 1975.

[74] John L Lumley and Hans A Panofsky. The structure of atmospheric turbulence. 1964.

[75] Cristian Marchioli. Large-eddy simulation of turbulent dispersed flows: a review of modelling approaches. *Acta Mechanica*, 228(3):741–771, 2017.

[76] Cristian Marchioli, Maurizio Picciotto, and Alfredo Soldati. Particle dispersion and wall-dependent turbulent flow scales: implications for local equilibrium models. *Journal of Turbulence*, (7):N60, 2006.

[77] Atsushi Matsumoto, Yasutaka Nagano, and Toshihiro Tsuji. Direct numerical simulation of homogeneous turbulent shear flow. In *5th Numerical Fluid Dynamics Symposium*, pages 361–364, 1991.

[78] WD McComb, A Berera, SR Yoffe, and MF Linkmann. Energy transfer and dissipation in forced isotropic turbulence. *Physical Review E*, 91(4):043013, 2015.

[79] Charles Meneveau and Joseph Katz. Scale-invariance and turbulence models for large-eddy simulation. *Annual Review of Fluid Mechanics*, 32(1):1–32, 2000.

[80] Aaron Meurer, Christopher P. Smith, Mateusz Paprocki, Ondřej Čertík, Sergey B. Kirpichev, Matthew Rocklin, AMiT Kumar, Sergiu Ivanov, Jason K. Moore, Sartaj Singh, Thilina Rathnayake, Sean Vig, Brian E. Granger, Richard P. Muller, Francesco Bonazzi, Harsh Gupta, Shivam Vats, Fredrik Johansson, Fabian Pedregosa, Matthew J. Curry, Andy R. Terrel, Štěpán Roučka, Ashutosh Saboo, Isuru Fernando, Sumith Kulal, Robert Cimrman, and Anthony Scopatz. SymPy: symbolic computing in Python. *PeerJ Computer Science*, 3:e103, January 2017. ISSN 2376-5992. URL: https://doi.org/10.7717/peerj-cs.103.

[81] Frederick J Miller, Donald E Gardner, Judith A Graham, Robert E Lee Jr, William E Wilson, and John D Bachmann. Size considerations for establishing a standard for inhalable particles. *Journal of the Air Pollution Control Association*, 29(6):610–615, 1979.

[82] Romain Monchaux, Mickaël Bourgoin, and Alain Cartellier. Preferential concentration of heavy particles: a voronoi analysis. *Physics of Fluids (1994-present)*, 22 (10):103304, 2010.

[83] Romain Monchaux, Mickael Bourgoin, and Alain Cartellier. Analyzing preferential concentration and clustering of inertial particles in turbulence. *International Journal of Multiphase Flow*, 40:1–18, 2012.

[84] DO Mora, M Bourgoin, PD Mininni, and M Obligado. Clustering of vector nulls in homogeneous isotropic turbulence. *Physical Review Fluids*, 6(2):024609, 2021.

[85] C Nicolai, B Jacob, and R Piva. On the spatial distribution of small heavy particles in homogeneous shear turbulence. *Physics of Fluids (1994-present)*, 25(8):083301, 2013.

[86] Y Niño and MH Garcia. Experiments on particle-turbulence interactions in the near-wall region of an open channel flow: implications for sediment transport. *Journal of Fluid Mechanics*, 326:285–319, 1996.

[87] Martín Obligado, Tomás Teitelbaum, Alain Cartellier, Pablo Mininni, and Mickaël Bourgoin. Preferential concentration of heavy particles in turbulence. *Journal of Turbulence*, 15(5):293–310, 2014.

[88] Steven A Orszag. Numerical simulation of the taylor-green vortex. In *Computing Methods in Applied Sciences and Engineering Part 2*, pages 50–64. Springer, 1974.

[89] Matthew R Overholt and Stephen B Pope. A deterministic forcing scheme for direct numerical simulations of turbulence. *Computers & Fluids*, 27(1):11–28, 1998.

[90] Simon Parker, James Nally, Timothy Foat, and Steve Preston. Refinement and testing of the drift-flux model for indoor aerosol dispersion and deposition modelling. *Journal of Aerosol Science*, 41(10):921–934, 2010.

[91] GS Patterson Jr and Steven A Orszag. Spectral calculations of isotropic turbulence: Efficient removal of aliasing interactions. *The Physics of Fluids*, 14(11):2538–2541, 1971.

[92] M Piper and Julie K Lundquist. Surface layer turbulence measurements during a frontal passage. *Journal of the atmospheric sciences*, 61(14):1768–1780, 2004.

[93] S. B. Pope. *Turbulent Flows*. Cambridge University Press, 2001.

[94] Stephen B Pope. Ten questions concerning the large-eddy simulation of turbulent flows. *New journal of Physics*, 6(1):35, 2004.

[95] Sarma L Rani and S Balachandar. Preferential concentration of particles in isotropic turbulence: a comparison of the lagrangian and the equilibrium eulerian approaches. *Powder technology*, 141(1):109–118, 2004.

[96] Baidurja Ray and Lance R Collins. Preferential concentration and relative velocity statistics of inertial particles in navier–stokes turbulence with and without filtering. *Journal of Fluid Mechanics*, 680:488–510, 2011.

[97] Baidurja Ray and Lance R Collins. A subgrid model for clustering of high-inertia particles in large-eddy simulations of turbulence. *Journal of Turbulence*, 15(6): 366–385, 2014.

[98] W. C. Reade and L. R. Collins. Effect of preferential concentration on turbulent collision rates. *Physics of Fluids*, 12(10):2530–2540, 2000.

[99] PJ Richards, S Fong, and RP Hoxey. Anisotropic turbulence in the atmospheric surface layer. *Journal of wind engineering and industrial aerodynamics*, 69:903–913, 1997.

[100] Lewis F Richardson. Atmospheric diffusion shown on a distance-neighbour graph. *Proceedings of the Royal Society of London. Series A, Containing Papers of a Mathematical and Physical Character*, 110(756):709–737, 1926.

[101] Robert Sugden Rogallo. Numerical experiments in homogeneous turbulence. 1981.

[102] Michael M Rogers. The structure of a passive scalar field with a uniform mean gradient in rapidly sheared homogeneous turbulent flow. *Physics of Fluids A: Fluid Dynamics*, 3(1):144–154, 1991.

[103] Pierre Sagaut and Yu-Tai Lee. Large eddy simulation for incompressible flows: An introduction. scientific computation series. *Applied Mechanics Reviews*, 55:B115, 2002.

[104] S. J. Scott. *A PDF Based Method for Modelling Polysized Particle Laden Turbulent Flows Without Size Class Discretization.* PhD thesis, Imperial College London, 2006.

[105] S. J. Scott, A. U. Karnik, and J. S. Shrimpton. On the quantification of preferential accumulation. *International Journal of Heat and Fluid Flow*, 30(4):789–795, 2009.

[106] Alfredo Soldati and Cristian Marchioli. Physics and modelling of turbulent particle deposition and entrainment: Review of a systematic study. *International Journal of Multiphase Flow*, 35(9):827–839, 2009.

[107] Alfredo Soldati and Cristian Marchioli. Sediment transport in steady turbulent boundary layers: Potentials, limitations, and perspectives for lagrangian tracking in dns and les. *Advances in Water Resources*, 48:18–30, 2012.

[108] K. D. Squires and J. K. Eaton. Preferential concentration of particles by turbulence. *Physics of Fluids a-Fluid Dynamics*, 3(5):1169–1179, 1991.

[109] Kyle D Squires and John K Eaton. Lagrangian and eulerian statistics obtained from direct numerical simulations of homogeneous turbulence. *Physics of Fluids A: Fluid Dynamics*, 3(1):130–143, 1991.

[110] S Stolz, NA Adams, and L Kleiser. An approximate deconvolution model for large-eddy simulation with application to incompressible wall-bounded flows. *Physics of Fluids (1994-present)*, 13(4):997–1015, 2001.

[111] Roland B Stull. An introduction to boundary layer meteorology. *Atmospheric Sciences Library, Dordrecht: Kluwer, 1988*, 1988.

[112] Parvez Sukheswalla, T Vaithianathan, and Lance R Collins. Simulation of homogeneous turbulent shear flows at higher reynolds numbers: numerical challenges and a remedy. *Journal of Turbulence*, 14(5):60–97, 2013.

[113] Paul J Sullivan. Some data on the distance-neighbour function for relative diffusion. *Journal of Fluid Mechanics*, 47(3):601–607, 1971.

[114] Sholpan Sumbekova, Alain Cartellier, Alberto Aliseda, and Mickael Bourgoin. Preferential concentration of inertial sub-kolmogorov particles: The roles of mass loading of particles, stokes numbers, and reynolds numbers. *Physical Review Fluids*, 2 (2):024302, 2017.

[115] S. Sundaram and L. R. Collins. Collision statistics in an isotropic particle-laden turbulent suspension .1. direct numerical simulations. *Journal of Fluid Mechanics*, 335:75–109, 1997.

[116] Oliver Graham Sutton. Micrometeorology. 1953.

[117] S Tavoularis and U Karnik. Further experiments on the evolution of turbulent stresses and scales in uniformly sheared turbulence. *Journal of Fluid Mechanics*, 204:457–478, 1989.

[118] Geoffrey Ingram Taylor and Albert Edward Green. Mechanism of the production of small eddies from large ones. *Proceedings of the Royal Society of London. Series A-Mathematical and Physical Sciences*, 158(895):499–521, 1937.

[119] Hendrik Tennekes and John Leask Lumley. *A first course in turbulence*. 1972.

[120] MAT van Hinsberg, JHM ten Thije Boonkkamp, F Toschi, and HJH Clercx. Optimal interpolation schemes for particle tracking in turbulence. *Physical Review E*, 87(4):043307, 2013.

[121] Christina Vanderwel and Stavros Tavoularis. Coherent structures in uniformly sheared turbulent flow. *Journal of Fluid Mechanics*, 689:434–464, 2011.

[122] Christina Vanderwel and Stavros Tavoularis. Scalar dispersion by coherent structures in uniformly sheared flow generated in a water tunnel. *Journal of Turbulence*, pages 1–18, 2016.

[123] J Christos Vassilicos. Dissipation in turbulent flows. *Annual Review of Fluid Mechanics*, 47:95–114, 2015.

[124] Ivana Vinkovic, Delphine Doppler, J Lelouvetel, and Marc Buffat. Direct numerical simulation of particle interaction with ejections in turbulent channel flows. *International Journal of Multiphase Flow*, 37(2):187–197, 2011.

[125] L. P. Wang and M. R. Maxey. Settling velocity and concentration distribution of heavy-particles in homogeneous isotropic turbulence. *Journal of Fluid Mechanics*, 256:27–68, 1993.

[126] J. H. Williamson. Low-storage runge-kutta schemes. *Journal of Computational Physics*, 35(1):48–56, 1980.

[127] WE Wilson, Judith C Chow, Candis Claiborn, Wei Fusheng, Johann Engelbrecht, and John G Watson. Monitoring of particulate matter outdoors. *Chemosphere*, 49 (9):1009–1043, 2002.

[128] Thorsten Wittemeier. Performance Analysis of the DNS and Particle Transport Model PANDORA. Technical report, University of Southampton, 2016.

[129] Thorsten Wittemeier, Timothy G Foat, Steven Herring, John S Shrimpton, and Zheng-Tong Xie. A new method for the evaluation of puff dispersion field experiments for the validation of time-resolved dispersion simulations. *Atmospheric Environment*, 210:171–176, 2019.

[130] Thorsten Wittemeier, David Scott, and John Shrimpton. Pandora upgrade: Particle dispersion in bigger turbulent boxes.

[131] Thorsten Wittemeier and John S Shrimpton. Explanation of differences in experimental and computational results for the preferential concentration of inertial particles. *Computers & Fluids*, 2018.

[132] A. M. Wood, W. Hwang, and J. K. Eaton. Preferential concentration of particles in homogeneous and isotropic turbulence. *International Journal of Multiphase Flow*, 31(10-11):1220–1230, 2005.

[133] JC Wyngaard and OR Coté. The budgets of turbulent kinetic energy and temperature variance in the atmospheric surface layer. *Journal of the Atmospheric Sciences*, 28(2):190–201, 1971.

[134] PK Yeung, DA Donzis, and KR Sreenivasan. Dissipation, enstrophy and pressure statistics in turbulence simulations at high reynolds numbers. *Journal of Fluid Mechanics*, 700:5–15, 2012.

[135] MV Zagarola, AE Perry, and AJ Smits. Log laws or power laws: The scaling in the overlap region. *Physics of Fluids*, 9(7):2094–2100, 1997.